Thesis presented to the Instituto Tecnológico de Aeronáutica, in partial fulfillment of the requirements for the degree of Doctor of Science in the Graduate Program of Physics, Field of Nonlinear Dynamics and Complex Systems.

Sophia Rodrigues Laranja

A LONG-TERM QUIET- AND STORM-TIME INVESTIGATION OF THE IONOSPHERE USING SATELLITE AND RADAR DATA

Thesis approved in its final version by signatories below:

Dr. Marco Antonio Ridenti

Advisor

Dr. Jayr de Amorim Filho

Co-advisor

Dr. Bela G. Fejer

Co-advisor

Campo Montenegro
São José dos Campos, SP - Brazil
2024

BIBLIOGRAPHIC REFERENCE

CESSION OF RIGHTS

Documento assinado digitalmente
gov.br **SOPHIA RODRIGUES LARANJA**
Data: 14/08/2024 19:31:23-0300
Verifique em https://validar.iti.gov.br

Sophia Rodrigues Laranja
Rua Abolição, 87 - Bl. 3, Ap. 125
12.245-500 – São José dos Campos–SP

A LONG-TERM QUIET- AND STORM-TIME INVESTIGATION OF THE IONOSPHERE USING SATELLITE AND RADAR DATA

Sophia Rodrigues Laranja

Thesis Committee Composition:

Prof. Dr.	Érico Luiz Rempel	Chairperson	-	ITA
Prof. Dr.	Marco Antonio Ridenti	Advisor	-	ITA
Prof. Dr.	Jayr de Amorim Filho	Co-advisor	-	ITA
Prof. Dr.	Bela G. Fejer	Co-advisor	-	USU
Prof. Dr.	Maurício Tizziani Pazianotto	Internal Member	-	ITA
Dr.	Eurico Rodrigues de Paula	External Member	-	INPE
Dr.	Paulo Roberto Fagundes	External Member	-	UNIVAP

ITA

To my parents, who believed in me and supported me every step of the way.

Acknowledgments

I would first like to thank my mentors from beyond the physical matter, who have guided me and given me strength throughout my academic journey.

I thank my mother, Alessandra, for all the encouragement, support, and affection throughout every moment of my life. She is my greatest strength, and without her, none of this would have been possible. I thank my father, Mário Sérgio, for all the effort and hard work to provide for me and my siblings.

I thank my siblings, Mayra and Arthur, for always being by my side and for all the life advice, including professional guidance. I am very lucky to call my siblings my best friends.

To Caroline, for being my greatest support in every moment and never letting me doubt myself. You are a blessing in my life, and I am very fortunate to have you.

I thank my advisor, Dr. Marco Antonio, for all his patience and shared wisdom throughout this work. I am very grateful for the opportunities he gave me, for his dedicated guidance and trust in me. I also thank my co-advisor, Dr. Jayr de Amorim, for his guidance, suggestions, and valuable contributions.

A special thank you to my co-advisor as well, Dr. Bela Fejer, who guided me during my time at Utah State University. I thank him for all the learning and patience with me. His dedication to my growth and his expertise have deeply influenced my academic journey.

To the friends with whom I shared the classrooms of ITA and that I made in São José dos Campos, for their kindness and friendship.

To the Aeronautics Institute of Technology for the infrastructure, and to Coordenação de Aperfeiçoamento de Pessoal de Nível Superior (CAPES) for the financial support during the execution of this research project.

"Remember to look up at the stars and not down at your feet. Try to make sense of what you see and wonder about what makes the universe exist. Be curious. And however difficult life may seem, there is always something you can do and succeed at. It matters that you don't just give up."

— STEPHEN HAWKING

Resumo

A ionosfera da Terra exibe o mais alto nível de complexidade em latitudes médias e baixas. Para entender a física dessas regiões, é comum recorrer a técnicas experimentais e modelos teóricos. Portanto, esta tese investiga os processos fundamentais em latitudes médias e baixas sob condições geomagnéticas tanto calmas quanto ativas, utilizando dados experimentais e fundamentos teóricos para este fim. Através da integração de dados de satélite e de solo, foram conduzidos três estudos principais: exame da climatologia da densidade iônica usando a sonda de Langmuir FPMU (Floating Potential Measurement Unit) a bordo da Estação Espacial Internacional, análise da climatologia da velocidade de deriva vertical utilizando o IVM (Ion Velocity Meter) a bordo do satélite C/NOFS, e investigação de campos elétricos de perturbação equatorial durante tempestades geomagnéticas utilizando dados do radar de espalhamento incoerente de Jicamarca e modelos empíricos de deriva vertical. As descobertas a partir da análise da densidade de íons revelaram variações significativas ao longo das estações e longitudes, com anomalias notáveis observadas durante os solstícios, incluindo a descoberta de um bulbo na crista sul da Anomalia de Ionização Equatorial (EIA) sobre o Atlântico Sul. Dados da deriva vertical de íons em momentos quietos perto do equador mostraram variações sazonais e longitudinais significativas devido a fatores como marés troposféricas, ventos na região F e o deslocamento entre os equadores geográfico e geomagnético. Além disso, foram observadas derivas negativas durante a tarde em todas as estações, contradizendo o conhecimento existente sobre esta região. Durante tempestades geomagnéticas, características comuns incluíram mudanças nos campos elétricos equatoriais impulsionadas por variações na componente Bz do campo magnético interplanetário, subtempestades, e campos elétricos de dínamo perturbado, com sua intensidade variando com base em fatores como hora local e magnitude do vento solar. Destacou-se que, durante tempestades intensas, a prolongada dominância dos campos elétricos de penetração atrasou a transição da deriva ascendente para descendente. Esta tese evidencia a dinâmica complexa da ionosfera equatorial, promovendo a necessidade de modelos aprimorados para prever com precisão as respostas ionosféricas a condições geomagnéticas diversas.

Abstract

The Earth's ionosphere exhibits the highest level of complexity in middle and low latitudes. To understand the physics of these regions, it is common to resort to experimental techniques and theoretical models. Therefore, this thesis investigates the fundamental processes at middle and low latitudes under both quiet and active geomagnetic conditions, utilizing experimental data and theoretical foundations for this purpose. Through the integration of satellite and ground-based data, three primary studies were conducted: the examination of ion density climatology using the FPMU (Floating Potential Measurement Unit) Langmuir probe on board the International Space Station, analysis of vertical drift velocity climatology utilizing the IVM (Ion Velocity Meter) on board the C/NOFS satellite, and investigation of equatorial perturbation electric fields during geomagnetic storms utilizing Jicamarca ISR (Incoherent Scatter Radar) data and empirical vertical drift models. Our findings from the ion density analysis revealed significant variations across seasons and longitudes, with notable anomalies observed during the solstices, including a newly found bulge in the equatorial ionization anomaly southern crest over the South Atlantic. Quiet-time vertical ion drift data near the equator showed significant seasonal and longitudinal variations due to factors like tropospheric nonmigrating tides, F region winds, and the geographic-geomagnetic equator displacement. Additionally, downward afternoon drifts were observed in all seasons, contradicting the existing knowledge of this region. During geomagnetic storms, common features included changes in equatorial electric fields driven by IMF Bz variations, substorms, and disturbance dynamo electric fields, with their strength varying based on factors like local time and solar wind intensity. Notably, during intense storms, the dominance of prompt penetration electric fields was prolonged, delaying the transition from upward to downward drifts. This thesis underscores the complex dynamics of the equatorial ionosphere, promoting the need for improved models to accurately predict the ionospheric responses to diverse geomagnetic conditions.

List of Figures

List of Tables

Contents

1 Introduction

1.1 Motivation and goals

The ionosphere at middle and low latitudes is characterized by several phenomena driven by complex interactions between ionospheric and magnetospheric electric fields, E- and F-region neutral winds and atmospheric waves mediated by the magnetic field (RISHBETH; GARRIOTT, 1969). The use of Low Earth Orbit (LEO) satellites enhances our ability to understand the distinct characteristics of the middle and low latitude ionosphere, offering valuable insights into the Earth's upper atmosphere. Many new ionospheric phenomena were recently discovered using satellites. For example, Liu *et al.* (2022) discusses in detail the contributions of FORMOSAT-3/COSMIC (F3/C) on the low- and mid-latitudes ionosphere using data from 2006 to 2020. They give a comprehensive explanation on the new findings that this constellation of satellites acquired over the ionosphere of these regions, such as the longitudinal structure wavenumber-4 (WN4) (CAI *et al.*, 2020; LIN *et al.*, 2007; REN *et al.*, 2009; SAGAWA *et al.*, 2005; WAN *et al.*, 2008), the annual asymmetry, i.e., the electron density near December solstice being larger than near the June solstice (BURNS *et al.*, 2012; ZENG *et al.*, 2008), the semi-annual variation, i.e., the equatorial ionization anomaly (EIA) during equinox being stronger than during solstices (QIAN *et al.*, 2013), and the interhemispheric asymmetry near the solstices (LUAN *et al.*, 2015) and equinoxes (BALAN *et al.*, 2013).

In the present work, we use data from two satellites to investigate the ionosphere at middle and low-latitudes. Data from the Langmuir probe that is part of the Floating Potential Measurement Unit (FPMU) aboard the International Space Station (ISS) was used to give a comprehensive view of the ionosphere at middle and low latitudes at about 400 km. In more details, we use FPMU measurements from 2008 to 2019 for the first comprehensive study of the seasonal and solar cycle-dependent quiet time mid- and low-latitude F region climatology and large-scale structures at $\sim$400 km. We focus on the evolution of evening and nighttime low-latitude ionospheric structures during moderate solar activity (130 sfu – solar flux unit, 1 sfu = 10^{-22} W m^{-2} Hz^{-1}) and magnetically quiet conditions (Kp < 3). The ISS altitude coincides with that of the F-layer peak ($\sim$400

km), making this instrument a unique ionospheric investigation tool.

We also use data from the Communication/Navigation Outage Forecasting System (C/NOFS) satellite. C/NOFS was a mission of the Air Force Research Laboratory whose primary purpose was to forecast the presence of ionospheric irregularities that impact communication and navigation systems. More precisely, plasma structures are created in the lower layers of the ionosphere during the day, and they can reside in these regions most of the time also at night. However, if specific conditions allow the penetration of the structured regions into the F layer of the ionosphere, then the plasma structures may be of sufficient magnitude to create disturbances in the form of *scintillations* (e.g., WOODMAN, 1970; BOOKER; WELLS, 1938). Moreover, the scintillation effect has not yet been resolved, in terms of their prediction, due to the complicated interactions of electromagnetic signals and their reflections with the highly irregular and inhomogeneous medium of the equatorial plasma bubbles (EPBs), which can be briefly defined as regions of low ionospheric plasma density. Another satellite mission worth mentioning here is the SPORT (Scintillation Prediction Observations Research Task) project (e.g., SPANN *et al.*, 2017), a joint US-Brazil mission whose main objective is also to forecast ionospheric irregularities.

For the C/NOFS, we performed a vertical drift velocity climatology to show how this parameter behave during quiet-times (Kp < 3) and in different seasons in the low-latitude American sector. We use C/NOFS data from 2009 to 2015 and separate it in two different solar flux levels and two longitude sectors within the low-latitude American region. Additionally, we use vertical drift velocity measurements from the Jicamarca Radio Observatory (JRO), located in Lima, Peru, during storm-time periods. Hence, the goal is to provide a complete view of the vertical drift velocity at ionospheric F-region heights, i.e., during quiet (using C/NOFS data) and disturbed (using JRO data) times. The JRO operates in two main modes, the incoherent scatter radar (ISR) mode, employing high-power transmitters, and the Jicamarca Unattended Long-term Investigations of the Ionosphere and Atmosphere (JULIA) mode, utilizing low-power transmitters. We evaluate five geomagnetic storms using these modes to investigate the effects of the penetration of multi-process magnetospheric electric fields in low-latitudes. Additionally, three empirical vertical drift models are studied to assess the different storm-time electric fields at low latitudes.

Geomagnetic storms strongly disturb the low latitude ionosphere and thermosphere. Studies spanning several decades have investigated ionospheric electrodynamic disturbances driven by the interplanetary magnetic field (IMF), extending from high to equatorial latitudes (e.g., MATSUSHITA, 1953; NISHIDA, 1968a; RASTOGI, 1962). Since the early 1970s, advancements in ionospheric radar measurements have provided detailed insights into the response of middle and low latitude ionospheric electric fields

to geomagnetic disturbances (BLANC, 1978; CHANDRA; RASTOGI, 1974; FEJER *et al.*, 1976; MATSUSHITA; BALSLEY, 1973; RASTOGI; PATEL, 1975). These studies reveal that large-scale magnetospheric electric fields, driven by the IMF and affecting the high-latitude ionosphere, can be transmitted almost instantaneously to middle and low latitudes through the Earth-ionosphere waveguide (e.g., KIKUCHI *et al.*, 1978). During magnetic storms, ionospheric disturbance electric fields result from complex interactions of multi-source driven prompt penetration and disturbance dynamo electric fields (e.g., FEJER *et al.*, 2007; MARUYAMA *et al.*, 2005), making the understanding of the vertical drift in low latitudes even harder.

To summarize, this thesis has three main goals: to explore the underutilized FPMU data in view of the long-term ion density climatology of the mid- and low-latitude ionosphere under varying geospace conditions; to use the ion velocity meter (IVM) aboard the C/NOFS satellite for the first time in a climatological study of the American sector at low latitudes; and to investigate the penetration of magnetospheric-origin electric fields at low latitudes during geomagnetic storms using JRO vertical drift data, empirical vertical drift models and solar wind parameters. Specifically, the first goal is the understanding of the ionosphere's ion density behavior, namely, how it usually presents itself in a long-term basis. In other words, the first objective is to learn about the ionospheric ion density climatology and use it to recognize the standard plasma density background of the ionospheric F-region when different geospace conditions are present (i.e., different solar cycle phases and seasons). To get to this standard ionospheric behavior, data from the FPMU is used, spanning a period from 2008 to 2019. Data from the International Reference Ionosphere 2020 (IRI-2020), an empirical model that describes the ionosphere, is also used for comparisons with the FPMU/ISS data, in an expectation of comparing theory (IRI-2020) with what is actually observed (FPMU/ISS). This climatological study with the FPMU ion density generated an article published in December 2023 in *Journal of Geophysical Research: Space Physics*, entitled "Ion Density Climatology Based on FPMU Measurements on Board the International Space Station", available at `https://agupubs.onlinelibrary.wiley.com/doi/abs/10.1029/2023JA031980`. We also use electron temperature FPMU measurements for a brief evaluation of the phenomenon called morning overshoot and to statistically analyze this parameter. We did not use the electron temperature in details, because it is currently being re-evaluated (DEBCHOUDHURY *et al.*, 2021), hence, the temperature shown here is preliminary. However, since other works (see Section 1.3.1) validated and used the FPMU electron temperature scientifically, we consider the analysis performed here reliable.

The second goal of this thesis is to generate a climatology of the vertical drift velocity in the American sector at low latitudes. This will allow a significant contrast when

investigating storm-time effects. The second objective is achieved using the ion velocity
meter (IVM) aboard the C/NOFS satellite. The vertical drift velocity provided by the
IVM is still largely unexplored in its entirety, so that we use it for the first time in a
climatological study of the American sector and evaluate its reliability. In many cases, as
will be demonstrated here, the velocity returned by the IVM does not behave as expected.
Therefore, the content of the second objective is more concise compared to the others.
Consequently, only a brief analysis of the vertical velocity in the low-latitude American
sector under quiet conditions will be provided, although sufficient for a climatological
comprehension.

The third main objective of this thesis is the analysis of different geomagnetic storms
to investigate how the penetration of magnetospheric-origin electric fields is observed at
low latitudes. The penetration of these electric fields is due to various magnetospheric
processes. How these distinct processes individually affect the ionosphere is still a matter
of debate in the literature. For the thesis' third goal, vertical drift velocity data from
JRO during five geomagnetic storms are utilized, along with solar wind parameters and
geomagnetic indices. Three widely used empirical vertical drift models are also used in
detail in these storms, aiming a comparison with the JRO data and to understand in
more details the different storm-time electric field contributions. One of the evaluated
storms occurred on April 23-24, 2023, which resulted in a scientific paper published in
February 2024 in the journal *Frontiers in Astronomy and Space Sciences*, available at
`https://www.frontiersin.org/articles/10.3389/fspas.2024.1351735/full`.

1.1.1   Organization of the text

In this first chapter, the scientific motivation and goals of this thesis are set, along with
a general introduction to the ionosphere at middle and low latitudes. The next section
gives a broad general introduction to the terrestrial ionosphere region. To close the first
chapter, considerations on previous works that used the FPMU probe on board the ISS
and the IVM on board the C/NOFS for scientific purposes will be given, reinforcing the
main differences between these and what is done in the present work.

After the brief introduction to the ionosphere given in this chapter, Chapter 2 will
focus on the ionospheric low-latitude and mid-latitude electrodynamics, so that the
experimentally observed behavior may be theoretically explained. Given the scope of
this work, there is no space to start from the first principles of the ionospheric science,
particularly with regard to its chemistry and related topics. Hence, hopefully the first
two chapters will provide enough background to make the remainder of the text
understandable.

Chapter 3 explains in detail the methods used, that is, all the instrumentation

necessary to return the ionospheric parameters in question: ion density, electron temperature, and vertical drift velocity, as well as the methodology utilized to treat the FPMU, C/NOFS, JRO, and IRI data. Chapter 4 encompasses all the results of this thesis, reinforcing and supporting what is seen in the literature, but also suggesting new characteristics on some ionospheric phenomena poorly explored or detected by models. Furthermore, discussions about these results are made, in an attempt to generate a more contemporary ionospheric climatology and a more detailed understanding of storm-time electric fields in low latitudes.

Lastly, Chapter 5 closes the text with the main conclusions obtained throughout this thesis.

1.2 Theoretical and experimental background

1.2.1 Earth's ionosphere fundamentals

The ionosphere is considered to be that region of an atmosphere where a significant number of free thermal (< 1 eV) electrons and ions are present (SCHUNK; NAGY, 2009). However, a high or relevant density of free electrons and ions is not the ideal definition because these particles are present at all altitude in the lower and upper atmosphere of the Earth. Thus, there are many definitions for the Earth's ionosphere, an interesting one chosen to be put here is: *"The ionosphere of the Earth is taken to be that portion of the upper atmosphere where ions and electrons of thermal energy are present in quantities sufficient to affect the propagation of radio waves"* (ZOLESI; CANDER, 2014). Specifically, the Earth's ionosphere is situated between 60 km and 1000 km altitude, where free electrons and ions are produced via ionization of the neutral particles both by extreme ultraviolet (EUV) radiation from the Sun and by collisions with energetic particles that penetrate the atmosphere.

Due to the strong influence of gravity, the atmosphere and ionosphere are to first order horizontally stratified (KELLEY, 2009). The atmosphere can be organized by a representative temperature profile, whereas the ionosphere can be better represented by the number density of the plasma. Hence, when considering the level of electron density, the ionosphere can be structured in layers (Figure 1.1), despite the fact that different processes dominate in different latitudinal domains: D, E and F (under certain solar-terrestrial conditions the F region is split into the F_1 and F_2 layers during the daytime. Occasionally, an additional F_3 layer may also form, though this phenomenon is beyond the scope of this discussion). The E layer was the first one to be detected, followed by the F and D layers. In general, the F layer is characterized by a high degree of ionization

and presents variations in electron density due to the production, loss and transport of electron-ion pairs with changes in solar activity and time of day.

More specifically, the F region is usually divided into three subregions. The lowest region, where photochemistry dominates, is called the F_1 region. The region where there is a transition from chemical to diffusion dominance is called the F_2 region, and the upper F region, where diffusion dominates, is called the topside ionosphere. The latter is defined to be the region above the F_2 peak where O^+ is the dominant ion, extending from about 600 km to 1500 km at midlatitudes, for example. Regarding to the most important chemical reactions, photoionization of neutral atomic oxygen and ion loss in reactions with N_2, O_2 and NO by charge exchange can be cited in the F_1 layer, and its photochemistry is simpler because only one ion, the atomic oxygen (O^+), dominates. Transport processes become important in the F_2 and upper F regions, including ambipolar diffusion and wind-induced drifts along the magnetic field, **B**, and electrodynamic drifts across **B** (SCHUNK; NAGY, 2009). Also, the region above the topside ionosphere, i.e., the outer part of the ionosphere, is referred to as protonosphere (also called plasmasphere), where H^+ becomes the dominant ion.
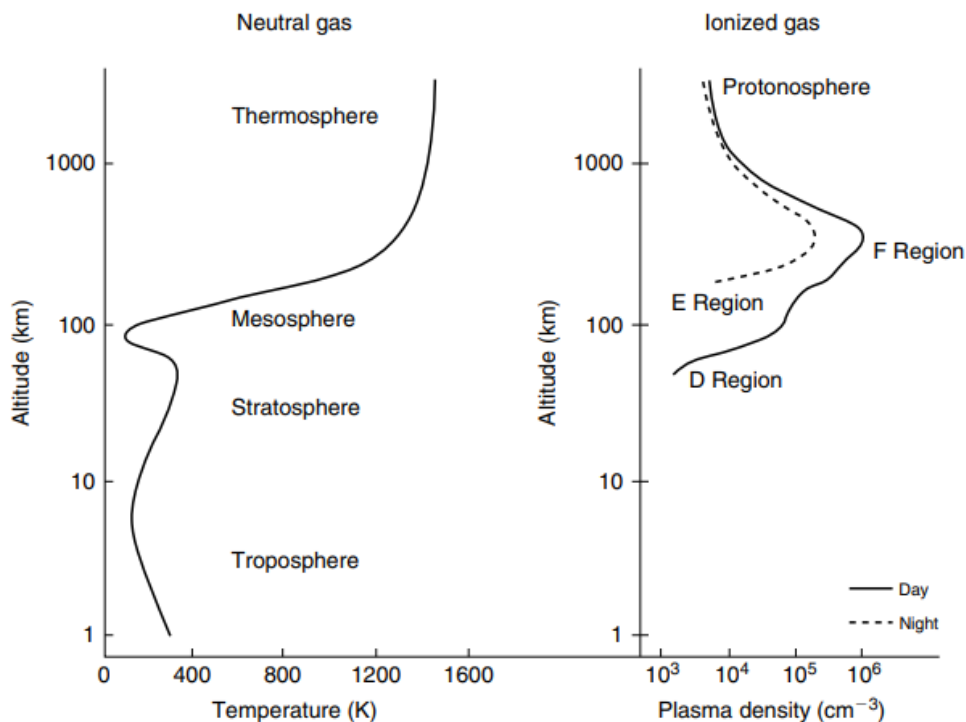
FIGURE 1.1 – Typical midlatitude profiles of neutral atmospheric temperature and ionospheric plasma density with its various layers (KELLEY, 2009).

Figure 1.1 displays important ionospheric and atmospheric patterns. The atmospheric temperature initially decreases with altitude from the surface, with a rate of about 7 K/km in the troposphere. At about 10 km altitude this temperature trend reverses at the tropopause. That is where the stratosphere begins, being in control of the absorption, by

ozone, of part of the ultraviolet portion of the solar radiation, a process that increases
the temperature. This effect maximizes at 50 km, where the temperature trend again
reverses at the stratopause. For heights above the altitude of the temperature minimum,
the mesopause, the temperature increases due to absorption of ultraviolet (UV) and EUV
radiation from the Sun. A key feature of this ionization process is that equal numbers
of positive ions and electrons are produced. This is especially important because one
requirement for a gas to be termed a plasma, which is the case of the ionosphere, is that
it very nearly satisfies the requirement of charge neutrality. Thus, the number density
of ions, N_i (also found as n_i throughout this text), must be nearly equal to the number
density of electrons, N_e, that is, $N_e \approx N_i$, in the Earth's ionosphere (KELLEY, 2009).

Furthermore, Figure 1.1 shows two plasma density profiles on the right side, one typical
of daytime (solid line) midlatitude conditions and one typical of nighttime (dashed line).
In the daytime, the density increases exponentially with decreasing altitude. This can
be explained owing to the fact that when the photons are absorbed in the process of
photoionization, the solar flux, when penetrating the atmosphere, decreases in intensity.
The combination of decreasing solar flux, increasing neutral density, and diffusion provides
a simple explanation for the basic large scale vertical layer of ionization shown (KELLEY,
2009). The peak plasma density occurs in the F layer and can reach values as high as 10^6
cm^{-3} near noon time. In this case, the peak density value is limited by the recombination
rate, which is the rate at which ions and electrons combine to form neutral molecules or
atoms. This depends, in turn, on the type of ion that exists in the plasma as well as its
corresponding interaction with the neutral gas (KELLEY, 2009). Also, in the case of the
F layer, the F_1 layer decays at night and a distinct E-F valley can appear, separating the
E and F_2 layers.

Generally, the E and F layers are described by critical frequencies (f_0E, f_0F_1, f_0F_2).
The critical frequency, which is proportional to $n_e^{1/2}$, is the maximum frequency that can
be reflected from a layer. In other words, electromagnetic waves with frequencies higher
than the critical will penetrate the layer and propagate to higher altitudes. Associated
with each critical frequency is a peak density (N_mE, N_mF_1, N_mF_2) and a peak height
(h_mE, h_mF_1, h_mF_2), which is the altitude of the density maximum (SCHUNK; NAGY,
2009).

1.3   State-of-The-Art

1.3.1   FPMU probe

To illustrate how this work differs from previous researches in using FPMU data for scientific purposes, a brief summary of past studies will be provided in this section. FPMU data has frequently been used to validate its measurements during geomagnetic storms, as demonstrated by Coffey *et al.* (2008). They associate the importance of the validation of plasma density and temperature with spacecraft charging issues, which includes hazards to the ISS crew during extravehicular activities (EVAs). Coffey *et al.* (2008) also mention that the knowledge of the ionospheric plasma environment is applied as input to ISS spacecraft charging models. These models are important because they are able to predict the severity and frequency of occurrence of ISS charging. Also, the validation of these charging models requires the comparison of their predictions with measured FPMU values. Finally, Coffey *et al.* (2008) make this comparisons and consider them successful since they demonstrate that FPMU instruments are measuring in-situ ionospheric density and temperatures consistent with those obtained from independent remote sensing techniques.

As an another example of using FPMU during geomagnetic storm conditions aiming its validation, Coffey *et al.* (2017) present strong responses of concomitant particle measurements from the high-altitude Magnetospheric Multiscale Mission (MMS) and from the low-altitude (F region) FPMU data. They analyzed the potential causes of the dramatic particle flux dropouts observed by both instruments by contextualizing them within storm-time electrodynamics. Their observations indicated that both MMS flux dropouts and the onsets of ionospheric FPMU-observed equatorial instabilities are electrodynamic responses to large and sudden changes in the IMF southward component (B_z).

Hartman *et al.* (2019) also use FPMU data to support the ISS with charging issues. Additionally, they correlated the environmental conditions they studied with IRI values. This model was used to forecast what could occur to the ionospheric region in the event of a severe geomagnetic storm. If the FPMU fails, the ISS team needs another source of data to support a short-term forecast for EVAs. Hence, the work is responsible for the IRI Real-Time Assimilative Mapping (IRTAM) model, an ionospheric model that uses real-time measurements from a large network of digisondes. The outputs of the IRTAM model were compared to FPMU measurements and had excellent agreement. To conclude, IRTAM has been identified as the FPMU backup system to support the ISS Program if FPMU fails.

Another work that is focused on forecasting the ISS environment is the one by

Broadwater (2013). This author uses ionospheric models to predict the ISS environment due to the limited availability of FPMU data. An ionospheric model that accurately predicts the ISS plasma region is desirable for ISS mission planning when FPMU data is unavailable. Thus, this author's thesis uses electron densities and temperatures from four ionospheric models (IRI, Coupled Thermosphere Ionosphere Plasmasphere Electrodynamics model - CTIPe, Ionospheric Forecast Model - IFM, and Global Assimilation of Ionospheric Measurements model - GAIM) and compare them to in-situ FPMU values across a range of geomagnetic and solar conditions. The author concluded that the climatological and assimilative models (IRI and GAIM) performed the best overall across all conditions, while the pure physics based models (IFM and CTIPe) struggled the most to accurately predict the ISS plasma environment. Most of the struggling was during severe solar minimum conditions and periods of moderate and high solar activity. Finally, IRI and GAIM represent the best candidates for use by NASA as an ISS mission planning tool.

The rapid increase of electron temperature in the early morning hours at low latitudes is a well-known ionospheric phenomenon called *morning overshoot.* This phenomenon will be studied in some detail in Chapter 2. That being said, Yang *et al.* (2020) extensively investigates the dependence of the morning overshoot on local time, season, geographic location (latitude, longitude, altitude), and magnetic activity. The electron temperature and density data used in this study were obtained from the Swarm satellite constellation and FPMU. The Swarm is at two different altitudes, 470 km and 520 km, and FPMU is around 400 km. Hence, Swarm and FPMU are at different altitudes, providing a broader view to the morning overshoot problem. Based on data between 2014 and 2019, they found that on a global average, the morning overshoot generally weakens with decreasing altitude and is stronger around the dip equator. As latitude increases, the overshoot gradually decreases and shifts to later local times. Another important finding of the study by Yang *et al.* (2020) is that in off-equatorial regions the overshoot is stronger in the winter than in the summer hemisphere, especially at higher altitudes. Lastly, the morning overshoot shows multiday oscillations, which are negatively correlated with plasma density.

As a more recent work, Debchoudhury *et al.* (2021) (in which the main author is one of the researchers responsible for developing the FPMU output data algorithm) use the FPMU data aiming the validation of plasma density, temperature and O^+ abundance. The O^+ composition is a new parameter returned by FPMU after changes in the original data algorithm. In more details, the work by Debchoudhury *et al.* (2021) gives details of the changes made in the FPMU algorithm to address aging instrumentation, changing solar activity, as well as enhancements to the algorithm to give new data products. In particular, one source of error in the original FPMU analysis algorithm is the uncertainty associated with photoelectron emission current, which may contribute to errors in estimated densities.

Another possible source of error is during times of low solar activity, where the erroneous assumption that the F-region ionosphere around the ISS orbit consists primarily of O^+ ions is often made. While this assumption may be true for solar maximum, the dominance of O^+ can decrease sufficiently enough during periods of low solar activity, so that the effects of H^+ ions cannot be neglected. The authors also validate the new FPMU data algorithm output making comparisons with the incoherent scatter radar at Millstone Hill and the IRI model.

The study by Debchoudhury *et al.* (2022) follows a similar line to the one mentioned in the last paragraph. However, this time the authors focus on the O^+ composition and its behavior during solar minimum. The O^+ composition dataset from the recent minimum in the Solar Cycle 24 is studied with FPMU data, where it revealed orbits with dropouts in O^+ to below 80% of the total background ion density at ISS orbital altitudes. Moreover, the observed O^+ percentages during these dropouts are much lower than the values predicted by the IRI-16 empirical model. The authors present the climatology of these O^+ dropouts with their dependency on season, local time and geographical location. The results show that the lowered O^+ percentages are more significant in the winter hemisphere and more observed in orbits in the pre-sunrise period. To summarize, the patterns in O^+ dropouts can be partially explained by the lowering of the O^+/H^+ transition height during solar minimum along with neutral wind variations.

To conclude this section, Newheart *et al.* (2022) present a few days of in-situ F-region electron density data with support from ground-based Global Navigation Satellite System (GNSS) and total electron content (TEC) to indicate the well-defined presence of the EIA at and around local midnight during geomagnetically quiet periods. Also, the magnitudes of the EIA crests during these periods appear to be modulated in longitude to display a 3-wave variation.

As mentioned above, previous FPMU studies either examined plasma density data only briefly or did not primarily focus on ionospheric investigation. The study performed here is an unprecedented use of FPMU densities since we are employing them for an in-depth climatological investigation of F-region ionospheric middle and low latitudes. We present observations and new characteristics of long-term structures of these regions, demonstrating the efficacy of a novel data set as a scientific tool for investigating ionospheric phenomena and providing a unique view of the low- and mid-latitude ionosphere.

1.3.2   C/NOFS satellite

In this section, a brief summary of past studies using the ion velocity meter aboard the C/NOFS satellite will be provided to clarify the differences from the present study. Unlike the FPMU, a large number of studies have utilized the IVM on board the C/NOFS. Therefore, only a few relevant to the current research will be briefly described.

A few studies used C/NOFS IVM to examine the characteristics and generation of EPBs during a solar minimum period (e.g., HUANG, 2017; HUANG et al., 2013; 2014; KIL et al., 2011; 2015). In the study conducted by de la Beaujardiere et al. (2009), significant vertical drifts of approximately 200 m/s were observed at dawn in the America-Africa and India-Indonesia longitude sectors, following substantial plasma depletion, even during quiet conditions. In contrast, Yizengaw et al. (2014) reported vertical ionospheric drift velocities over Africa ranging from -25 m/s to 25 m/s during daytime.

Rodrigues et al. (2011) used ion drift velocities from C/NOFS IVM to show the effects of the January 2009 sudden stratospheric warming (SSW) event on equatorial electric fields. Stoneback et al. (2011) observed C/NOFS vertical drifts within the range of -50 m/s to 50 m/s during quiet times in the longitude sector of 0° to 60°E. In more detail, Stoneback et al. (2011) used C/NOFS IVM to construct the mean meridional (vertical) ion drifts, ion densities, and O^+ concentrations during periods of low geomagnetic activity for the four seasons each year from late 2008 to 2010. As an illustration of comparisons between the IVM data and radar observations, Patra et al. (2014) conducted a study where they compared quiet-time C/NOFS IVM vertical drift observations with data from two radars situated over Kototabang (10.36°S magnetic latitude, Indonesia) and Gadanki (6.5°N magnetic latitude, India).

Dubazane and Habarulema (2018) established a numerical connection between the equatorial electrojet and the vertical drifts across the African region. They utilized magnetometer data and vertical drift observations obtained from C/NOFS IVM. Furthermore, they created models for vertical drift in the African sector by incorporating C/NOFS vertical drift data along with relevant physical and geophysical inputs.

Therefore, the study conducted here differs from those mentioned above because we utilized vertical velocity data from 2009 to 2015 focused on the American sector at low latitudes. Our approach provides a detailed climatology of this sector under two different solar flux conditions, one low and the other moderate, across all seasons.

2 The Low- and Mid-Latitude Ionosphere

The plasma parameters in the Earth's ionosphere exhibit significant variation with altitude, latitude, longitude, local time, season, solar cycle, and magnetic activity. It is a very complex part of the Earth's atmosphere, since its detailed dynamics is governed by a complicated interaction between motions of the neutral atmosphere, gravity, electromagnetic forces, pressure gradients, and plasma production and loss. However, the scope of this chapter is to provide sufficient theoretical background in order that the discussions in Chapter 4 may be intelligible. This chapter aims to succinctly present the current knowledge of the Earth's ionosphere climatology at low and middle latitudes, since one of the main goals of the thesis is to produce a climatology of its own, and for that it seems fair to review what is already known.

The data used in this study is from ionospheric regions at low and middle latitudes, in accordance with the ISS and C/NOFS orbits and Jicamarca's location. In this chapter, the dynamics and electrodynamics of the equatorial, low and mid-latitude ionosphere will be exposed, These regions exhibit distinct patterns from each other, particularly influenced by the orientation of the geomagnetic field. At the geomagnetic equator, where the field is horizontal, electric fields become more pronounced, leading to strong vertical drifts of ionization.

2.1 The ionosphere at equatorial and low latitudes

The knowledge that we have today of the equatorial ionosphere comes largely from measurements taken at the Jicamarca Radio Observatory, located in Lima, Peru (WOODMAN *et al.*, 2019). This incoherent scatter radar facility was designed to optimize measurements of plasma flow perpendicular to the Earth's magnetic field, which is nearly horizontal over the site. In this work, focus will be given in the study of the F region ionosphere, since it concentrates most of the phenomena observed in this text. Furthermore, the ISS orbits at an altitude of approximately 400 km, coinciding with the

height of the ionospheric F layer.

Due to vertical drifts of ionization, the equatorial ionosphere is higher in altitude when compared to midlatitudes, with the electron density presenting a minimum near the magnetic equator, i.e., a trough at the magnetic equator in the F_2 layer (APPLETON, 1946), and maxima at latitudes $\pm$ 15° to $\pm$ 20° on each side of the magnetic equator (in fact, these maxima are the highest average electron density throughout the whole Earth's ionosphere). This phenomenon of displayed minimum and maxima is called *Appleton anomaly* or *equatorial ionization anomaly* (EIA). The Appleton anomaly has its origin in the dynamo electric fields that are generated in the equatorial E region by thermospheric winds, being transmitted along the magnetic field lines to F region altitudes due to the high parallel conductivity. During the day, the dynamo electric fields are eastward, which causes an upward $\mathbf{E} \times \mathbf{B}$ plasma drift, where $\mathbf{E}$ is the electric field and $\mathbf{B}$ the magnetic field, while the reverse occurs at night. Hence, the plasma that is uplifted during the daytime diffuses down (away from the equator) due to the action of gravity and pressure gradients. This combination of electromagnetic drift and diffusion produces a fountain-like pattern of plasma motion called *equatorial fountain*. Finally, the result of the fountain effect is that ionization peaks are formed in the subtropics on both sides of the magnetic equator, the main characteristic of the above-mentioned EIA (SCHUNK; NAGY, 2009). Figure 2.1 shows schematically the EIA.
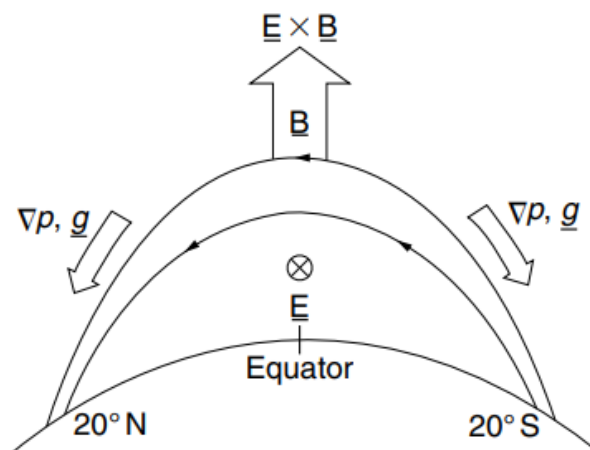
FIGURE 2.1 – The various forces acting on the plasma lifting via electric fields, which transport plasma from equatorial to tropical zones. Here, ∇p is the pressure gradient and $\underline{g}$ is the acceleration due to gravity (KELLEY, 2009).

2.1.1   Equatorial F-region

The various forces acting on charged particles drive electric currents that create electric fields, modifying the plasma dynamics. Thus, the electrical conductivity of the medium is of extreme importance, as well as the neutral wind variations, since the

ionosphere electrodynamics has a significant dependence on these two parameters (ZHANG; PAXTON, 2021). Hence, it is difficult to discuss the equatorial F region dynamics without understanding first the main characteristics of the thermospheric winds in this region, given the important role they play on the dynamo of the F layer. As will be seen in Chapter 4, thermospheric neutral winds are the main source of EIA latitudinal asymmetries. Thermospheric winds are a type of motion of the neutral atmosphere that occurs above about 120 km altitude, driven by pressure imbalances resulting from daily temperature variations (RISHBETH; GARRIOTT, 1969). Although the winds display a high degree of variability from day to day, to a first approximation the winds are eastward and very strong ($\sim$150 m/s) in the postsunset period, decaying in amplitude to less than 50 m/s after midnight (KELLEY, 2009). A simple model for the thermospheric wind would be that it is eastward and has a magnitude u uniform with height, with its vertical component considered to be small all the time. The wind vector is of the form $U = (u, v, w)$, where u, v, and w are the zonal (positive eastward), meridional (positive northward), and upward components, respectively.

As for the conductivities, these are highly anisotropic. The Pedersen conductivity (σ_P) is perpendicular to the geomagnetic field $\mathbf{B}$ and is in the direction of the electric field $\mathbf{E}$, whereas Hall conductivity (σ_H) enables current to flow perpendicular to both $\mathbf{B}$ and $\mathbf{E}$. In the ionosphere, the field-line integrated conductivities (conductances) are important. During the daytime, the conductances are largest in the E region, where the Hall conductivity dominates. Above the E layer, the Hall conductance decreases more rapidly with height than the Pedersen, which leads to the Pedersen conductivity dominating in the F region. During the nighttime, the E region Hall conductivity is very small due to the absence of solar incidence, and therefore the F region Pedersen conductivity dominates. However, due to the different path length of a field line in the E and F regions, the daytime Hall and Pedersen conductances can have similar magnitudes at low latitudes (CRAIN; HEELIS; BAILEY, 1993).

Figure 2.2a shows a schematic postsunset plasma density profile of the equatorial F layer. As can be seen in this Figure, there is a steep upward-density gradient at the bottomside due to the recombination of the molecular ions, resulting in a dense O$^+$ plasma with a well-defined lower boundary (KELLEY, 2009). The dominant O$^+$ ions support the F layer. Figure 2.2b details the physical processes occurring in the equatorial F-region. This Figure presents a slab geometry with σ_P constant inside the slab and zero elsewhere, also with a zonal wind u constant everywhere. In the neutral wind reference frame, $\mathbf{J}' = \sigma \cdot \mathbf{E}'$. However, since $\mathbf{E}' = \mathbf{E} + \mathbf{U} \times \mathbf{B}$ and $\mathbf{J} = \mathbf{J}'$ for nonrelativistic transformations, the current equation becomes

$$\mathbf{J} = \sigma \cdot (\mathbf{E} + \mathbf{U} \times \mathbf{B}) \tag{2.1}$$

where all parameters are measured in the Earth-fixed frame. From the equation above, an electric current will flow with magnitude and direction given by

$$\mathbf{J} \simeq \sigma \cdot (u\mathbf{a}_x \times \mathbf{B}) \tag{2.2}$$

that means that the wind-driven current is vertically upward inside the layer in Figure 2.2b, with magnitude $J_z = \sigma_P u B$ and zero outside. Then, charges pile up at the two boundaries (as shown in the Figure), and the magnitude of the electric field generated as a result of these charges is:

$$J_z = \sigma_P E_z + \sigma_P u B = 0 \tag{2.3}$$

Hence,

$$E_z = -uB \tag{2.4}$$
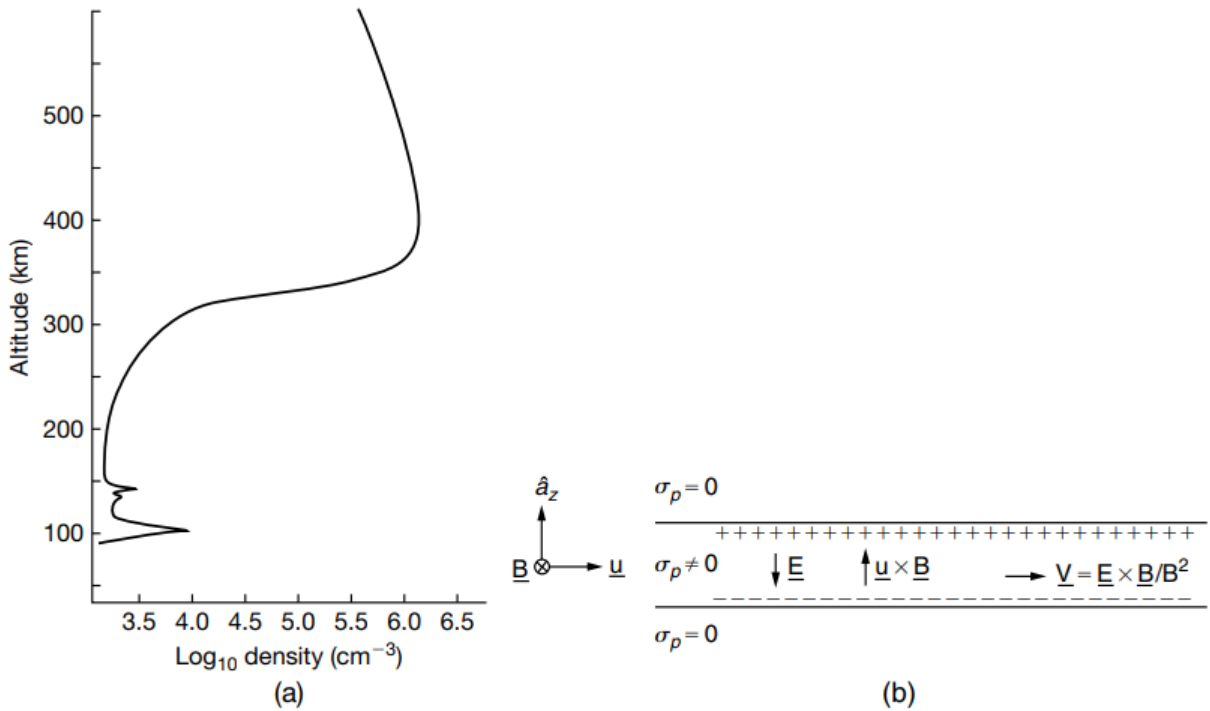
FIGURE 2.2 – (a) Equatorial plasma density profile in the evening local time period. (b) Equatorial F region density and conductivity profiles modeled with a slab geometry, subject to a constant zonal eastward neutral wind (KELLEY, 2009).

Also, the electric field in the neutral wind reference frame, $\mathbf{E}' = \mathbf{E} + \mathbf{U} \times \mathbf{B}$, vanishes, as can be seen in Equation (2.2). In more details, the current is independent of the reference frame as it was set to be equal to zero, $\mathbf{J} = \mathbf{J}' = \sigma_P \mathbf{E}' = 0$, so $\mathbf{E}'$ must be zero. Furthermore, the plasma inside the slab will drift with a velocity equal in magnitude and

direction to the zonal wind speed, that is, an $\mathbf{E} \times \mathbf{B}/B^2$ drift. As can be seen in Figure 2.2b, despite being a simple model, a strong shear in the plasma flow velocity can be observed at the interfaces, where the velocity changes notably from u to 0.

2.1.2 Pre-reversal enhancement

The EIA is closely related to the pre-reversal enhancement (PRE) of the zonal electric field or, equivalently, of the $\mathbf{E} \times \mathbf{B}$ vertical drift. The PRE is a sharp increase in the vertical ion drift velocities occurring shortly after local sunset, which is added to the usual daily pattern of upward drifts during the day and downward drifts at night (WOODMAN, 1970). This enhancement occurs due to the increase in the zonal electric field near the terminator on the dayside, which may vary with solar activity, seasons and magnetic declination (ABDU; BITTENCOURT; BATISTA, 1981; WOODMAN, 1970). From about dusk to midnight, the evening PRE plays a major role on the low latitude F-region plasma density. The PRE causes a brief and intense uplift in the height of the equatorial F-region, being the main driver of nighttime plasma density structures and small-scale irregularities (e.g., KELLEY *et al.*, 2009). We note that the PRE becomes maximum during dusk, with values ranging from 40 m/s to 80 m/s depending on the solar flux and seasons (ABDU *et al.*, 2010).
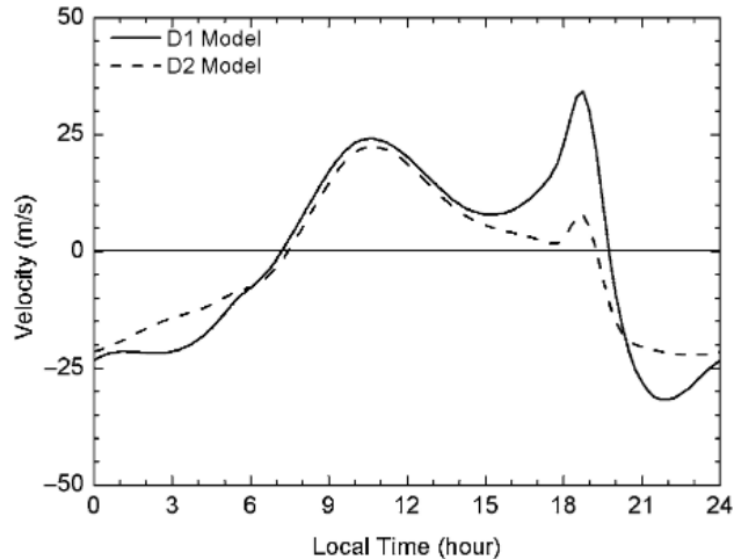
FIGURE 2.3 – Illustration of typical Brazilian equinoctial quiet-time vertical ion drift velocity for two different solar flux levels, D1 (high) and D2 (low) (BATISTA *et al.*, 2011).

Figure 2.3 shows an example of a typical equinoctial quiet-time variation of the vertical ion drift velocity as a function of local time, generated using SUPIM (Sheffield University Plasmasphere-Ionosphere Model) (BAILEY; SELLEK, 1990; BAILEY; SELLEK; RIPPETH, 1993), which was run for the Brazilian region (45°W) for two solar flux levels. The extent of development of the post-sunset EIA is directly linked to the amplitude of the PRE. The impact on the EIA can persist for long periods depending on the PRE

amplitude. As shown in Figure 2.3 the solar cycle effect of the PRE amplitude appears around sunset and at nighttime. In drift model D1 (high solar flux), the PRE amplitude is significantly higher than in model D2 (low solar flux). Additionally, in model D1, the enhancement begins much earlier, and the reversal happens later compared to model D2. These solar cycle aspects in the PRE behavior are reflected in the EIA development, as will be seen in the FPMU analysis (Chapter 4).

The mechanisms to explain the vertical $\mathbf{E} \times \mathbf{B}$ drift are based on the existence of a longitudinal conductivity gradient (east-west), which is greater at times close to the transition from day to night. In this way, near such a steep gradient, a zonal electric field is established to maintain $\nabla \cdot \mathbf{J} = 0$. Figure 2.4 schematically shows the mechanism for the development of the PRE, in which the equatorial plane is the vertical one. On the dayside, a zonal wind ($\mathbf{U}$) flows in the F region through the terminator, generating a vertical electric field E_z (responsible for the dynamo in the F region), directed downwards on both sides of the terminator. This field is much smaller on the dayside than on the nightside, but it is not negligible. Thus, this electric field (E_z) is mapped to lower altitudes through the magnetic field lines, $\mathbf{B}$. The E region, which has the highest conductivity during the daytime, receives this mapped field directed towards the equator (E_θ), giving rise to a Hall current towards the west ($J_{\theta\phi}$) on either sides of the terminator. However, even though E_z is smaller on the dayside, the Hall conductivity is more than ten times its nighttime value. This effect results in an accumulation of negative charges near the terminator, which generates an eastward zonal electric field, E_ϕ, the latter being the PRE. A current in the same direction, $J_{\phi\phi}$, cancels the Hall current ($J_{\theta\phi}$) mentioned above.
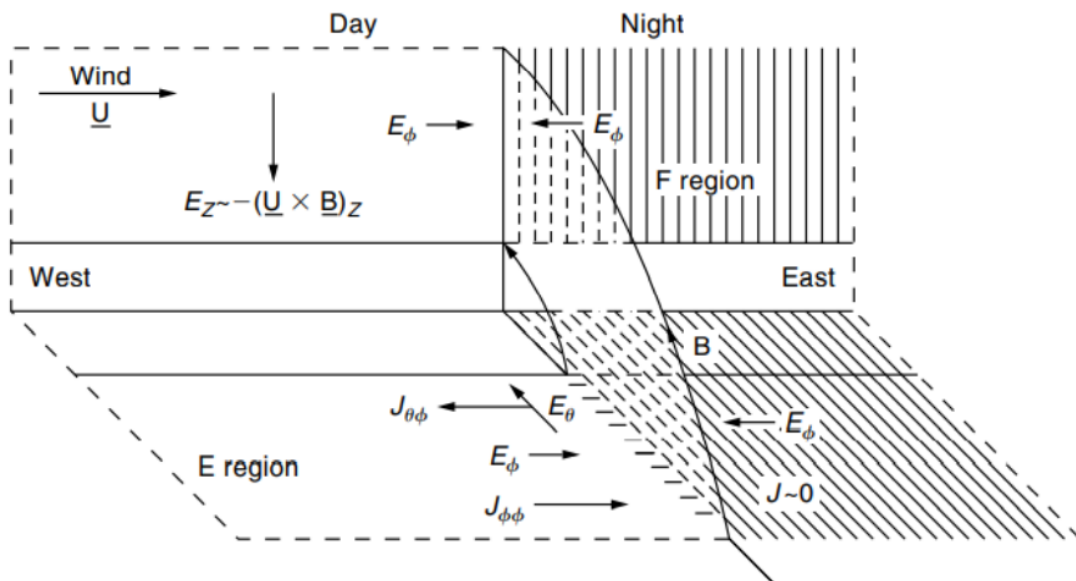
FIGURE 2.4 – Simplified model showing the pre-reversal enhancement mechanism (FARLEY et al., 1986).

Finally, the electric field E_ϕ, which is also present on the nightside due to the

accumulation of negative charges on the terminator, is mapped again to the F region on both sides and, when interacting with **B**, generates a vertical drift of the ionospheric plasma directed upwards on the dayside and downwards on the nightside (FARLEY *et al.*, 1986; KELLEY, 2009).

2.1.3 Asymmetries in the equatorial ionization anomaly

The occurrence of large ion density gradients associated with vertical plasma drifts and thermospheric neutral winds in the equatorial F-region has been known for over five decades (e.g., HANSON; SANATANI, 1971; WHARTON *et al.*, 1980). Longitudinal and seasonal (e.g., ENGLAND *et al.*, 2006; LIU *et al.*, 2006) differences in the winds are well-recognized, commonly generating seasonal (equinoxes versus solstices) and longitudinal (east versus west) asymmetries in the EIA. Seasonal differences in the meridional winds are associated with differences in the solar energy received and longitudinal differences in the winds have been associated with tides. It is known that the initial EIA latitudinal distribution is modified by the neutral-ion collisional drag that transports the ionization along the magnetic field lines at the same velocity as that of the wind component along it (BITTENCOURT; SAHAI, 1978). This plasma movement will give rise to asymmetric crests with respect to the magnetic dip equator with unequal values of electron densities and heights due to an inter-hemispheric transport of ionization. The ionization is moved upward in the upwind side and downward in the downwind side of the magnetic field line into regions of different recombination rates (BATISTA *et al.*, 2011). In the equatorial region, the daytime meridional winds are directed from the summer (upwind) to the winter (downwind) hemisphere (HUANG *et al.*, 2010). Additionally, the crest that is in the winter hemisphere tend to be closer to the dip equator than the crest in the summer hemisphere, which is associated with the upwind and downwind effect, shifting the crests' latitudes (e.g., CAI *et al.*, 2020; EASTES *et al.*, 2023; KHADKA *et al.*, 2018).

In general, the **E** × **B** motion creates latitudinally symmetric structures with respect to the geomagnetic equator. However, in the case of imbalanced meridional components of neutral wind on both sides of magnetic equator, induced field aligned motion of ions will cause asymmetries in the plasma density along the magnetic equator (BAILEY; SU; OYAMA, 2000; MACPHERSON *et al.*, 1998). Bankov *et al.* (2009) state that effects of geographic zonal and meridional neutral wind components on plasma distributions along the magnetic field are intrinsically dependent on magnetic declination, i.e., during the morning the zonal wind will have a north-to-south component in the magnetic meridian in regions of positive declination and a south-to-north component in regions of negative declination. During the evening this scenario reverses. Luan and Solomon (2008), using TIE-GCM (Thermosphere-Ionosphere-Electrodynamics General Circulation Model) simulations of

the neutral winds in both magnetic and geographic coordinates, revealed that most of the longitudinal variations of the magnetic meridional winds are a result of zonal wind and magnetic declination. Denoting the geographic zonal and meridional wind components as U_G and V_G, the magnetic meridional wind component (also called effective wind) can be expressed as:

$$V_M = V_G \cos(D) \mp U_G \sin(D) \tag{2.5}$$

The signs "-" and "+" correspond to winds in the Northern and Southern Hemisphere, respectively, and D is the magnetic declination angle (positive eastward). Zonal winds (U_G) are positive eastward, meridional winds (V_G) are positive equatorward. It can be noticed that V_M and V_G can differ significantly when D is nonzero and a strong zonal wind is present. When V_M is asymmetric between the hemispheres, the EIA becomes asymmetric with respect to the magnetic dip equator with stronger crest occurring in the hemisphere of equatorward or less poleward V_M (BALAN; LIU; LE, 2018b; BATISTA et al., 2011). This is because in the hemisphere of equatorward V_M the ionosphere is raised to high altitudes of reduced chemical loss and reduced downward diffusion, where the gain of ionization exceeds over the one in the opposite hemisphere of enhanced fountain due to poleward V_M (e.g., BALAN et al., 1997a). Hence, a wind component toward the magnetic equator will raise the F-layer producing a higher F-peak density at a higher altitude, while at the conjugate location the F-layer will be depressed producing a lower F-peak density.

The study by Balan et al. (2018a) expresses that the neutral wind modifies the ionosphere through its mechanical and neutral composition change effects. The mechanical effect comes through the effective magnetic meridional neutral wind velocity given in Equation (2.5). According to this Equation, when the magnetic declination angle D is nonzero, the magnetic meridional wind V_M and the geographic meridional wind V_G differ significantly. Batista et al. (2011) uses the Sheffield University Plasmasphere-Ionosphere Model (SUPIM) (BAILEY et al., 1997 and references therein) to investigate the EIA response to changes in zonal electric fields and thermospheric winds. They found that the thermospheric meridional wind can introduce asymmetries in height and density of the EIA crests and that the response of the equatorial F layer height to the meridional wind is very fast compared to the density asymmetry response. Thus, neutral winds have a major effect in the EIA general structure. Winds can also influence the vertical drifts, which have been linked to the strength of the EIA.

The latitude of the EIA crests also varies with the altitude of the equatorial F layer. The EIA bands tend to be farther from the magnetic equator at lower altitudes compared to higher altitudes during daytime (LIU et al., 2022). Xiong et al. (2013) found that the magnetic latitude of the EIA at ~400 km can reach higher latitudes around December

solstice during both high and low solar activity years, while at ∼480 km the crests are observed closer to the dip equator during low solar activity years. They observe a clear EIA inter-hemispheric asymmetry during solstice seasons.

The density variation during December solstice is greater than June solstice, as will be shown in the FPMU maps in Chapter 4. This is the so-called *annual asymmetry*. Based on the discussion by Zeng *et al.* (2008), the annual asymmetry of EIA can be attributed to the different solar radiation due to different Earth-Sun distance in June and December solstice, the offset of the geomagnetic center from the geographic center, and the lower atmospheric forcing. Additionally, the density variation during the equinox is stronger than during the solstices, which is the so-called *semi-annual density variation* (e.g., BALAN *et al.*, 1997b; BALAN *et al.*, 1998; BURNS *et al.*, 2012; QIAN *et al.*, 2013). Balan *et al.* (1997b, 1998) attribute this variation to solar zenith angle, thermospheric composition, and equinox-neutral winds, influencing chemical and dynamical processes. In more details, it is believed that this phenomenon occurs due to the optimized effect of the thermospheric composition and solar zenith angle at the equinoxes when the thermospheric circulation is most symmetric. Furthermore, Ma *et al.* (2003) suggest that the semi-annual variation of the diurnal tidal induces the semi-annual variation of the equatorial electrojet, and then it induces the semi-annual variation of the EIA by the fountain effect.

To conclude, the zonal electric field and the magnetic meridional neutral wind are the primary drivers that define the geometry and characteristics of the equatorial ionization anomaly. Moreover, the EIA crests display strong asymmetries in all seasons, solar flux levels and local time periods mainly due to the effect of neutral winds. Hence, neutral winds have a major effect in the EIA general structure. However, there are several other factors that can influence the EIA north-south asymmetry besides neutral winds. Liu *et al.* (2016) states that since the electron density in the F region is also determined by ambipolar diffusion, which in turn depends on electron temperature, it is possible that the electron temperature in both crests is different, causing different ambipolar diffusion. Alternatively, the occurrence of different density in each hemisphere changes the ambipolar diffusion. Khadka *et al.* (2018) found that the seasonal, solar activity, temporal, and longitudinal variations in EIA asymmetry also depend on the displacement of the geographic and geomagnetic equators. They also express that asymmetries between the geomagnetic field in each hemisphere give rise to an asymmetry in the solar radiation and neutral composition, possibly leading to hemispheric differences of the plasma density. A recent work by Eastes *et al.* (2023) point out that the latitude crests of the EIA during the equinoxes and winter solstice present similarities, indicating that the distance of the magnetic equator to the subsolar point influences the crests' location possibly more significantly than neutral winds, tides or magnetic declination. They state that some dependence on the subsolar point is not

surprising since ion production rates on the dayside have a solar zenith angle dependence. The subsolar point is a significant factor also during nighttime, given that the EIA within a few hours of sunset consists primarily of ions produced on the dayside.

2.1.4 Relevant equatorial daytime and nighttime phenomena

In this section, three significant equatorial phenomena will be addressed: the equatorial plasma bubbles, a vertical drift, the wavenumber-4 structure, a longitudinal drift, and the plasma depletion bays, a longitudinal structure. These three features are important in our Results and Discussion chapter (Chapter 4), thus, its main characteristics and formation mechanisms will be discussed in some detail.

2.1.4.1 Equatorial plasma bubbles

Plasma irregularities occurring in the F-region ionosphere are generally grouped under the name of *Equatorial Spread F* (ESF) (OSSAKOW, 1981). At night, the fully developed ESF is characterized by plasma bubbles, regions with large and medium scale dimensions that can rise to significant altitudes. Plasma bubbles are rarefied regions of plasma that develop in the nighttime ionosphere under peculiar electrodynamic conditions (near the daylight side of the terminator, the equatorial F layer rises due to the dynamo action of electric fields and subsequently goes down). These bubbles are developed by the growth of instabilities seeded by plasma perturbations that occur in the region of strong density gradient, that is, the bottom side of the F layer (approximately at 300 km altitude) (ABDU, 2001).

Presently, the most accepted theory to explain the generating mechanism of plasma bubbles is the rapid rise of the F layer ($\mathbf{E} \times \mathbf{B}$ drift), together with the Rayleigh-Taylor (RT) instability and a perturbation that triggers this instability at the bottom of the F_2 layer, that is, a seeding mechanism for the development of the RT instability (HAERENDEL; ECCLES; CAKIR, 1992; KELLEY, 2009). Although still a subject of debate, gravity waves (HINES, 1960; HUANG; KELLEY; HYSELL, 1993; HYSELL *et al.*, 1990; PRAKASH, 1999; RÖTTGER, 1973; SINGH; JOHNSON; POWER, 1997) and travelling ionospheric disturbances (TIDs) (FRITTS; VADAS, 2008; ŠAULI *et al.*, 2006; SETTY; GUPTA; NAGPAL, 1973; SINGH; JOHNSON; POWER, 1997; TAYLOR *et al.*, 2009; ZOLESI; CANDER, 2014) are understood as the possible main seeds of this instability.

The Rayleigh-Taylor instability explains how fluctuations in the electron density at the bottom of the F_2 layer give rise to plasma bubbles and how they develop and ascend to the upper part of the ionosphere in the presence of a gravitational field. Since the ionosphere can be modeled as a fluid (BITTENCOURT, 2004; RISHBETH; GARRIOTT, 1969), a simple

criterion for the RT instability to occur is: *"If the denser fluid pushes the less dense fluid, the interface between them is stable. If the less dense fluid pushes the denser, then the interface is unstable"* (SHARP, 1983). This is what naturally occurs in the ionosphere of the F region, in which the F_2 layer is denser and experiences a disturbance in its lower part, which propagates to the denser fluid by means, for example, of gravity waves (FARLEY *et al.*, 1970; NAPPO, 2013).
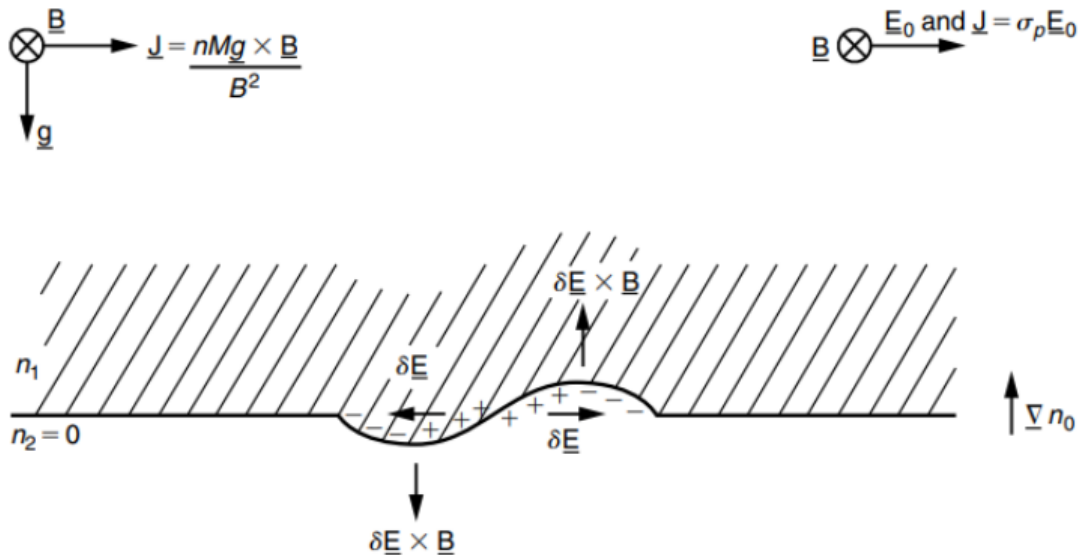
FIGURE 2.5 – Illustration of the Rayleigh-Taylor instability mechanism in the equatorial F-region. Two layers with different plasma densities are represented (n_1 and n_2), where there is an upward-directed electron density gradient (∇n_0). A disturbance in the electron density between the layers causes a horizontal current (**J**). This current generates the polarization electric field $\delta\mathbf{E}$, that, combined with **B**, produces the $\delta\mathbf{E} \times \mathbf{B}$ and the plasma bubbles (KELLEY, 2009).

The most accepted scenario for the formation of EPBs involves a few mechanisms in the E and F regions, in which the F region processes are summarized in Figure 2.5. During the day, the thermospheric wind generates, by dynamo effects, an electric field in the lower ionosphere (E region) directed towards east (not shown in Figure 2.5). The electric field in the east direction, combined with the magnetic field **B** directed northward produces the $\mathbf{E} \times \mathbf{B}$ vertical plasma drift in the F region. As the ionosphere corotates with the Earth towards dusk, the zonal (eastward) component of the neutral wind increases, with the wind blowing predominantly through the terminator from the dayside to the nightside. The increase in the eastward wind component, in combination with the steep gradient across the terminator leads to the PRE of the electric field to the east. The F layer, therefore, rises as the ionosphere corotates on the nightside. Now referring to Figure 2.5, in the absence of sunlight, the lower ionosphere decays rapidly, so that the upper (n_1) and the lower (n_1) ionosphere, where $n_1 \neq 0$ and $n_2 = 0$, have different plasma densities, developing a sharp vertical density gradient, ∇n_0, on the bottom of the F layer.

This produces the classical configuration for the Rayleigh-Taylor instability, in which a denser fluid is situated above a less dense. Additionally, there is a perturbation in the electron density between the two layers. The magnetic field $\mathbf{B}$, when gravity $\mathbf{g}$ is present, gives rise to a current in the horizontal direction ($\mathbf{J}$). Due to the initial disturbance, there is a divergence in the current flow, causing an accumulation of charges at the edges of the disturbed region. This accumulation of charges produces a polarization electric field $\delta\mathbf{E}$. This electric field, when combined with $\mathbf{B}$, produces the $\delta\mathbf{E} \times \mathbf{B}$ vertical drift of the plasma in the F region, shifting the depletion region upwards and the high-density region downwards. This generates the plasma bubbles.

As aforementioned, a significant and necessary, but not sufficient characteristic for the occurrence of EPBs is the PRE. The PRE, when raising the F layer, directs it to very high regions, where the recombination is low and collisions are rare (KELLEY, 2009). In reality, plasma bubbles develop more effectively if the bottom of the F layer is at high altitudes, which is usually seen during the sunset (KELLEY, 2009).

2.1.4.2 Wavenumber-4 structure

One interesting longitudinal variation related to the quiet-time equatorial vertical drifts is the so-called *wavenumber-4 (WN4) longitudinal structure.* Figure 2.6 shows an example of how this structure is observed through the FPMU ion density data at 20-22 LT (local time) during the 2008 equinox (March, April, September, and October). This structure is also visible in our FPMU climatological investigation shown in Chapter 4. Ionospheric signatures of the WN4 structure were identified initially from in-situ observations of the EIA and the equatorial electrojet (IMMEL *et al.*, 2006). Today, it is known that this structure is strongest during the equinox (KIL *et al.*, 2009), exhibits both interannual and intra-annual variability, and moves eastward during the day. The comprehensive study conducted by Scherliess *et al.* (2008) showed that the wavenumber-4 pattern is created during the daytime hours at the equinox and June solstice, but is nearly absent or washed out by other processes during the December solstice, which is confirmed by our climatological study (Chapter 4). During the June solstice, the wave-4 pattern is also observed in the afternoon hours, but differently to the equinox cases, it exhibits a clear hemispheric asymmetry and is not observed during the night. Onohara *et al.* (2018) showed that this four-peak structure is present in both low and high solar activity periods in the equatorial and low-latitude ionosphere, becoming more prominent around or above the F-region peak.

Regarding its generating mechanism, the WN4 structure has been considered to have some relation to nonmigrating tides, which are generated by latent heat release in the troposphere and that can propagate upward (HAGAN; FORBES, 2003). One nonmigrating
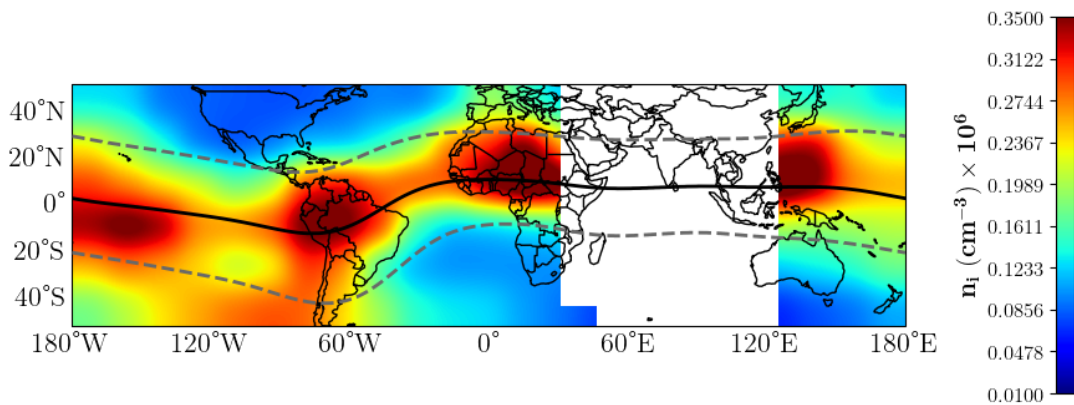
FIGURE 2.6 – FPMU ion density map for the 2008 equinox. The data is for 20:00-22:00 local time interval, Kp < 3, and for an average solar flux of 70 sfu.

tide of special interest in this matter is the eastward propagating zonal wave number 3 diurnal tide (DE3, "E" for eastward), which has a wave number 4 longitudinal structure as viewed in the local-time fixed reference. Specifically, this kind of structure possibly has tropospheric origins related to the tidal waves propagating from below that modulate the E-region dynamo, mainly the DE3. This wave, when combined with the migrating diurnal tide (DW1, "W" for westward) presents a wavenumber-4 structure under a general view. There is evidence that the DE3 tide can propagate into the upper thermosphere and induce zonal perturbation electric fields, which are added to the background F-region dynamo field, modulating the ionospheric fountain process. Hence, this tide can modify the F-region dynamo (JIN et al., 2008). The WN4 structure can be observed in several ionospheric parameters, such as N_e, TEC and h_mF_2. These parameters can exhibit a 4-wave longitudinal variation at a fixed local time when averaged over several days, which includes variations in the intensity of the EIA emissions, in the vertical drift/zonal electric field at the magnetic equator, and in the magnitude of the equatorial electrojet (ENGLAND et al., 2006).

2.1.5 Plasma depletion bays

Reported for the first time by Chang et al. (2020) through F3/C measurements during 2007-2014, plasma depletion bays (PDBs) are a broad region of low-density plasma at low latitudes in the winter hemisphere that extends to the summer hemisphere of generally high plasma density. Chang et al. (2020) found a simultaneous weakening in electron density and airglow intensity in the F3/C and TIMED/GUVI (Thermosphere, Ionosphere, Mesosphere Energetics and Dynamics/Global Ultraviolet Imager), respectively, around 2100 LT. This occurred over Southwest America (75-135°W) during the December solstice of 2007, with a southward curving towards the Southern Hemisphere, forming a North Plasma Depletion Bay (North PDB). Similar features were observed in the North Atlantic

(60°W to 30°E), Indian Ocean (45-110°E), and Southeast Asia (120-170°E) longitudes during the June solstice of 2007, forming three South Plasma Depletion Bays (South PDBs) with a slightly northward curving. The nomenclature follows the origin of the depleted plasma region. If it comes from the south, it is a South PDB, if it comes from the north, it is a North PDB. The consistent findings from both F3/C and TIMED/GUVI observations suggest that the PDB is a nighttime electron density depletion feature caused by ionospheric variations, regardless of measurement techniques or inversion algorithms. This feature prominently appears during the nighttime in solstice months. These authors also state that the PDBs yield more prominent structures during the low solar activity than in high solar activity years. In contrast, using the FPMU data, the PDB structure is stronger during higher solar activity periods, as will be shown in Chapter 4.
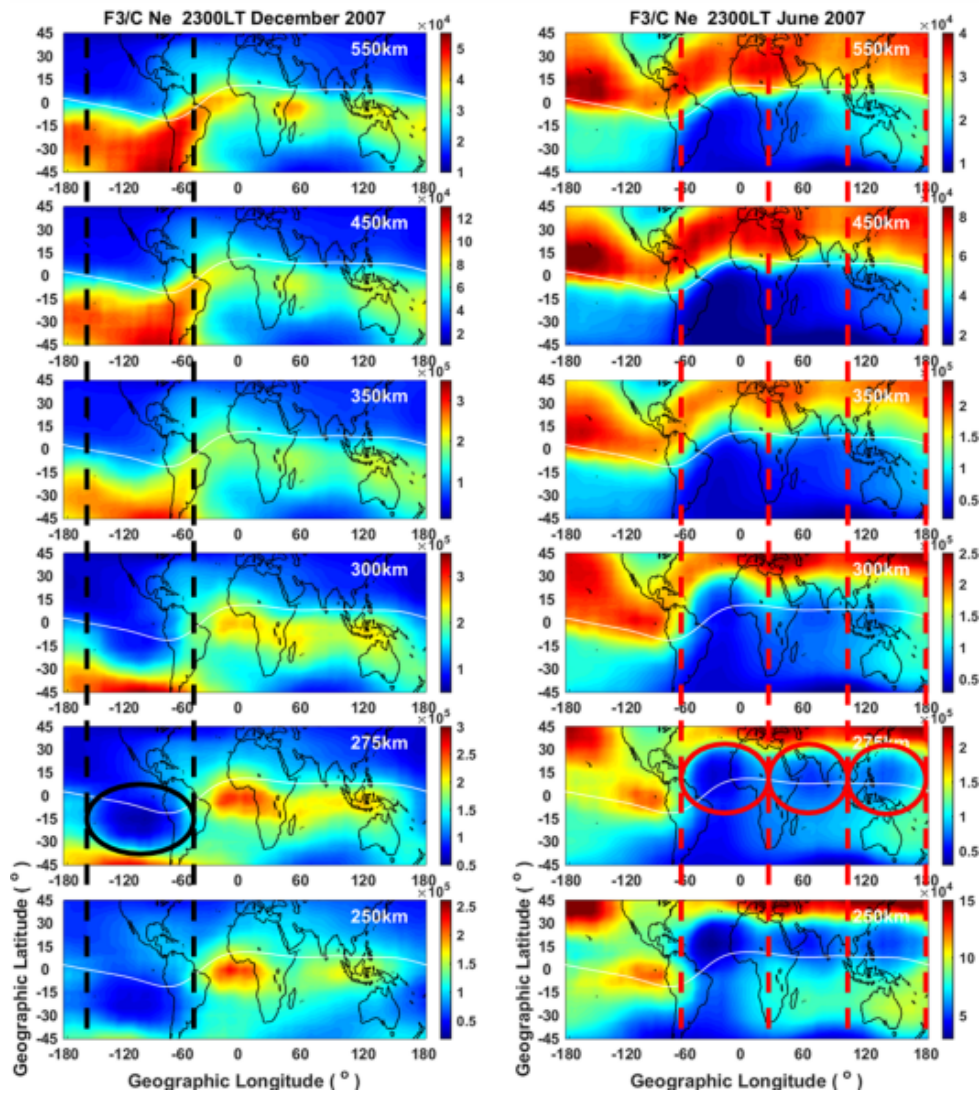
FIGURE 2.7 – Electron density (N_e) altitudinal plots at 250 km to 550 km altitudes in constant local time maps at 2300 LT during both solstices revealed North PDB and three South PDBs at 275 km altitude, indicated by black and red circles (CHANG et al., 2020).

Figure 2.7 displays electron density across altitudes from 250 km to 550 km during

December and June of 2007. Both North PDB and South PDBs are clearly visible in the 250 km to 550 km altitude range, with the most distinct features observed at 275 km. Interestingly, as altitude increases, the North PDB and South PDBs exhibit northward and southward shifts (towards the equator). It will be shown in Chapter 4 that at the ISS height ($\sim$400 km), we only observe one South PDB in the June solstice, and that this structure is closer to the dip equator, as suggested.

The seasonal pattern of PDB occurrence, with the North PDB prominent in the Southern Hemisphere during December (southern summer) and the South PDBs pronounced in the Northern Hemisphere in June (northern summer), suggests a potential influence of summer-to-winter neutral wind in their formation. To investigate this effect, Chang *et al.* (2020) analyzed the transequatorial field-aligned winds. Their findings support the notion that summer-to-winter winds, primarily driven by zonal neutral winds, likely contribute to ionospheric plasma density variations over the PDBs longitude sectors during nighttime.
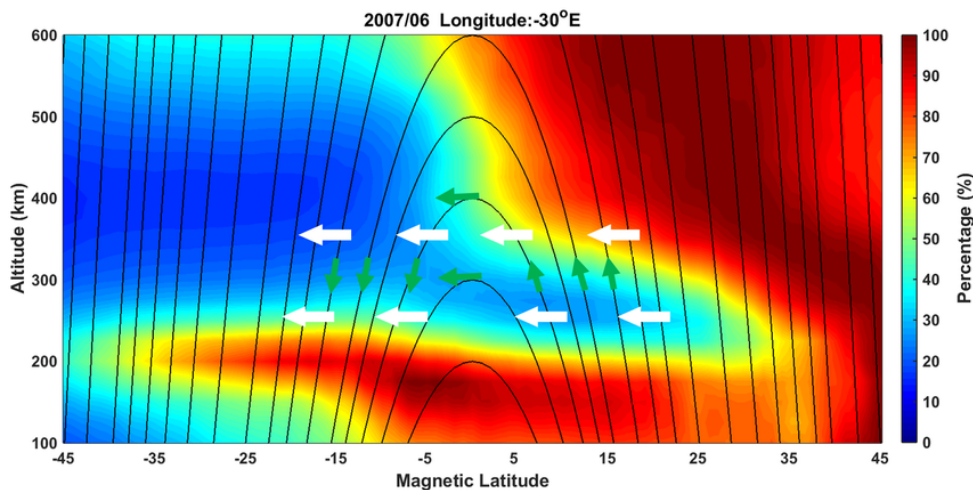
FIGURE 2.8 – The impact of summer-to-winter winds (white arrows) on the PDB longitudinal sector. The background electron density, derived from Figure 2.7, illustrates an altitude-latitude cut along the -30°E longitude, normalized at each altitude. The green arrows depict the parallel plasma drift (CHANG *et al.*, 2020).

Figure 2.8 illustrates the processes behind PDB generation. Summer-to-winter winds induce equatorward plasma motion along magnetic field lines, leading to PDB formation at lower altitudes in the summer hemisphere. In the winter hemisphere, poleward winds enhance downward plasma diffusion, causing an overall density decrease at lower altitudes with faster recombination. This results in the summer-to-winter winds dragging plasma along magnetic field lines, ascending from the low-latitude ionosphere in the summer hemisphere, traversing the magnetic equator horizontally, and descending to the low-latitude ionosphere in the winter hemisphere. The less dense plasma in the low-latitude ionosphere in the summer hemisphere is pulled upward/equatorward, causing the PDB's curving feature to move equatorward with increasing altitude in the summer hemisphere

(see Figure 2.7). As the wind carries plasma to the winter hemisphere over the magnetic equator, it moves downward/poleward along the same magnetic field line, resulting in a significant reduction in plasma density at the low-altitude off-equator ionosphere in the winter hemisphere, due to recombination loss processes inversely proportional to altitude.

2.1.6 Temperature: The morning overshoot

Even though the FPMU electron temperature is going through modifications in its algorithm, meaning that the data we present here is preliminary, a few words on a plasma thermal feature observed at mid- and low-latitudes seem necessary, since we observe it through the FPMU data. An interesting thermal phenomenon is the so-called *predawn effect* or *morning overshoot*. It is characterized by a rapidly increase in the electron temperature, T_e, before local sunrise, as can be seen in Figure 2.9. In this Figure, T_e measurements at 375 km are plotted as a function of local time for Millstone Hill, an incoherent scatter radar facility located in Massachusetts. The temperature starts to increase at $\sim$0230 LT, while local sunrise occurs at $\sim$0530 LT. This early electron temperature onset occurs at a time that corresponds to sunrise in the magnetically conjugate ionosphere. Thus, the heating is caused by photoelectrons arriving from the conjugate hemisphere (SCHUNK; NAGY, 2009), in which photoelectrons are transported along geomagnetic field lines from the more sunlit (summer) hemisphere into the darker (winter) one. Consequently, this effect is expected to be stronger in the winter hemisphere (OYAMA *et al.*, 1996). At sunrise, the ionosphere generates photoelectrons through the ionization of neutral particles exposed to sunlight. As these photoelectrons exchange energy with surrounding electrons, the electron temperature undergoes a rapid increase, primarily driven by the initially low electron density in the early morning (YANG *et al.*, 2020).

The sudden increase of electron temperature in the early morning hours at middle and low latitudes was first observed by Evans (1965), and since then this phenomenon has been extensively investigated. As an example of its main characteristics, Yang *et al.* (2020) showed that on a global average, the morning overshoot generally weakens with decreasing altitudes, is stronger around the dip equator (OYAMA *et al.*, 1996), presents multiday oscillations, and is affected by geomagnetic activity (WANG; BURNS; KILLEEN, 2006). Moreover, according to Farley *et al.* (1967), the morning overshoot is stronger at an altitude of about 400 km, which is the average altitude of the FPMU/ISS. This phenomenon will be investigated in some detail using the FPMU data in Chapter 4.

In the next section, descriptions of the ionospheric electrodynamics at mid-latitudes will be given. In this region, a series of phenomena occur and are observed in the FPMU data, therefore it is important to at least study its main features.
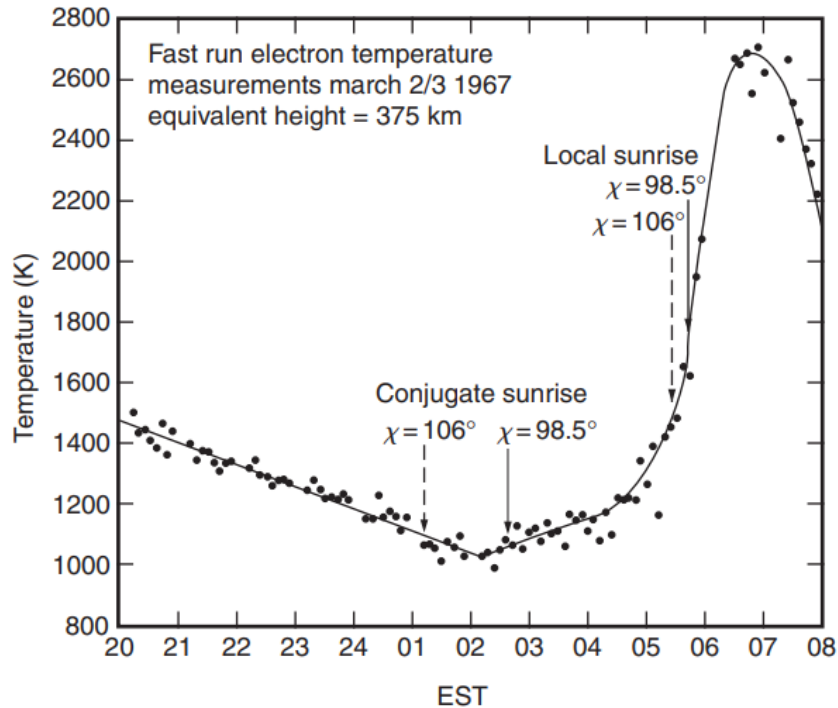
FIGURE 2.9 – Electron temperature measurements obtained with the Millstone Hill ISR on 2-3 March 1967 as a function of the Eastern Standard Time (EST) (SCHUNK; NAGY, 2009).

2.2   The mid-latitude ionosphere

It can be said without a doubt that the ionosphere at midlatitudes is a very interesting region because, being between the low and the high latitude zones, it encompasses a series of phenomena generated by both and, to increase its complexity, processes unique to the mid-latitude ionosphere also seem to exist. The mid-latitude ionosphere is controlled by two largely unconstrained mechanisms: the inner magnetospheric electric field and the dynamic properties of the thermosphere (KINTNER *et al.*, 2008). Hence, electric fields and perturbed neutral winds are able to penetrate from high-latitude sources and so is the equatorial plasma, since it enters the region along the magnetic field lines. Differently, at midlatitudes the length of the magnetic field lines containing high-density plasma is shorter when compared to the equatorial zone, gravity is parallel to the magnetic field, and wind effects are as important as electric fields.

The effects that geomagnetic storms have over the ionosphere are more pronounced at midlatitudes, in terms of the most extreme changes observed. The magnetic perturbations that occur at midlatitudes during geomagnetic storms can change the TEC by factors of three to ten over the duration of a magnetic storm when compared to low and high latitudes (KINTNER *et al.*, 2008).

In the mid-latitude ionosphere, the magnetic field is basically straight and uniform at

F region altitudes, but it is inclined to the horizontal at an angle I. The mid-latitude ionosphere is horizontally stratified, which means that the density and temperature gradients (and gravity) are in the vertical direction. The inclined $\mathbf{B}$ field, therefore, reduces the effectiveness of diffusion because the charged particles are constrained to diffuse along $\mathbf{B}$ as a result of the small collision-to-cyclotron frequency ratios (SCHUNK; NAGY, 2009). Hence, drifts are parallel to $\mathbf{B}$ and because of that they are more complex since gravity, neutral winds, and pressure gradients all contribute (KELLEY, 2009).

Aiming to derive an equation for the forces that act on the ionospheric plasma in the direction parallel to $\mathbf{B}$, it is first adequate to write the momentum equation for an ionized species j:

$$\rho_j d\mathbf{V}_j/dt = -\nabla p_j + \rho_j \mathbf{g} + \frac{q_j \rho_j}{m_j}(\mathbf{E} + \mathbf{V}_j \times \mathbf{B}) - \sum_{\substack{k \\ j \neq k}} \rho_j \nu_{jk}(\mathbf{V}_j - \mathbf{V}_k) \qquad (2.6)$$

Again, j stands for the charged species, i.e., i (the single-ion gas) or e (the electron gas); k has the same meaning as j, but represents a different species from j; ρ_j is the mass density; ν_{jk} is the momentum transfer collision frequency; and ∇p_j is the pressure gradient.

The equilibrium fluid velocity of each species may now be found from the previous equation by setting the total time derivative equal to zero and specifying the force fields and pressure distributions:

$$0 = -\nabla(n_j k_B T_j) + n_j m_j \mathbf{g} + q_j n_j (\mathbf{E} + \mathbf{V}_j \times \mathbf{B}) - \sum_{\substack{k \\ k \neq j}} n_j m_j \nu_{jk}(\mathbf{V}_j - \mathbf{V}_k) \qquad (2.7)$$

Where n_j is the particle number density and k_B is the Boltzmann's constant. It is useful to solve Equation 2.7 for the ion and electron velocities based on the driving forces. To simplify, we focus now on one type of ion with mass M, using m for electron mass and e for elemental charge, assumed positive. For spatially uniform ion and electron temperatures, the equations are

$$0 = -k_B T_i \nabla n + nM\mathbf{g} + ne(\mathbf{E} + \mathbf{V}_i \times \mathbf{B}) - nM\nu_{in}(\mathbf{V}_i - \mathbf{U}) \qquad (2.8)$$

$$0 = -k_B T_e \nabla n + nm\mathbf{g} + ne(\mathbf{E} + \mathbf{V}_e \times \mathbf{B}) - nM\nu_{en}(\mathbf{V}_e - \mathbf{U}) \qquad (2.9)$$

here, n is the plasma density when quasi-neutrality is assumed. We now transform the

terms in the two previous equations to a reference frame moving with the neutral wind $\mathbf{U}$, since $\mathbf{V}_j' = \mathbf{V}_j - \mathbf{U}$, this equation becomes

$$0 = -k_B T_j \nabla n + n M_j \mathbf{g} + q_j n \mathbf{E}' + q_j n (\mathbf{V}_j' \times \mathbf{B}) - n M_j \nu_{jn} \mathbf{V}_j' \tag{2.10}$$

where j stands for i or e. Dividing by $n m_j \nu_{jk}$ and gathering terms, Equation (2.10) can be written as:

$$\mathbf{V}_j' - \kappa_j (\mathbf{V}_j' \times \hat{\mathbf{B}}) = -D_j \nabla n / n + b_j \mathbf{E}' + (D_j / H_j) \hat{\mathbf{g}} \equiv \mathbf{W}_j' \tag{2.11}$$

In the equation above, $\hat{\mathbf{B}}$ is a unit vector in the $\mathbf{B}$ direction; $\hat{\mathbf{g}}$ is a unit vector in the $\mathbf{g}$ direction; D_j is the diffusion coefficient ($k_B T_j / m_j \nu_{jn}$); b_j is the mobility ($q_j / m_j \nu_{jn}$); H_j is the so-called *scale height* (general way to describe how a parameter, such as pressure or density, decreases by a factor of $1/e$ in an isothermal atmosphere. It is commonly used to describe the atmosphere of a planet) ($k_B T_j / m_j g$); κ_j is the ratio of gyrofrequency to collision frequency ($q_j B / m_j \nu_{jn}$), which has the same sign as the particle charge; and $\mathbf{W}_j'$ is the fluid velocity.

For κ_j very large (a "collisionless" plasma), the component parallel to $\mathbf{B}$ is

$$V_{j\parallel}' = [b_j \mathbf{E}' - D_j \nabla n / n + (D_j / H_j) \hat{\mathbf{g}}] \cdot \hat{\mathbf{B}} \tag{2.12}$$

transforming to the earth-fixed reference frame where the neutral wind has a value $\mathbf{U}$, the parallel component of the velocity V_j is:

$$V_{j\parallel} = \mathbf{U} \cdot \hat{\mathbf{B}} + V_{j\parallel}' \tag{2.13}$$

As one can note, temperature gradients (which must be included in a complete treatment of the total pressure gradient) were ignored in Equation (2.12) for simplicity. In reality, because of its light mass, the electron gas diffuses much faster than the ions down a pressure gradient, a process that would tend rapidly to destroy any gradient in electron pressure. However, the resultant charge separation is accompanied by an electric field that restrains the electrons and enhances the ion diffusion and this should be taken into account in a more complete treatment (this is the so-called *ambipolar diffusion*). Also, according to Equation (2.13) the plasma is closely coupled to the neutral gas motion along $\mathbf{B}$, but its velocity is modified by the term $V_{j\parallel}'$. During the day, plasma production or loss by photoionization and recombination dominates the plasma profiles in the E and lower F regions, organizing the ionospheric plasma content in a horizontally stratified manner (KELLEY, 2009). However, above the F peak the plasma is

expected to be in a state similar to diffusive equilibrium in the gravitational field, but that is not what is actually seen, as will be explained following.

The electric field, when projected parallel to $\mathbf{B}$ ($E_\parallel$) is small due to the high conductivity in that direction, and perpendicular to $\mathbf{B}$ this electric field is negligible. The force on the ions associated with the parallel electric field and the gravitational force is countered by the plasma pressure gradient. Since the assumed dynamic equilibrium is between electrons and the dominant ion species, minor light ions such as He^+ and H^+ can be accelerated outward from the ionosphere by the parallel electric field. Since hydrogen atoms and molecules can escape the Earth's gravitational field, the Earth is surrounded with what is called *geocorona*, which is basically a hydrogen gas.

The geocorona interacts with oxygen ions in a very rapid process, resulting in a transition between an oxygen and a hydrogen plasma between 500 km and 1000 km, depending on season and other effects (VICKREY; SWARTZ; FARLEY, 1979). Hence, the simple assumption of diffusive equilibrium is not appropriate because a net upward flux of plasma is possible during the day at the outer part of the ionosphere, the plasmasphere.   In more details, the closed magnetic flux tubes at tropical and midlatitudes act as a reservoir for plasma, which is the plasmasphere, created in the daytime by photoionization and transported upward by light ions. At night the plasma flows back down due to the absence of sunlight to maintain it at higher altitudes, tending to maintain the density in the ionosphere (KELLEY, 2009). Therefore, in the midlatitudes there is a complex interaction between the ionosphere and a region of hydrogen plasma trapped by the dipole magnetic field.

As can be observed, the plasmasphere plays an important role in the dynamics of the mid-latitude ionosphere. This region corresponds to latitudes where the geomagnetic flux tubes corotate, since such tubes can fill with plasma on the dayside. Furthermore, sunlight creates an abundant F-region atomic oxygen plasma, which exchanges charge with neutral hydrogen atoms along the field lines. At night these flux tubes are not completely depleted, and, on average, a dense and cold hydrogen ion plasma permeates the upper plasmasphere. Since the magnetospheric electric field is rather variable, the plasmasphere's effect on the mid-latitude ionosphere, as a plasma reservoir, is a strong function of the applied magnetospheric electric field. Far from being a simple region, magnetic activity and solar wind conditions affect the mid-latitude ionosphere through electron dynamics as well as the atmosphere's chemistry, because of neutral composition changes. Also, high latitude heating and momentum transfer can also affect this region since they are responsible for driving thermospheric neutral winds.

Additionally, many situations are possible for the interplay between the mid-latitude ionosphere and the plasmasphere. For example, solar cycle, seasonal, and geomagnetic activity conditions can affect this interation. In more details, when the ionosphere and

plasmasphere are in equilibrium, diffusive equilibrium prevails and there is a light interchangeable flow of ionization between the two regions. During the day, the flow is upward from the ionosphere, when the O^+ density is relatively high, and downward at night, when the O^+ density decays. In accordance with what was mentioned above, the downflowing H^+ ions charge exchange with O to produce O^+, and this process helps to maintain the nighttime F region. Near the solstices a different situation can occur, since the flow can be interhemispheric. In this case, in the summer hemisphere the flow is upward and out of the topside ionosphere throughout the day and night. As for the winter hemisphere, the flow is upward during the day and downward at night.

In summary, the role that many effects have, such as finite dip angle, neutral waves, and plasma instabilities, additionally to neutral winds and electric fields, make the ionosphere of midlatitudes quite unique. Given its complexity, the electrodynamics of this region is controlled by tidal and higher-frequency atmospheric wave modes in the E region during the day, while at night a very complicated combination of the thermospheric wind dynamo, high-latitude electric field penetration, conjugate hemisphere effects, and gravity waves all act at the same time.

2.2.1   Mid-latitude summer nighttime anomalies

A very significant phenomenon occurring at mid-latitudes and remarkable in our FPMU climatology is the *mid-latitude summer nighttime anomaly* (MSNA). This term refers to an unusual occurrence in the Earth's ionosphere where electron density or TEC is higher at night than at noon, representing a phase reversal in the typical diurnal cycle of these parameters (YIN *et al.*, 2022). MSNAs are identified in three regions within middle magnetic latitudes (CHANG *et al.*, 2015; LIN *et al.*, 2010; LIU; THAMPI; YAMAMOTO, 2010; XIONG; LÜHR, 2014). The first, known as the Weddell Sea Anomaly (WSA), was discovered in the Southern Hemisphere in the 1950s using ionosonde measurements around -90° geographic longitude (PENNDORF, 1965). The other two regions, observed in the Northern Hemisphere, are collectively referred to as MSNAs (CHEN *et al.*, 2012; LIN *et al.*, 2009; LIN *et al.*, 2010; LIU; THAMPI; YAMAMOTO, 2010; XIONG; LÜHR, 2014). One is near the Bering Sea (around 150° geographic longitude, region West of Alaska) and termed the Bering Sea Anomaly (BSA) (YIN *et al.*, 2022). The second is observed in the North Atlantic region around -45° geographic longitude, referred to here as the North Atlantic MSNA. Figure 2.10 shows density differences between day (1200 LT) and night (2200 LT) at a moderate solar flux level to illustrate the three MSNAs (one in the December solstice and two in the June solstice). The absolute difference is shown here to avoid possible exaggeration by small electron density values.

The most extensively studied MSNA is the WSA in the Southern Hemisphere, being the first discovered and more prominent than the Northern Hemisphere anomalies. In Chapter 4, we observe the WSA and North Atlantic MSNA through the FPMU data, with no evidence of the BSA, possibly due to altitudinal effects.
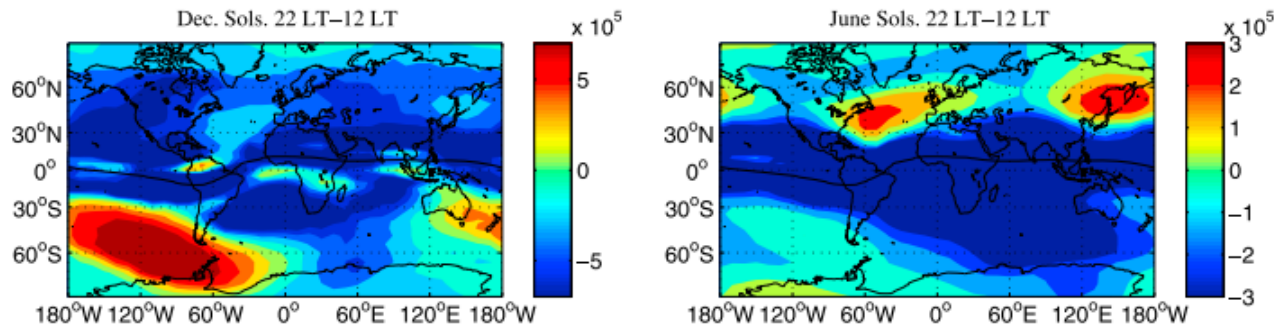
FIGURE 2.10 – Difference between the geographical distribution of the electron density at 2200 LT and 1200 LT at 400 km for (left) the December solstice and (right) the June solstice. The data is from 2001 to 2006 (LIU; THAMPI; YAMAMOTO, 2010).

The WSA formation is believed to result from a combination of factors, including thermospheric neutral winds, solar photoionization, magnetic declination effects (DUDENEY; PIGGOTT, 1978), and a downward flux of plasma from the plasmasphere (BURNS et al., 2008). The effective wind reaches its maximum near the magnetic dip angle of 45° in both hemispheres (LIU; THAMPI; YAMAMOTO, 2010). At the specific geographic longitudes and magnetic latitudes where MSNAs are observed, the magnetic dip angle is close to 45°. Hence, the highest effective wind values cause significant plasma drift along the magnetic field lines at MSNA locations. This leads to an increased amount of ionized material transported upward and equatorward from high latitudes during local summer. Importantly, this transport leaves the plasma at higher altitudes, where recombination is lower, allowing the plasma to persist for longer periods during the nighttime. Numerous observational studies support this interpretation (CHANG et al., 2015; LIN et al., 2010; LIU; THAMPI; YAMAMOTO, 2010; THAMPI et al., 2011).

The offset between the geomagnetic and geographic equators is also suggested to contribute to MSNA formation. This offset results in larger ionization anomaly crests at higher geographic latitudes, which combined with the specific configuration of declination angles in the MSNA locations, generates a stronger equatorward neutral wind in MSNA locations. This supports the accumulation of ionized material at higher altitudes (LIN et al., 2009). Burns et al. (2008) propose that an evening downward flux of plasma from the plasmasphere may be at least partly responsible for the WSA formation. As the topside ionosphere cools, it contracts, moving plasma downward. This process is facilitated by a decrease in O^+ ions at higher altitudes, allowing H^+ ions (which are heavier and more influenced by gravity) to flow down, leading to higher

electron densities and an increased F_2 peak height. The WSA's prominence in the Weddell Sea region may be linked to more significant cooling of electron temperatures in the Southern Hemisphere's lower plasmasphere during summer evenings compared to the Northern Hemisphere.

In conclusion, the recent studies by Richards *et al.* (2017; 2018) analyzed the BSA and the WSA to show that their longitudinal features can largely be explained by changes in composition and winds. They suggest that the BSA and WSA can be viewed as existing primarily because they are at moderate magnetic latitudes, away from direct auroral influences, and at high geographic latitudes, experiencing extended sunlight. In summary, the MSNAs share, in general, the same formation mechanisms described above.

2.3   Storm-time effects

The mid- and low-latitude ionosphere present remarkable variations in association with geomagnetic storms compared to its quiet-time pattern. The response of the ionosphere-thermosphere system to different geomagnetic storms can be extremely different, and even for a given storm, the system's response can be very different in different latitudinal and longitudinal sectors. In the next chapter, radar data from Jicamarca will be used to study some of the main phenomena that occur in the low and mid-latitude ionosphere when geomagnetic storms are present, where severe changes in the dynamics are shown.

In addition to the electric field generated by neutral winds, which are driven by the solar heat input carried by photons, energy also comes from the sun via particles in the solar wind and via the electromagnetic flux in the solar wind (KELLEY, 2009). These energy sources affect primarily the high-latitude polar cap and auroral zones but can also be detected at the equator mostly during disturbed geomagnetic periods.

All the phenomena studied here until now can also occur during active geomagnetic times, especially the ESF, which can be very severe during storm times because the vertical drift described in Section 2.1.4.1 can lift the F region to higher altitudes, where the bubbles are more possible to grow. Additionally, the equatorial ionization anomaly signature produced by a large upward drift perturbation during a geomagnetic storm can be later maintained even in the presence of a downward drift perturbation.

Another important aspect of the EIA during magnetic disturbed periods is its widening to higher latitudes. Near the equator, the chemistry and the field-aligned transport act to rapidly reduce the vertical flux of plasma with altitude. Thus, an increase in the $\mathbf{E} \times \mathbf{B}$ drift, in this case due to geomagnetic storms, will widen in latitude the region of enhanced density rather than increase in altitude the region of large vertical fluxes (HEELIS, 2008). Figure 2.11 shows a schematic representation of the

so-called superfountain effect that displaces the EIA peaks to higher latitudes. This effect highlights that plasma enhancements in the anomaly region are produced by the small upward, but largely horizontal, motion of plasma on neighboring flux-tubes and not by the transport of plasma to higher altitudes at the equator region (KINTNER et al., 2013).
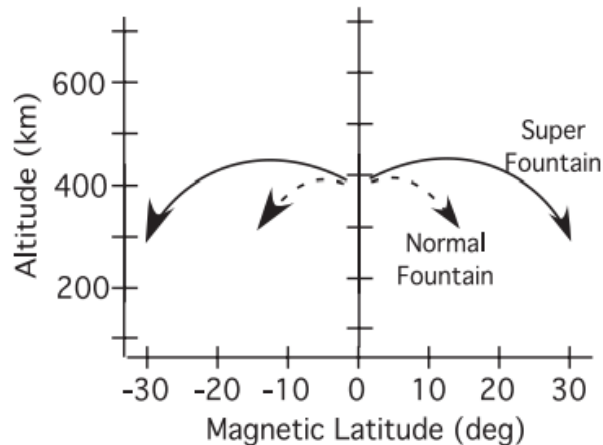
FIGURE 2.11 – Schematic representation of the plasma flux induced by the superfountain. It can be observed that the plasma transport is largely horizontal (KINTNER et al., 2013).

2.3.1 Geomagnetic indices

The disturbance field D' is the magnetic field that results after the quiet-variation fields have been subtracted from the total field. The characteristic times associated with most disturbances extend from minutes to days, and the largest disturbances are called *magnetic storms*. The disturbance field is commonly separated into two components, D' = Dst + Ds, where Dst is the storm-time variation and Ds is the disturbance-daily variation (SCHUNK; NAGY, 2009). The Dst component results from the magnetic disturbance generated by the Earth's ring current (discussed in the next section), while the Ds component is the magnetic field associated with the ionospheric response to auroral particles precipitated from the ring current. The hourly Dst index is derived from the average observations of four low-latitude stations and is commonly employed for characterizing geomagnetic storms. It is calculated at low latitudes and describes the ring current (BERGIN et al., 2023).

In more details, a magnetic storm generally has three phases: initial, main, and recovery phases (GONZALEZ et al., 1994). The initial phase results from a compression of the magnetosphere due to the arrival of the solar wind at the Earth. When storms begin abruptly they are called a sudden storm commencement (SSC), which is most of the cases, but storms can also begin gradually without an SSC. Also, sometimes an impulsive change in the magnetic field occurs, but a storm does not develop, and this is

called a sudden impulse (SI). The initial phase of a storm typically lasts 2-8 hours, during which Dst is increased due to the compression of the magnetosphere. However, during the main phase of the storm, Dst is decreased, often by more than 100 nT relative to prestorm values, and this is explained by the effective coupling of the solar wind and the magnetosphere. More specifically, magnetic storms are generally associated with a southward interplanetary magnetic field (IMF), which allows for the efficient coupling mentioned, resulting in an intensification of the ring current. This induces a horizontal magnetic field that is southward (opposite to the Earth's dipole field), which explains for the negative Dst during the main phase of a storm. Finally, the recovery phase occurs when Dst gradually increases to its prestorm value, which can last more than a day. The degree of the Dst main phase decrease is a measure of the intensity of the storm and may be characterized as intense/super, moderate and weak for the Dst < -100 nT, -100 nT < Dst < -50 nT, -50 nT < Dst < -30 nT, respectively (OLABODE; ARIYIBI, 2020).

Several indices have been used to describe the magnetic activity in addition to Dst. The AE, AL, and AU indices are calculated at auroral latitudes, and the K indices are calculated at all latitudes. All these indices are calculated by the World Data Center (WDC) for Geomagnetism, Kyoto, available at `https://wdc.kugi.kyoto-u.ac.jp/wdc/Sec3.html`. The AE index is derived from geomagnetic variations in the horizontal component observed at selected (10-13) observatories along the auroral zone in the Northern Hemisphere. Among the data from all the stations at each given time (Universal Time – UT), the largest and smallest values are selected. The AU and AL indices are defined by the largest and the smallest values selected, respectively. The difference AU-AL gives the AE index. The AU and AL indices are intended to express the strongest current intensity of the eastward and westward auroral electrojets, respectively. Hence, the AE index represents the overall activity of the electrojets. Equivalently, the SMR, SME, SML, and SMU indices correspond to the Dst, AE, AL, and AU indices, but they are obtained from the SuperMAG database (`http://supermag.jhuapl.edu/`). These indices are derived from ∼300 ground-based magnetometer data with a temporal resolution of 1 min (GJERLOEV, 2012).

The K index provides a measure of the magnetic deviations from the regular daily variation during a three-hour period. The information about magnetic activity is provided via a semi-logarithmic numerical code that varies from 0 to 9, with different numbers corresponding to different magnetic activity levels. Additionally, the K indices from twelve observatories are combined to produce a three-hour planetary index, Kp, which provides information on the average level of magnetic activity globally. The Kp index is specified to one-third of a unit, with the steps varying as follows: 0, 0+, 1-, 1, 1+, ..., 8-, 8, 8+,

9-, 9. In general, Kp = 4 means an active time, Kp = 5 means a minor geomagnetic storm, Kp = 6 is a moderate storm, Kp = 7 is a strong storm, Kp = 8 is a severe storm, and Kp = 9 is an intense geomagnetic storm. This index was used here to have only quiet-time FPMU and C/NOFS data (Kp < 3), as well as to classify the storms studied in its intensity, as will be seen in Chapter 4.

There are two other indices provided by WDC for Geomagnetism, Kyoto. To describe detailed changes in the mid-latitude geomagnetic field every minute, two indices, longitudinally symmetric (SYM) and asymmetric (ASY), were introduced for the horizontal component (H) of the geomagnetic field. SYM-H, representing symmetric disturbances in H, is similar to the hourly Dst index but uses 1-minute values from different stations and a slightly adjusted coordinate system. SYM-H is an averaged, baseline-corrected, and latitude-adjusted measure, combining disturbance components from six stations at each minute (BERGIN *et al.*, 2023; IYEMORI *et al.*, 2010; WANLISS; SHOWALTER, 2006). The ASY-H index is generally well correlated with the AE index (FEJER *et al.*, 2007). A few studies use SYM-H and its rate of change, d(SYM-H)/dt, as well as Dst and d(Dst)/dt to characterize and evaluate geomagnetic storms (e.g., GONZALES *et al.*, 1979; KARAN *et al.*, 2023).

Another important index that is used here is the F10.7 index, the solar radio flux at 10.7 cm (2800 MHz), which is an indicator of solar activity and one of the most widely used for that matter (TAPPING, 2013). The 10.7 cm solar flux measurement is a determination of the strength of solar radio emission in a 100 MHz-wide band centered on 2800 MHz (a wavelength of 10.7 cm), averaged over an hour. In other words, the F10.7 index is a measure of the noise level generated by the Sun at a wavelength of 10.7 cm at the Earth's orbit. It is expressed in solar flux units (sfu). It can vary from below 50 sfu to above 300 sfu over the course of a solar cycle.

2.3.2 Main current systems in the magnetosphere affecting mid- and low-latitudes

Since a geomagnetic storm initiates in the Earth's magnetosphere, it is necessary to distinguish between the main magnetospheric currents systems that can affect the mid- and low-latitude ionosphere. First, when the solar wind reaches the Earth, it interacts with the planet's magnetic field and eventually finds its way into the ionosphere and upper atmosphere. This interaction powers the auroras, triggers magnetic storms and substorms, heats the polar upper atmosphere, drives large neutral atmospheric winds, charges a considerable amount of the plasma along the Earth's magnetic field lines, and generates an extensive circulating network of heated plasma within and surrounding Earth's immediate space environment. One of the circulating network of plasma is the so-called *ring current*,

which is an electric current trapped in the Earth's magnetosphere. It consists of a band lying in the equatorial plane and circulating clockwise (westward) around the Earth (when viewed from the north) at distances between $\sim$3 R$_e$ and $\sim$8 R$_e$ (R$_e$ = 6370 km, a mean value for the Earth's radius) from its center (DAGLIS et $al.$, 1999).

The Earth's ring current is responsible for shielding the lower latitudes from magnetospheric electric fields, significantly impacting the electrodynamics during geomagnetic storms. The particles of this region produce a magnetic field in opposition to the Earth's internal magnetic field, meaning that there is a depress in the magnetic field at the Earth's surface. The measured disturbances of the ground magnetic field during geomagnetic storms are attributed to the ring current increase and decrease (GANUSHKINA; LIEMOHN; DUBYAGIN, 2018). The ring current is created by the injection of ions from the solar wind and Earth's ionosphere. The injection involves electric fields linked to intensified magnetospheric convection and/or substorms. Normally, protons from the solar wind dominate, but during active periods, there is a surge in O^+ ions from the ionosphere, leading to a stronger ring current with O^+ dominance at storm peaks (DAGLIS et $al.$, 1999). As previously noted, the Dst index measures the depletion of the Earth's magnetic field due to the ring current.

Within the Earth's plasma environment, there are also currents flowing along the magnetic field lines, known as *field-aligned currents* (FACs). These currents are primarily carried by electrons and connect magnetospheric with ionospheric currents (SISCOE; LOTKO; SONNERUP, 1991). The field-aligned currents were first suggested by Birkeland (1908) to explain the magnetic field fluctuations observed in the ground-based measurements in polar regions, which is why they are also termed *Birkeland currents*. Later, observations of the magnetic field onboard the low-altitude polar orbiting Triad satellite (IIJIMA; POTEMRA, 1976) found that there were distinct variations with large amplitudes transverse to the main geomagnetic field in the magnetic east-west direction. In the premidnight sector, disturbances moved eastward; in the postmidnight sector, they moved westward. Hence, the magnetic field initially increased and then decreased, suggesting opposing currents. These currents likely ran along magnetic field lines (field-aligned), flowing outwards from the ionosphere at the poleward boundary during premidnight and inwards at the equatorward boundary. In the postmidnight sector, it was the opposite, with currents flowing towards the ionosphere at the poleward boundary and away at the equatorial boundary. Iijima and Potemra (1976) categorized these as *Region 1* (poleward) and *Region 2* (equatorward) currents, where Region 1 (R1) currents are the poleward currents and Region 2 (R2) are the equatorward currents.

R1 currents originate from outer magnetospheric processes, while the generation and variation of R2 currents are dominated by inner magnetospheric processes. The field-aligned currents result from charge separation mechanisms in the magnetosphere, creating

a potential difference along magnetic field lines. This potential difference is carried to the ionosphere along these field lines. In the ionosphere, high conductivity allows for a transverse current. Essentially, the magnetospheric charge separation drives a system with currents along Earth's field lines in the magnetosphere and across these lines in the ionosphere (CUMMINGS; DESSLER, 1967).

As stated above, the magnetospheric current system forms two concentric rings above the auroral ionosphere: the poleward (region 1) and the equatorward (region 2) rings. R1 currents link the ionosphere to the magnetopause and magnetotail, while R2 currents connect to the inner magnetosphere's ring current (COWLEY, 2000). These currents close through the ionosphere via horizontal Pedersen currents. R1 currents dominate the dayside, while R2 currents dominate the nightside. The R1/R2 FACs flow into/out of the ionosphere on the dawn side, and the opposite polarity on the dusk side (COXON *et al.*, 2014). Figure 2.12 shows schematically these currents. Asymmetric features related to FACs include stronger FAC intensity in local summer and in the Northern Hemisphere compared to other seasons and the Southern Hemisphere. Additionally, R1 FACs are generally stronger than R2 FACs (e.g., XIONG *et al.*, 2021).
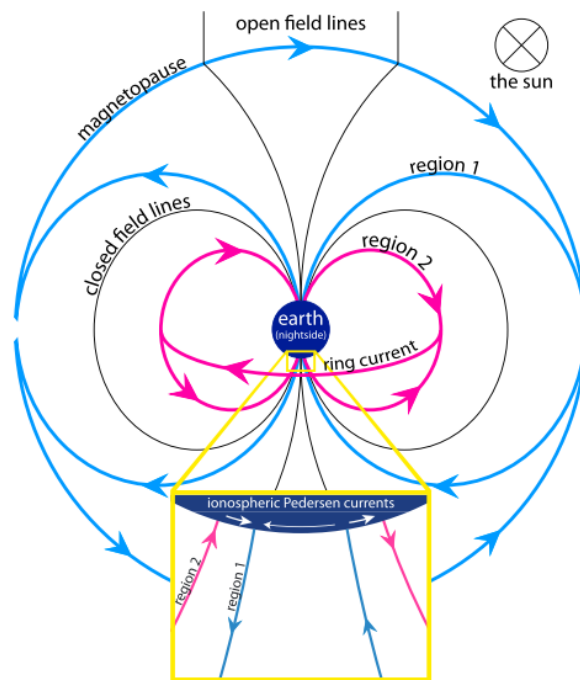
FIGURE 2.12 – Schematic illustration depicting Region 1 and Region 2 currents. It showcases Region 1, Region 2, Pedersen, magnetopause, and ring currents, along with the positioning of open and closed terrestrial magnetic field lines. The arrow representing Pedersen current flow across the polar cap is depicted smaller than the auroral zone arrows, indicating the relative strength of the Pedersen currents (COXON *et al.*, 2014).

The IMF strength and orientation govern the polarity, local time, and magnetic latitude distribution of FACs (GANUSHKINA; LIEMOHN; DUBYAGIN, 2018). A southward

IMF shows clearer R1/R2 pairs, while a northward IMF sometimes shows intense FACs poleward of R1, commonly termed Region 0 (R0) FACs (e.g., ERLANDSON *et al.*, 1988). The behavior of the R0 current is closely dependent on the IMF By component. In the Northern Hemisphere, this current predominantly flows out of the ionosphere when the IMF By is positive and into the ionosphere when it is negative. In the Southern Hemisphere, FACs flow predominantly into the polar cap region for positive IMF By and away from the ionosphere for negative By (LÜHR; KERVALISHVILI, 2021). Essentially, the Region 0 current is not an independent system; it is consistently paired with the Region 1 current (GANUSHKINA; LIEMOHN; DUBYAGIN, 2018). As the IMF becomes more southward, the total intensity of FACs generally rises. However, in instances of a strongly negative IMF Bz, the impact of By on the distribution of FACs diminishes (GANUSHKINA; LIEMOHN; DUBYAGIN, 2018; LÜHR; KERVALISHVILI, 2021).

Another current system in the magnetosphere affecting ionospheric electric fields is the so-called *Substorm Current Wedge* (SCW). Magnetospheric substorms generate significant disruptions in the magnetic field in the magnetosphere, particularly on the nightside. Early studies (AKASOFU; MENG, 1969; BONNEVIER; BOSTRÖM; ROSTOKER, 1970; BOSTRÖM, 1964; CLAUER; MCPHERRON, 1974; MCPHERRON; RUSSELL; AUBRY, 1973) proposed the SCW as the underlying system behind magnetospheric substorms. Energy from the solar wind entering on the dayside accumulates in the magnetospheric tail, and about one hour later, this stored energy is abruptly released by means of a trigger, accelerating plasma towards the Earth. This leads to the establishment of a circuit for substorm currents, known as the SCW. In other words, magnetospheric substorms occur due to a global plasma instability in the magnetotail triggered by the onset of magnetic field line reconnection (MCPHERRON, 2015). The primary elements of this large-scale system include strong upward FACs concentrated in the premidnight sector and a broader distribution of downward FACs in the postmidnight sector (CLAUER; MCPHERRON, 1974). In particular, the premidnight upward FACs are very strong and correlate with intense auroras, commonly associated with the onset of substorm activity (substorm breakup). Over the course of a substorm, the opposing FACs expand on both sides to local times further away from midnight and propagate toward the poles. During periods of enhanced solar wind interactions with the magnetosphere, the cycle of energy accumulation and release has a period of approximately three hours, with the actual substorm activity typically lasting around an hour due to the shielding effect by the ring current system, although longer periods may exist (MANOJ *et al.*, 2008). Hence, substorms are intense yet transient phenomena (LÜHR; KERVALISHVILI, 2021).

2.3.3   Storm-time equatorial electric fields

As discussed in the previous section, numerous solar wind and magnetospheric phenomena are responsible for significant disturbances in the ionosphere. One such phenomenon involves the southward turning of the IMF, leading to the generation of *prompt penetration electric fields* at low latitudes (HUANG, 2020; HUANG; FOSTER; KELLEY, 2005; KELLEY; FEJER; GONZALES, 1979; NICOLLS *et al.*, 2007). It is well-known that the presence of a steady magnetospheric electric field leads to a divergence in the ring current, causing a charge separation known as Alfvén layer, shielding the magnetospheric electric field from low latitudes (e.g., VASYLIUNAS, 1972). However, when the magnetospheric field experiences rapid increases or decreases, the charges become momentarily unbalanced with the new configuration, enabling high-latitudes electric potentials to result in the appearance of electric fields at low latitudes (SPIRO; WOLF; FEJER, 1988a). These electric fields are observed equatorward of the shielding layer (HUANG, 2020; HUANG *et al.*, 2006). In other words, penetration electric fields are the electric fields of solar wind/magnetospheric origin observed in the low-latitude ionosphere (HUANG, 2009). Chapter 4 shows real storm-time examples of penetration electric fields effects.

The first observations of penetration electric fields were reported by Nishida (NISHIDA, 1968a; NISHIDA, 1968b), who noted a clear correlation between quasiperiodic IMF variations and ground geomagnetic fluctuations at the magnetic equator (known as *DP2* current system). Magnetospheric convection electric fields propagate to the high-latitude ionosphere through Alfvén layer waves along geomagnetic field lines. Following a southward turning of the interplanetary magnetic field, enhanced magnetospheric convection leads to high-latitude ionospheric electric fields penetrating toward equatorial latitudes, an effect also called *undershielding*. Consequently, penetration electric fields observed at low latitudes are associated with IMF southward turning because of reconnection between the geomagnetic field and the IMF (although prompt penetration may also occur while IMF Bz is northward), in which a short-lived southward IMF causes a short-lived penetration electric field (HUANG, 2019). Huang *et al.* (2005) suggests that the interplanetary electric field can persistently penetrate the low-latitude ionosphere for many hours during storm conditions without effective shielding. Huang (2019) discusses a prompt penetration event in the equatorial ionosphere lasting 14 hours, encompassing the storm recovery phase. His study revealed strong correlations between vertical ion drift (zonal electric field) fluctuations and variations in other ionospheric parameters, such as ion density, ion composition, electron temperature, and zonal drifts.

As previously mentioned, equatorial daytime ionospheric electric fields display

significant day-to-day variability.   A portion of this variability is attributed to wind-induced diurnal variations, influenced by factors such as location, season, solar irradiation, and local time (SCHERLIESS; FEJER, 1999).   Another component of the electric field variation is attributed to variations in the solar wind interplanetary electric field (IEF) (MANOJ et al., 2008). Abrupt changes as well as quasi-periodic fluctuations of the IEF are known to correlate with the penetration electric fields.   The IEF can persistently penetrate the equatorial ionosphere during the intensification of geomagnetic activity as long as there is a continuous southward IMF (HUANG; FOSTER; KELLEY, 2005).   Prompt penetration electric fields generate a nearly instantaneous response in the ionosphere. This means that modifications in electric fields within the polar ionosphere due to solar wind or magnetospheric processes prompt analogous changes in equatorial electric fields almost instantly, with no apparent time delay. These changes can also be observed in the equatorial vertical and zonal plasma drifts, corresponding to electric fields in the zonal and vertical directions, respectively.

Additionally, apart from the IMF southward turning, sudden variations in solar wind dynamic pressure and magnetospheric substorms can also cause penetration electric fields in the low-latitude ionosphere (FEJER; EMMERT, 2003; HUANG, 2009; HUANG et al., 2008; KIKUCHI et al., 2001; MOTOBA et al., 2003; XIONG; LÜHR; FEJER, 2016). A sudden increase in solar wind dynamic pressure leads to an increased vertical ion drift in the dayside equatorial ionosphere, resulting in an eastward electric field (FEJER; EMMERT, 2003; HUANG et al., 2008; KIKUCHI et al., 2001; MOTOBA et al., 2003).   In isolated substorms triggered by IMF northward turning, a counterelectrojet with a westward electric field occurs in the dayside equatorial region (HUANG, 2019). In cases of substorm onset during continuous southward IMF, both an increased vertical ion drift and an eastward electrojet, corresponding to an eastward electric field, occur in the dayside equatorial region, whereas a westward electric field is observed at night (HUANG, 2009; 2019; 2020; TULASI RAM et al., 2017), showing a quasi-periodicity of ∼3 h associated with the so-called sawtooth events (e.g., REEVES et al., 2003), although shorter substorm recurrence periods may also exist (KEILING et al., 2022; MCPHERRON; CHU, 2018).

There are also electric fields observed at low latitudes during disturbed periods associated with the shielding layer. In the transient state of the middle- and low-latitude ionosphere when the external magnetic field vanishes, an eastward perturbation occurs on the nightside, and a westward perturbation takes place during the day. In essence, the low-latitude electric field may be attributed to Alfvén layer charges, even if no external field exists in the outer regions to shield out, a phenomenon termed as *overshielding* electric fields (HUANG, 2019; HUANG; ZHANG, 2021).   In more details, during intensified magnetospheric convection resulting from a southward turning of the IMF, the convection electric field is not effectively shielded.   The electric field

penetrating into the plasmasphere and the middle- and low-latitude ionosphere is the penetration electric field (undershielding electric field). When the IMF abruptly turns northward, the previously strong magnetospheric convection experiences a sudden reduction. The Region 1 FACs, driving high-latitude ionospheric convection, are rapidly reduced, causing a temporary imbalance in the Region 2 FACs. As the southward IMF, the driver for the penetration electric field, ceases, a dominant shielding electric field is produced by the unbalanced Region 2 FACs. This phenomenon is termed overshielding. Figure 2.13 depicts, in an oversimplified manner, the undershielding and overshielding processes according to changes in the IMF Bz. In the polar cap, the penetration electric field is tied to R1 FACs, while the shielding field is tied to R2 FACs. The imbalance between these FACs influences prompt penetration electric fields in the mid- and low-latitude ionosphere. A southward turn in IMF BZ causes rapid R1 FAC increase, leading to undershielding with a duskward electric field. Conversely, a northward turn can cause overshielding, with a dawnward field, typically occurring during geomagnetic storms.
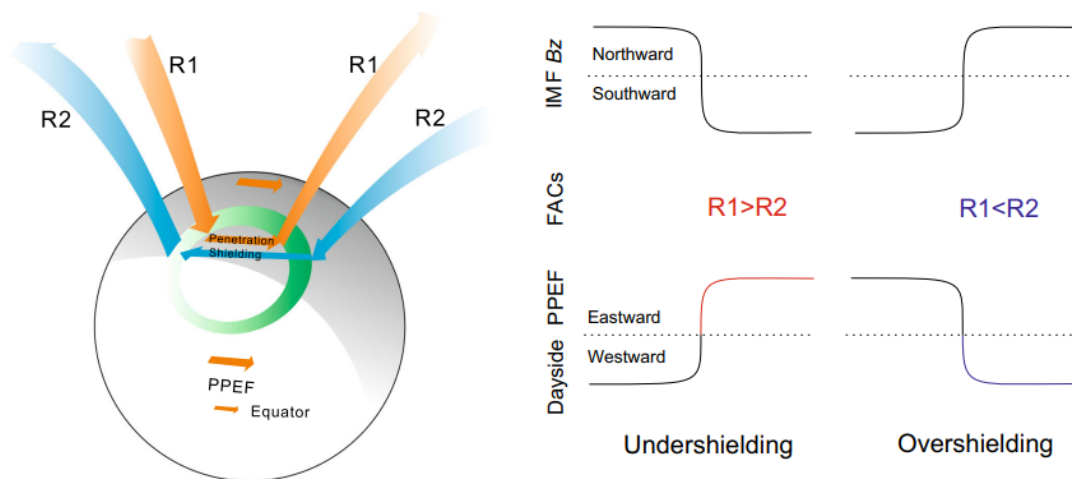
FIGURE 2.13 – (Left) The conventional view of electric field penetration and shielding associates the prompt penetration electric field (PPEF) with Region 1 Field-Aligned Currents (R1 FACs) and the overshielding electric field with Region 2 Field-Aligned Currents (R2 FACs). These electric fields originate in the magnetosphere. (Right) A simplified phenomenological explanation of how prompt penetration electric fields affect the dayside equatorial ionosphere in response to changes in the IMF BZ can be understood through two scenarios, based on different imbalances between R1 and R2 FACs (Adapted from Wei *et al.*, 2015).

The shielding process by Region 2 FACs, proposed to influence the duration of penetration electric fields (VASYLIUNAS, 1972), involves the generation of a dusk-to-dawn electric field opposing the dawn-to-dusk convection electric field across the inner magnetosphere (opposite to penetration electric fields), the so-called *shielding* electric field. When only Region 1 FACs are present (i.e., ideally, Region 2 FACs are 0),

or when Region 1 FACs exceed Region 2 FACs, penetration electric fields prevail at the equator – eastward on the dayside and in the evening sector, and westward in the midnight-dawn sector. If Region 1 FACs are equal to Region 2 FACs, equatorial electric fields become eastward in the dawn-morning sector and westward in the afternoon and evening sector, signifying the dominance of shielding electric fields (FEJER *et al.*, 1990; HUANG, 2020; KELLEY; FEJER; GONZALES, 1979; NOPPER; CAROVILLANO, 1978). It should be noted that the dominance of the shielding effect does not necessarily require a change in the IMF from southward to northward. A sudden decrease in the magnitude of a negative Bz, while maintaining a southward IMF, weakens the magnetospheric convection. This leads to a reduction in energetic particle injection to the ring current, causing it to stop growing or start to decay. Consequently, the magnetic activity strength (Dst index) diminishes, marking the onset of the recovery phase. In this scenario, with a persistent southward IMF, shielding electric fields may become dominant in the middle- and low-latitude ionosphere (HUANG, 2019; HUANG; ZHANG, 2021).

Another mechanism inducing large changes in low-latitude electric fields during magnetic storms is known as a *disturbance dynamo* (BLANC; RICHMOND, 1980; FULLER-ROWELL *et al.*, 2008; MARUYAMA *et al.*, 2005; RICHMOND; LATHUILLERE; VENNERSTRØM, 2003). When auroral zone heating and momentum sources are sufficiently enhanced, they can also impact the neutral atmospheric winds at low latitudes. Consequently, these winds generate distinct electric field patterns through the conventional E- and F-region dynamo process. In contrast to the prompt and nearly instantaneous changes caused by penetration electric fields, the disturbance winds take more time to develop and to travel from the auroral zones to the equatorial region. Hence, they lag behind the auroral inputs by several hours (∼2-12 hrs), making the equatorial electric fields generated by disturbance dynamo occur typically during the recovery phase of magnetic storms (HUANG, 2020; HUANG; ZHANG, 2021). Furthermore, disturbance dynamo electric fields generated by disturbance neutral winds typically exhibit an opposite direction to penetration electric fields (FEJER; JENSEN; SU, 2008b; FULLER-ROWELL *et al.*, 2002; HUANG; FOSTER; KELLEY, 2005). The disturbance dynamo process induces an electric field in the equatorial region with an upward component and a westward component in the evening sector (HUANG; CHEN, 2008), corresponding to a westward drift velocity component and a downward drift velocity component, respectively. Additionally, gravity waves originating from high-latitude processes may propagate to low latitudes and generate dynamo electric fields. The wind fields associated with gravity waves vary over time with the wave period. A time delay of several hours is expected if the gravity wave source is situated in the auroral zone (KELLEY, 2009).

2.3.4   Empirical vertical drift models

The IEF and disturbance dynamo electric field have long been known to strongly influence equatorial plasma drifts during storms (BLANC; RICHMOND, 1980; FEJER; SCHERLIESS, 1997a; KELLEY; FEJER; GONZALES, 1979). In this way, empirical vertical drift models have been used to explain electric field variations observed at mid and low latitudes. Nevertheless, as discussed in the previous section, diverse phenomena give rise to similar fluctuations in the equatorial electric fields, creating a challenge in discerning the individual contributions to the observed variations in the drift velocity. Therefore, current models can only provide an estimate of the expected variation. In Chapter 4, we use current empirical vertical drift models in comparison with vertical drift velocity data from the Jicamarca radar, in an attempt to evaluate their performance given different geomagnetic storm conditions.

Three widely used storm-time empirical vertical drift models were applied here. The Fejer and Scherliess (1997a) (F-S) model estimates equatorial storm-time prompt penetration and disturbance dynamo vertical drifts using times series of 15 min averaged AE indices and transfer functions derived from extensive Jicamarca radar measurements. F-S is the only study to model vertical drift variations caused by disturbance winds separately, which exemplifies the difficulty in separating these components. The input of the F-S are 15 minute resolution AE indices and local time. Because the AE index does not completely describe the state of high-latitude ionospheric currents, this model averages the effects of various high-latitude processes, including substorm and convection enhancements, along with energy deposition in different local time sectors.

The Fejer and Scherliess (1997a) model integrates the prompt penetration component from Fejer and Scherliess (1995) with the disturbance dynamo model developed by Scherliess and Fejer (1997). This model starts from the principle that equatorial zonal electric field disturbances resulting from magnetospheric and ionospheric disturbance dynamos can be separated if their storm-time evolution is considered. The F-S model initially determines the perturbation drifts by removing seasonal and solar cycle effects. This is performed by subtracting the corresponding season and solar flux-dependent quiet time average drift from each quarter-hourly averaged measurement. The resulting perturbations are from prompt penetration, disturbance dynamo electric fields, and day-to-day variability in the ionospheric dynamo electric fields. These perturbation drifts are then modeled based on a time series of AE indices spanning the preceding 28 hours, assuming a linear relationship between the disturbance electric fields and the AE indices. The final step involves modeling these perturbation drifts by separating them into prompt penetration and disturbance dynamo components.

For the prompt penetration component, the direct penetration vertical drift (zonal

electric field) at a given time t is modeled based on changes in the AE indices at times $t - 30$ min and $t - 90$ min (FEJER; SCHERLIESS, 1995). For the disturbance dynamo component, they demonstrate that the effects of disturbance dynamo electric fields on equatorial vertical drifts can be expressed in terms of (positive) hourly averaged values of AE (to remove prompt penetration effects) over the preceding periods of 1-6, 7-12, and 22-28 hours (SCHERLIESS; FEJER, 1997), which take into account the average auroral current effects with time delays of 1-6, 7-12, and 22-28 hours. Their results indicate that the largest disturbance dynamo electric field values occur in the postmidnight sector, with largest amplitudes in the 02-05 local time sector, where this mechanism generates upward velocity (eastward electric field) perturbations. In the morning sector, the disturbance drifts are downward, with smaller amplitudes. The local time dependence of the F-S drifts is described by nine normalized cubic-B splines of order 4. Eight nodes were evenly distributed across local time intervals at 0, 3, 6, ..., 21 hours, and an additional node was placed at 4.5 local time to accommodate rapid changes near dawn. The F-S model works with 45 coefficients determined by a least squares fit to the entire data set and constrained to ensure periodicity in a 24-hour cycle.

The equatorial storm-time empirical models by Kelley and Retterer (2008) and Manoj *et al.* (2008) both utilize interplanetary electric fields measured by the NASA's Advanced Composition Explorer (ACE) satellite to estimate equatorial prompt penetration electric fields, which correspond to vertical plasma drifts. They were motivated by numerous earlier studies pointing out that the magnetosphere-ionosphere system generally acts like a high-pass filter in response to interplanetary electric field variability (e.g., HUANG *et al.*, 2007; KELLEY, 2009; NICOLLS *et al.*, 2007).

Based on a number of earlier studies, Kelley and Retterer (2008) proposed an average ratio of the equatorial zonal prompt penetration electric field to the dawn-to-dusk interplanetary electric field, which is 0.1 (10%) for southward IMF and 0.03 (3%) for northward IMF. This parametrization, referred here as the K-R model, has been employed in subsequent studies of daytime equatorial prompt penetration electric fields (e.g., HUANG, 2019; 2020; HUANG; ZHANG, 2021).

The model developed by Manoj *et al.* (2008) was later integrated by Manoj and Maus (2012) with the outputs of Scherliess and Fejer (1999) quiet-time vertical drift model to offer real-time global equatorial zonal electric field predictions. Additionally, the prompt-penetration model by Manoj *et al.* (2008) was developed using daytime zonal electric field data only. Manoj and Maus (2012) extended it to all local times using a scaling function. These predictions are available at `https://ppefm.geomag.info/`, with documentation available at `http://www.geomag.us/models/PPEFM`. The model inputs are date, UT, and longitude. Manoj *et al.* (2008) developed a transfer function to predict daytime ionospheric disturbances from IEF data using the ACE satellite, eight years

of ionospheric drift measurements from the low-latitude JULIA (Jicamarca Unattended Long-term Investigations of the Ionosphere and Atmosphere) radar, and eight years of Jicamarca ISR measurements from Manoj and Maus (2012). To formulate the model, they assessed the coherence and phase difference between the IEF and the equatorial electric field, considering their relationship across different frequencies. Coherence, ranging from 0 to 1, quantifies how well one input corresponds to the output at each frequency. The frequency-dependent transfer function between the IEF and the equatorial ionospheric zonal electric field is established as the ratio of their cross-spectra to the auto-spectra of the input. This transfer function characterizes the average behavior of the system, specifically a certain aspect of the coupling between the magnetosphere and the ionosphere. Notably, the model's transfer function exhibits sensitivity solely to changes in the IEF, not its absolute value. The most significant feature of the transfer function is the broad peak around 2 hours, indicating the highest admittance of the IEF to the equatorial zonal electric field during this time.

To conclude this chapter, it is important to mention that two quiet-time empirical vertical drift models were also used in the present work, the model by Scherliess and Fejer (1999) (S-F model) and the one by Fejer *et al.* (2008a) (ROCSAT model). We will briefly discuss them in this section, even though they are not storm-time models. The former was used as a reference for the ionospheric quiet-time pattern both in the storm-time analysis and in the C/NOFS climatology. In this study, they combine Atmospheric Explorer E satellite (AE-E) data with extensive Jicamarca incoherent scatter radar vertical drift. This analytical model describes the local time and longitudinal variations of vertical drifts for each season and solar flux interval. It employs univariate normalized cubic-B splines of order four, with coefficients determined through least squares fit to binned data, constrained for periodicity in 24 hours and 360°. Only data during geomagnetically quiet conditions (Kp $\leq$ 3) were utilized. Input parameters are continuous values of local time, longitude, F10.7 cm solar flux index, and day of the year. The model's longitudinal and temporal resolution is approximately 30° and 1/2 hour, respectively. In greater detail, the Scherliess and Fejer (1999) model uses the curl-free nature of the electric field to constrain drift amplitudes. The vertical plasma drift at the geomagnetic equator is directly influenced by the zonal component of the electric field. This electric field component must be irrotational at any given time, constraining the line integral of this electric field along the equator to be zero:

$$\oint \mathbf{E} \, d\varphi = \oint B v_z \, d\varphi = 0 \tag{2.14}$$

where B denotes the equatorial magnetic field strength, φ is the geographic longitude, and v_z is the vertical drift. They applied this restriction to each quarter-hourly Universal Time

by initially multiplying the drift velocities on a 5° longitudinal grid by the corresponding magnetic field strength B. Subsequently, they integrated the resulting zonal electric field component along the geomagnetic equator. The obtained quarter-hourly velocity offsets were then employed to adjust the drift amplitudes, ensuring the preservation of near-conservative electric fields.

As for the quiet-time model by Fejer *et al.* (2008a), we used this model to be compared with the C/NOFS vertical drift velocity. It is a global empirical model for equatorial F-region vertical plasma drifts developed using five years of measurements from ROCSAT-1 (Republic of China Satellite 1). The model, which is most accurate during equinox and December solstice, describes in 15° latitudinal bins the local time, seasonal, and longitudinal dependence of the vertical drifts for an altitude of 600 km under moderate and high solar flux conditions (the model works best for a flux in the range 100-200 sfu). They determined that the variations of the drift velocities with solar flux were best reproduced by using bi-linear relationships. The model was derived with Kp ≤ 3 for each season and it also uses the curl-free nature of the electric field to constrain drift amplitudes given in Equation 2.14.

3 Instrumentation and Methodology

This chapter aims to expose the instruments, methods, and theory used in the FPMU, C/NOFS, and Jicamarca radar data analysis. Moreover, in view of the ionospheric climatological model used in this work, this chapter will address the particularities of the International Reference Ionosphere 2020 and how it relates to the objectives of the data analysis. Here, all the procedure used in the data treatment will be explained in detail.

3.1 Floating Potential Measurement Unit

The Floating Potential Measurement Unit (FPMU) was developed by Utah State University Space Dynamics Laboratory to study surface charging of the International Space Station. It has been in operation since 2006. The ISS surface charging is a complex problem due to its large size, its variety of conductive/dielectric areas, and the exposed solar cell edges on its high voltage solar arrays (BARJATYA *et al.*, 2009). FPMU most important use is during extravehicular activity (EVA). When an EVA is planned, FPMU is activated to collect the number density of ions (N_i), the electron temperature (T_e) and the plasma floating potential (ϕ_f) data 2-3 weeks prior to the EVA date (HARTMAN *et al.*, 2019), since the spacecraft charging is a matter of safety for manned activities. Additionally, any resultant surface charging can lead to functional anomalies and surface degradation of the ISS. Thus, the FPMU development was judged critical for ISS safety operations. More particularly, the objective of the FPMU is to provide the ISS Program with a monitoring of variations in the vehicle floating potential due to the interactions of the high voltage power system with the ionospheric plasma environment (COFFEY *et al.*, 2008), and to validate the Plasma Interaction Model (PIM) developed to predict ISS charging (DEBCHOUDHURY *et al.*, 2021).

A secondary purpose of the FPMU is the measurement of electron density and temperature of the F region of the ionosphere to understand why the ISS charges. Hence, this instrument suite can be also powered on to obtain measurements for expected active space weather conditions and science campaigns (COFFEY *et al.*, 2017).

In fact, the FPMU operates on a campaign basis of less than ~30% of a year and this includes periods of a few days to weeks. For this reason, this suite of instruments does not operate continuously; it is activated by ground commands and data are recorded only for specific data campaign durations. The data is open to the public at `https://spdf.gsfc.nasa.gov/pub/data/international_space_station_iss/sp_fpmu/`. Furthermore, NASA provides the FPMU data in the CDF (Computable Document Format) file format. Each file output includes the year, month, day, Universal Time, geographic latitude (degrees), geographic longitude (degrees), altitude (km), ion density (m^{-3}), electron temperature (K), and sunlight (this parameter can only assume two values, 0 corresponding to no sunlight and 1 for the opposite).

As cited above, the plasma density product provided by the FPMU is ion density and not electron density as it is commonly seen in ionospheric scientific data, and this is explained by Debchoudhury *et al.* (2021). They mention that the electron and ion densities from the wide Langmuir probe analysis generally agree with each other, but the standard deviation in the derived electron density was higher than that of the derived ion density for the FPMU data. This is largely due to noisier measurements in the electron saturation region of the measured *I-V* curve. Thus, ion density is used as a better proxy for quasi-neutral plasma density. Since the ionosphere is a quasi-neutral plasma, the ion and electron densities are theoretically the same. Due to this, ion densities are reported as the same as electron densities when downloading the FPMU data.

All data from the FPMU is transmitted through the Ku frequency band (12 GHz to 18 GHz), which is the high-bandwidth communications band for the ISS. However, data from other ISS activities often take priority over FPMU data transmission, resulting in gaps in FPMU data. Additionally, all of the Ku-band data is relayed through the Tracking and Data Relay Satellite System (TDRSS), a network of American communications satellites and ground stations used by NASA for space communications, to stations on the ground in the United States. Due to TDRSS communications limitations over Asia, very little or (often) no Ku-band data can be transmitted when the ISS is at 40°-90° longitude (BROADWATER, 2013). Figure 3.1 shows an example of ISS orbital data coverage. The very low and sparse amount of data over 40°-90° longitude is a feature present in all of the maps generated in this work, with the maps appearing more or less complete depending on the number of data points in each case.

The FPMU consists of a suite of four plasma instruments, providing plasma densities, temperatures, and spacecraft charging potentials, that is, the floating potential of the ISS. It includes a wide Langmuir probe (WLP), a narrow Langmuir probe (NLP), a floating potential probe (FPP), and a plasma impedance probe (PIP). Also, the nominal data rate is 1 Hz. The FPMU is the only resource of in-situ Langmuir probe observations at an altitude of ~400 km that covers low and mid latitudes for over 15 years. According

to Coffey *et al.* (2008), the accuracy of the ISS/FPMU for electron temperature is about 500 K over a range of 500 K to 4800 K and about 100 cm^{-3} within the range of 10^4 cm^{-3} to 10^7 cm^{-3} for the density. The ISS orbits the Earth approximately every 92 min or about 16 times per day, has a varying altitude of about 400 km, a maximum latitude of about 52°, and an inclination of 51.6°. A large portion of the orbiting period is spent in sunlight.
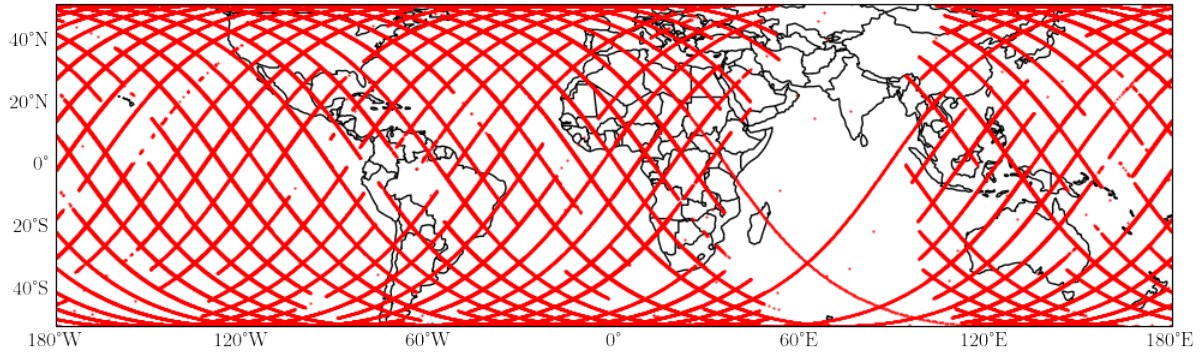
FIGURE 3.1 – Example of FPMU data coverage for the 7-10 February 2010 orbits. The 40°-90° longitude region where there is nearly a lack of data points can be noticed.

The WLP is a gold-plated sphere of radius 5.08 cm and its working principle is to apply to the probe a voltage sweep from -20 V to +80 V relative to chassis ground and to measure the resulting currents. The small step size from 0 V to 50 V allows the determination of T_e after several samples in the electron retarding portion of the sweep. The NLP is a gold-plated cylinder with radius 1.43 cm and length 5.08 cm. A sweep from -4.9 V to +4.9 V, in 512 equal steps, is applied to the NLP during 1 s, followed by a sweep down from +4.9 V to -4.9 V the next second. This sweep voltage is referenced to the floating potential as measured by the FPP. Thus, even this small sweep range should cover the electron retardation region and some electron saturation regions, which enables the determination of N_e and T_e at 1 Hz (BARJATYA *et al.*, 2009). As for the FPP, it is also a gold-plated sphere of radius 5.08 cm that is isolated from the chassis ground by a high impedance circuit. This instrument measures the ISS ϕ_f at the FPMU location between ±180 V at 128 Hz sample rate (DEBCHOUDHURY *et al.*, 2021).

Finally, the PIP is unique in that its impedance is used to obtain information about the main plasma's characteristics (COFFEY *et al.*, 2008). It consists of an electrically short dipole antenna that is electrically isolated from the ISS and is oriented perpendicular to the ram flow. It is operated in two different modes. In the plasma sweeping probe (PSP) mode, the instrument measures the electrical impedance (magnitude and phase) of the antenna sweeping at a frequency of 256 Hz over a 100 KHz to 20 MHz range, from where electron density, electron-neutral collision frequency, and magnetic field strength can be deduced. In the plasma frequency probe (PFP) mode, the antenna tracks the frequency at which an electrical resonance associated with the upper hybrid frequency occurs. The

upper hybrid frequency is a resonance phenomenon for electromagnetic waves with **E** perpendicular to **B** propagating across an static magnetic field, which in this case is the Earth's static magnetic field generated in the Earth's core. This frequency consists of long wavelength oscillations, corresponding to a "hybrid", or mix, of the electron plasma and electron cyclotron frequencies. The principle behind the operation of an impedance probe is the observation of the variations of an input impedance of an electrically short antenna immersed in a plasma as the antenna is swept with a changing RF (radio frequency) source. The impedance versus frequency profile displays strong plasma features as the antenna resonates with the fundamental plasma frequencies. Also, this profile, along with an appropriate theory, can be used to determine a number of plasma parameters such as electron density, electron-neutral collision frequency, cyclotron frequency, etc. It can be said that the main advantage of an impedance probe is that the antenna input impedance is primarily sensitive only to the dielectric properties of the antenna, being largely independent of the grounding scheme and of the surface properties of the antenna itself. Hence, this technique is not affected by the spacecraft charging (BARJATYA *et al.*, 2009).

To summarize, the WLP and NLP current-voltage (I-V) curves give measurements of plasma potential, electron and ion density, and electron temperature. The PIP impedance-frequency curves give measurements of absolute electron density by providing the location of the upper hybrid frequency (DEBCHOUDHURY *et al.*, 2021). In reality, NLP performance has degraded over the years and is no longer utilized to reduce plasma parameters, but FPP, WLP, and PIP have continued to operate nominally. Table 3.1 shows the data products derived from FPMU, as well as their sampling frequency and the instrument returning this data product. Additionally, the table contains a classification of these data products as primary or secondary, where the primary corresponds to the ones derived directly from in-situ measurements, and the secondary are derived from either further analysis of the primary products with some assumptions or incorporating external model outputs such as the International Geomagnetic Reference Field (IGRF) (DEBCHOUDHURY *et al.*, 2021).

It is important to consider the sources of the ISS charging, since it is a function of ambient plasma density and temperature. More precisely, the situations that can cause issues in the charging measurements are the sources due to the motion of ISS through the Earth's geomagnetic field, i.e., background $V_{ISS} \times \mathbf{B}$, where V_{ISS} is the magnitude of the ISS velocity; due to additional electron collection on the exposed edges of solar cells as the ISS passes from eclipse to sunlight; and due to high densities and low temperatures of the equatorial anomaly as the ISS passes through the Earth's geomagnetic equator region (BARJATYA *et al.*, 2009).

Owing to the charging issues cited above, the WLP, which is the instrument that

TABLE 3.1 – Parameters returned by the FPMU suite of instruments.

Parameter	Instrument	Type	Frequency (Hz)
Electron density (n_e)	WLP	Primary	1
Electron density (n_e)	PIP	Secondary	1
Electron temperature (T_e)	WLP	Primary	1
Plasma potential (ϕ_p)	WLP	Primary	1
Floating potential (ϕ_f)	FPP	Primary	128
O$^+$ percentage	WLP	Secondary	1

provides the main FPMU data for scientific investigations (plasma density and electron temperature, sampled at a temporal cadence of 1 s), has undergone refinements in its analysis algorithm. The refinements also address aging instrumentation, changing solar activity, as well as enhancements to the algorithm to give new data products (e.g., O$^+$ composition) (DEBCHOUDHURY *et al.*, 2022). Besides the sources of the ISS charging already mentioned, one particular source of error in the original FPMU analysis algorithm was the uncertainty associated with photoelectron emission current from the metal probe surface, which may contribute to errors in estimated densities. Moreover, uncertainties in estimates during solar minimum are greater than the corresponding years of solar maximum. This is because the low current levels recorded by electrical probes when the background densities are reduced lead to low signal-to-noise ratios (SNRs). Hence, uncertainties due to photoelectric currents are also magnified for years in solar minimum and especially when the ISS comes out of eclipse. Another possible source of error during times of low solar activity is the assumption that the F-region ionosphere around the ISS orbit consists primarily of O$^+$ ions. This can be true most of the time during solar maximum, but in periods of low solar activity the dominance of O$^+$ can decrease significantly. Consequently, the effects of H$^+$ ions on the measured *I-V* curve cannot be ignored in order to achieve better accuracy in the derived ion density (DEBCHOUDHURY *et al.*, 2021).

Since the FPMU does not operate continuously, as mentioned in the text, it is important to clarify the amount of data this probe returned for the time period used in this study. Figure 3.2 illustrates the days when FPMU was operational from 2008 to 2019, which corresponds to the amount of data used in this thesis. These days are shown as grayed-out blocks against the day of the year (DOY) on the left y-axis, corresponding to which data exists. Overlaid on top of the figure is a plot of the F10.7 solar flux (see Section 2.3.1) on the right y-axis showing the behavior of this index throughout the end

of Solar Cycle 23 and the entire Solar Cycle 24. This index has been smoothed using a 61-day moving average filter. Additionally, the shadowed sections in blue show the last two solar minima of solar cycles 23 and 24, whereas the yellow shadowed section represents the solar maximum of Solar Cycle 24. The black dashed horizontal lines separate the day of year in every two months (the lines were set approximately every 61 DOY), aiming to bring an idea of the amount of data in each pair of months.

Despite having a considerable amount of data gaps, the instrument was operated over a major part of Solar Cycle 24 (i.e., 2008-2019). The total number of FPMU operational days from 2008 to 2019 corresponds to approximately 39% of the total calendar days, where the significant bulk of these measurements is concentrated in the years 2011-2019, totaling ∼82% of the whole FPMU operational days. Since 2019, FPMU has been operated sparingly due to an intermittent ISS-provided power supply (DEBCHOUDHURY *et al.*, 2021), and for this reason there is a decrease in the number of days of operation for that year.
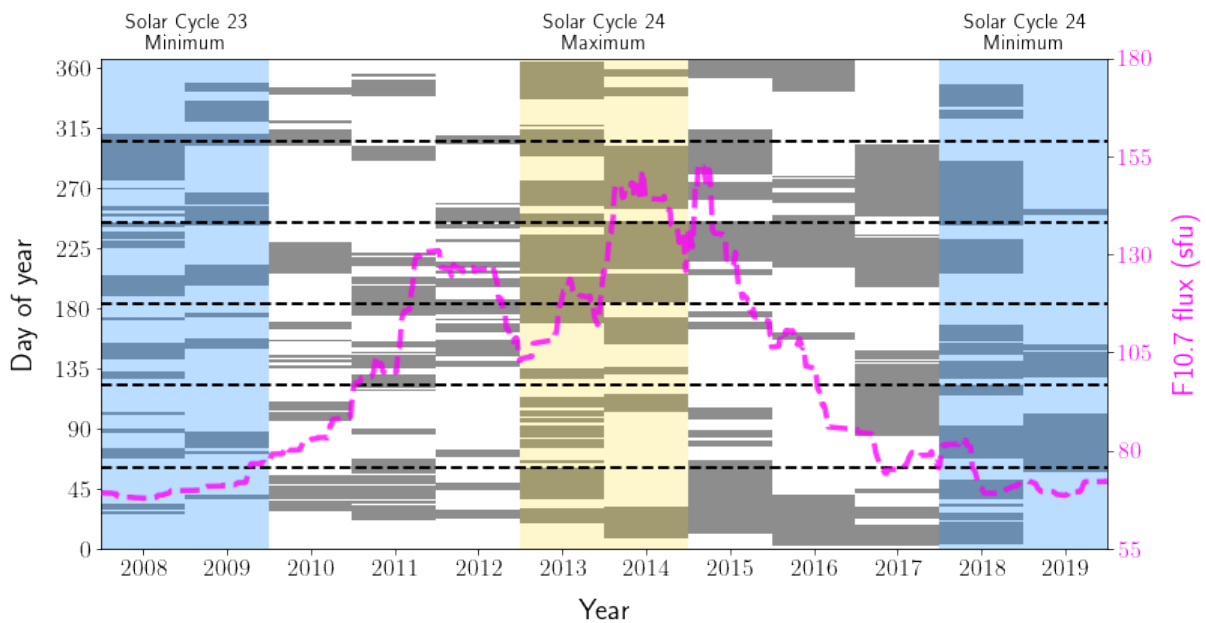
FIGURE 3.2 – FPMU data coverage with solar cycle progression for the period used here, i.e., 2008-2019. The F10.7 solar flux index is also shown, overlaid on top of the figure. The blue shadowed sections correspond to the last two solar minima of solar cycles 23 and 24, and the yellow shadowed section represents the solar maximum of Solar Cycle 24. The black dashed horizontal lines separate the day of year into pairs of months (∼61 DOY).

3.2   Communications/Navigation   Outage   Forecasting   System

The Communications/Navigation Outage Forecasting System (C/NOFS) is a collaborative US minisatellite mission led by the Space Test Program (STP) in partnership with the Department of Defense (DoD), Air Force Research Laboratory (AFRL), and Space and Missile Command Test and Evaluation Directorate (SMC/TEL). Project contributors include NASA, Naval Research Laboratory (NRL), the University of Texas at Dallas (UTD), and the Aerospace Corporation. C/NOFS main objective was to provide the first-ever forecasting of ionospheric irregularities in Earth's equatorial region, specifically those impacting satellite communication and navigation systems (DE LA BEAUJARDIERE, 2004). The objective was then to identify conditions that may result in scintillation in specific regions, enabling the provision of outage forecasts with a lead time of 3-6 hours before its onset.

C/NOFS was launched into a low-inclination orbit of $\pm 13°$ geographic latitude in April 2008, with an orbital period of approximately 100 minutes. The apogee and perigee initially were 850 km and 400 km, respectively, in 2008, gradually decreasing to 635 km and 377 km by April 2014. Notably, C/NOFS had the capability to fly along, or close to, the magnetic equator over a significant longitude and local time range (HUANG; HAIRSTON, 2015). In more details, C/NOFS was launched during a period of unusually low solar activity, where it experienced a slower orbit decay than anticipated. The apogee began decreasing more significantly as solar activity rose in 2011. By the first quarter of 2015, the apogee had dropped below 500 km, with the perigee falling below 350 km. In late November 2015, the spacecraft's orbit circularized, leading to re-entry on November 28, 2015, concluding its approximately 7.5 years in orbit (PFAFF et al., 2021).

The satellite payload comprises five instruments. The Planar Langmuir Probe (PLP), a dual-disk probe designed to monitor ionospheric plasma densities. The PLP serves a dual purpose by providing both low time-resolution density inputs for background ionosphere models and high time-resolution density irregularity measurements for specifying disturbance microphysics. Additionally, the PLP monitors the spacecraft surface potential. Another instrument, the Vector Electric Field Instrument (VEFI), is primarily composed of three orthogonal 20 m tip-to-tip double probe antennas. VEFI plays a crucial role in measuring DC electric fields that cause plasma drift motions, driving ionospheric instability. It also captures quasi-DC electric fields within plasma depletions to discern their motions relative to the background ionosphere. Furthermore, VEFI measures vector AC electric fields, helping in characterizing the microphysics of ionospheric irregularities (PFAFF et al., 2021). The

instrument package is completed with a fluxgate magnetometer, optical lightning detector, and fixed-bias Langmuir probe. The Coherent Electromagnetic Radio Tomography (CERTO) is a tri-band (150 MHz, 400 MHz and 1067 MHz) radio beacon contributing to multi-frequency scintillation studies. It works in conjunction with ground receivers to specify plasma conditions between the location of the satellite and Earth. CERTO is also employed for tomographic reconstruction of electron density profiles.

Furthermore, the C/NOFS Occultation Receiver for Ionospheric Sensing and Specification (CORISS) is a GPS dual-frequency receiver tasked with measuring TEC during occultations. By observing lines-of-sight between C/NOFS and GPS satellites, CORISS provides remote sensing capabilities, offering vertical profile information during occultations. Limb profiles of TEC can be inverted to produce vertical profiles of electron density. Overall, these instruments collectively contribute to a deeper understanding of ionospheric conditions and enhance modeling capabilities (DE LA BEAUJARDIERE, 2004).

Finally, the C/NOFS instrument used in the present work is the Coupled Ion Neutral Dynamics Investigation (CINDI) Ion Velocity Meter (IVM), which consists of two sensors: an ion drift meter and a retarding potential analyzer. The ion drift meter directly measures the ion drift vector, ion temperature, and major ion composition along the satellite track with a spatial resolution of about 4 km. Additionally, the IVM provides measurements of local vertical and horizontal ion drift components, offering high-resolution insights at a spatial resolution of 500 m. The data obtained from the IVM instruments are crucial for understanding ionospheric dynamics, providing valuable information to both scientific research and operational capabilities (STONEBACK et al., 2011).

3.3   Jicamarca Radio Observatory

The Jicamarca Radio Observatory (JRO) radar has been using two main modes over several years. The ISR mode, employing high-power transmitters (1.5 MW), operates approximately 1000 hours annually for ionospheric surveys, extracting parameters like drifts, densities, and composition. The JULIA mode, utilizing low-power transmitters (20 kW), operates around 4000 hours per year, focusing on measuring coherent echoes such as from the equatorial electrojet, spread F regions, and 150 km echoes to serve as a proxy for ionospheric behavior (KUYENG et al., 2023). In the next section, we will briefly describe the radar main operating mechanisms.

3.3.1 Jicamarca incoherent scatter radar

Normally, the terrestrial ionosphere can be considered a quiescent plasma under regular conditions. Thus, studying the ionosphere using radars operating at frequencies of 40 MHz or higher, values considerably above not only the frequency of the E-region plasma ($\sim$3 MHz), but also the maximum frequency of the plasma in the ionosphere ($\sim$20 MHz), results in most of the transmitted power being lost to space. Therefore, only a small part of the energy is re-radiated by free electrons, whose densities vary due to thermal fluctuations (FEJER; KELLEY, 1980). This is the fundamental idea behind the operation of the incoherent scatter radar, that is, the incoherent scatter technique.

The incoherent scatter radar located in Jicamarca, Peru, became operational in 1961, and at the end of April of this same year, the first echoes were obtained. The first electron density profiles generated by the Jicamarca ISR showed, for the first time at equatorial latitudes, the exponential decay of electron density above the F-peak (BOWLES, 1961), in the same way as shown for midlatitudes in Figure 1.1.

Succinctly, an ISR works by sending a high-powered radar pulse into the ionosphere and measuring the echoes that return. The measurement of the total scattered power and the power spectrum (autocorrelation function) of the scattered signals provide important information about basic parameters of the ionosphere, such as plasma density, temperatures, and electric fields. The power is determined by the electron density, the Debye length (scale over which mobile charge carriers, such as electrons, screen out electric fields in plasmas and other conductors. The Debye length is a characteristic distance over which ions and electrons can be separated in a plasma), and the ratio of electron to ion temperatures. As for the shape of the power spectrum, it also depends on several parameters, including the Debye length, electron and ion temperatures, collision frequencies, ion constituents, plasma shifts and currents, and the magnetic field strength and its orientation relative to the radar wave vector (FEJER; KELLEY, 1980). The main advantages of the incoherent scatter method are the ability to make quantitative measurements of numerous ionospheric parameters as a function of altitude (varying from $\sim$80 km to 2000 km), and the possibility of obtaining almost a continuous monitoring of the ionosphere remotely from the ground.

A general characteristic in scattering is that it comes from irregularities whose dimensions are on the order of the wavelength of the radiation (KIRCHHOFF, 1978). Thus, unlike a usual radar, which deals with reflected signals that are "exact" copies of the transmitted signals, measuring only the delay in the propagation of the signal to determine the distance to the target in question, an incoherent scatter radar deals with "objects" that are distributed in space, i.e., deals with thermal fluctuations of the plasma, where the targets are a mass of billions of ions and electrons distributed in

space. The power of the scattered signal is extremely low because the region of the plasma that is, for a millisecond, instantly "illuminated" in the space sector radiated by the radar is very small. Accordingly, radars transmit power in megawatts (10^6 watts) and receive a signal in picowatts (10^{-12} watts), that is why it is common to average the measurements in seconds to minutes, to allow sufficient signal to be collected (JOHANSSON, 2009). More specifically, an ISR works through a secondary effect called *backscatter*. As stated above, a small part of the ionosphere is "illuminated", that is, is excited with the energy of the frequency transmitted by the radar. A small part of this energy is directed back and detected by the ISR, which can be used to deduce different parameters of the ionosphere, as mentioned previously.

The Jicamarca ISR consists of four 1.5 MW transmitters, with a large antenna composed of 18432 half-wave dipoles (an antenna that converts electric energy into electromagnetic waves, as well as electromagnetic waves into electric signals. Its name derives from the fact that this antenna has a length equal to half the wavelength to be radiated), covering an area of about 90000 m² (300 m × 300 m). Although this ISR offers flexibility to direct the radar beam, changes cannot be made quickly as it needs to be changed manually (JOHANSSON, 2009). The main antenna of the Jicamarca ISR can be seen in Figure 3.3, which is one of the largest in the world. The transmitter has a peak power of 5 MW and operates at a frequency of 50 MHz. It consists of two main parts, a power supply and plate modulator and a 50 MHz power amplifier.
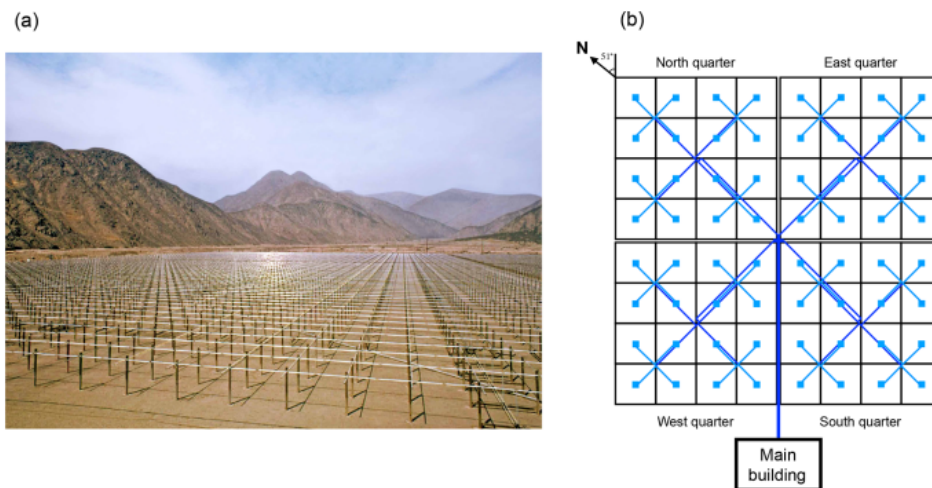
FIGURE 3.3 – (a) JRO main radar antenna assembly. (b) The main array is divided into quarters, each of which is composed of 16 antenna modules, encompassing a total of 64 modules (WOODMAN *et al.*, 2019).

The vertical plasma drift velocities in the F region measured by the JRO ISR have high precision. This is achievable by directing the radar beam perpendicular to the magnetic field, resulting in long signal correlation times and simple derivation of velocities from the phase of the autocorrelation function (WOODMAN; HAGFORS, 1969). The ISR provides

semi-routine measurements (10-45 days/year) of vertical drift velocity as a function of local time and altitude. The altitude range covered by the Jicamarca radar extends from about 200 km to beyond 700 km during high solar flux conditions. Typical altitude resolution is about 15 km, and temporal resolution is approximately 5 minutes (KUDEKI; BHATTACHARYYA; WOODMAN, 1999).

The data of the ISR radar used here was downloaded from the Madrigal Database, which is an upper atmospheric science database. The data is available publicly at `http://jro-db.igp.gob.pe/madrigal/`. The data is also not continuous. The user can choose which parameters to download and, in the present case, the outputs included the year, month, day, hour, minute, second, geodetic latitude (degrees), geodetic longitude (degrees), altitude range (km), electron density (m^{-3}), and electron temperature (K).

Finally, the term "incoherent" was coined due to the randomness of electron motion, as it was believed in early theories that such motion was completely incoherent, scattering energy in all directions. This term prevails today, although later theoretical investigations have shown that the presence of ions in the terrestrial ionosphere introduces a certain degree of coherence (SCHUNK; NAGY, 2009) into the scattering. Another name was therefore suggested, namely *Thomson scattering* (KIRCHHOFF, 1978).

3.3.2 Jicamarca Unattended Long-term Investigations of the Ionosphere and Atmosphere Medium Power

For several years, the Jicamarca ISR had the limitation to obtain drifts for periods not longer than 1000 hours per year since the ISR was only able to get drifts during operations with big transmitters. This changed in 2022, when the JRO integrated two new solid-state transmitters, each with a peak power of 96 kW (Figure 3.4). This advancement enables the detection of not only coherent echoes but also the estimation of zonal and vertical drifts in the ionosphere. Termed Jicamarca Unattended Long-term Investigations of the Ionosphere and Atmosphere Medium Power (JULIA MP), this new mode retains the capability to measure coherent echoes, similarly to the original JULIA mode, while extending its functionality to estimate zonal and vertical drifts up to 500 km. In summary, the JULIA MP mode was designed to obtain the coherent echoes detected with the JULIA mode plus the ISR medium power mode, to be able to obtain the vertical and zonal drifts. This means that the JULIA MP mode obtains drifts not only during ISR campaigns (around 1000 h/year) but also during low power campaigns (around 4000 h/year) (KUYENG et al., 2023).

JULIA MP is a lower power (and lower operational cost) mode, operated with a 10% duty cycle, allowing for nearly continuous operation of the radar. The main disadvantage

of this mode is that, under low plasma density conditions (i.e., after about midnight), the incoherent scatter measurements have very large errors. In the JULIA MP mode, the interpulse period (IPP) is 1500 km, the pulse length is 45 km, and the radar beams are directed about 2.4° eastward and 4.3° westward in the plane perpendicular to the magnetic field. The data acquisition and signal processing techniques and the procedure for deriving the vertical (positive upward) and zonal plasma (positive eastward) drifts from the line-of-sight values are the same as in standard Jicamarca radar drift experiments. These were described by Kudeki *et al.* (1999) and Woodman (1970), respectively.

FIGURE 3.4 – The JULIA MP 96 kw solid-state transmitters (KUYENG *et al.*, 2023).

To conclude this section, the Jicamarca drift experiments also provide temporal and spatial information on nighttime small-scale (3-m) equatorial spread F plasma irregularities. However, ambient F-region plasma drifts cannot be reliably derived in regions of strong spread F echoes and when the plasma is strongly inhomogeneous in the east-west plane over the altitudinal range of about 200-800 km. Therefore, measurements from these coherent scatter regions are routinely removed from the Jicamarca drifts.

3.4   International Reference Ionosphere 2020

Among the many different models that exist for the ionosphere, the International Reference Ionosphere (IRI) is one of the most widely used for predicting ionospheric climatology. The international project IRI is an empirical ionospheric model supported by the Committee on Space Research (COSPAR) and the International Union of Radio Science (URSI) with the goal of developing and improving an international standard for the parameters in the Earth's ionosphere. The main data sources of IRI are the worldwide network of ionosondes, incoherent scatter radars (Jicamarca, Arecibo, Millstone Hill, Malvern, and St. Santin), the ISIS (Intelligent Spacecraft Interface Systems) and

Alouette topside sounders, and in-situ instruments flown on a large amount of satellites and rockets (BILITZA; REINISCH, 2008). Many of these data sources are at midlatitudes, making IRI to perform better in this region than at low latitudes (BROADWATER, 2013). Also, IRI is considered the international standard for the ionosphere by the International Organization for Standardization (ISO).

Several improved editions of the model have been released as new measurement data emerges, turning IRI into a climatological reference to compare to forecasts from other models. Actually, IRI is updated biannually during special IRI Workshops (i.e., during COSPAR general assembly). It is also widely used for various different applications as is demonstrated by the many papers in science and engineering journals that recognize its use. In reality, about 11% of all radio science papers each year employ IRI as part of their data (BILITZA *et al.*, 2016). For given location, time and date, IRI provides values of the electron density, electron temperature, ion temperature, and ion composition (O^+, H^+, N^+, He^+, O_2^+, and NO^+) in the ionospheric altitude range of 50 km to 2000 km (BILITZA; REINISCH, 2008).

In more details, IRI represents monthly averages of electron and ion densities and temperatures in the altitude range of 50 km to 2000 km. It also provides the vertical total electron content (VTEC) from the lower boundary (60 km to 80 km) to a user-specified upper boundary. Additional IRI output includes the ion drift near the magnetic equator and the probability for the occurrence of the F_1 layer and of spread F (BILITZA *et al.*, 2017).

All major versions of IRI are available for download as FORTRAN code at `https://irimodel.org/`. IRI-1990 was the first version of the IRI model to be released as a computer model. IRI-2020 is the current version of the IRI model and is the one used in this thesis. The model can also be run online at `https://kauai.ccmc.gsfc.nasa.gov/instantrun/iri`, but this instant online running is most used for single data points and not for satellite input orbits such as ISS.

In this work, IRI-2020 was run using FORTRAN codes to ingest ISS times, locations, and heights, returning as output a text file containing electron density (m^{-3}) and electron temperature (K) at each point in space and time where FPMU data existed. More precisely, the output is what IRI predicted in accordance with FPMU input. The text file input variables were the year, day of year (DOY), hour, minute, second, geographic latitude (degrees), geographic longitude (degrees), and height (km) of all the FPMU data used, from 2008 to 2019.

3.5 Data analysis methods

The main goal of this section is to explain the methodology used in the treatment of the FPMU, C/NOFS, and IRI data. The Jicamarca did not have a specific methodology because the Madrigal database provides the final drift velocity data, hence, we only had to limit the altitudinal range, which varied depending on the storm. Ultimately, effort was put in demonstrating that all the data used here are reliable and that they lie within the statistical variability of other plasma data sources. To come to this conclusion, the IRI data was processed experimentally in the very same manner that the FPMU data. All the data was plotted using the Python programming language version 3.8.8 (see `https://docs.python.org/3/` for Python documentation).

3.5.1 FPMU data

Three types of analyses were carried out using the FPMU data: a statistical distribution of ion density and electron temperature gathering all available data from all the years that cover the study executed here; a spatial dynamics analysis; and a temporal temperature analysis. The motivation behind each of the three analyses share the same idea: to understand the climatology of the ionosphere in a long-term fashion. The statistical distribution aims to show how the FPMU data can be used to describe the ion density and electron temperature in the altitude of the ISS, demonstrating the shape of the distribution of these parameters in order to statistically understand the data. The spatial dynamics analysis, the one that we give more focus, aims to give a broad geographical view of the parameters. Since the ISS orbits the Earth, it makes sense to display the data in geographic coordinates in an attempt to describe the behavior of the ionosphere according to sections or regions in the globe. Finally, the temporal temperature analysis seeks to succinctly show the morning overshoot phenomenon on the FPMU data.

Ion density data was converted to cm^{-3} for convenience. Additionally, it is important to mention that the ion density data were filtered in the years 2008 and 2009, so that densities greater than 4×10^6 cm^{-3} were excluded from the data analysis. The reason for such filtering was due to the fact that these data were inconsistent with the expected pattern, possibly being associated with instrumental errors. In other words, densities greater than the mentioned value are not expected to occur in years of low solar activity, and this inconsistency was only seen in the years 2008 and 2009. To clarify that, Figure 3.5a shows ion density data for 2008 without the filtering, whereas Figure 3.5b shows the same parameter but making use of the filtering. A separation between day and night was done through the sunlight parameter.
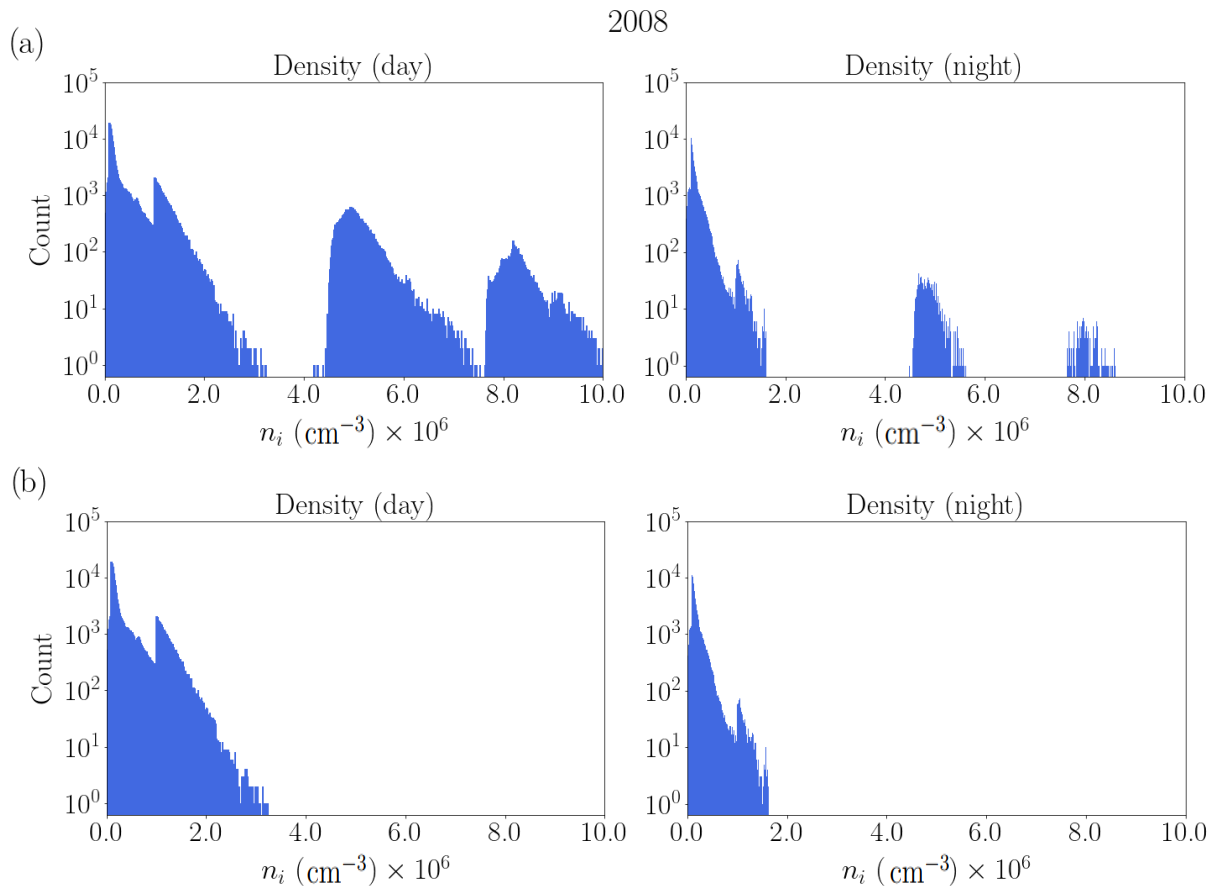
FIGURE 3.5 – 2008 statistical distribution of ion density obtained by the FPMU data. (a) Day (left) and night (right) distribution without filtering densities greater than 4×10^6 cm^{-3}. (b) Same as (a), but with the filtering, that is, data greater than 4×10^6 cm^{-3} were excluded.

As can be noticed, the density distributions in Figure 3.5a show three different "humps": one in low densities, one in high densities, and one in between. This is not expected for years of low solar activity. For comparison, Figure 3.6 shows the ion density distribution for 2014 (Figure 3.6a), one of the years of Solar Cycle 24 maximum, and 2018 (Figure 3.6b), one of the years of Solar Cycle 24 minimum. Figure 3.6a shows a long tail for 2014, spanning densities from low to high regions of the graphs, in accordance with what would be expected for years of significant solar activity. As for 2018, the densities are concentrated in the low density portion of the graphs in 3.6b. The pattern seen in 2018 is comparable with the one seen for 2008 in 3.5b, and that is why the filtering was executed: to be in line with what is expected for years of low solar activity. As previously mentioned, the same was done for 2009, since the behavior before filtering was similar to that seen in 3.5a.
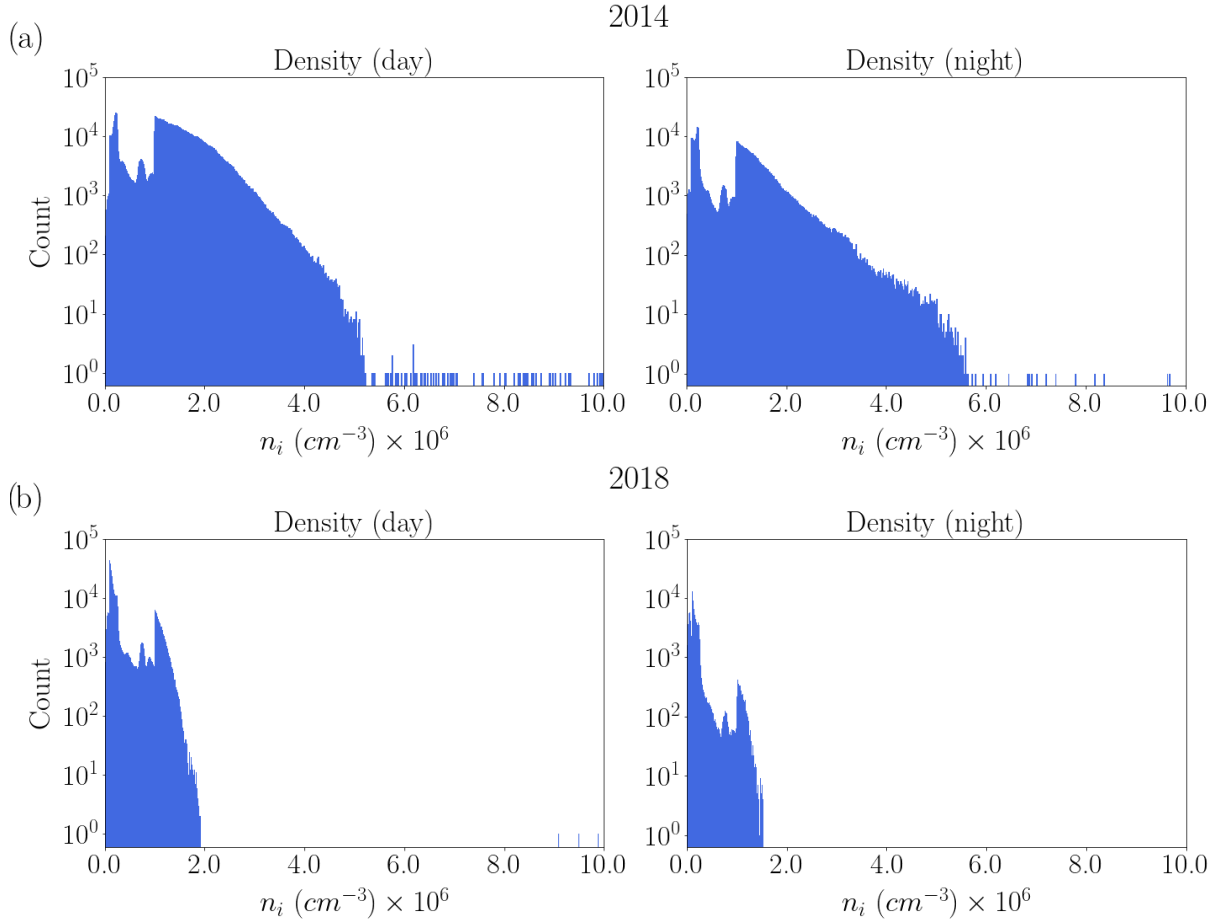
FIGURE 3.6 – Statistical distribution of ion density obtained by the FPMU data, separating day (graphs on the left) and night (graphs on the right), for (a) 2014 and (b) 2018.

3.5.1.1   Statistical distribution

The first of the three analyses was performed concatenating all the data. This analysis was the simpler one because all the ion density data was concatenated and the same was done for the electron temperature. In this way, these parameters were plotted aiming to demonstrate and, more importantly, to understand how they behave in a long-term basis. Specifically, histograms containing this information were generated to show the statistical distribution of the parameters for the daytime and nighttime.

3.5.1.2   Spatial dynamics analysis

The second and main type of analysis aims the visualization and understanding of the spatial distribution of the ion density. For that, maps showing the geographic coordinates of each FPMU data point were plotted. More specifically, we used FPMU plasma densities measured during magnetically quiet periods (Kp < 3) from December 2008 to December 2019. This period encompasses the Solar Cycle 24, which was mostly characterized by

low solar activity. Our data was divided into low ($\Phi < 100$ sfu) and moderate ($\Phi > 100$ sfu) solar flux levels, with mean values of 75 sfu and 130 sfu, respectively; and three seasons: December solstice (November-February), equinox (March, April, September, and October), and June solstice (May-August). We then divided our data into twelve different local time periods: 06:00-08:00 LT, 08:00-10:00 LT, 10:00-12:00 LT, 12:00-14:00 LT, 14:00-16:00 LT, 16:00-18:00 LT, 18:00-20:00 LT, 20:00-22:00 LT, 22:00-24:00 LT, 24:00-02:00 LT, 02:00-04:00 LT, and 04:00-06:00 LT. The steps used for the maps generation, shown in Figure 3.7, in which each map represents a four-month density variation and a two-hour local time period, are summarized as:

1. The plasma densities were first averaged in each bin of a $5° \times 5°$ grid covering latitudes up to $\pm 50°$ and longitudes from $-180°$ to $180°$;

2. After the gridding process, the FPMU data points of each trajectory contained within the four-months period were subjected to a conditional search: every point that fell in a specific area element of the grid was counted and stored as belonging to that area element. In other words, each point counted was stored in the area element closest to its coordinate. A division by $5°$ corresponds to a grid of 72×21 squares or area elements. Thus, the points that fall between the area element with corners in the coordinates $(180°, 3.2°)$, $(180°-5°, 3.2°)$, $(180°-5°, 3.2°+5°)$, and $(180°, 3.2°+5°)$, for instance, will be part of the area element with central coordinates of $(177.5°, 5.7°)$, as seen in Figure 3.7c;

3. The density value associated with that data point is stored. The mean of the respective parameter for each single trajectory is performed, and after that, the mean of the values related to all the trajectories that fall into that area element is also taken. More specifically, a single area element will have many trajectories crossing it, and hence the mean will be taken on each of these trajectories, i.e., each trajectory will have a mean value. Next, a second mean is performed with the values associated with every trajectory contained in each every element. In the end, there is only one density value for each area element.

After these steps, the maps were smoothed using a Savitzky-Golay filter (SAVITZKY; GOLAY, 1964) with a $9°$ longitude window length and a second-degree polynomial along each latitude.

Since we plot a few dip latitude, which is a latitudinal coordinate system defined in terms of the local (dipolar) magnetic field, and magnetic longitude lines in our maps, their generation will be briefly described. Data from the IGRF model was used to convert the coordinates from geographic to dip latitude. In more details, a Fortran code using the latest version of IGRF (IGRF-13) was downloaded at `https://www.ngdc.noaa.gov/`

(a)

(b)

(c)
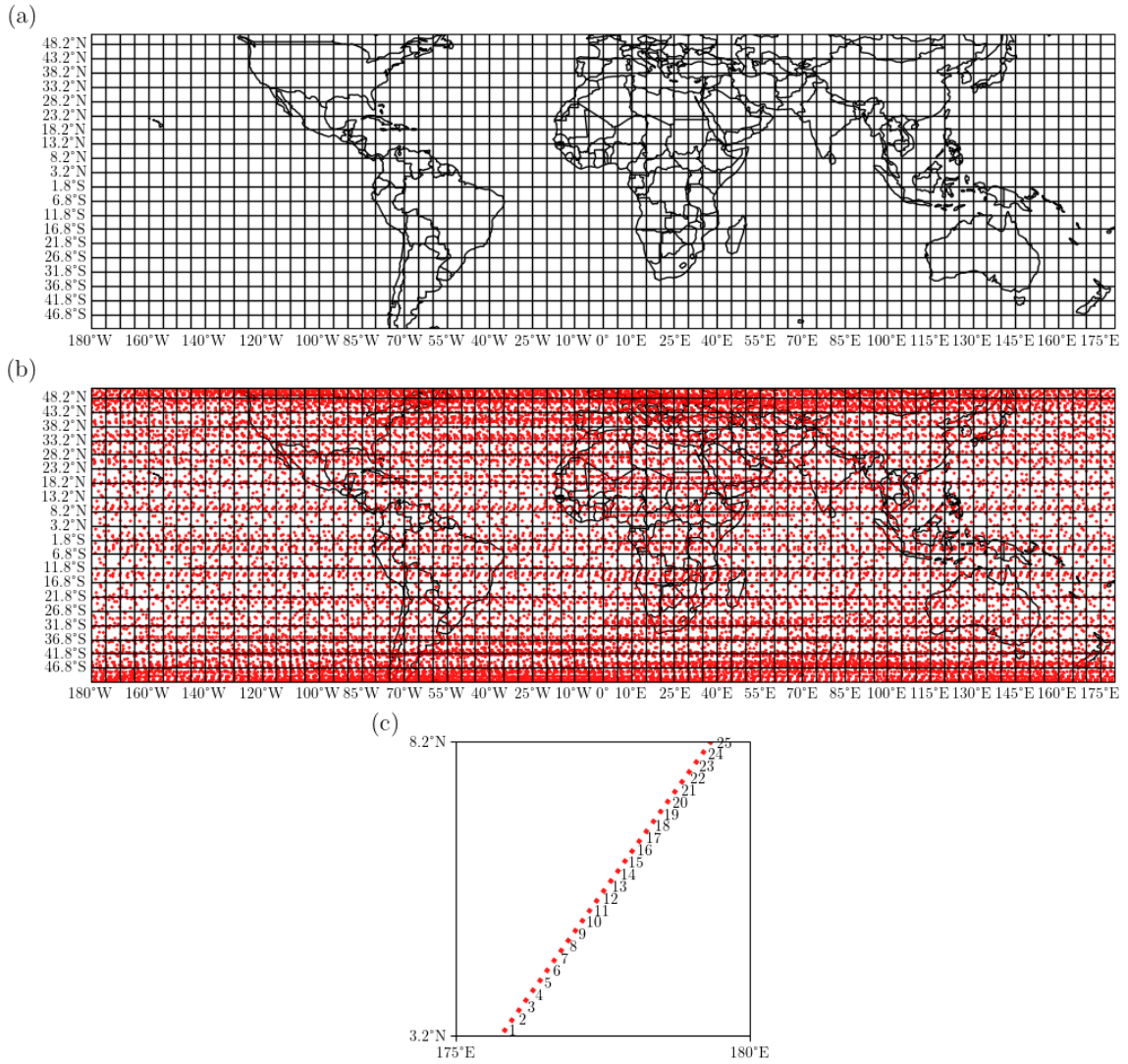
FIGURE 3.7 – Grid process illustration, where a 72×21 grid size is shown. (a) The map is divided into an equal-spaced number of elements, that is, the grid of the map is set. (b) The coordinate points of each trajectory are subjected to a conditional search to check in which element area they will fall into. The red dots are the trajectories data points for February 2019. (c) The density is stored and its mean value for each single trajectory is executed, and then the mean of the values associated with all the trajectories that fall into that area element is also executed. The red dots are points of a single trajectory, with its respective number associated with the direction of the FPMU pass.

`IAGA/vmod/igrf.html`. The input of this code are the initial and final values of latitude and longitude in degrees, as well as the increment, the year, and the altitude in km. The output is a text file containing, among others, the dip angle of each input coordinate. Finally, the dip angle was converted to dip latitude using the following equation:

$$\lambda_l = \arctan(\tan(\delta) \times 0.5) \tag{3.1}$$

Here, λ_l is the dip latitude and δ is the dip angle. The methodology just described was

also used to plot the dip equator line, since it is the line where $\delta = 0$. For the magnetic longitude, the lines were generated using a centered dipole magnetic coordinate system provided by the Spacepy Python library (NIEHOF *et al.*, 2022) (documentation available at `https://spacepy.github.io/`).

The spatial dynamics analysis also involved the density variation at specific local time periods along the -5°, -10°, and 25° magnetic longitudes. In this case, the density variation in each field line was smoothed using a non-parametric fitting technique with a locally weighted smoothing regression algorithm provided by the Python module Statsmodels (SEABOLD; PERKTOLD, 2010) (documentation available at `https://www.statsmodels.org/stable/index.html`).

3.5.1.3   Temporal temperature analysis

In this analysis, we gathered all the temperature data and separated it into specific dip latitude sections: from -40° to -20°, -20° to 0°, 0° to 20°, and from 20° to 40°. Three conditional searching were performed in the data, and the methodology steps are:

1. The coordinates were separated according to the dip latitude sectors;

2. All points that fell into a corresponding dip latitude sector were separated by local time. The points that had the same LT hour were stored. Hence, our local time bin is one hour. The electron temperature of these points was stored;

3. A conditional search was done to take the mean of the points that, once having the same LT, were also in the same trajectory, that is, points that also belonged to the same FPMU pass. This was done to smooth the data values.

It is important to mention that the data was converted to LT using the UT information returned by the FPMU. Finally, following the steps above, bar plots were generated: LT $\times T_e$ for the dip latitude sectors.

3.5.2   C/NOFS data

The analysis conducted with the ion velocity meter aboard the C/NOFS satellite was basically excluding data not pertinent to our study. First, we used all IVM data available, i.e., from 2009 to 2015. We only used quiet-time data, with Kp < 3. Also, we only used data in the American sector, separated into two longitudinal sectors, -90° to -60° and -60° to -30°. Additionally, we limited altitudes to be greater than 350 km and less than 550 km, excluded data with O^+ fraction < 0.8, and only kept densities (N_i) greater than

5×10^4 cm^{-3}. The limits for the O$^+$ and N_i concentration were chosen to ensure a sufficient signal to the drift meter for each data point. We also divided our data into two different solar flux levels: $\Phi < 120$ sfu and $\Phi > 120$, with mean values of 95 sfu and 150 sfu, respectively; and performed a two-month separation: January-February, March-April, May-June, July-August, September-October, and November-December. Each pair of months has a similar plasma density variation. Stoneback *et al.* (2011) explained the methodology for determining the IVM ambient ion drifts used here. They apply this same month separation justifying that a two-month period is ideal because all local times are sampled equally in this case as perigee precesses in local time.

The final steps consisted in only using data confined in the $\pm 7.5°$ dip latitude sector, averaging these every 30 seconds, and excluding data with standard deviation greater than 5 m/s. Finally, these velocities were averaged every 15 min. Fejer *et al.* (1995) demonstrated that the diurnal patterns of vertical drifts, when averaged seasonally and longitudinally, remain essentially unchanged for dip latitudes ranging up to $\pm 7.5°$. We have adopted this dip latitudinal range to maximize the number of available drift observations. The value of 5 m/s for the deviation from the average was chosen aiming to limit the influence of plasma irregularities on the averages. We also compared our results with two quiet-time empirical vertical drift models, the Scherliess and Fejer (1999) and the Fejer *et al.* (2008a) (see Section 2.3.4).

Additionally, we only use ion drift velocity data from 10:00 LT to 24:00 LT. In more details, Stoneback *et al.* (2011) employ a first-order correction in the drifts determination to address errors from asymmetric photoemission suppression in the IVM detectors. Since photoemission typically occurs between 05:00 LT and 10:00 LT, the drifts during this period display an additional degree of uncertainty. Stoneback *et al.* (2011) also reported erroneous IVM measurements between 08:00 LT and 09:00 LT due to particular solar incidence angles with respect to the spacecraft. Moreover, the measurements after midnight showed a great effect of irregularities. Therefore, for these reasons, we decided to restrict our velocity measurements from 10:00 LT to 24:00 LT.

To conclude this section, it is necessary to add a few words of caution regarding the methodology for determining the IVM ambient ion drifts. Accurate ambient ion drift measurements require the spacecraft's velocity to be precisely removed. This involves accurately specifying the spacecraft's inertial attitude and any offsets between the attitude determination system and the instrument measurement system. Therefore, these measurements require precise pointing accuracy. Stoneback *et al.* (2011) identify the offsets by ensuring the average meridional ion drift is zero and by evaluating the symmetry of ion drift components across the magnetic equator. Mean meridional drift calculations over all local times and longitudes help isolate and remove symmetric and antisymmetric offset terms. Corrected drifts are produced by subtracting the offsets

from measurements, allowing for evaluation of the corrected meridional ion drift as a function of local time, longitude, and season. However, this represents a rough estimate of the offsets, as ideally, a better criteria would be that the average longitudinal electric field should be zero. The satellite traverses various latitudes and longitudes where the electric field, and particularly its intensity, fluctuates. Fejer *et al.* (2008a) partially address this challenge in the development of the ROCSAT model.

3.5.3   IRI data

The IRI-2020 data was treated in the same way as the FPMU, aiming to compare what this ionosphere model predicts using the same conditions and methodology evaluated in the FPMU data. That means that the model was considered and treated as it was an experimental data. Additionally, every time FPMU plasma density presented a NaN (Not a Number) value, the value returned by IRI was also set to NaN. The same approach was taken for FPMU; that is, if IRI's plasma density output was NaN, the corresponding value for FPMU was also set to NaN during comparison. This was done to compare the two data in the most reliable and similar manner as possible. We only used IRI in the spatial dynamics analysis.

4 Results and Discussion

In this chapter, the results from the three main studies performed for this thesis will be presented in the following order: the ion density climatology using the FPMU probe (Section 4.3), the vertical drift velocity climatology using the IVM on board the C/NOFS satellite (Section 4.4), and the investigation of equatorial perturbation electric fields during five geomagnetic storms using Jicamarca data and empirical models (Section 4.5). These sections also encompass the discussion and conclusions of each major study.

Before we show the results on the FPMU ion density data, we first show the statistical distribution of the FPMU data followed by our brief results on the temperature morning overshoot.

4.1 Statistical distribution through the FPMU data

Figure 4.1 shows the concatenation of all the ion density and electron temperature information from 2008 to 2019. The data was separated between day and night according to the sunlight parameter of the probe. Vertical lines displaying the three main measures of central tendency are also shown: mean, median and mode. The methodology applied to generate this Figure is described in Section 3.5.1.1. In general, the temperature (Figure 4.1b) is more well-behaved than the density (Figure 4.1a). However, since the mean, median and mode have different values, the temperature distributions are not symmetric. The distribution for the daytime temperature can be classified as left skewed (or negative skewed), that is, mean < median < mode, where the left tail is longer than the right tail. As for the nighttime temperature distribution, the asymmetry is reversed: it is classified as right skewed (or positive skewed, mean > median > mode, in which the right tail is the longer one). Hence, as one can expect, high temperature values are more correlated to daytime hours, whereas during the nighttime the peak temperature shifts to lower values. Again, it is important to keep in mind that the FPMU temperature data is preliminary.

The density distributions are similar for both daytime and nighttime, as shown in Figure 4.1a. In reality, the nighttime density appears to have the same shape as for the daytime, but with a much smaller amount of data. These distributions seem to have more

Data from 2008 to 2019

(a)

Density (day)

Mean: $4.21 \times 10^5 \; cm^{-3}$
Median: $1.96 \times 10^5 \; cm^{-3}$
Mode: $1.02 \times 10^5 \; cm^{-3}$

Density (night)

Mean: $2.39 \times 10^5 \; cm^{-3}$
Median: $1.07 \times 10^5 \; cm^{-3}$
Mode: $1.01 \times 10^5 \; cm^{-3}$

$n_i \; (\mathbf{cm^{-3}})$

(b)

Temperature (day)

Mean: $1665 \; K$
Median: $2314 \; K$
Mode: $2384 \; K$

Temperature (night)

Mean: $1712 \; K$
Median: $1549 \; K$
Mode: $1413 \; K$

$T_e \; (\mathbf{K}) \times 10^2$
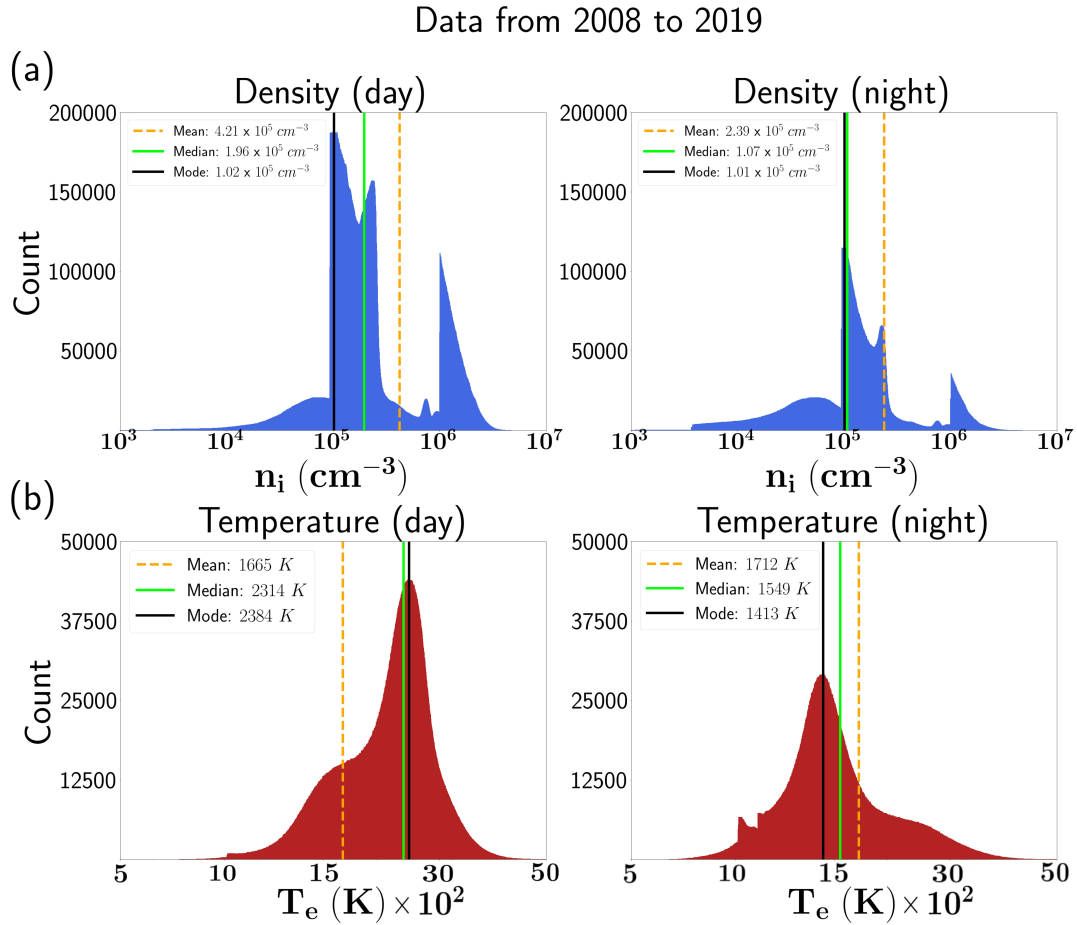
FIGURE 4.1 – Statistical distribution of ion density and electron temperature separating day and night of all FPMU data from 2008 to 2019. (a) Statistical distribution of the ion density for the daytime (left) and for the nighttime (right). (b) Same as (a) but for the electron temperature. Vertical lines representing the mean, median and mode are also shown.

than one type of distribution embedded in it, given the many peaks they present. For instance, the peaks greater than the mean in both panels in Figure 4.1a are interesting because they show how the density values go up and down in a very abrupt manner. Investigating in more detail these values for the daytime density distribution, Figure 4.2 is the corresponding year information for when $n_i > 4.21 \times 10^5 \; \text{cm}^{-3}$, along with the solar index information. It can be noticed that the high density values in Figure 4.1a can be associated mostly to the years of maximum activity of the Solar Cycle 24: 2013, 2014 and 2015. The years in which there is the greatest amount of high density data follow the same trend as the solar flux intensity. Therefore, years of solar cycle maximum are responsible for the greatest densities in the ionosphere at the altitude of this study ($\sim$400 km).

Figure 4.2 helped motivating us to separate our ion density data in two different solar flux levels to perform the climatological study, given the disparity between the solar cycle phases.
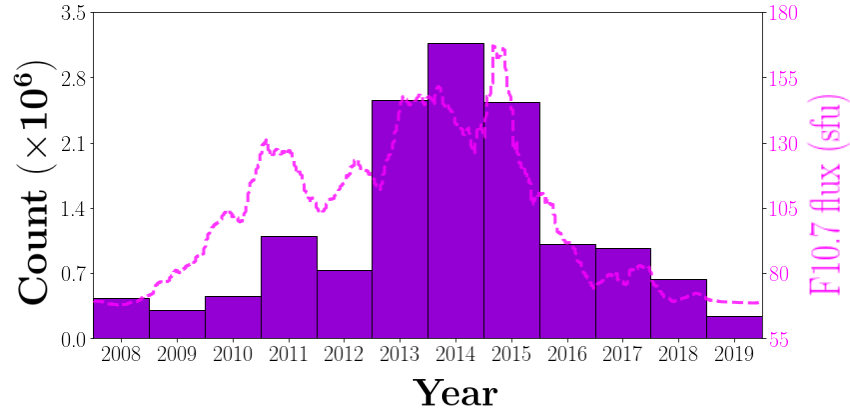
FIGURE 4.2 – Years with greater influence in the formation of the high density region $(n_i > 4.21 \times 10^5 \text{ cm}^{-3})$ seen in Figure 4.1a, together with the plot of the solar flux index F10.7.

4.2   The morning overshoot demonstrated by the FPMU

In order to evaluate the morning overshoot temperature effect, Figure 4.3 shows data from 2008 to 2019 separated in four different dip latitude sectors encompassing both the Northern and Southern hemispheres. The bar plots represent the mean values at each local time bin (one hour). The methodology used to generate this Figure can be found in Section 3.5.1.3.

According to Figure 4.3, the electron temperature has two different patterns, one for midlatitudes and one for low and equatorial latitudes. At midlatitudes, the temperature increases at around 05 LT, assumes a plateau-shape until ∼17 LT, and then decreases. On the other hand, at low and equatorial latitudes the temperature is lower than at the other dip latitude sectors and have its peak intensity during the morning, from 05 LT to 07 LT, and then decreases and again assumes a plateau-shape until around 17 LT, when it starts to decrease. The peak intensity seen in the morning hours can be associate with the morning overshoot phenomenon explained in Section 2.1.6. According to previous studies (e.g., OYAMA et al., 1996; YANG et al., 2020), this phenomenon is stronger at low latitudes, as is confirmed by the FPMU data.
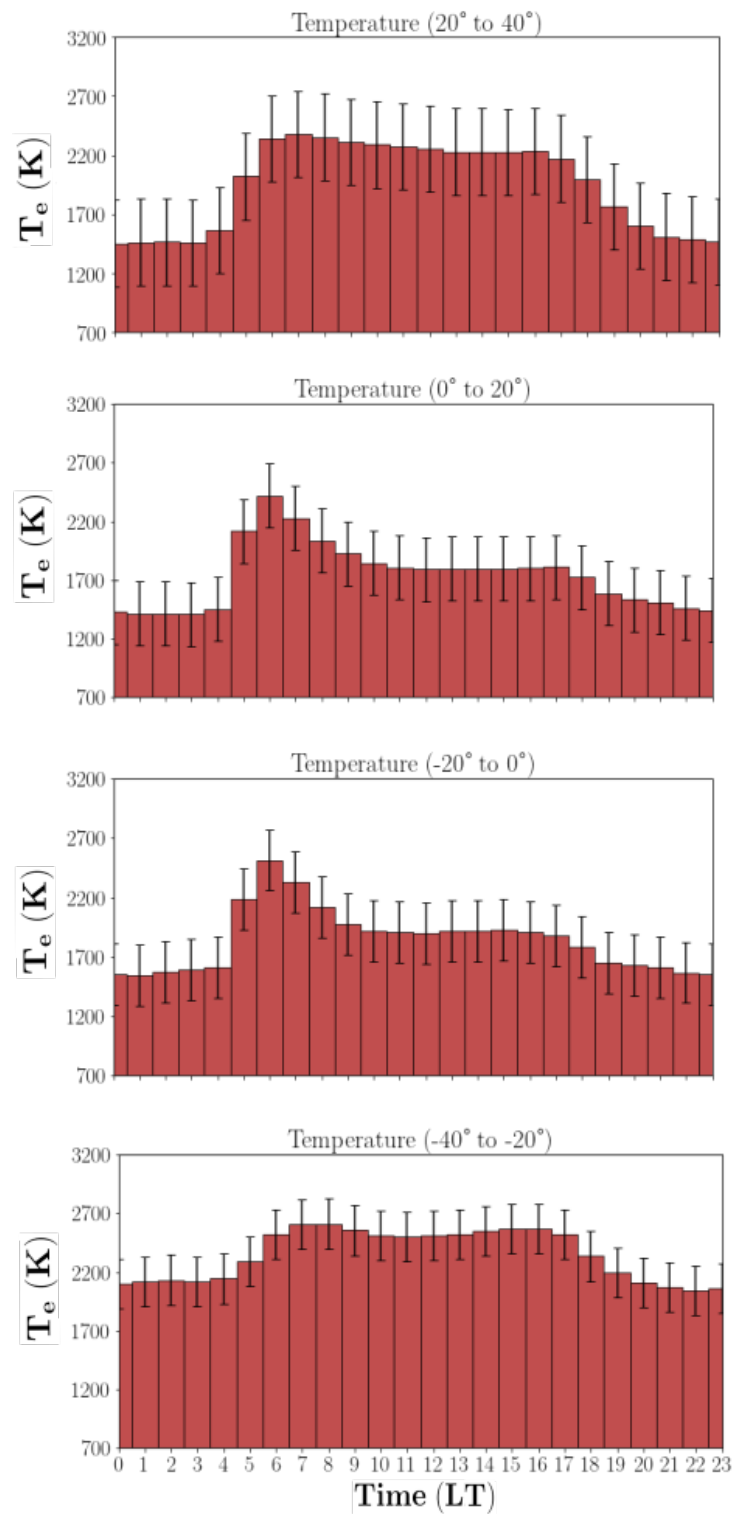
FIGURE 4.3 – Dip latitude and local time separation of the electron temperature gathering all the years from 2008 to 2019. Standard deviation bars of the FPMU data relative to each dip latitude sector are also plotted.

4.3   Ion density climatology based on FPMU measurements

In this section, FPMU measurements from 2008 to 2019 were used for the first comprehensive study of the seasonal and solar cycle-dependent quiet time mid- and low-latitude F region climatology and large-scale structures at $\sim$400 km. Focus will be given on the evolution of evening and nighttime low-latitude ionospheric structures during moderate solar activity and magnetically quiet conditions. The methodology used here is the one described in Section 3.5.1. Our study was published in December 2023 as an original research article in *Journal of Geophysical Research: Space Physics* (LARANJA *et al.*, 2023).

Ionospheric Density Climatology at the ISS height

Figures 4.4-4.6 present climatologies of afternoon and evening mid- and low-latitude plasma densities at about 400 km measured by FPMU from 2008 to 2019 during the December solstice, equinox, and June solstice, respectively. These Figures show the largest densities at 14:00-16:00 LT (panels c-d) and decreasing values toward the night. In general, the peak densities increase from about 10^6 cm^{-3} during low solar flux to about 2.5×10^6 cm^{-3} during moderate solar flux conditions, while the equatorial ionization anomaly crests remain at about the same geomagnetic latitudes until $\sim$14:00 LT. Later, the low solar flux anomaly significantly weakens with time and essentially disappears close to sunset, while under moderate solar flux conditions, the anomaly intensifies towards sunset with crests further poleward and increasing crest-to-trough density ratios. This is readily explained by the transport of plasma to higher equatorial altitudes and geomagnetic latitudes in response to the increase of late afternoon and evening upward plasma drifts with solar flux (FEJER, 1991; FEJER; JENSEN; SU, 2008a).

Our solstice data (Figures 4.4 and 4.6) show that the winter hemisphere crests tend to be closer to the dip equator than the summer hemisphere crests, as reported earlier (e.g., CAI *et al.*, 2020; KHADKA *et al.*, 2018; XIONG *et al.*, 2013). This was attributed to the upward and downward shifting of the EIA crests driven by meridional neutral winds. The neutral wind effect is also responsible for the greater densities seen in the summer hemisphere crests. In contrast to the result by Luan *et al.* (2015), our data show that this solstitial asymmetry is more evident for low solar flux conditions. On the other hand, the absence of a clear southern crest during the June solstice in both flux levels of Figure 4.6 indicates a weaker solar flux effect on the EIA response to the thermospheric wind. Additionally, Figure 4.4 indicates that the December solstice EIA crest latitude separation is smaller in the region of large magnetic declination, i.e., roughly from Eastern Asia to Western South America, consistent with the study of Eastes *et al.* (2023). This is especially true during the evening. Furthermore, the December solstice densities are greater than the

June solstice. This is the so-called annual asymmetry (see Section 2.1.3), consistent with previous studies (e.g., BURNS *et al.*, 2012; ZENG *et al.*, 2008).
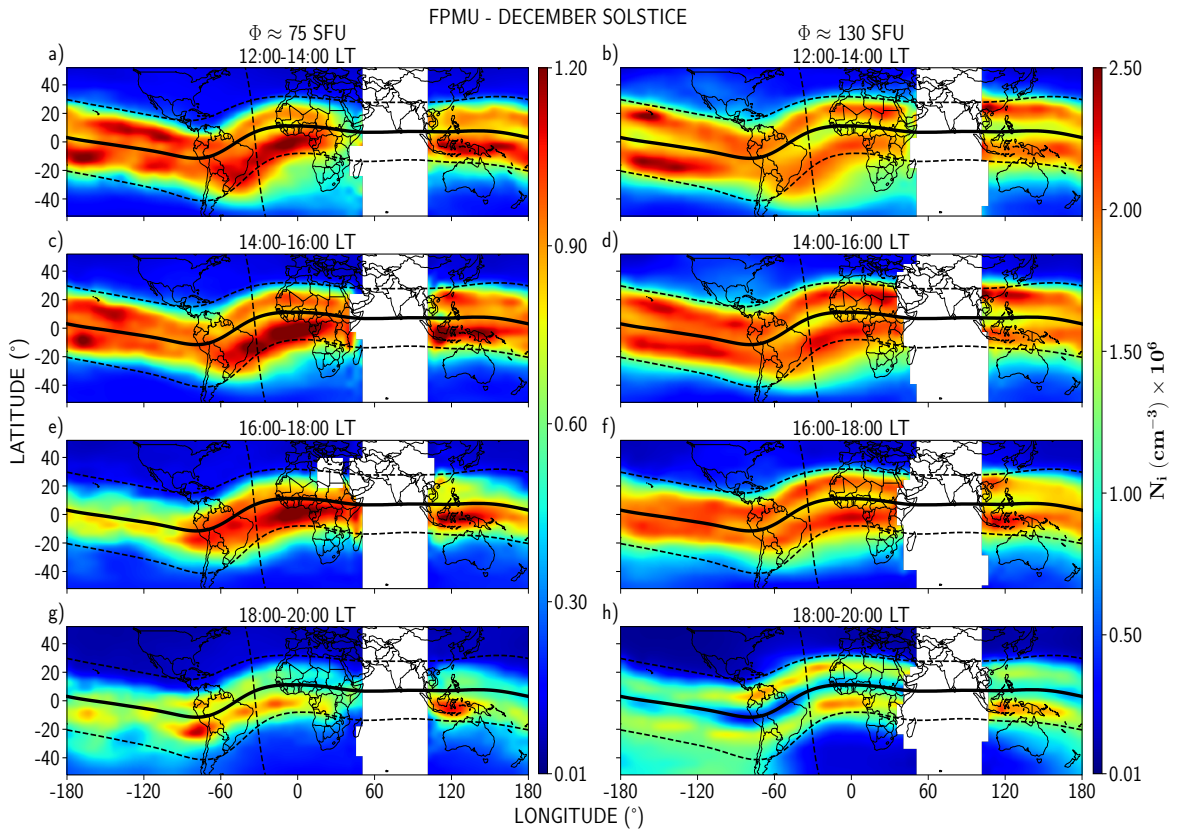
FIGURE 4.4 – Middle and low latitude average December solstice plasma densities measured by the FPMU for low (left panels) and moderate (right panels) levels of solar activity. The solid black line is the magnetic dip equator and the dashed black lines represent the dip latitudes of $\pm 20°$ and the $40°$ magnetic longitude (LARANJA *et al.*, 2023).

The equinox exhibits the most dramatic density changes with solar flux. The low flux panels in Figure 4.5 indicate that the northern EIA crest is, in general, stronger and at higher latitudes than the southern until 16:00 LT. During the evening, the separation between the two crests is not evident, but instead, the EIA appears as a single peak at the dip equator. The crests are possibly at a lower altitude given that the corresponding PRE amplitude is reduced in a low solar flux (BATISTA *et al.*, 2011). Additionally, there is an intrinsic 4-wave modulation in the evening EIA which we associate with the wavenumber-4 longitudinal structure. The longitudinal structure shown in Figures 4.5a, c, e, and g has density peaks in the Pacific, South American, African, and Eastern Asian sectors, in agreement with solar minimum ion density measurements presented by Choi *et al.* (2023). The vertical $\mathbf{E} \times \mathbf{B}$ drift, which is generally associated with the WN4, is the most effective driver of this structure in the daytime (BANKOV *et al.*, 2009; FEJER; JENSEN; SU, 2008a).

In contrast to the generally single density peak at the magnetic equator during equinoctial low flux conditions, the evening and early night EIA is symmetric around
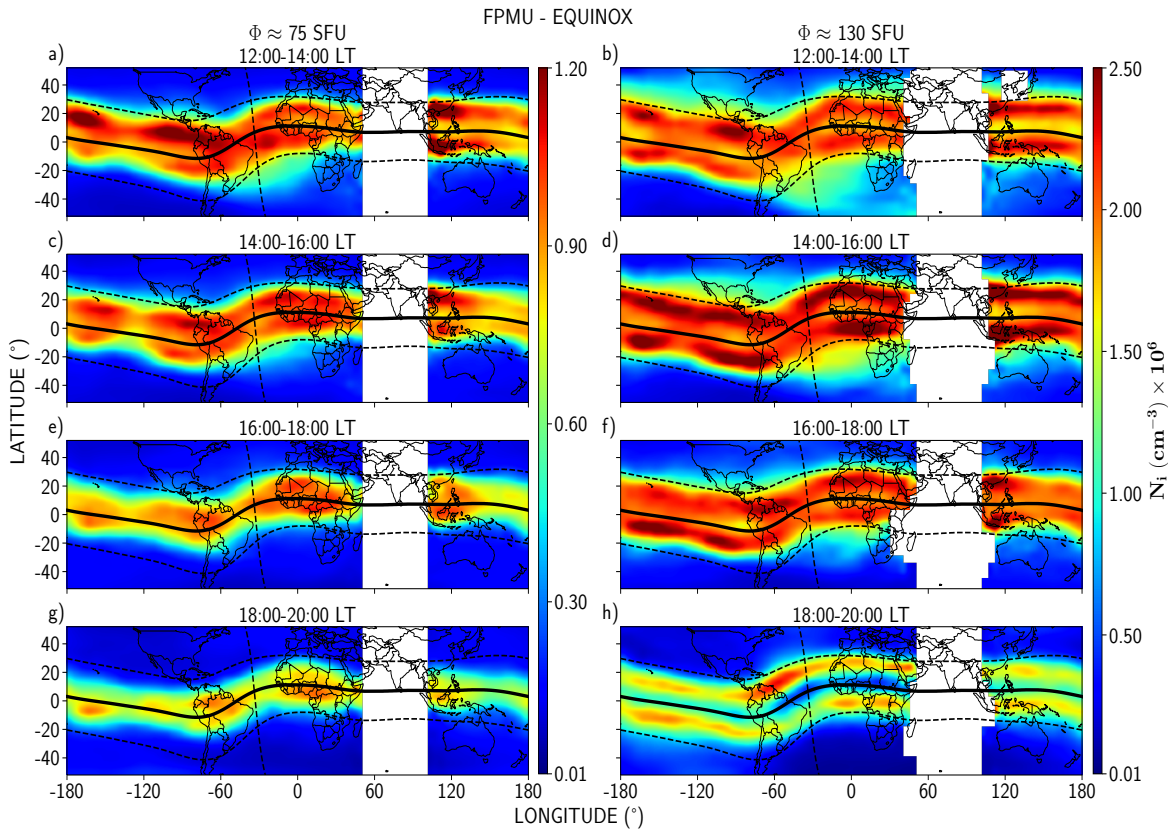
FIGURE 4.5 – Same as Figure 4.4, but for the equinox (LARANJA *et al.*, 2023).

the dip equator during equinoctial moderate flux conditions, as illustrated in Figures 4.5f and 4.5h. In the equinox, the meridional wind effect is minimal compared to that during solstices due to a weaker pressure gradient between the two hemispheres (CAI *et al.*, 2020; HUANG *et al.*, 2010). Balan *et al.* (2013) and Tulasi Ram *et al.* (2009) stated that zonal winds have a continuous and substantial influence throughout the equinox. Indeed, a wave-4 pattern exists in the evening ion density for the low flux, demonstrating the small effect of the meridional winds. Our data at the ISS height show the greatest densities during the equinox, illustrating the semi-annual density variation (see Section 2.1.3). Balan *et al.* (1997b) and Balan *et al.* (1998) attribute this variation to solar zenith angle, thermospheric composition, and equinox-neutral winds, influencing chemical and dynamical processes, as discussed in Section 2.1.3. As indicated above, the EIA displays symmetric crests' latitudes and densities only during the equinoxes, which is in accordance with the comprehensive study by Xiong *et al.* (2013).

The June solstice data also displays a wavelike density modulation. This can be seen in Figures 4.6a, c, and e where there is a 3-wave longitudinal modulation from 12:00 LT to 18:00 LT in the northern EIA crest. A similar wave-3 pattern in the northern summer was found by Huang *et al.* (2010) and Liu *et al.* (2010), who also observed it at 12:00 LT. Moreover, our low and moderate June solstice data show plasma depletions in the South American sector northern crest at 18:00-20:00 LT, which are more pronounced for low
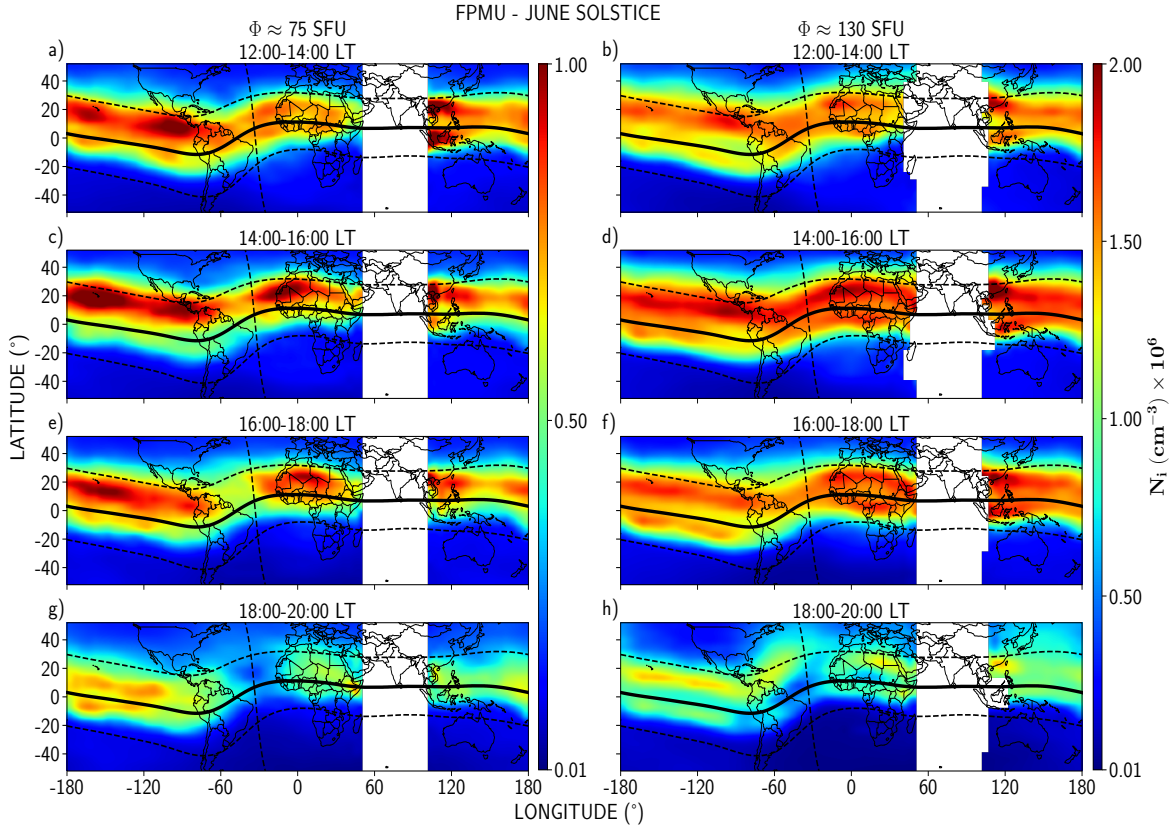
FIGURE 4.6 – Same as Figure 4.4, but for the June solstice (LARANJA *et al.*, 2023).

solar flux conditions. We associate these structures to a plasma depletion bay, although seen at later local times in previous studies (e.g., LIU *et al.*, 2022).

To summarize, the zonal electric field and the magnetic meridional neutral wind are the primary drivers that define the geometry and characteristics of the equatorial ionization anomaly. The EIA crests display strong asymmetries in all seasons, solar flux levels and local time periods shown here mainly due to these two effects. As described above, longitudinal and seasonal differences in the thermospheric neutral winds are well-recognized, being responsible for the equinox versus solstice and east versus west asymmetries in the EIA.

Comparison with IRI-2020

We compared the FPMU climatology shown in Figures 4.4-4.6 with corresponding results from IRI-2020 (BILITZA *et al.*, 2022). We observed generally a very good agreement between the IRI and the FPMU daytime plasma densities at about 400 km, although the model slightly overestimates the densities during low solar flux conditions and underestimates them for moderate conditions. The largest variations were observed for moderate solar flux near dusk at low latitudes. Therefore, we focus on results only during these conditions.
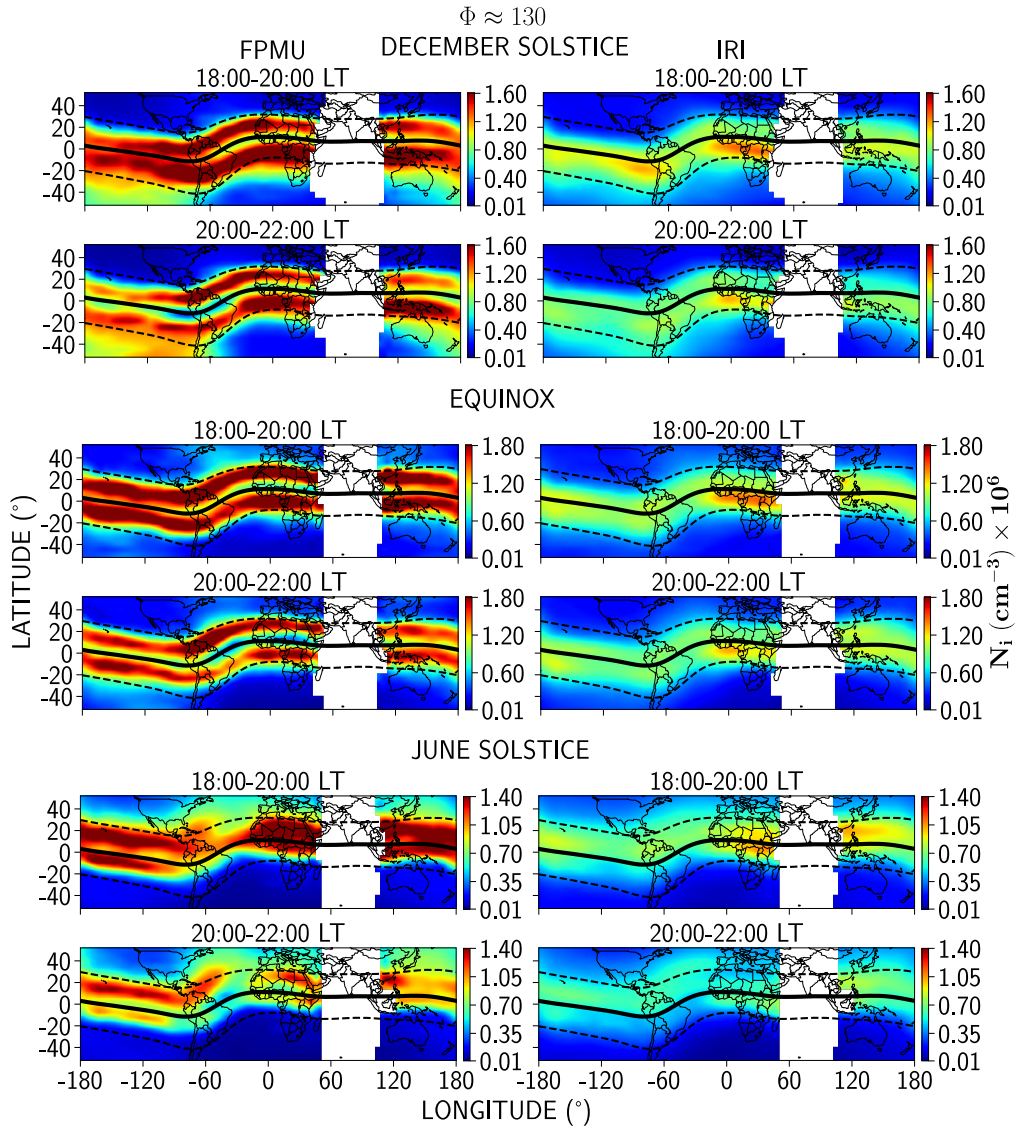
FIGURE 4.7 – FPMU (left panels) and IRI-2020 (right panels) moderate solar flux evening and early night plasma densities (LARANJA *et al.*, 2023).

Figure 4.7 illustrates that the IRI strongly underestimates the moderate solar flux evening and early night FPMU densities. In particular, the well-defined EIA crests are not seen in any season in the IRI data. The IRI densities are higher in the summer hemisphere, but they are much smaller than the corresponding FPMU values. The largest discrepancies are observed during the equinox where the symmetric crests shown in the data are not reproduced by the model. The main differences shown in Figure 4.7 can be attributed to the IRI's use of monthly averages and its mid-latitude main data sources (BILITZA *et al.*, 2022), leading to better performance there compared to low-latitudes and the smoothing of evening and early night PRE effects, which play a major role in the anomaly generation. We note that the PRE increases with solar flux and is generally strongest during equinox (e.g., SCHERLIESS; FEJER, 1999). We now proceed to examine this effect in more detail.

Evening results

Figure 4.8 shows the FPMU densities at 18:00-20:00 LT and 20:00-22:00 LT for $\Phi \approx 130$ sfu, along with the peak values of the evening vertical plasma drift velocity (PRE peak) and their time-integrated (integrated PRE) values. These parameters were retrieved from Stolle *et al.* (2008) and obtained from ROCSAT-1 measurements (FEJER; JENSEN; SU, 2008a). The integrated PRE values were obtained by summing the vertical drift values at each local time and multiplying them by the time difference between adjacent local time bins, therefore its unit is length. For the PRE peak, Stolle *et al.* (2008) used the highest drift value between 17:00 LT and 21:00 LT at each longitude for each season. The PRE is season- and longitude-dependent and is strongest when the sunset terminator and magnetic field lines are aligned (ABDU; BITTENCOURT; BATISTA, 1981). It peaks between about 18:30 LT and 19:30 LT and affects the F-region plasma densities in approximately half the typical daytime response time of 3-4 hours, as shown by extensive VTEC and airglow observations (KUMAR *et al.*, 2021).
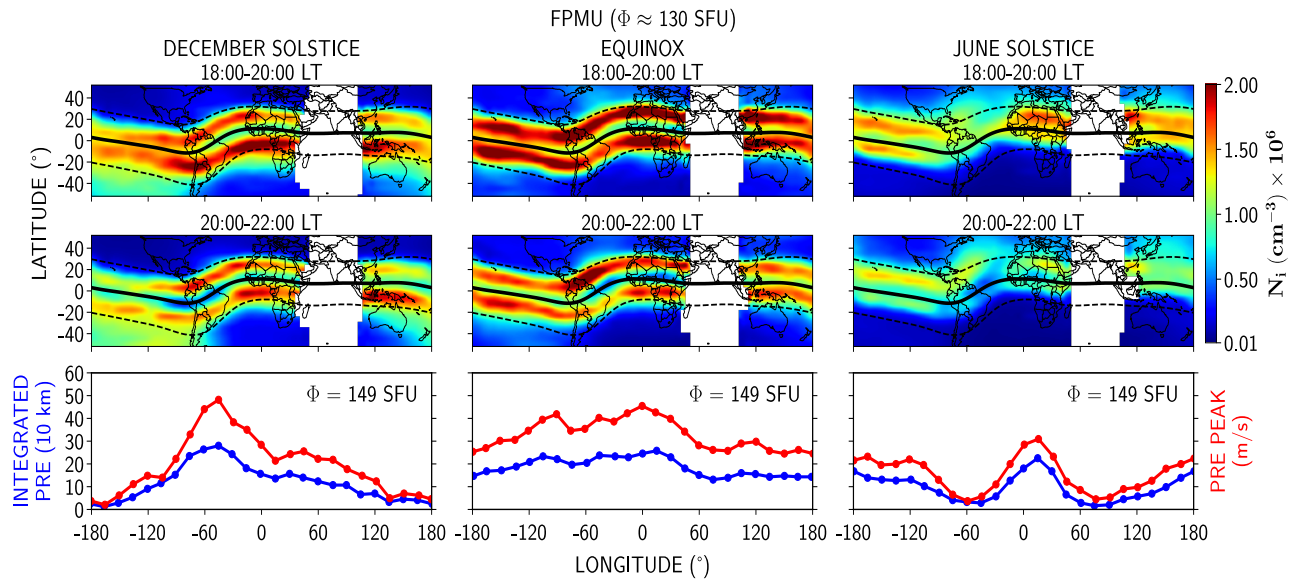
FIGURE 4.8 – Upper panels. FPMU evening average plasma densities. Lower panels. Peak PRE plasma drifts and their time-integrated values in units of 10 km (LARANJA *et al.*, 2023).

Figure 4.8 shows that during the December solstice, the PRE and its integrated value are maximum at approximately -45° longitude, coinciding with the location where the EIA crests density increase and have the greatest latitudinal separation. During the equinox, the PRE and its integrated value peak around -100° and 0° longitudes but have little longitudinal variation. In this case, the strongest plasma densities in the anomaly occur at about 10° further east, which is consistent with the evening eastward motion of the F-region plasma (e.g., FEJER; MAUTE, 2021). During the June solstice, the PRE peak and integrated PRE are both close to zero in the South American and South Atlantic

sectors, concordant with the absence of the EIA. These results are consistent with earlier studies indicating that the longitudinal distribution of the evening and nighttime anomaly is determined primarily by the PRE (e.g., LI *et al.*, 2008; WHALEN, 2004).

We have considered moderate solar flux conditions only; however, evening vertical drifts can strongly affect nighttime ambient low-latitude F region electron density also for solar minimum conditions (e.g., DAO *et al.*, 2011). As mentioned earlier, neutral winds also play important roles in the morphology of the anomaly. In addition, the north-south crest asymmetry is also affected by ambipolar diffusion from high and subauroral latitude ionosphere (LIU *et al.*, 2016), displacement of the geographic and geomagnetic equators (BALAN *et al.*, 2013; KHADKA *et al.*, 2018; ZENG *et al.*, 2008), and by the distance of the subsolar point to the magnetic equator (EASTES *et al.*, 2023).

Plasma Density Structure in the Atlantic and American Sectors

The FPMU climatologies presented above illustrate the occurrence of strong daytime and nighttime plasma density structures or so-called anomalies. We now proceed to examine them in detail focusing on the Atlantic and American sectors.

- **Midlatitude Summer Nighttime Anomalies**

Figures 4.9-4.11 show nighttime average FPMU plasma densities in the 95°W-15°E longitude sector. These Figures illustrate the midlatitude summer nighttime anomalies, which here encompass the Weddell Sea anomaly and the nighttime June solstice density enhancement, for low (left panels) and moderate (right panels) solar flux conditions. We will now present their season-dependent characteristics at the ISS altitude.

December solstice. The enhanced plasma densities in the far southward-displaced southern EIA crest at the 20:00 LT December solstice panels (Figures 4.9c-d) appear to give rise to the Weddell Sea anomaly by 22:00 LT (Figures 4.9e-f). In our flux levels and ISS height, this anomaly is centered at South Pacific and South American longitudes until 02:00 LT, when it moves eastward until the early morning. It is stronger and concentrated to the north for moderate solar flux. In a broader perspective, the WSA is merged with the EIA southern crest. Additionally, the shape and location of the plasma excursion from the EIA southern crest suggest a strong connection with the excursion of the magnetic dip equator into the southern hemisphere.

June solstice. In this season, Figure 4.11 shows density peak structures along the 20° dip latitude line in the North Atlantic sector. These are the above-mentioned nighttime June solstice density enhancement or North Atlantic MSNA. For $\Phi \approx 130$ sfu, this anomaly starts between 18:00 LT and 20:00 LT (Figure 4.11b) as a density bulge in the northern EIA crest, developing into a tongue-like shape at 20:00-22:00 LT. At 22:00-24:00 LT
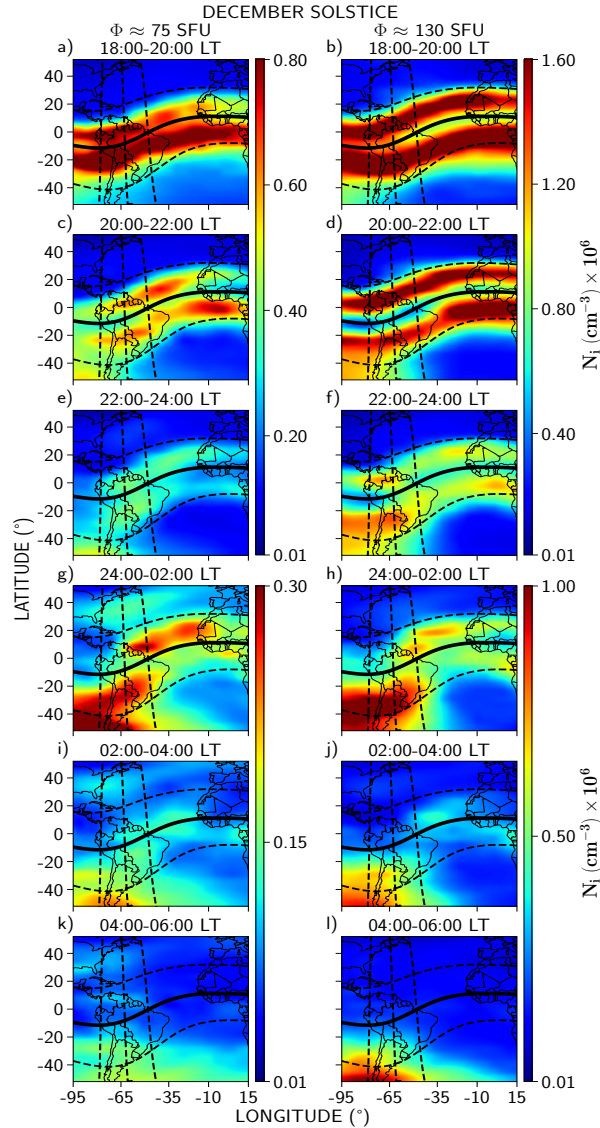
FIGURE 4.9 – FPMU-measured December solstice plasma density in the 95°W-15°E longitude sector in low (left panels) and moderate (right panels) solar flux conditions. The solid black line denotes the magnetic dip equator and the dashed gray lines correspond, from left to right, to the -5°, 10°, and 25° magnetic longitudes (LARANJA *et al.*, 2023).

(Figure 4.11f), the structure is now displaced to the east and to the north, following the tilt of the 20° dip latitude line. Although the density decreases over the nighttime hours, the structure still retains the highest plasma density in the middle and low-latitude ionosphere.

The June solstice low flux density anomaly shown in the left panels of Figure 4.11 starts at 20:00-22:00 LT, which is later compared to the moderate flux case. During most of the nighttime, it displays the same behavior as at the higher flux level, but with a lower area and density. At 02:00-04:00 LT (Figure 4.11i), the anomaly moves north of the 20° dip latitude line and maintains this pattern until the early morning. From 06:00 LT, the North Atlantic MSNA is no longer seen (not shown here).
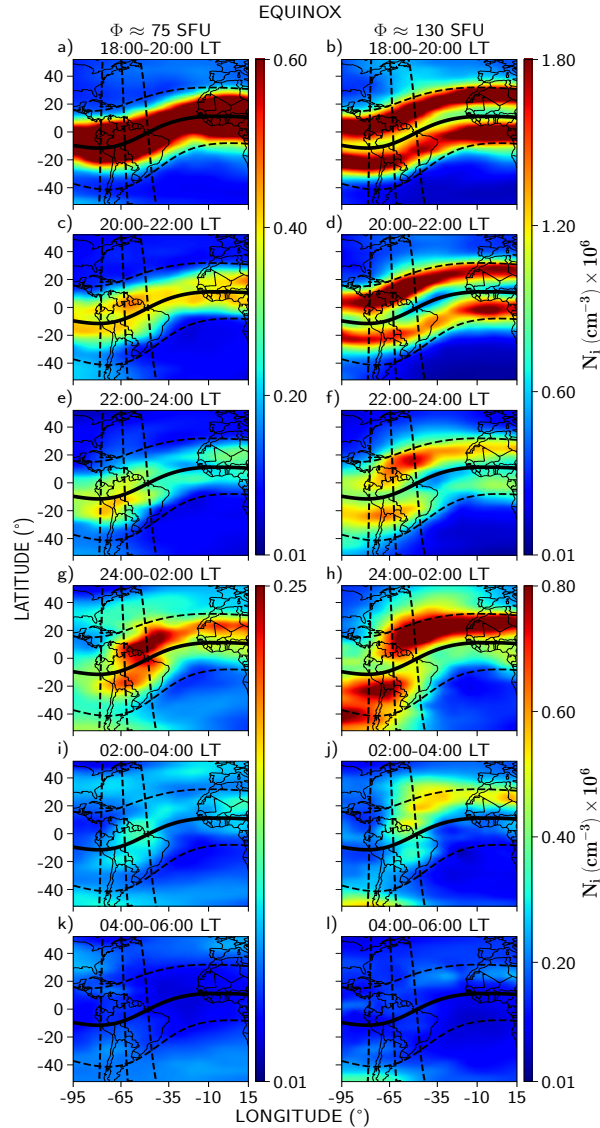
FIGURE 4.10 – Same as Figure 4.9, but for the equinox (LARANJA *et al.*, 2023).

We can also notice the evolution of the June solstice anomaly by following the three dashed gray lines in Figure 4.11, which correspond to the -5°, 10°, and 25° magnetic longitudes. The anomaly holds until ∼02:00 LT and then slowly decreases due to the weakening of the EIA during post-midnight hours, but it can be clearly observed until 06:00 LT. Albeit not clear in Figure 4.11, the anomaly is accompanied by a decrease in the plasma density at the conjugate location in the southern hemisphere. In contrast to the low solar flux case, in the right panels of Figure 4.11, the North Atlantic MSNA is observed at a nearly constant longitude range from the nighttime until the early morning and contains the greatest densities from low- to mid-latitudes.

Equinox. The equinoctial data (Figure 4.10) shows both the Weddell Sea anomaly and the North Atlantic June solstice density enhancements appearing at 24:00-02:00 LT (Figures 4.10g-h), though less prominently. This is particularly the case for the WSA, in
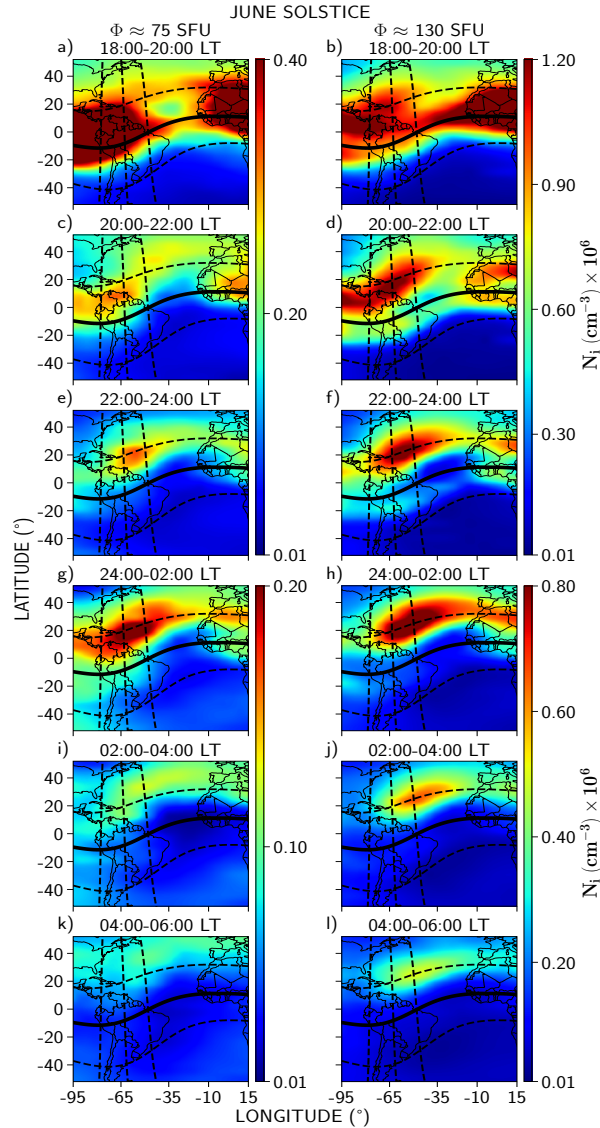
FIGURE 4.11 – Same as Figure 4.9, but for the June solstice (LARANJA *et al.*, 2023).

which only a weak anomaly is seen in the South Pacific. As is the case for the June solstice, from 20:00-22:00 LT to 02:00-04:00 LT the equinoctial northern hemisphere density enhancements are accompanied by density decreases in the conjugate hemisphere. Compared to the June solstice, the equinoctial North Atlantic MSNA is seen only until 02:00-04:00 LT, after which the anomaly is no longer clearly seen.

The MSNAs characteristics inferred from the FPMU data are consistent with those reported by Lin *et al.* (2010) and Liu *et al.* (2010), who suggested that these midlatitude structures are restricted to longitudes where the magnetic and geographic equators are apart from each other. Moreover, Figures 4.9 and 4.11 indicate that the December solstice WSA plasma density and its spatial coverage are greater than in the June solstice North Atlantic region, also in agreement with Liu *et al.* (2010). In our data, the WSA encompasses a very large longitude and latitude area, from the

Australian to South Atlantic sectors (the total WSA area is not shown in Figure 4.9), whereas the North Atlantic structure in June solstice is seen restricted from Eastern Central America to Western Europe. This can be explained by the large declination angle near the South American anomaly, which produces a zonal wind more effective in the South Pacific than in the North Atlantic.

In contrast to previous results (e.g., CHEN *et al.*, 2012), the FPMU data show that the MSNAs during December and June solstice have similar local time occurrences. Additionally, our data show that both the WSA and the June density anomaly are stronger and have a longer lifetime during moderate solar flux conditions, which differs from the negative solar activity dependence suggested by Chen *et al.* (2012) and Liu *et al.* (2010). These different results might be explained by our in-situ ion densities at 400 km, near h_mF_2 at night, where the MSNAs are expected to be more prominent (LIU; THAMPI; YAMAMOTO, 2010). Many earlier studies used plasma densities from TEC and N_mF_2 measurements, which often do not correspond to the height of our in-situ plasma density data.

- **Plasma Depletion Bays**

There is another feature clearly seen at the nighttime June solstice. Plasma depletion bays are observed almost at all local times shown in Figure 4.11. The PDBs appear as regions of depleted plasma density "curving in" to the northern hemisphere from the southern over North Atlantic longitudes. This feature is one of the South PDBs described by Chang *et al.* (2020). In the left panels of Figure 4.11, this depletion is seen from 18:00-20:00 LT, but only from 20:00-22:00 LT in the right panels, suggesting its earlier predominance during a low solar flux level. Our data shows that this feature appears at night during solstice months, consistent with previous studies (e.g., CHANG *et al.*, 2020). Liu *et al.* (2023) state that the number of PDBs can be affected by the observation altitude. Hence, at the ISS height, we only observe one PDB.

The equinox (Figure 4.10) shows a density depletion forming at 24:00-02:00 LT, seen until the early morning for both flux ranges. This depletion is located between South America and Africa, but it is not clear if it is associated with a plasma depletion bay, although there are similarities with this same phenomenon during the June solstice.

Relevant Atlantic and American Sectors Nighttime and Daytime Structures

The phenomena described in the previous sections highlighted the peculiarity of the Atlantic and American sectors. We proceed to examine some of their phenomena in more detail to investigate their evolution.

- **Nighttime**

Figure 4.12 shows the density variation at 20:00-22:00 LT along the -5°, 10°, and 25° magnetic longitudes drawn in Figures 4.9-4.11. A clear longitudinal variation can be observed in the three seasons. During the December solstice, the strongest increase in the crest-to-trough density ratio with solar flux occurs along the 10° magnetic longitude line. The densities along the other two longitudes display well-defined crests for both fluxes. Additionally, the -5° and 10° lines show a density asymmetry with larger values in the northern crest. Comparing this result with those in Figures 4.8 and 4.9, we suggest that the asymmetry is a consequence of the EIA longitudinal variations.

The Weddell Sea anomaly significantly influences the December solstice densities in Figures 4.12a and 4.12b, as well as the equinoctial densities in Figure 4.12a, particularly at southern dip latitudes, with higher values toward the west. Hence, Figure 4.12 shows that the Weddell Sea anomaly is observed at 20:00-22:00 LT during the equinox for low, but not for moderate flux. The 10° magnetic longitude line displays an opposing behavior compared to the other two in Figure 4.12a during the equinox since it is the only one with a northern EIA crest greater than the southern. In Figure 4.12b, the three lines show well-developed and asymmetric EIA crests, with the northern having higher densities than the southern.
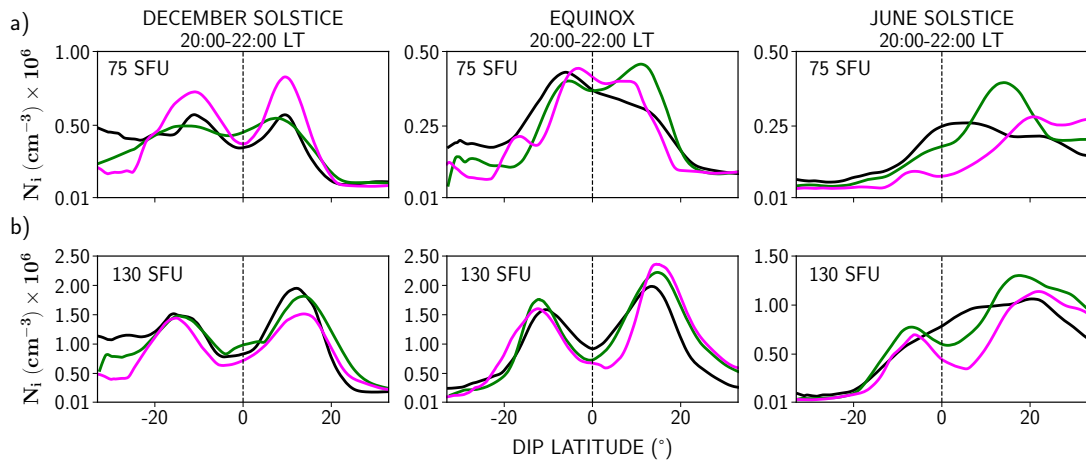
FIGURE 4.12 – FPMU densities at 20:00-22:00 LT along the -5° (black), 10° (green), and 25° (pink) magnetic longitude lines for our a) low and b) moderate solar flux conditions (LARANJA *et al.*, 2023).

During the June solstice, Figure 4.12a shows only a single density peak at the -5° line, but strong asymmetries at 25° and 10° longitudes, with a much larger northern than southern crest. In fact, there is no southern crest at all at 10° longitude. In Figure 4.12b, the asymmetry for these two lines holds, but now the -5° also displays the same asymmetry between the southern and northern EIA crest. These equinox and June solstice asymmetries for both fluxes correspond to the northern hemisphere MSNA shown in

Figures 4.10-4.11. As above-mentioned, the 10° magnetic longitude, which essentially crosses all of South America, is the one with the largest density variation with solar flux among all three seasons. Furthermore, it is evident from Figure 4.12 that the South American sector displays marked longitudinal plasma density variations.

- **Daytime**

There is a pronounced feature in the daytime December solstice and equinox for both solar fluxes shown in Figures 4.4-4.5. A density bulge can be seen in the southern EIA crest in the -60° to 0° longitude sector from 12:00 LT to 16:00 LT. This bulge is identified as an increase in the latitudinal width or range of the South Atlantic EIA crest from 08:00 LT to 16:00 LT. Except for the work by Liu *et al.* (2010), which shows a similar bulge at 12:00 LT during the December solstice but does not mention it in the text, this is the first time this EIA bulge is examined in some detail along with a suggestion of its possible origin.

Figure 4.13 shows the local time evolution of the plasma density in the bulge region and along the 40° magnetic longitude lines (also drawn in Figures 4.4-4.5) during low and moderate solar flux levels for the December solstice and equinox and in three different local times prior to the ones presented in Figures 4.4-4.5: 06:00-08:00 LT, 08:00-10:00 LT and 10:00-12:00 LT. The 40° magnetic longitude line crosses the bulge region. The density variation in each field line was smoothed using a non-parametric fitting technique with a locally weighted smoothing regression algorithm. The 40° magnetic longitude lines were drawn in the June solstice maps in Figure 4.6 only for comparison since no bulge can be observed during this season.

December solstice displays the most distinctive bulge for both solar flux levels when compared to the equinoctial. This feature is more prominent in the moderate flux (Figures 4.13b, f, j) than in the low data (Figures 4.13a, e, i). At 06:00-08:00 LT, the Weddell Sea anomaly is still evident for all the maps at this local time period, except for the equinox during the low solar flux period. Most of the earlier studies cited previously observed the WSA until ~04:00 LT. At 08:00-10:00 LT in Figure 4.13f, the WSA has moved north to lower latitudes. At 10:00-12:00 LT the December solstice enhancement moved northward (Figure 4.13j), merging with the EIA southern crest to form the bulge seen in Figure 4.4. The same process occurs during the equinox, but the bulge is less prominent. For $\Phi \approx 75$ sfu, the northern displacement of the WSA is less pronounced during both the December solstice and equinox, but a faint bulge can still be noticed in the EIA southern crest.

From the line plots perspective (Figures 4.13m-p), there is a density peak at approximately -38° dip latitude for both fluxes during the December solstice and only for $\Phi \approx 130$ sfu during the equinox. This peak becomes more intense and moves northward
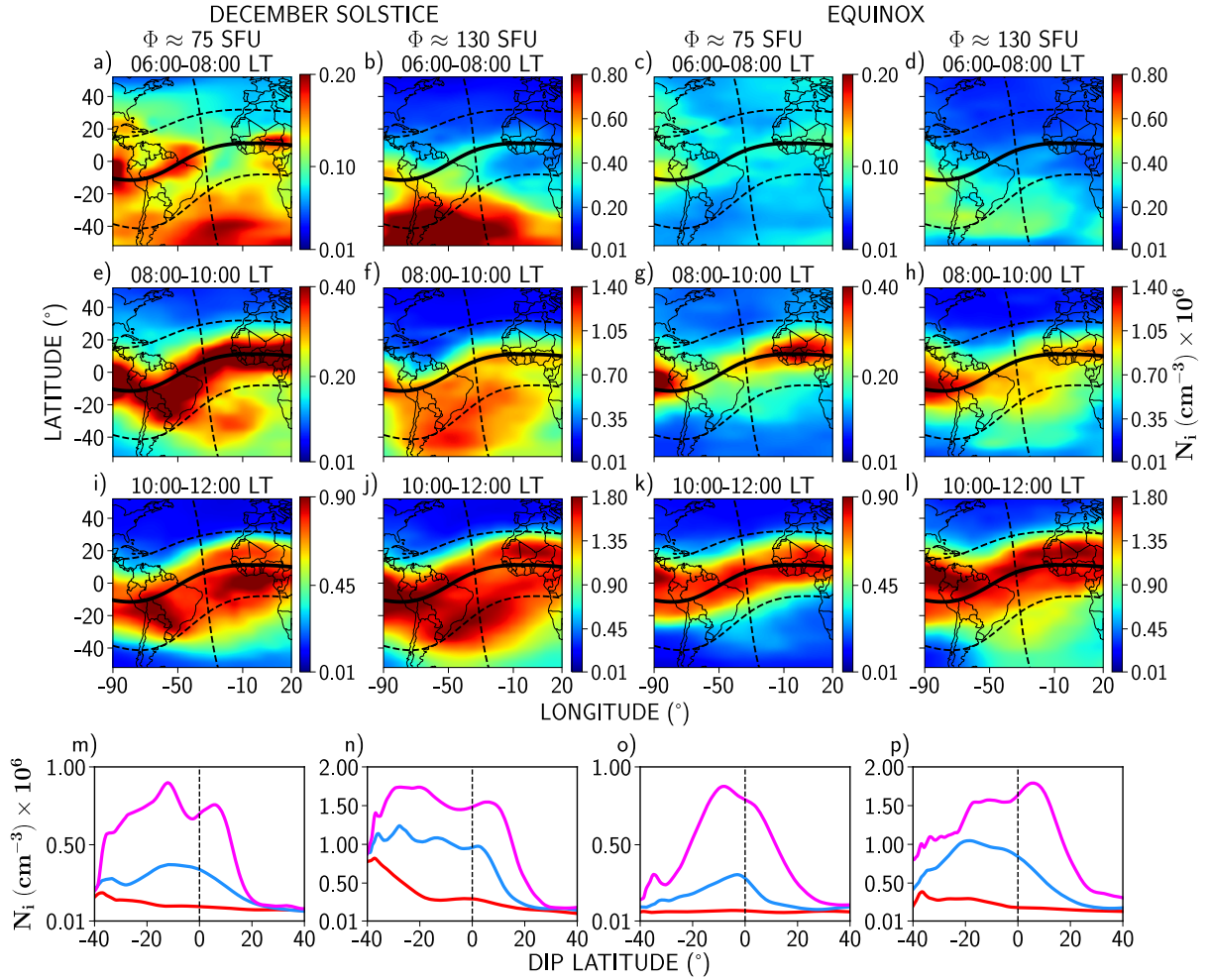
FIGURE 4.13 – Local time evolution of the plasma density bulge region during December solstice (first and second columns) and equinox (third and fourth columns). The line plots in m-p show the plasma density variation along the 40° magnetic longitude line at 06:00-08:00 LT (red), 08:00-10:00 LT (blue), and 10:00-12:00 LT (pink) corresponding to columns in panels a-l (LARANJA *et al.*, 2023).

until it merges with the EIA southern crest, adding a bulge to it. From 08:00 LT to 12:00 LT, the asymmetry between the southern and northern crests is evident for both fluxes and seasons. We speculate that the bulge is associated with the WSA. The effect of the WSA is still observed during the early morning in our data and is responsible for the density peak at 06:00-08:00 LT in Figures 4.13m-n, p. Also, the bulge appears to be related to the WSA since it occurs in the region of greater separation between the geographic and magnetic equators, where the mid-latitude nighttime enhancements are preferred to take place. Therefore, an equatorward meridional wind may oversee the WSA shift northwards. However, more detailed observations and numerical modeling are clearly necessary to determine the origin of this unusual plasma density feature.

Summary and Conclusions on the FPMU ion density climatology

We presented the first climatological study of mid- and low-latitude plasma densities derived from 12 years of FPMU measurements onboard the ISS during low and moderate solar flux conditions. Our daytime climatological results on the development, seasonal, and solar flux dependence of the EIA and location of their crests are consistent with earlier experimental results and can be largely explained as due to corresponding variations in the zonal electric fields and thermospheric neutral winds. Our middle and low-latitude daytime data also generally agree well with corresponding IRI ion densities. The FPMU evening and early night densities highlight the fundamental role of the PRE on the longitudinal variation of the crest-to-trough EIA anomaly crest ratios and of the meridional thermospheric winds on their hemispheric asymmetries. During this period the IRI density signatures strongly underestimate the moderate flux in-situ data for all three seasons.

We have shown a structuring in the daytime EIA southern crest during the December solstice and equinox that, to the best of the authors knowledge, was not noticed in previous studies. In the South Atlantic sector, this EIA latitudinal density bulge was stronger during moderate solar flux conditions. We suggest that this bulge is formed by the transport of plasma from the Weddell Sea anomaly. We showed that the ion density in the American and Atlantic sectors displays strong seasonal and longitudinal variations during the evening and the nighttime. This is particularly the case in the South American region. We also examined two midlatitude summer nighttime anomalies, the Weddell Sea anomaly in the South Pacific during the December solstice and the North Atlantic density enhancement during the June solstice. Our results indicate similarities between these anomalies. Both are stronger during a higher solar flux period and have all-night lifetimes at the ISS height, which is not consistent with earlier results, perhaps due to altitudinal effects. Additionally, since we have shown for the first time the WSA in the early morning, we discussed whether this supports its correlation with the density bulge in the EIA.

4.4 Vertical drift velocity climatology according to C/NOFS data

The ion drift velocity plays a crucial role over the spatial distribution of ionization and the dynamics of ionospheric irregularities in the equatorial ionosphere. In this section, we will briefly outline the quiet-time behavior of the equatorial upward plasma drifts using IVM measurements on board the C/NOFS satellite. The goal is to explore whether the IVM data, which remains largely unexamined in full, could be utilized for the first time in

a climatological study of the low-latitude American sector vertical drift velocity. Finally, despite the caveats and limitations identified at the conclusion of this section, this analysis will be valuable for future examination and discussion of drift data under geomagnetically disturbed conditions, as will be shown in the next section.

Results

Figures 4.14-4.19 show the seasonal and solar cycle quiet-time (Kp < 3) variation of the $\mathbf{E} \times \mathbf{B}$ vertical plasma drift velocity measured by the IVM on board the C/NOFS satellite from 2009 to 2015 in two different longitude sectors as a function of local time. The S-F and ROCSAT model outputs are also plotted. The black lines are for the 60°W-90°W longitude sector, whereas the red ones represent the 30°W-60°W longitude sector. The methodology applied to calculated these means is described in Section 3.5.2. We plot the velocities from 10 LT to 24 LT, setting aside measurements after midnight and early morning because these contained substantial effects of irregularities and measurement errors, as described in Section 3.5.2. According to the IVM ambient drifts determination methodology given by Stoneback *et al.* (2011), the relative measurements of C/NOFS are much more precise than the absolute ones, so that we compare the results of the longitudinal (east-west) variation with the hypothesis that the errors are of the same order, which is not necessarily true.

First, it is important to clarify that at equatorial latitudes the F region vertical plasma drifts are upward during the day and downward at night (e.g., SCHERLIESS; FEJER, 1999), as was shown in Figure 2.3 (Chapter 2). The variation of the ion drift velocity for January and February shown in Figure 4.14 displays in general the typical pattern as a function of the local time except for the downward drifts during the afternoon. Additionally, we observe the typical PRE pattern as a function of the solar flux level. The PRE increases from a lower solar flux (95 sfu, upper panel) to a higher (150 sfu, lower panel), in accordance with the expected trend of a greater PRE for a higher solar flux period. In general, the PRE measured by the IVM throughout all the seasons shown here increases from ∼20 m/s during a low solar flux level to ∼40 m/s during a high.

During the day, Figure 4.14 shows that the effect of the solar flux is more evident at the 60°W-90°W longitude sector for January/February, since the velocities are more negative at the afternoon and have more fluctuations during a higher solar flux level. Moreover, the longitudinal asymmetries, in this case, are more significant for the higher solar flux level, in particular during the night. For both solar flux levels shown in Figure 4.14, the PRE occurs about 30 minutes later at the 60°W-90°W longitudinal sector. As for the models, although ROCSAT is more suitable for solar flux levels greater than 130 sfu (FEJER; JENSEN; SU, 2008a), it is consistent with the measured drifts, except during the daytime, when it overestimates the velocity variations. The S-F model is very similar
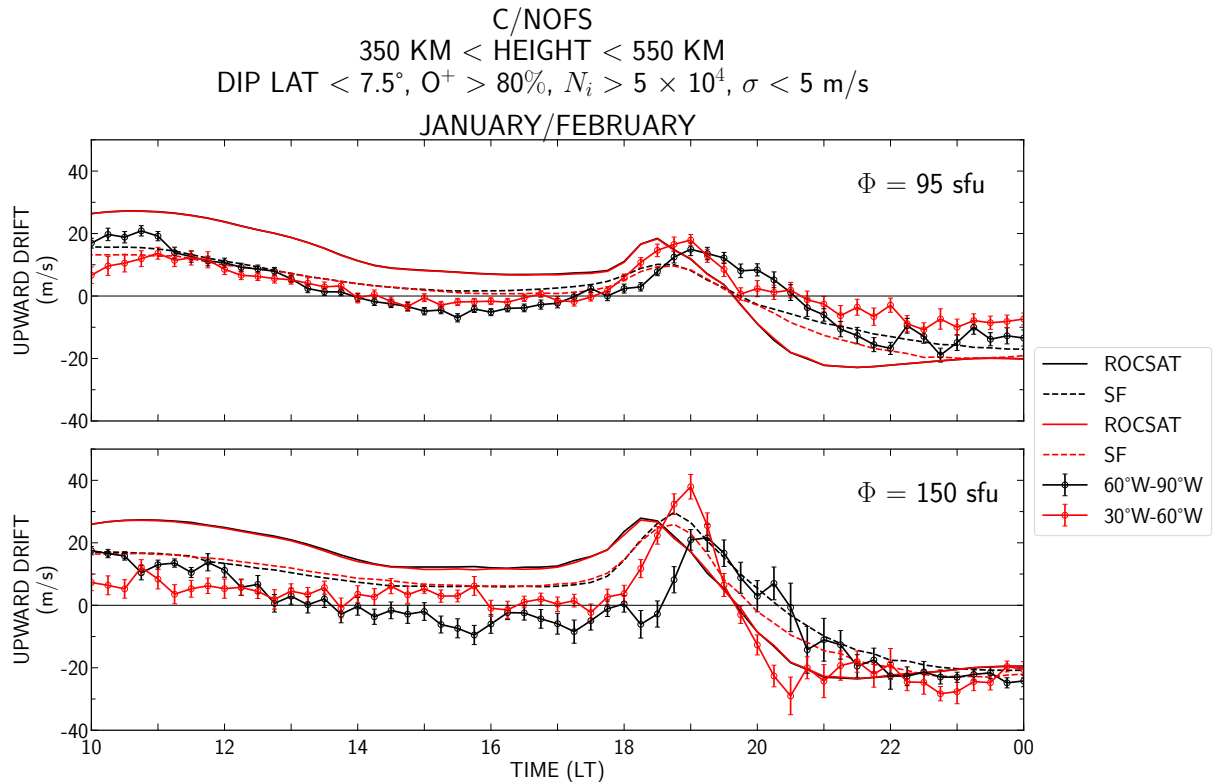
FIGURE 4.14 – C/NOFS and empirical vertical drift models January and February means from 2009 to 2015 for 95 sfu (upper panel) and 150 sfu (lower panel) in the 60°W-90°W (black lines) and 30°W-60°W (red lines) longitude sectors. σ, in this case, represents the standard deviation. The standard deviation is also plotted for each data point.

to the drifts, particularly for the lower solar flux level. Finally, it is important to mention that these models do not show great differences between the two longitudinal sectors due to the binning process used in their derivation. The ROCSAT uses 15° overlapping 30° wide longitudinal bins and the S-F was derived using 30° overlapping longitudinal bins spaced by 10°.

The irregularities (spread F) effect seems to be more predominant in a lower solar flux level and at the 30°W-60°W longitude sector, as we speculate by the deviation from the quiet-time pattern given by the models after 20 LT in the upper panel of Figure 4.14. In contrast, Figure 4.15 shows that plasma irregularities affected the March and April vertical drifts after 20 LT for both solar flux levels. The effect of irregularities is stronger during March and April than during January and February, as we can note by upward drift velocities after 20 LT in Figure 4.15. Also in opposition to Figure 4.14, Figure 4.15 displays a later PRE in the 30°W-60°W longitude sector. As for the model velocities, for a lower solar flux level (upper panel of Figure 4.15), the IVM velocities are closer to the S-F model during the day, whereas only the 60°W-90°W longitude sector follow the ROCSAT after the PRE (up to 22 LT), where the 30°W-60°W longitude sector exhibits fluctuations and does not follow the models. The higher solar flux velocities

(lower panel of Figure 4.15) are closer to the S-F model only during the night, after the PRE, when these are closer to the ROCSAT output. The downward velocities observed during the day, especially for the higher solar flux level, make them very different from the expected models outputs. Additionally, the strong fluctuations seen in the velocities of the 30°W-60°W longitude sector from 20 LT to 22 LT, probably associated with spread F, distinguish them markedly from the quiet-time pattern.
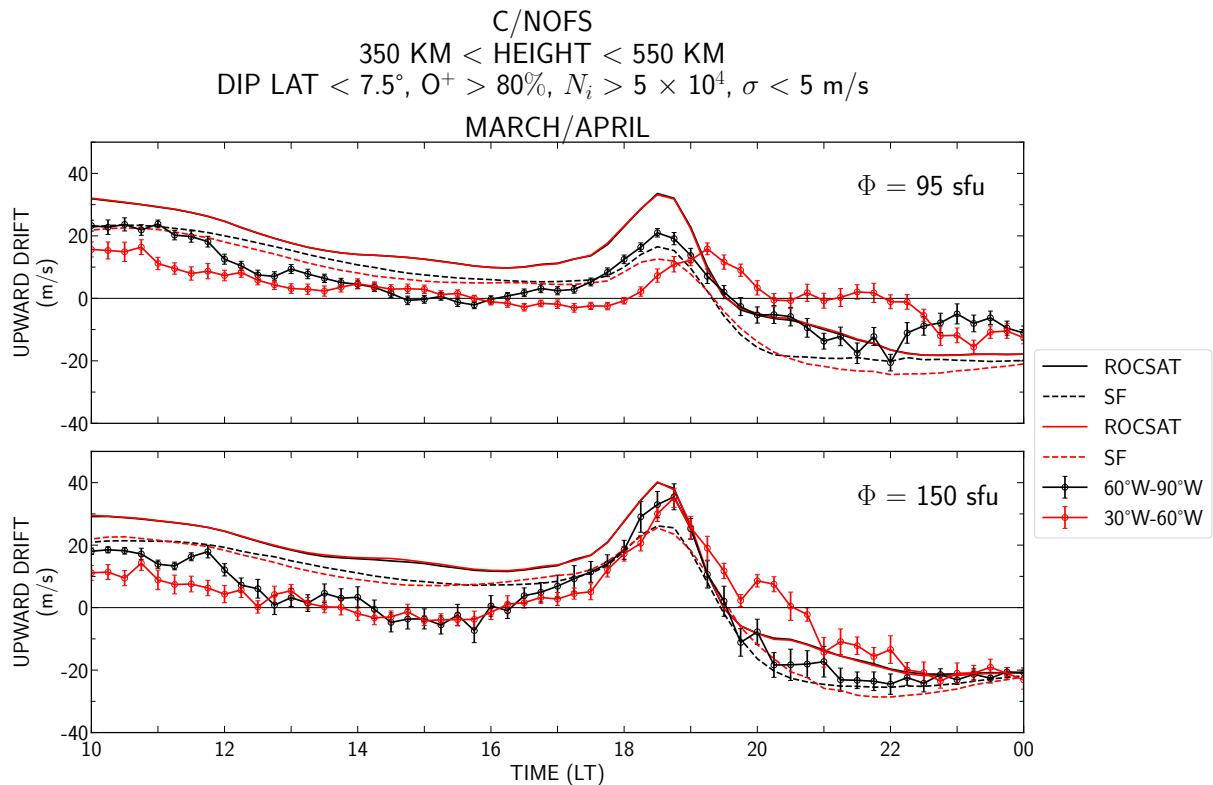
FIGURE 4.15 – Same as Figure 4.14, but for March and April.

Figure 4.16 shows the drift velocity variation for May and June. In the upper panel (lower solar flux level), the 60°W-90°W longitude sector displays only a small PRE. The ROCSAT model slightly overestimates the variation at this longitude sector until ∼22 LT, when the IVM drifts are start to deviate from the quiet-time/ROCSAT model and then become upward at ∼00 LT. The 30°W-60°W velocities in the upper panel of Figure 4.16 are downward from 12 LT to 00 LT, except around the PRE, when they assume values between 0 m/s and 2 m/s. The S-F model predicts very different drifts compared to the IVM. As for the higher solar flux level (lower panel), Figure 4.16 shows a peak between 10 LT and 12 LT at the 60°W-90°W longitude sector and an earlier PRE time compared to the low flux. In reality, the 10 LT to 12 LT peak is also seen at this same longitude sector in the upper panels of Figures 4.14-4.15. The high solar flux 30°W-60°W longitude sector is similar to the low solar flux, in which mostly downward velocities are observed throughout the day and after the PRE time. This encompasses a large part of the Brazilian sector. As mentioned previously, this is not the well-known ion drift velocity
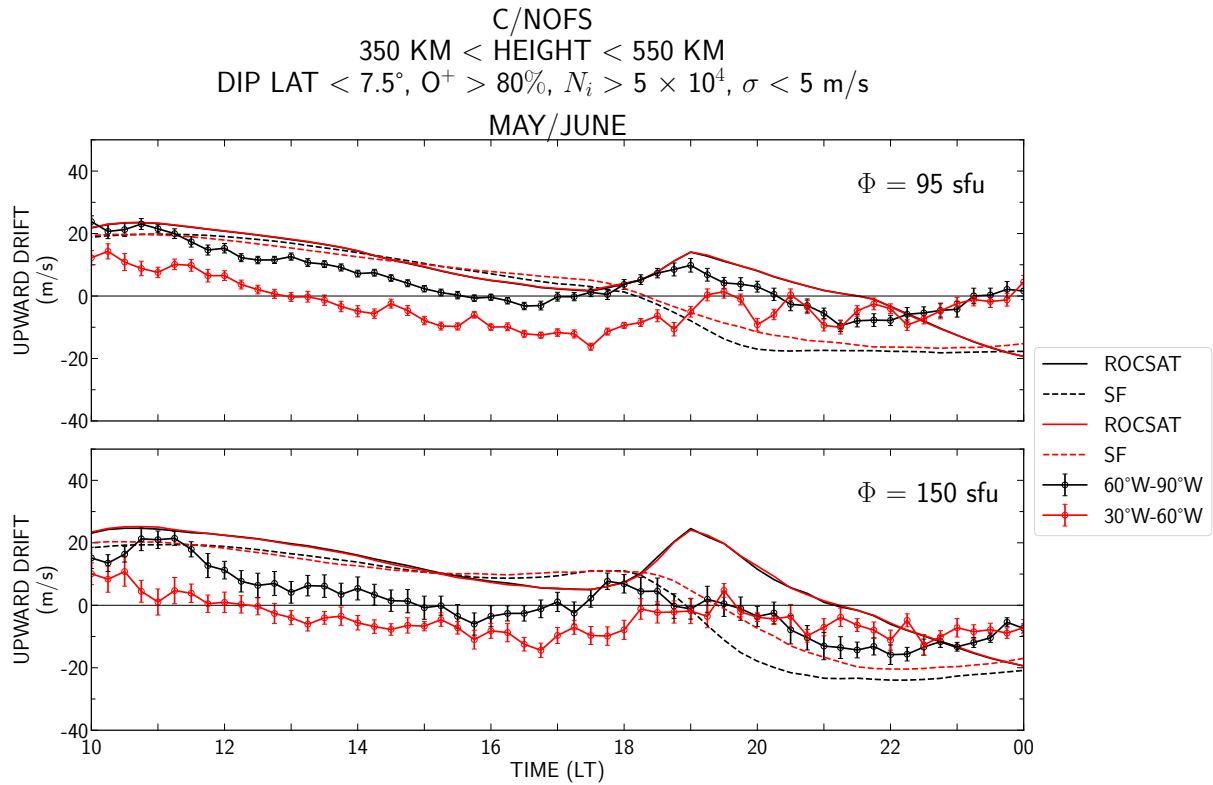
FIGURE 4.16 – Same as Figure 4.14, but for May and June.

at low latitudes for this season (June solstice), where we expect small upward velocities during the day, a PRE around 10 m/s and downward drifts afterwards (e.g., BATISTA *et al.*, 1996).

The upward drift velocity variation for July/August shown in Figure 4.17 is similar to the May/June variation. In more details, mostly downward velocities are observed at the 30°W-60°W sector, although during July and August the drifts reversal from upward to downward are different for the two solar flux levels, being earlier for a higher solar flux. The models outputs show the expected quiet-time velocity pattern, where the S-F model closely follows the low flux 60°W-90°W velocities during the day. However, it can be said, from Figures 4.16 and 4.17, that the IVM velocities in general do not show the expected pattern during the June solstice. Measurement errors are also possible to explain the June solstice drifts, since departures from the curl-free condition are increased in this season (FEJER; JENSEN; SU, 2008a). Additionally, the longitudinal asymmetry is more evident in this season than in the others.

Figure 4.18 shows the drift velocity for September and October. There are clear PRE peaks for both solar flux levels occurring at about the same local time (~1830 LT). Again, downward velocities during the afternoon are observed at the 30°W-60°W longitude sector in both solar flux levels. Upward velocities after 20 LT are also observed in this sector, in particular for a lower solar flux (upper panel). For the low flux, a clear

longitudinal asymmetry is also seen. The low solar flux 60°W-90°W velocities predicted by the ROCSAT model follow reasonably well the IVM velocities, except during the PRE, where the model overestimates the data. Additionally, during low solar flux, the 60°W-90°W velocities are the only ones where no downward velocities are observed in the afternoon. As for the higher solar flux shown in Figure 4.18, a clear PRE is observed, where the S-F predicts more accurately its magnitude, as well as the drifts after the peak. During the daytime, both models overestimate the vertical drifts.
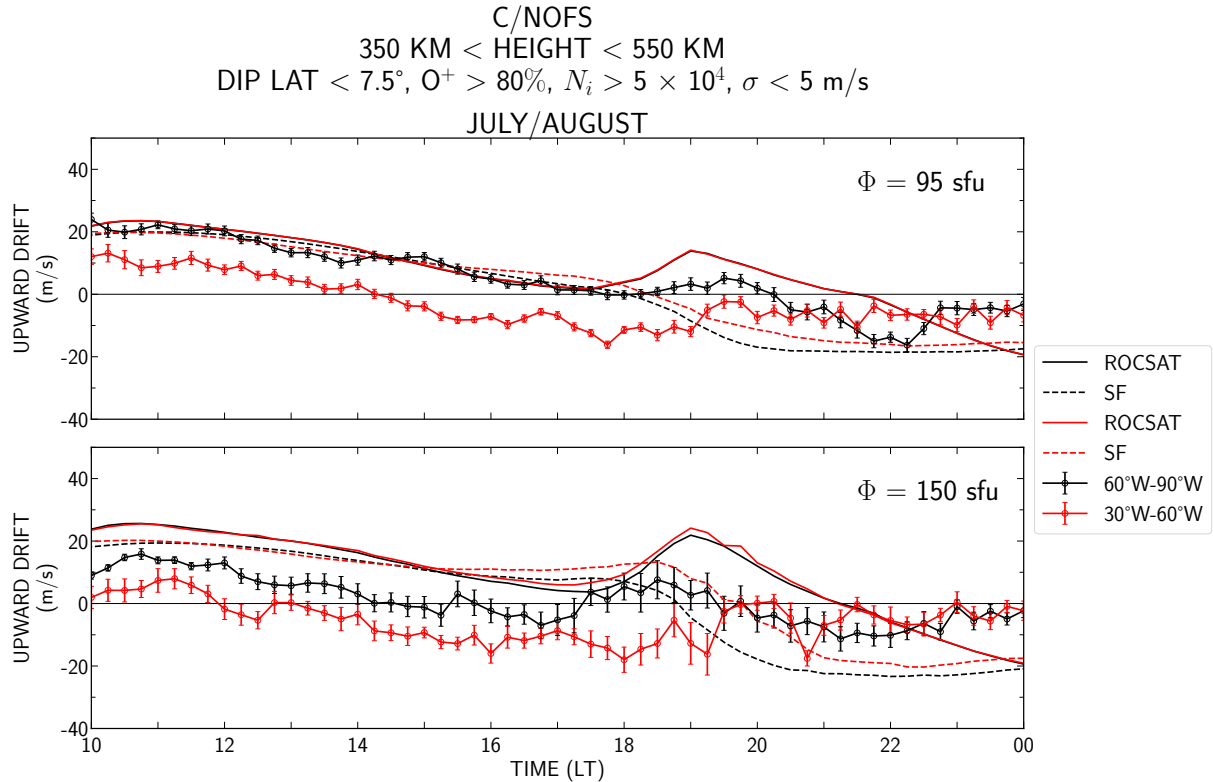
FIGURE 4.17 – Same as Figure 4.14, but for July and August.

Compared to Figure 4.18, the November/December velocity variation shown in Figure 4.19 displays PRE peaks occurring at different local times in the two longitude sectors. The 30°W-60°W sector presents an earlier PRE, about 30 minutes ahead the 60°W-90°W sector. This difference is more evident for the greater solar flux level. Additionally, the velocities during the low solar flux were apparently more affected by plasma irregularities, given the upward drifts seen in particular at the 60°W-90°W sector. These drifts reach ~20 m/s at 2145 LT, when we expect the drifts to be downward. As for the models, ROCSAT strongly overestimates the drifts during the daytime in both fluxes, whereas it is similar to the data during nighttime for the higher flux. The S-F model predicts reasonable drifts compared to the data during the day for the low flux, and during the night for the higher solar flux level.
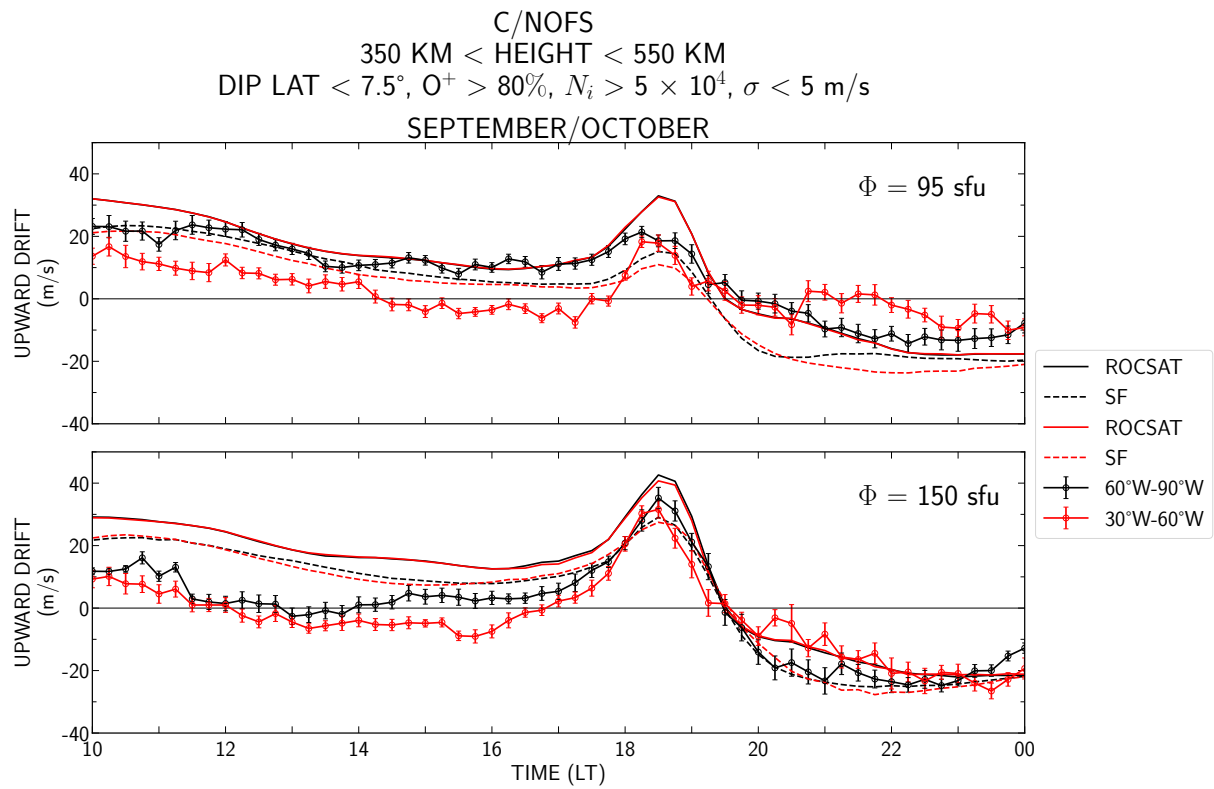
FIGURE 4.18 – Same as Figure 4.14, but for September and October.
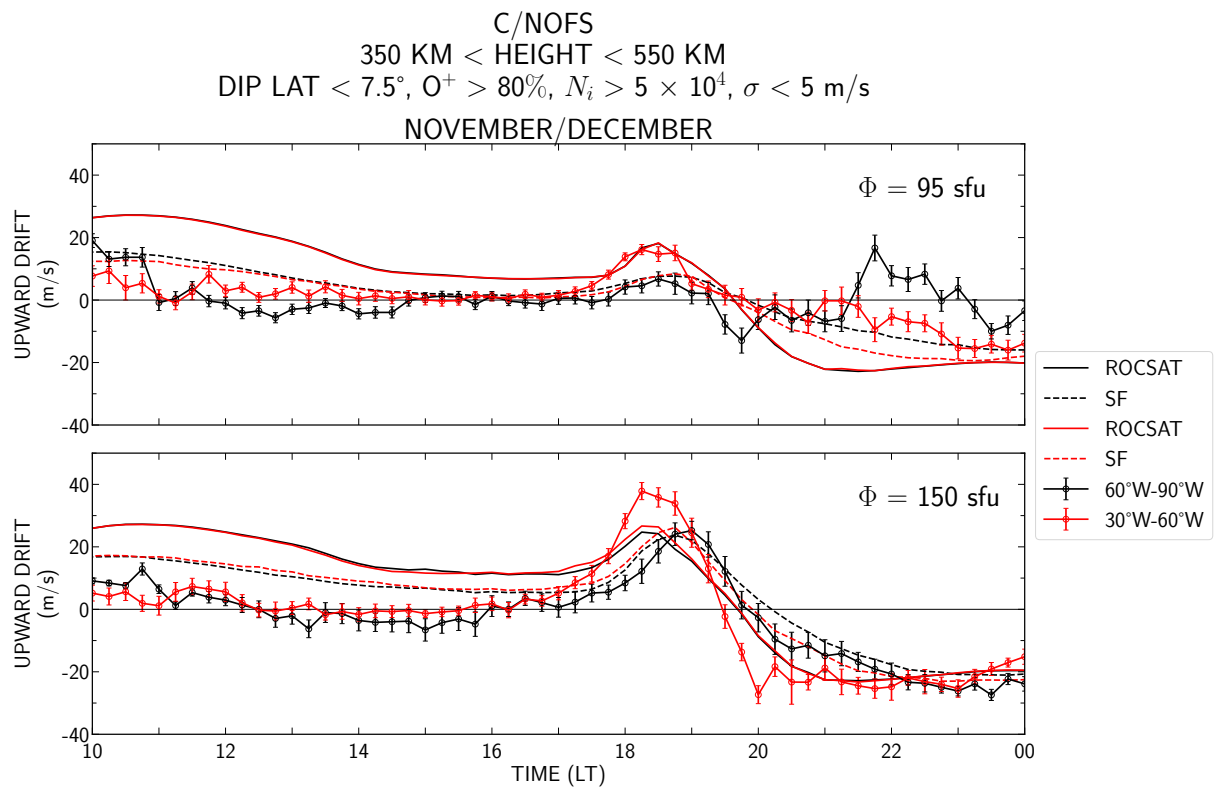
FIGURE 4.19 – Same as Figure 4.14, but for November and December.

Discussion and Summary

Downward afternoon drifts are consistently observed across all seasons examined and in the two longitude sectors shown here, spanning the entirety of the Brazilian territory. This is in complete disagreement with the current understanding of the vertical drift in these sectors, where negative velocities are not observed during the day. It is important to keep in mind that measurements of ambient ion drift require the spacecraft velocity to be removed with very high accuracy and that the offsets removal methodology is preliminary, as described in Section 3.5.2. This means that we cannot rule out a possible instrumental error in these measurements, since it is very difficult to calibrate ambient vertical drift velocity data. However, Stoneback *et al.* (2011) also discusses, albeit under lower solar flux conditions, similar negative velocities in the afternoon measured by the IVM aboard the C/NOFS, as we will point out later in this section.

Since the first Jicamarca ISR F-region vertical plasma drift measurements, other ground-based observations have been employed to determine vertical plasma drifts at specific local times, particularly during the pre-reversal enhancement. Since then, the pattern of upward drifts during the day and downward drifts at night has become well-known and clearly established. These studies also indicated significant longitudinal variation in the PRE over the South American region. Abdu *et al.* (1981) compare the PRE over Fortaleza (4°S, 38°W), Brazil, and Jicamarca to reveal opposite seasonal trends of the times of the PRE peak, which are also reflected in the spread F characteristics at the two stations. These differences mainly arise from the variation in the magnetic field declination angles, which leads to differences in the conjugate E region sunset duration and, consequently, in the F region polarization electric field development rates at the two stations. Over Fortaleza, the PRE peak occurs earlier in December solstice and later in June solstice, consistent with what is observed in our C/NOFS Figures (red lines), even though we note that the IVM performed worse in the Brazilian sector, in the sense that more negative velocities are observed during the afternoon.

Batista *et al.* (1986) also investigates longitudinal and seasonal differences in the evening ionospheric F region plasma vertical drift enhancements between Huancayo (12°S, 75°W), Peru, and Fortaleza. The asymmetries are explained by a numerical simulation of the electrodynamic coupling between the E and F regions, considering the magnetic declination angle. The results show that the time and seasonal variation of the evening F region vertical drift PRE peak are influenced by the magnetic declination angle, which affects sunset times and Pedersen conductivity gradients. The amplitude of the PRE peak is also influenced by the declination angle and thermospheric zonal winds. Batista *et al.* (1996) use ionosonde measurements in the evening and satellite measurements at other local times to develop a vertical plasma drift model for Brazilian longitudes, called IDM (Ionosonde Drift Model). This model, used as input for SUPIM, shows clear upward drifts

during the day and downward drifts during the night.

Moreover, the drifts given by the Scherliess and Fejer (1999) (F-S) and Fejer *et al.* (2008a) (ROCSAT) models represent extensive global vertical drift measurements, emphasizing that negative drifts during the day were not observed in the development of these models. However, the discrepancies observed between the models and the C/NOFS data may also be due to the models use of a four-month average, and not two as we are performing here. Additionally, the ROCSAT model does not have acceptable values for low fluxes. We chose to keep these results here because in some seasons they are not too far from the data, as discussed in the previous section, but we emphasize that they are much less precise. The last caveat of the ROCSAT model regarding the IVM data is that the model was derived at an altitude of 600 km, and we limited C/NOFS from 350 km to 550 km. All these remarks may have contributed to the differences observed between the models and Figures 4.14-4.19.

In contrast to the well-known vertical ion drift velocity trend, Stoneback *et al.* (2011) gives a plausible explanation for the downward velocities measured by the IVM during the day. Even though these authors study a period with much lower solar flux conditions (below 80 sfu) than the ROCSAT (150 sfu) and S-F (an average of 90 sfu for the low solar flux and 180 sfu for the high), and the ones we are evaluating here, they suggest the existence of a semidiurnal component in the observed ion drifts. This component is characterized by downward drift perturbations in the early afternoon and upward drift perturbations during the night. In more details, the most dramatic variations in the drift velocity with respect to local time might be due to the influence of E region migrating and nonmigrating tides on the electric field (MILLWARD *et al.*, 2001).

A semidiurnal tide in the E region will enhance the prenoon drift, leading to an increased local time gradient in the drift across sunrise, and it will also suppress or potentially reverse the afternoon drift induced by a dawn-to-dusk electric field. When zonal F region winds are in phase with the semidiurnal tide during the day, downward afternoon drifts imply upward drifts near midnight. Additionally, a meridional (northward) semidiurnal wind component is also expected, typically exhibiting a phase difference of several hours compared to zonal winds (FESEN; ROBLE; RIDLEY, 1991). These meridional winds may cause upward drifts after midnight, especially in regions with significant magnetic declination such as the Brazilian region. The IVM data shown here indicate that during the period of low solar activity for December solstice, fall equinox, and May/June, the presence of a semidiurnal tide may be consistently observed in the drift pattern at the magnetic equator between 10 LT and 12 LT. Again, it is important to look at this explanation of the semidiurnal tide effect with caution, since semidiurnal effects are more important during low fluxes (e.g., ANDRIOLI *et al.*, 2022).

The downward afternoon drifts exhibit their highest intensity during the June solstice

(May-August, Figures 4.16-4.17), reaching velocities of approximately -15 m/s. During the daytime the CINDI/IVM data shown here demonstrate that the region of upward drift is largely confined to the period before local noon. After local noon the drifts are very weak and may be upward or downward. In the afternoon sector, the vertical drift is generally very weak and can be substantially downward in the two longitude regions and different seasons. Downward drifts are more predominantly seen in the 60°W-90°W longitude sector in northern winter seasons (Figures 4.14 and 4.19) and in the 30°W-60°W longitude sector in the northern summer and fall seasons (Figures 4.16-4.18).

The equatorial vertical ion drift is also influenced by solar activity, as can be seen in Figures 4.14-4.19. There is a significantly PRE increase in the lower panel (high solar flux) of these figures, compared to the upper (low solar flux). Hence, solar cycle effects are most pronounced near dusk (FEJER; JENSEN; SU, 2008a). For the low flux panels, as illustrated by the S-F and ROCSAT models, a weak PRE is expected because of the low levels of solar activity. Drifts similar to the low flux models predictions are observed only during December solstice (Figures 4.14 and 4.19).

Regarding the longitudinal asymmetries, the daytime December solstice (Figures 4.14 and 4.19) and spring equinox (Figure 4.15) drifts show only small longitudinal variations. During the June solstice, the PRE is not observed in the 30°W-60°W longitude sector in both flux conditions. The vertical drifts in the late afternoon and evening display significant longitudinal variations, especially during the June solstice, except for a high solar flux during the equinox, where they occur around 1930 LT and 1945 LT. Furthermore, the reversal times in the evening also exhibit considerable longitudinal variations. The earliest reversal time was observed at approximately 19 LT in the 60°W-90°W longitude sector during May/June. In contrast, in this sector, January and February exhibited the latest reversal time at around 2030 LT. These findings are in accordance with the comprehensive study by Fejer *et al.* (2008a). In this way, the period that most closely matches the expected behavior of the low latitude ionosphere shown in Figures 4.14-4.19 is from 17 LT to 22 LT, which encompasses the PRE.

The nighttime measurements tend to display larger variations and possibly be more inaccurate due to the presence of irregularities, especially during the equinoxes (Figures 4.15 and 4.18) and in the Brazilian sector (30°W-60°W). During the northern summer (Figures 4.16 and 4.17), downward drifts following sunset are prevalent and effectively suppress the development of irregularities. Stoneback *et al.* (2011) identified a minimum occurrence of irregularities between 60°W and 120°W longitude during the northern summer, encompassing the two longitude sectors studied here. Fejer *et al.* (1999) demonstrated that irregularities occurring after midnight required preceding upward drifts following downward drifts. The prevalence of postmidnight irregularities observed during the June solstice/northern summer by Stoneback *et al.* (2011) indicates the

absence of PRE and the presence of upward drifts around midnight, the last two being observed in this study.

To conclude, in this section we investigated the climatology of the vertical drift velocity in the equatorial ionosphere based on vertical drift meter data from the C/NOFS satellite from 2009 to 2015. Figures 4.14-4.19 present strong seasonal and longitude variations near the equator. The influence of solar flux levels on the PRE is evident, with higher solar flux correlating with greater PRE. Daytime drifts predominantly exhibit upward motion, downward drifts are observed during the afternoon, and nighttime drifts vary, showing longitudinal asymmetries and being influenced by irregularities. Longitudinal asymmetries can be noticed, particularly during the June solstice, where PRE is absent in the Eastern South-American sector. The absence of PRE is prevalent during northern summer, along with the presence of upward drifts near midnight. In summary, these results highlight how solar activity, tidal effects, and variations along longitude interact to shape the dynamics of the equatorial ionosphere. Therefore, our results are more accurate than previously published on the IVM aboard C/NOFS, especially for a low solar flux level, and we highlight the difficulty of in-situ ion vertical drift measurements in the South American sector.

4.5 An investigation of equatorial perturbation electric fields during different geomagnetic storms using Jicamarca data and empirical models

In this section, we examine the effects of geomagnetic storms on the equatorial ionosphere generated by different magnetospheric processes. We will examine Jicamarca vertical velocity variations due to undershielding and overshielding prompt penetration electric fields driven by interplanetary electric fields and dynamic pressure changes, substorms, as well as disturbance dynamo electric fields (see Section 2.3.3). Additionally, the ultimate goal is to compare these variations with the current empirical models discussed in Section 2.3.4. In the next sections, we will investigate five geomagnetic storms with different levels of geomagnetic activity.

4.5.1 23-24 April 2023

In this section, we used radar measurements from the Jicamarca Radio Observatory, solar wind parameters, and ground-based magnetometer data to study the unusual electrodynamic response of the equatorial ionosphere to the 23-24 April 2023 severe geomagnetic storm. Our study was published in January 2024 as an original research

article in *Frontiers in Astronomy and Space Sciences* (FEJER; LARANJA; CONDOR, 2024). This study highlights in detail the simultaneous disturbance effects of various solar wind-magnetospheric processes on low latitude storm-time ionospheric electrodynamics.

Measurement Techniques and Data

For this storm, we used ISR MP radar measurements (see Section 3.3.2) of F-region $\mathbf{E} \times \mathbf{B}$ plasma drifts and spread-F irregularities, ACE satellite solar wind, and SuperMAG ground-based magnetic field measurements from 12 UT (07 LT) April 23, 2023 to 12 UT April 24, 2023.

In the present study, we used 5-min spread-F free drifts averaged from 250 km to 500 km for the vertical component and from 250 km to 450 km for the zonal. We deleted height-averaged drifts with standard deviations larger than 30 m/s and 100 m/s for the vertical and zonal components, respectively, and zonal drifts with magnitudes larger than 200 m/s. The standard deviations of our height-averaged drifts are ~1 m/s during the day and ~10 m/s during the night (up to ~06 UT) for the vertical component, and ~10 m/s during the day and ~25 m/s at night (up to ~04 UT) for the zonal. Over Jicamarca, eastward and downward electric fields of 1 mV/m correspond to upward and westward drifts of ~40 m/s.

We also used 5-min Advanced Composition Explorer (ACE) satellite solar wind measurements of IMF By and Bz components in geocentric solar magnetospheric (GSM) coordinates, solar wind dynamic pressure and speed, and Y (east-west) component of the interplanetary electric field time-propagated to the noon magnetopause obtained from the NASA Goddard database (`https://omniweb.gsfc.nasa.gov/`). The ACE satellite is located at the L1 Lagrangian point (a point of Earth-Sun gravitational equilibrium about 1.5 million km from Earth), hence, measurements are time-shifted to the magnetospher's bow shock nose. We also used 1-min ground-based ring current and auroral magnetic field SMR, SMU, SML, and SME indices obtained from the SuperMAG database. Additionally, preliminary AE indices obtained from the WDC for Geomagnetism, Kyoto AE index service, were used as input for the F-S model.

Results

Figure 4.20 shows solar wind parameters from the ACE satellite and geomagnetic indices from SuperMAG measured during the 23-24 April 2023 severe geomagnetic storm. This coronal mass ejection (CME) driven storm started at 09 UT on the 23rd. Following the initial slow strengthening of the southward IMF Bz and increase of the ring current, the storm became strong after 1737 UT. The storm first main phase lasted up to ~2140 UT with the SMR ring current index reaching a minimum of -184 nT. In the second main

phase, which lasted from 0134 to 0407 UT on the 24th, the SMR had a minimum of -203 nT at 0403 UT. The Kp index reached values of 8+ and 8 during the first and second storm main phases, respectively.
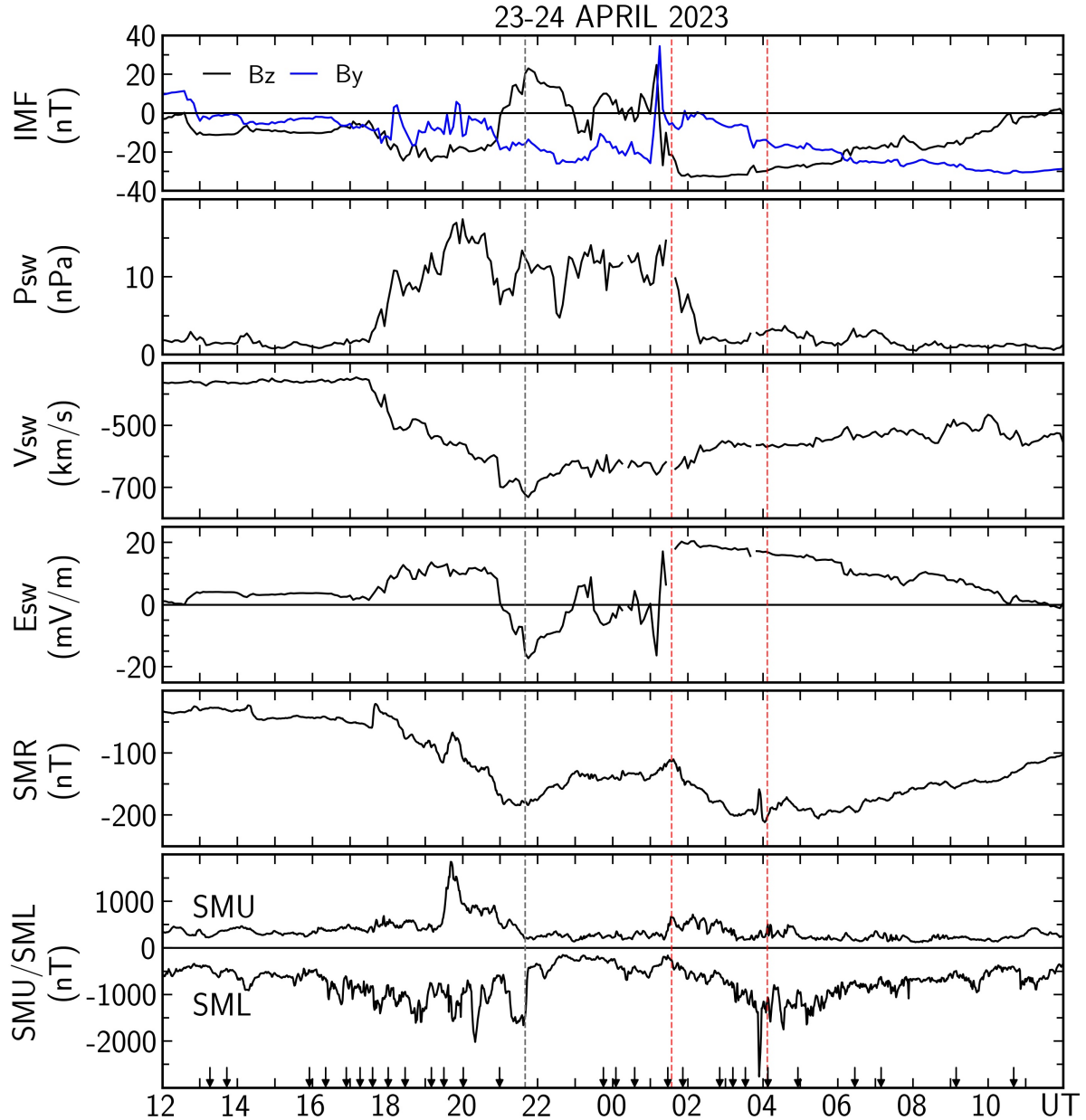
FIGURE 4.20 – (From top to bottom) IMF Bz/By, solar wind dynamic pressure, solar wind speed, solar wind east-west electric field, SuperMAG ring current (SMR), auroral current (SMU/SML) indices, and substorm onset times (small arrows in the bottom panel) during the 23-24 April 2023 geomagnetic storm. The vertical dashed gray line marks the end of the storm main phase, whereas the red delimit the storm second main phase (modified from FEJER; LARANJA; CONDOR, 2024).

Figure 4.20 shows that the IMF Bz was southward and nearly steady with values of ∼10 nT up to about 1737 UT when it turned increasingly southward reaching about -20 nT at 1820 UT. Later, it did not change much up to ∼21 UT when it first turned strongly

northward, and then decreased to small northward and southward values for ∼3 hours. After large northward and southward variations at ∼01 UT, the IMF Bz became strongly southward to about -30 nT, and then slowly decreased up to ∼12 UT on the 24th. The IMF By had generally small values up to ∼20 UT, was ∼-20 nT up to ∼01 UT when it underwent sign changes before becoming very small, and then turning steadily negative (toward dusk) up to ∼11 UT on the 24th. The solar wind dynamic pressure had large values and amplitude fluctuations from ∼28 UT on the 23rd to ∼02 UT on the 24th. The solar wind speed increased strongly from ∼1730 UT to 22 UT on the 23rd, which is indicative of strong solar wind-magnetosphere coupling conditions (e.g., NEWELL *et al.*, 2008), and then decreased slowly. The interplanetary electric field was weakly eastward prior to ∼1730 UT when it increased to ∼10 mV/m up to ∼21 UT on the 23rd, then it turned strongly westward up to ∼23 UT on the 23rd before oscillating with small amplitudes up to ∼01 UT on the 24th. Later, it underwent large amplitude fluctuations followed by a large eastward increase and a slow gradual decrease up to ∼11 UT on the 24th. The SMU was ∼500 nT on the 23rd, underwent a large increase associated with the large corresponding increase in the dynamic pressure during 19-20 UT on the 23rd, and had generally small values afterwards. The SML values were large and with large fluctuations indicating significant substorm activity with their onset times indicated by small arrows. Figure 4.20 shows numerous fast recurring (quasi-periods of ∼30 min) substorms from ∼16 UT to the end of the storm first main phase (∼22 UT) and from ∼2340 UT to ∼05 UT on the 24th. Later, there were also a few more substorms up to ∼11 UT on the 24th.

Figure 4.21 presents again in the three top panels the ACE interplanetary electric field and the SuperMAG ring current and auroral geomagnetic indices with substorm onset times. The fourth and fifth panels show the height averaged Jicamarca vertical and zonal plasma drifts with their standard deviations superposed on the corresponding quiet-time drift patterns. Figure 4.21 indicates that, prior to the storm onset, there were generally only small equatorial upward and eastward perturbation drifts over Jicamarca. The sudden increase of geomagnetic activity at 1737 UT resulted in an initial rapid increase followed by a nearly steady decrease of the ring current index over the storm first main phase. In this period, the upward perturbation drifts increased first rapidly, at the storm onset, and then more slowly up to ∼1930 UT when they increased strongly again, likely due to the large increase in the solar wind dynamic pressure (see Figure 4.20) and resulting increase in the SMU index. The corresponding short-lived vertical perturbation drifts, which are indicative of undershielding prompt penetration and substorm activity, lasted up to ∼21 UT when the interplanetary electric field reversed following the IMF Bz strong northward turning. Over this main storm phase, the equatorial zonal drifts did not show significant disturbance effects, except for the large and very brief first eastward and then westward perturbations at ∼1930 UT, when the

vertical drifts changed rapidly in response to the large sudden change in the solar wind dynamic pressure.
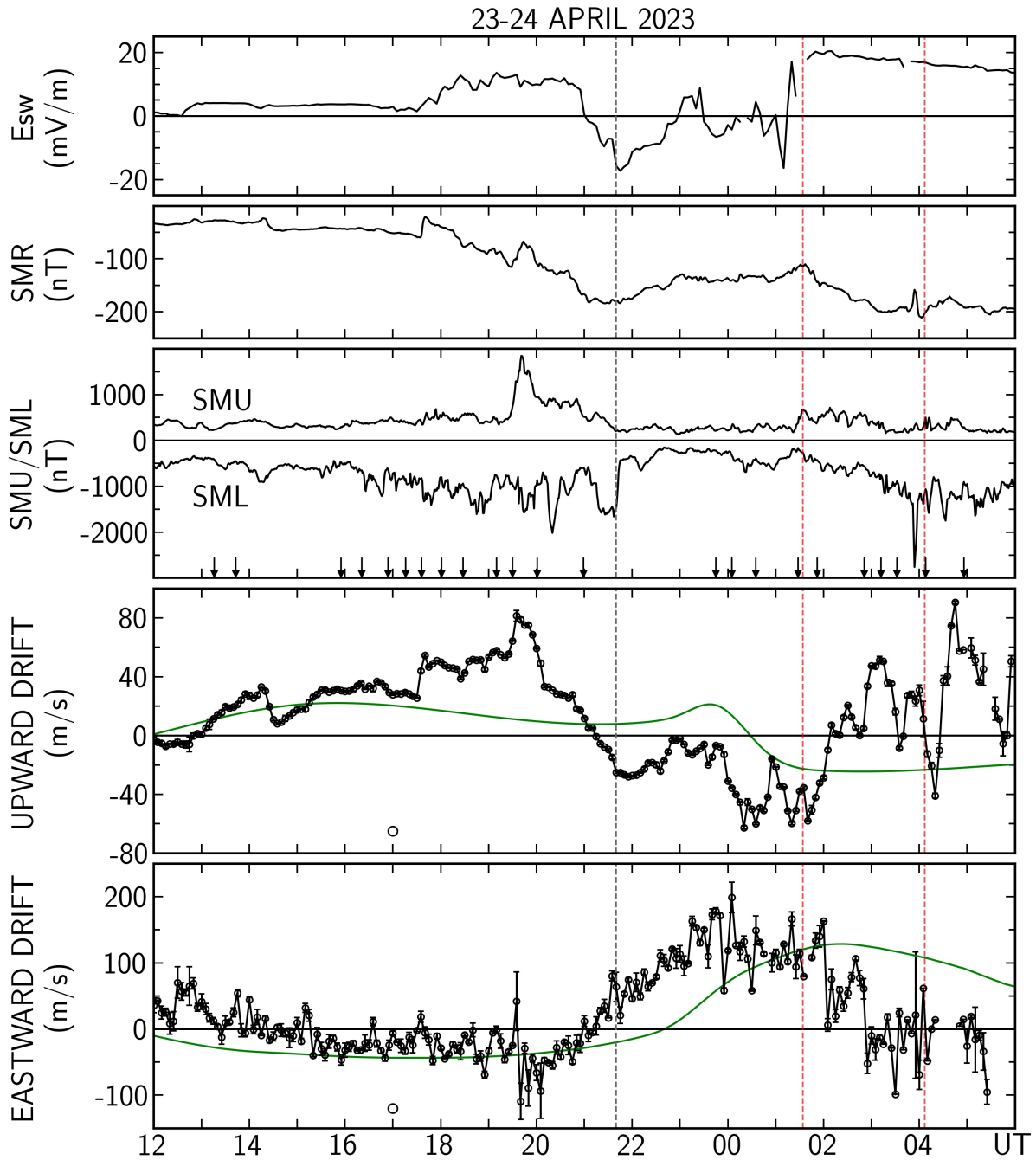
FIGURE 4.21 – (Top three panels) Solar wind motional east-west electric field, SuperMAG ring current (SMR), auroral current (SMU/SML) indices, and substorm onset times (small arrows). (Bottom panels) Height-averaged Jicamarca vertical and zonal plasma drifts. The circle at 17 UT indicates noon over Jicamarca and the green curves denote the quiet time vertical and zonal drift patterns. The vertical dashed gray line marks the end of the storm main phase, whereas the red delimit the storm second main phase (modified from FEJER; LARANJA; CONDOR, 2024).

The interplanetary electric field was mostly westward from ∼21 UT on the 23rd to

~01 UT on the 24th, except for brief and fast eastward turnings. Over this period, the equatorial vertical perturbation drifts were strongly downward, in general, due to westward disturbance dynamo and prompt penetration electric fields with occasional upward perturbation fields (i.e., near 2300 UT and 0030 UT). Figure 4.21 shows very large eastward disturbance drifts over this period, and also brief large eastward and westward drift perturbations during times of rapid vertical drift changes. The large and slowly varying late afternoon to early evening eastward disturbance dynamo drifts in Figure 4.21 are the largest ever recorded at Jicamarca over this period.

Figure 4.20 shows very large fluctuations in IMF Bz and By at ~01 UT, near the onset of the storm brief second main phase. Later, the initially very large southward IMF Bz slowly decreased up to 11 UT on the 24th, and the initially very small westward IMF By systematically increased to about -30 nT. From 0130 UT to 06 UT, the corresponding solar wind eastward electric field changed from 20 mV/m to 16 mV/m. Over this period, Figure 4.21 shows very large, substorm driven, vertical and zonal drift fluctuations superposed on large undershielding driven upward and westward drifts up to about 01 LT (06 UT). Substorm driven perturbations were particularly strong during ~03-05 UT with vertical drift fluctuations of ~120 m/s at ~0430 UT. We will point out later that disturbance dynamo electric fields did not appear to have contributed significantly to the nighttime upward drifts before ~04 UT. This premidnight period highlights simultaneous very large contributions from multiple storm-time electrodynamical mechanisms to equatorial disturbance electric fields. As noted earlier, the errors on the drift measurements were significantly larger in the postmidnight sector due to very low signal-to-noise ratios.

Figure 4.22 shows from top to bottom the solar wind electric field, auroral electrojet indices, Jicamarca vertical drifts, and backscattered power from 3-m equatorial spread F plasma irregularities from 02 to 09 UT. We note that measurements from these coherent scatter regions were not used in estimating the plasma drifts. Spread F irregularities first developed at ~0330 UT (2230 LT) following the vertical drift reversal to upward, they weakened at 0420 UT with the reversal to downward, and then strengthened strongly and rapidly rose to ~700 km following the large increase of the upward drifts at ~0440 UT. Later, their height range and strength varied considerably up to 0820 UT most likely due to highly variable vertical drifts likely caused by strong substorm activity. The weak late night and early morning irregularities were likely driven by disturbance dynamo drifts, as discussed below.

Discussion

In this section, we initially examine to what extent our disturbance drifts, obtained by removing the corresponding quiet-time values, can be explained by prompt
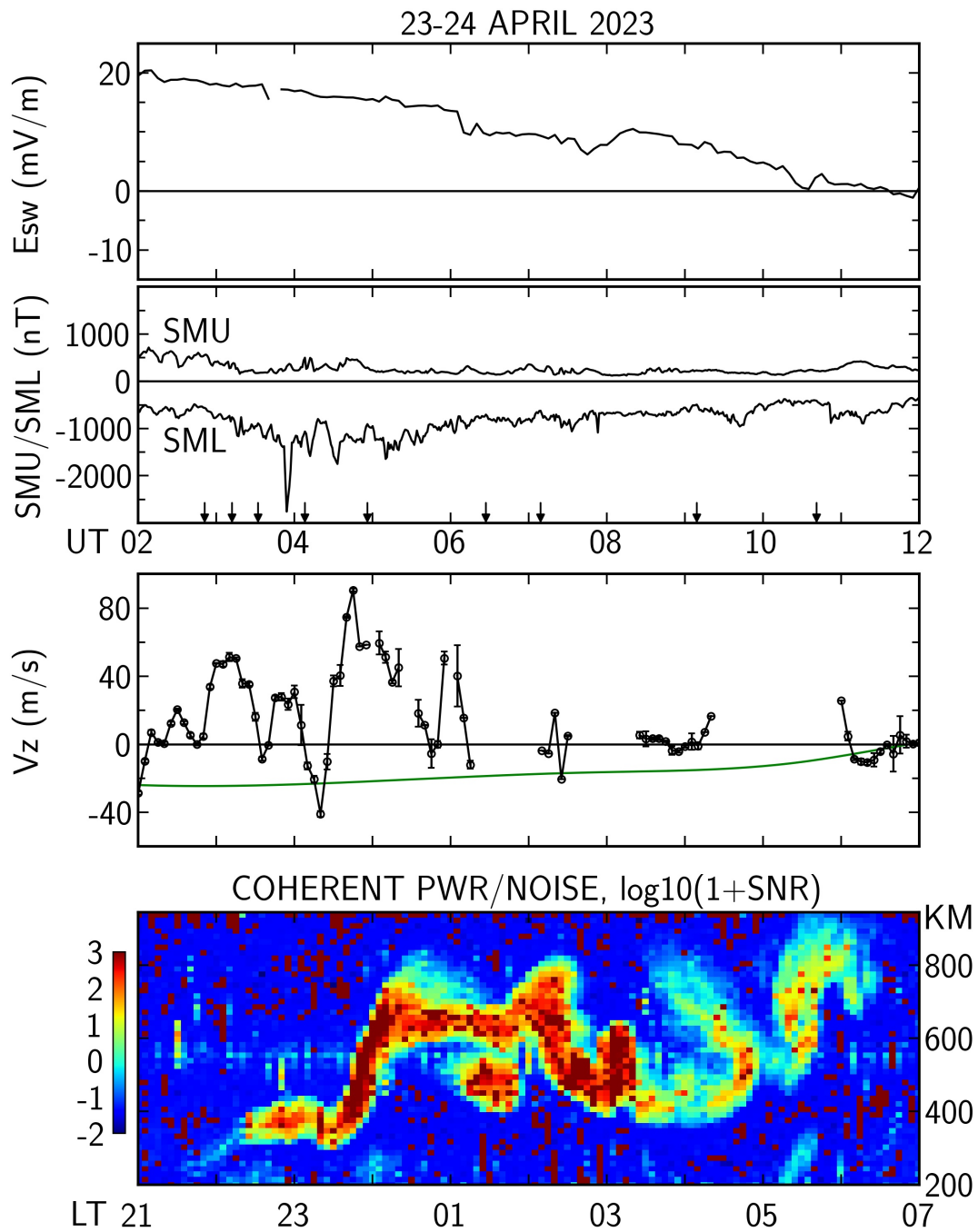
FIGURE 4.22 – (Top two panels) Solar wind east-west electric field, auroral current (SMU/SML) indices, and substorm onset times (small arrows). (Third panel) Height-averaged Jicamarca vertical plasma drifts and their quiet-time values (green curve). (Fourth panel) Coherent backscattered power from 3-m plasma density irregularities (FEJER; LARANJA; CONDOR, 2024).

penetration disturbance dynamo drifts predicted by empirical electric field models. Then, we briefly discuss processes possibly responsible for our early night unusual plasma drift observations.

Figure 4.23 shows, in the top panel, the interplanetary electric field for the period

illustrated in Figure 4.21. The bottom panel shows daytime and evening vertical drift perturbations obtained from Figure 4.21 by removing the corresponding quiet-time values, the prompt penetration derived using the prescription suggested by Kelley and Retterer (K-R) (2008) and shifted by 17 min to account the propagation time from the front of the magnetopause to the equatorial ionosphere, and the corresponding results from the Manoj and Maus (M-M) (2012) and the Fejer and Scherliess (1997a) (F-S) models. Although the K-R model does not specify when the early night undershielding electric fields change from upward to downward, in Figure 4.23 we extended its daytime prescription up to 06 UT (01 LT) considering our very large corresponding measured upward drifts. We note that, in addition to prompt penetration electric fields, the residual drifts were also clearly affected by other processes including dynamic pressure changes, substorms and disturbance dynamo electric fields.
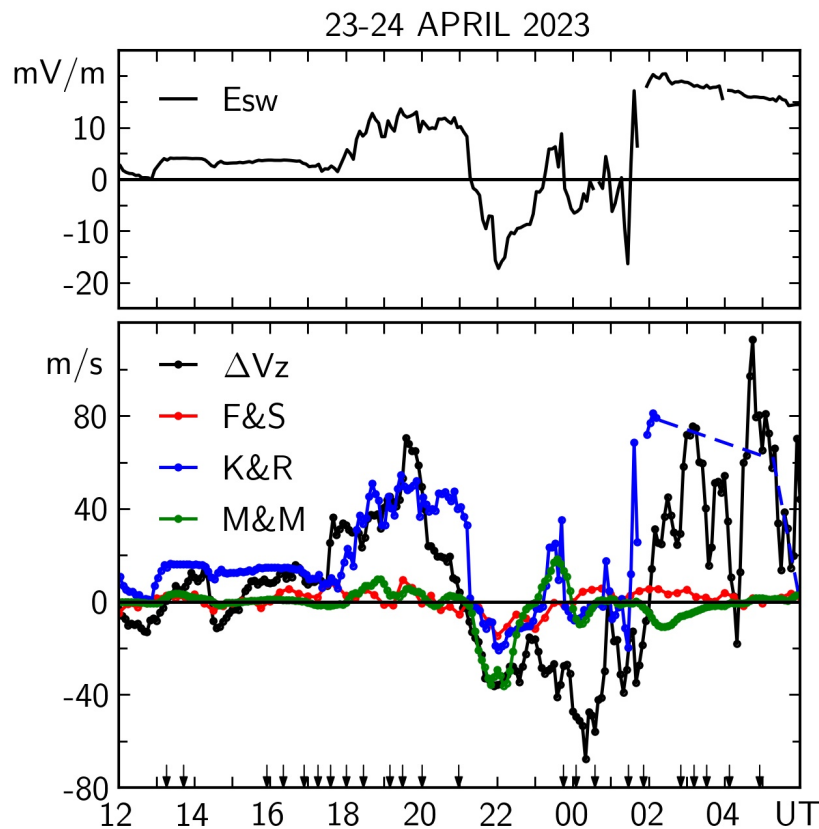
FIGURE 4.23 – (Top panel) Solar wind east-west electric field. (Bottom panel) Vertical disturbance drifts and their predictions from the Fejer-Scherliess (F&S), Manoj-Maus (M&M) and from the Kelley-Retterer (K&R) procedure. The small arrows indicate substorm onset times (modified from FEJER; LARANJA; CONDOR, 2024).

For this storm, we plot the Fejer-Scherliess (F-S) model using the SME parameter from SuperMAG, since the model output using AE from WDC, Kyoto, was very similar, only having smaller amplitudes. In this way, F-S predicts prompt penetration vertical drifts in general with the correct sign, but with much smaller amplitudes than inferred from Figure

4.23. The longer-lived disturbance dynamo zonal electric field predicted by this model for the 23-24 April storm will be discussed later. Figure 4.23 indicates that the equatorial daytime short-lived perturbation drifts are generally in reasonable agreement with the prediction of the K-R model. We note that this is often not the case. On the other hand, the Manoj and Maus (2012) model disturbance drifts, which are proportional to the average time rate of change of the solar wind electric field, significantly underestimate the observed prompt penetration electric fields except between about $\sim$21-24 UT (16-19 LT).

The solar wind dynamic pressure was very strong and highly variable during $\sim$18-02 UT (13-21 LT), as indicated in Figure 4.20. Over this period, Figures 4.21 and 4.23 show noticeable short-lived penetration electric fields associated with dynamic pressure changes and related substorm activity. Solar wind dynamic pressure increases drive equatorial upward and westward plasma drifts (eastward and northward electric fields) during the day (FEJER; EMMERT, 2003; HUANG, 2020; TSUNOMURA, 1999). The very large increase in SMU and upward drifts at $\sim$1940 UT, in particular, was associated with a fast and large increase in the solar wind dynamic pressure. In this case, the corresponding westward drift perturbation is not as clear probably due to larger measurement errors. Numerous substorms also occurred between 13 LT and 21 LT, as indicated in Figure 4.23. Magnetospheric substorms generally drive only small daytime equatorial upward drifts. The strong substorm during $\sim$2120-2135 UT, for example, just appear to have slowed down the decrease of the upward drift following the sudden weakening of the southward IMF Bz and solar wind electric field.

Figure 4.24 shows in the top panel the preliminary WDC-Kyoto AE and the SME indices for the 23-24 geomagnetic storm. The bottom panel presents the daytime and early night Jicamarca perturbation drifts, and the corresponding disturbance dynamo vertical drifts predicted by the Fejer and Scherliess (1997a) model. Surprisingly, during this large storm, both auroral indices are generally in good agreement. Figure 4.24 shows that the Fejer-Scherliess model predicts only very small disturbance dynamo drifts up to $\sim$04 UT ($\sim$23 LT) and increasing upward drifts thereafter up to $\sim$09 UT (04 LT). The model does not predict, in particular, the large disturbance downward drifts between $\sim$21-02 UT ($\sim$16-21 LT), which cannot be fully accounted for by overshielding prompt penetration electric field effects. As mentioned earlier, over these periods, the large eastward drift perturbations shown in Figure 4.21 are indicative of strong disturbance dynamo effects. We also note that strong downward evening drift perturbations are a climatological feature of the equatorial disturbance dynamo mechanism (e.g., FEJER, 2002; NAVARRO et al., 2019). Overall, these results clearly confirm that the equatorial disturbance dynamo electric fields during this storm were also highly unusual.

As for the substorms events, Figures 4.21 and 4.22 strongly suggest that the
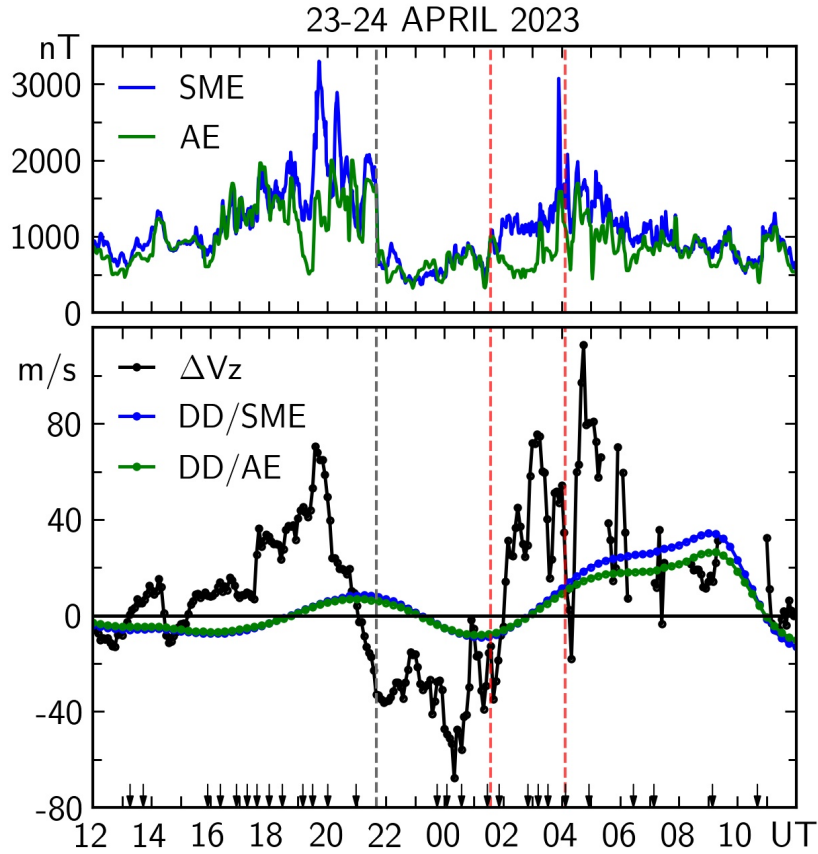
FIGURE 4.24 – (Top panel) Auroral AE and SME electrojet indices. (Bottom panel) Vertical disturbance drifts and corresponding predictions from the Scherliess-Fejer model using AE and SME indices as input parameters. The small arrows indicate substorm onset times (modified from FEJER; LARANJA; CONDOR, 2024).

substorms were associated with strong temporal and spatial structuring of equatorial spread F irregularities. This strong plasma irregularity structuring should cause strong spatial and temporal variability on low latitude TEC latitudinal profiles. We note that the drift velocities of the measured 3-m plasma irregularities cannot be determined with our radar operating mode.

Numerous model and experimental studies indicated that during southward IMF Bz the evening and early night equatorial prompt penetration vertical plasma drifts (zonal electric fields) are upward (eastward) up to about 22 LT with peak upward drifts (eastward electric fields) at ∼19 LT (e.g., FEJER *et al.*, 1990a, 2008b; FEJER; SCHERLIESS, 1997b; HUANG, 2015; 2020; SAZYKIN, 2000; SENIOR; BLANC, 1987; SPIRO *et al.*, 1988b; TSUNOMURA, 1999; TSUNOMURA; ARAKI, 1984). As pointed out earlier, disturbance dynamo effects are unlikely to have affected the 23-24 April 2023 storm late night vertical drift reversal. Therefore, the occurrence of mostly upward vertical drifts up to ∼01 LT during strong southward IMF Bz and undershielding conditions on the 23 April 2023 storm is highly unusual. To the best of our knowledge, the only similar event

reported occurred during the 07-10 November 2004 very large magnetic storm (discussed in detail in Section 4.5.4). These two storm-time late equatorial undershielding driven vertical drift reversal events suggest highly unusual solar wind-magnetospheric-ionospheric conditions.

Wolf (1970) pointed out that mid- and low-latitude magnetospheric dynamo electric fields are controlled by the high-latitude convection and potential distribution, driven by magnetic field aligned (Birkeland) currents, and strongly affected by longitudinal and latitudinal variation of high-latitude Pedersen and Hall conductances. The divergence-free condition for the ionospheric currents leads to poleward (equatorward) gradients in the meridional electric field near dusk (dawn). Furthermore, the enhanced auroral conductivities cause an eastward rotation of the high-latitude potential distribution (RILEY, 1994; WOLF, 1970). The combined effect of these processes is illustrated in Figure 6 of Fejer (1997). Phase changes of the polar cap potential distribution have significant effects on mid- and low-latitude magnetospheric electric fields near dawn and dusk (BLANC, 1983; SENIOR; BLANC, 1987; WOLF et al., 1982). Rice Convection Model simulations presented by Sazykin (2000) indicate that a rotation of the high latitude potential distribution to later local times increases the premidnight eastward and southward prompt penetration electric fields at all latitudes. These simulations indicate that a 2-hour rotation of the potential to later local times cause the eastward to westward nighttime electric field reversal to occur close to 24 MLT (magnetic local time). In this case, the simulation also indicates increased southward electric field (i.e., westward drifts) in the premidnight sector, which is consistent with the results in Figure 4.21.

Rotations of the high latitude convection in local time have been associated to solar cycle and seasonal changes and with IMF By sign and magnitude changes. However, since these rotations have opposite signs in the northern and southern high latitudes, it is not clear how they could explain our observations. We speculate that strong substorm activity and unusual high-latitude conductances in the early night period have a significant role on late night undershielding-driven vertical drift reversals. Clearly, additional experimental and modeling studies are needed to explain our complex observations and, in particular, the effects of additional solar wind-magnetospheric processes.

4.5.2   27-28 September 2017

In this section, we investigate the equatorial ionosphere F-region response over Peru during the 27-28 September 2017 moderate geomagnetic storm. The study utilizes data from the Jicamarca ISR, focusing on the vertical drifts. Additionally, low and high latitude ionospheric parameters and indices related to solar wind/magnetospheric

activity complement the analysis. From now on, we will try to be briefer in our storms' evaluation, since we are more interested in the comparisons between the Jicamarca vertical drifts and the empirical model outputs. Additionally, we will, in general, apply the same methodology as for the 23-24 April 2023 storm.

Measurement Techniques and Data

We used Jicamarca incoherent scatter radar measurements from 23 LT (04 UT) on September 27, 2017 to 01 LT (06 UT) September 28, 2017, which encompasses the storm main phase. Again, we also use 1-min SuperMAG ground-based magnetic field, WDC, 1-min Kyoto AE index, and 5-min ACE satellite solar wind measurements.

In the present study, we used 5-min vertical drifts averaged from 250 km to 500 km for the vertical component and from 250 km to 450 km for the zonal. These velocities contain spread F measurements. However, it is important to mention that ambient plasma drifts cannot be reliably obtained in strong spread F regions and when the plasma is strongly inhomogeneous in the east-west plane. We deleted height averaged drifts with standard deviations larger than 30 m/s and 90 m/s for the vertical and zonal components, respectively, and zonal drifts with magnitudes larger than 200 m/s. The standard deviations of our height averaged drifts are ∼1 m/s during the day and ∼3 m/s during the night for the vertical component, and ∼10 m/s during the day and ∼45 m/s at night for the zonal. It is important to keep in mind that over Jicamarca, eastward and downward electric fields of 1 mV/m correspond to upward and westward drifts of ∼40 m/s.

Results

The 27-28 September 2017 storm main phase lasted from 1906 UT on September 27 to 0800 UT on September 28. Figure 4.25 shows solar wind parameters from ACE and geomagnetic indices from SuperMAG during 27-29 September 2017. The SMR ring current index reached a minimum of -75 nT at ∼0800 UT 28 September. The Kp index reached a value of 6+ during the storm main phase.

During this storm, the IMF presented many fluctuations. The IMF Bz variation shown in Figure 4.25 displayed numerous southward excursions, the most remarkable being between 07 UT and 08 UT on the 27th, in which it had a minimum of ∼-15 nT, between 11 UT and 14 UT and 19 UT and 23 UT on the 27th, in which the IMF Bz was ∼-13 nT. After ∼12 UT on the 28th, the IMF Bz started to recover. The IMF By had in general small magnitudes throughout the storm, with a maximum of ∼10 nT at ∼07 UT on the 27th. The dynamic pressure had large fluctuations between 05 UT and 07 UT on September 27, with a maximum of ∼15 nPa at ∼07 UT, after which its value decreased to ∼5 nPa until the end of the storm main phase. Figure 4.25 shows that the solar wind

speed increased with the onset of the storm main phase and continued with large values of up to -700 km/s until the start of the recovery phase. The interplanetary electric field displayed many fluctuations up to ∼12 UT on the 28th, with maximum magnitude of ∼5 mV/m. The SMU and SML auroral current indices also showed large fluctuations during the storm main phase, in which SML presented numerous recurring substorms from about the start up to the end of the storm main phase.
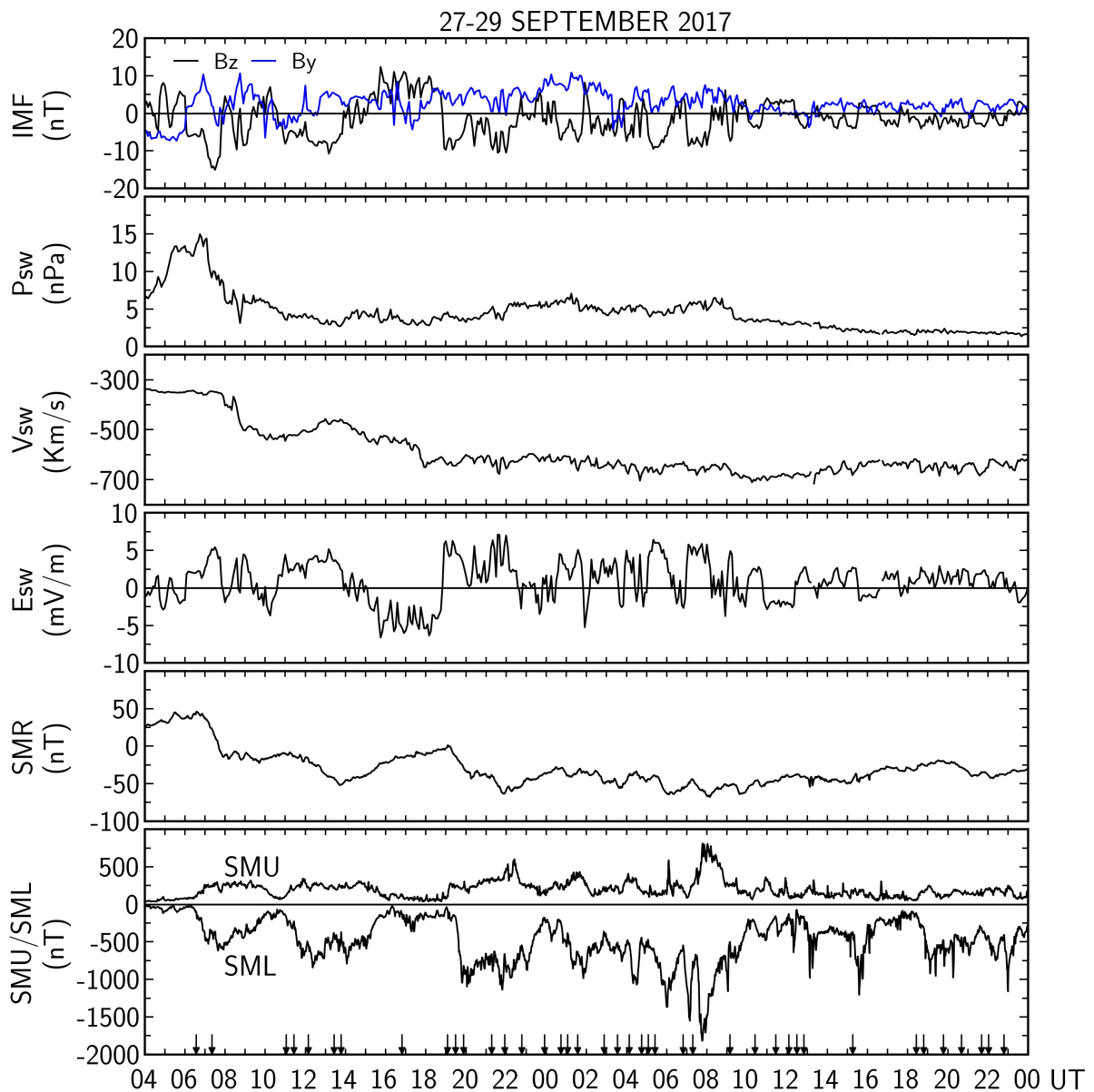
FIGURE 4.25 – (From top to bottom) IMF Bz/By, solar wind dynamic pressure, solar wind speed, solar wind east-west electric field, SuperMAG ring current (SMR), auroral current (SMU/SML) indices, and substorm onset times (small arrows in the bottom panel) during the 27-28 September 2017 geomagnetic storm.

Figure 4.26 presents in the three top panels the ACE IMF By and Bz components, the solar wind electric field, and the SuperMAG ring current and auroral geomagnetic indices with substorm onset times, whereas the fourth and fifth panels show the height-

averaged Jicamarca vertical and zonal plasma drifts, respectively, with their standard deviations superposed on the corresponding quiet-time drift patterns from 2040 UT to 1200 UT on 27-28 September 2017, which encompasses the storm main phase. Figure 4.26 shows a rapid decrease in the Jicamarca upward drifts from around 0600 UT to 0800 UT (0100-0300 LT) possibly associated, at least partially, with the IMF Bz reversal from northward to southward, generating westward undershielding electric fields (downward drifts) over Jicamarca. Furthermore, there are two substorm onsets during the 0600-0800 UT period, and they might also have contributed to the strong downward drifts. After 0800 UT, the IMF Bz starts to display numerous northward and southward excursions with small magnitudes. Hence, the strong upward drift velocity peak at 0900-1000 UT (0400-0500 LT) cannot only be accounted for by undershielding/overshielding electric fields. Additionally, the SML index does not indicate substorm activity around this time. Comparing the fourth panel with zonal drift shown in the fifth, we suggest that this strong upward drift was at least partially generated by disturbance winds, given that the zonal drifts are strongly westward at this time.

Figure 4.26 shows that after 1000 UT (0500 LT), the IMF Bz is turned southward until ∼1400 UT (0900 LT), with values up to -10 nT. Despite this southward turn for ∼4 hours, the upward drifts do not seem to be affected by prompt penetration electric fields, since they only present small fluctuations in comparison with the quiet time pattern. Hence, we associate these fluctuations with substorm activity. The IMF Bz northward turn from 1400 UT to 1900 UT (0900-1400 LT) also did not seem to affect the upward drifts. From 1900 UT to ∼2300 UT, the IMF Bz is southward again, with several fluctuations. The interplanetary electric field reached values up to ∼8 mV/m around this time, followed by a small increase in the upward drifts, that could also be associated with substorm activity. Hence, the evaluation of prompt penetration electric fields is a difficult task since there are simultaneous contributions from different sources. Additionally, in this case the evaluation is even harder since the penetration efficiency did not seem to be high, seen by the small drift perturbations, perhaps due to the various IMF Bz fluctuations and its small magnitudes. Moreover, the penetration efficiency is believed to be higher in the postmidnight sector (e.g., FEJER; SCHERLIESS, 1995; MANOJ et al., 2008).

From about 2300 UT (1800 LT) on the 27th to 1200 UT (0700 LT) on the 28th, the IMF Bz and the interplanetary electric field present numerous positive and negative fluctuations. Specifically, the interplanetary electric field was small and westward at ∼0000 UT, which might have suppressed the PRE, seen by the downward drift at ∼1900 LT. The zonal drifts at Jicamarca also had large fluctuations from 2300 UT to 1200 UT. Additionally, the upward drifts had large increases that deviated from the quiet-time pattern in both the premidnight and postmidnight sectors. By these local times, disturbance winds are expected to have arrived at the equator, and since the IMF Bz is
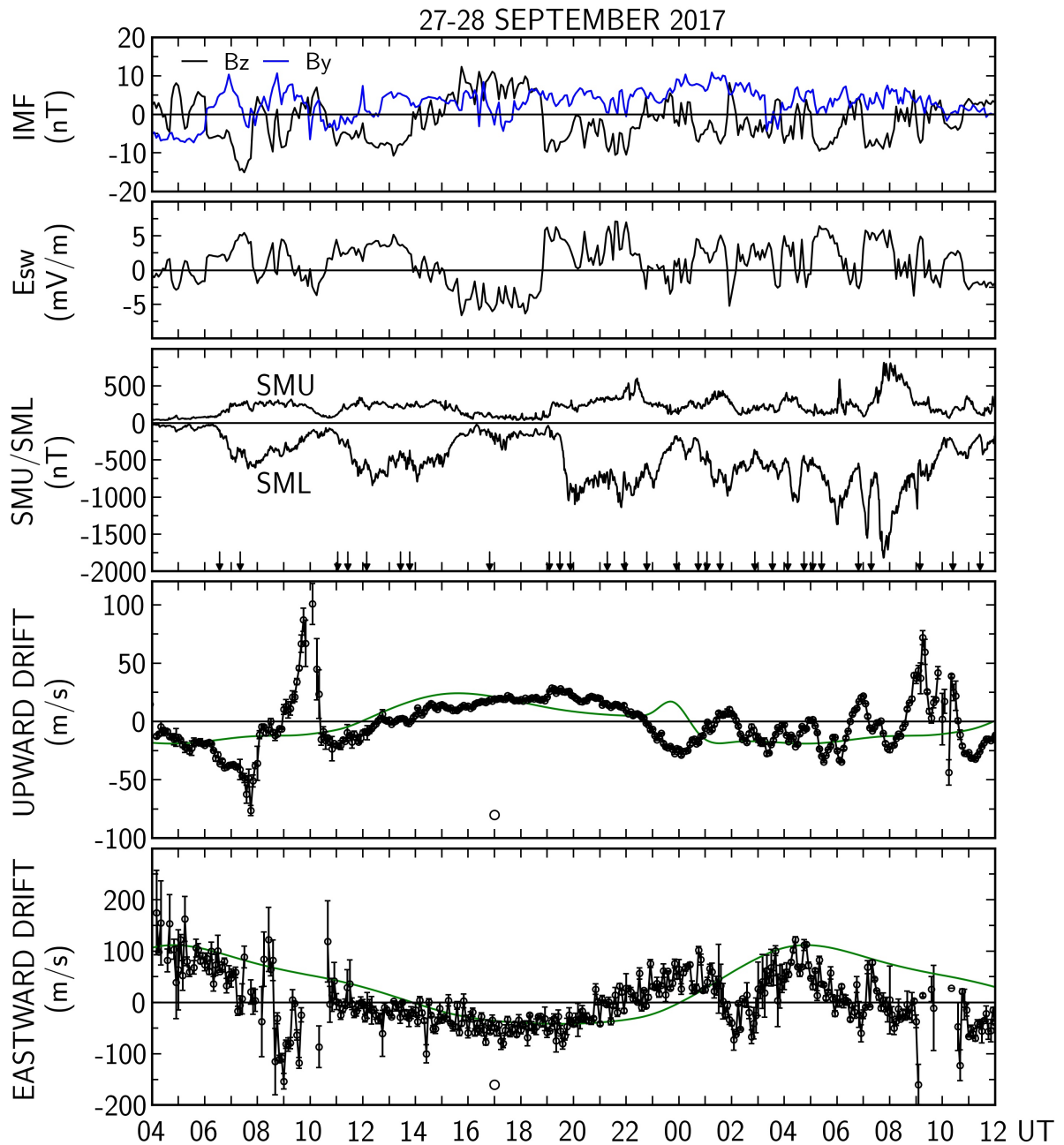
FIGURE 4.26 – (Top three panels) Solar wind motional east-west electric field, SuperMAG ring current (SMR), auroral current (SMU/SML) indices, and substorm onset times (small arrows). (Bottom panel) Height-averaged Jicamarca vertical plasma drifts. The green curve denotes the quiet time vertical drift pattern.

fluctuating between northward and southward with small magnitudes, we also associate the postmidnight drifts to disturbance dynamo electric fields. The large peaks between 0800 UT and 1200 UT (0300-0700 LT), in particular, are believed to be generated mostly by substorm activity superposed on disturbance dynamo drifts.

We speculate that the possible PRE suppression was associated with the consequent spread F suppression. To illustrate that, Figure 4.27 shows, from top to bottom, the solar

wind electric field, auroral electrojet indices, Jicamarca vertical drifts, and backscattered power from spread F plasma irregularities from 2300 LT on the 27th to 0700 LT on the 28th (0400-1200 UT). Spread F irregularities only developed at ∼2300 UT (0400 LT) on the 28th, following the strong increase in the upward vertical drift, reaching altitudes as high as ∼600 km. The irregularities weakened at 0600 UT with the drifts reversal to downward, remaining at low altitudes until 1200 UT, after which they disappeared. Thus, there were no irregularities generated after the PRE, only irregularities possibly driven by disturbance dynamo drifts and substorms.

Discussion

Similarly to the analysis conducted for the April 2023 geomagnetic storm, in this section, we first assess the extent to which our disturbance drifts, derived by subtracting the corresponding quiet-time values, can be explained by prompt penetration and disturbance dynamo drifts predicted by empirical electric field models. Subsequently, we briefly explore potential mechanisms responsible for our plasma drift observations during the 27-28 September 2017 storm.

Figure 4.28 shows, in the top panel, the interplanetary electric field for the 27-28 September 2017 geomagnetic storm.   The bottom panel shows the vertical drift perturbations obtained from Figure 4.26 by removing the corresponding quiet-time values, the prompt penetration drifts from the F-S model, the K-R model shifted by 17 min to account the propagation time from the front of the magnetopause to the equatorial ionosphere, and the M-M model. We used the K-R model for the whole period studied here, and since we do not know the exact drift reversal time to downward, we multiplied the K-R drifts from 0300 UT to 1200 UT (2200-0700 LT) by a factor of -1, because the Jicamarca residual drifts were, in general, downward during this period.

The F-S penetration model prediction for the 27-28 September 2017 storm shown in Figure 4.28 had, in general, the same sign as that of the residual drifts, but with much different magnitudes. For example, the model predicts the main velocity peaks at Jicamarca, especially the one between 0800 UT and 1200 UT on the 28th, but with smaller magnitudes. The F-S model predicts, also with smaller magnitude, the downward drift at ∼0000 UT, which is around the PRE time, supporting our hypothesis of PRE suppression. The fact that the F-S model predicts at least the main upward and downward peaks, even with much lower magnitude, may suggest that part of the explanation for these drifts lies in the auroral activity, since this model uses the AE index (or, in this case, the SME) as input. The M-M model is the least accurate compared to the other models in this case, since it only predicts, with smaller magnitudes, the prompt penetration fluctuations between 0200 UT and 0800 UT on the 28th.

The K-R model is able to predict the main fluctuations in the data, but underestimates
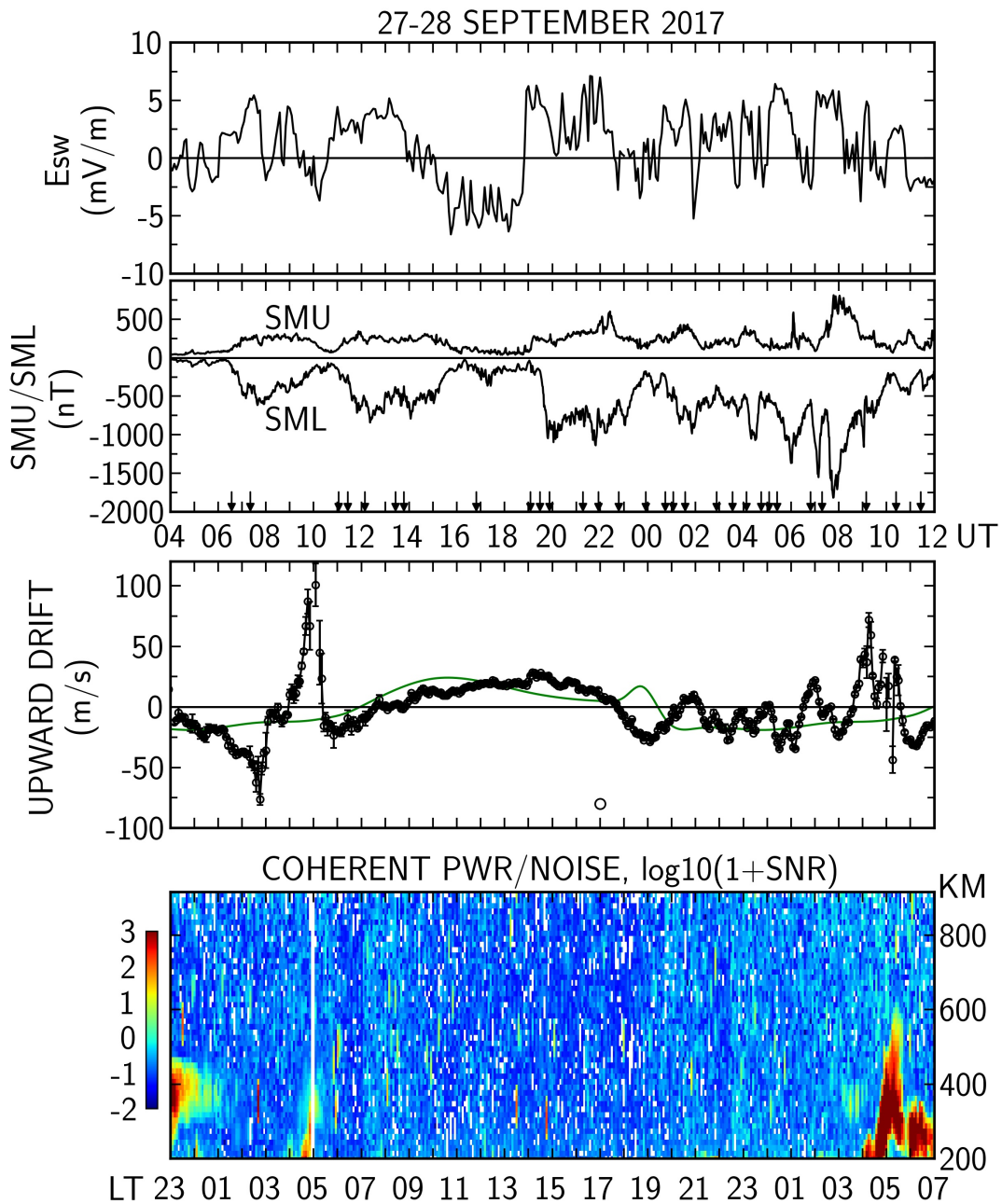
FIGURE 4.27 – (Top two panels) Solar wind east-west electric field, auroral current (SMU/SML) indices, and substorm onset times (small arrows). (Third panel) Height-averaged Jicamarca vertical plasma drifts and their quiet-time values (green curve). (Fourth panel) Coherent backscattered power from plasma density irregularities.

the residual drifts most of the time. However, the large upward drift at 0800-1000 UT does not have any prediction by this prompt penetration model. In contrast, the F-S model is able to predict the peak, even if with much lower amplitude, suggesting that auroral effects may exist. The K-R model predicts the residual fluctuations between 0300 UT and 1200 UT (2200-0700 LT) on the 28th, but still underestimates the data. We suggest that a different proportional factor would work better in this case. As an example, Figure 4.29 shows again, in the top panel, the interplanetary electric field for the 27-28 September
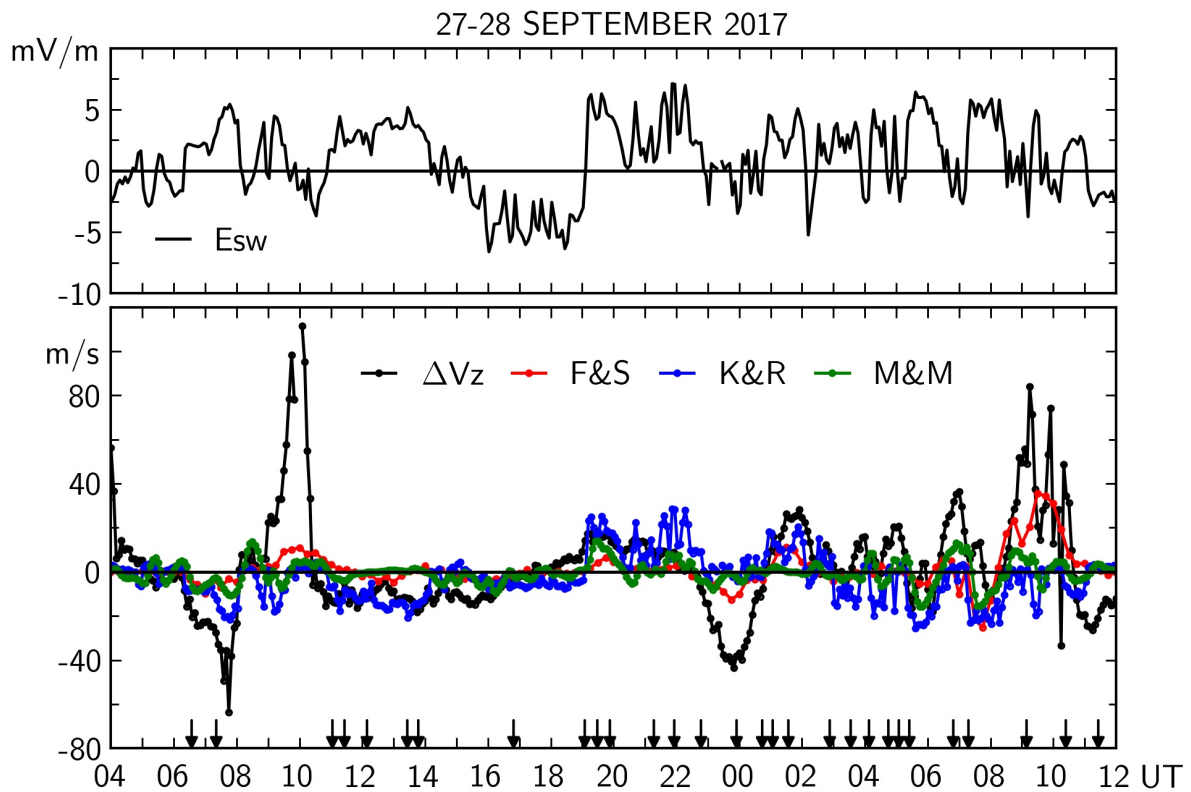
FIGURE 4.28 – (Top panel) Solar wind east-west electric field. (Bottom panel) Vertical disturbance drifts and their predictions from the F-S (F&S), M-M (M&M) and from the K-R (K&R) procedure. The small arrows indicate substorm onset times.

2017 geomagnetic storm, whereas the bottom panel illustrates the K-R using a different ratio of the interplanetary electric field to the equatorial zonal electric field between 0300 UT and 1200 UT on the 28th, which is 0.05 (5%) for southward IMF and 0.2 (20%) for northward IMF, called here K-R*. In Section 2.3.4, we explained that the regular K-R procedure uses 0.1 (10%) for southward IMF and 0.03 (3%) for northward IMF. The other periods in Figure 4.29 follow the same regular K-R procedure. As can be seen in this Figure, the K-R* model works better in the period from 0300 UT to 1200 UT on the 28th than the K-R, and this demonstrates how the proportionality factor from the interplanetary electric field to the equatorial can change depending on the local time sector and the IMF Bz pattern (i.e., from storm to storm), adding an extra layer of complexity to this subject.

The possible PRE and irregularities suppression mentioned earlier was generated due to the westward polarity of the interplanetary electric field at that time, driven by overshielding processes. Abdu *et al.* (2009) reported similar cases of PRE and consequent spread F suppression due to overshielding penetration electric fields. Furthermore, Abdu *et al.* (2018) investigated a case of PRE suppression due to overshielding to suggest that a possible contribution from disturbance dynamo cannot
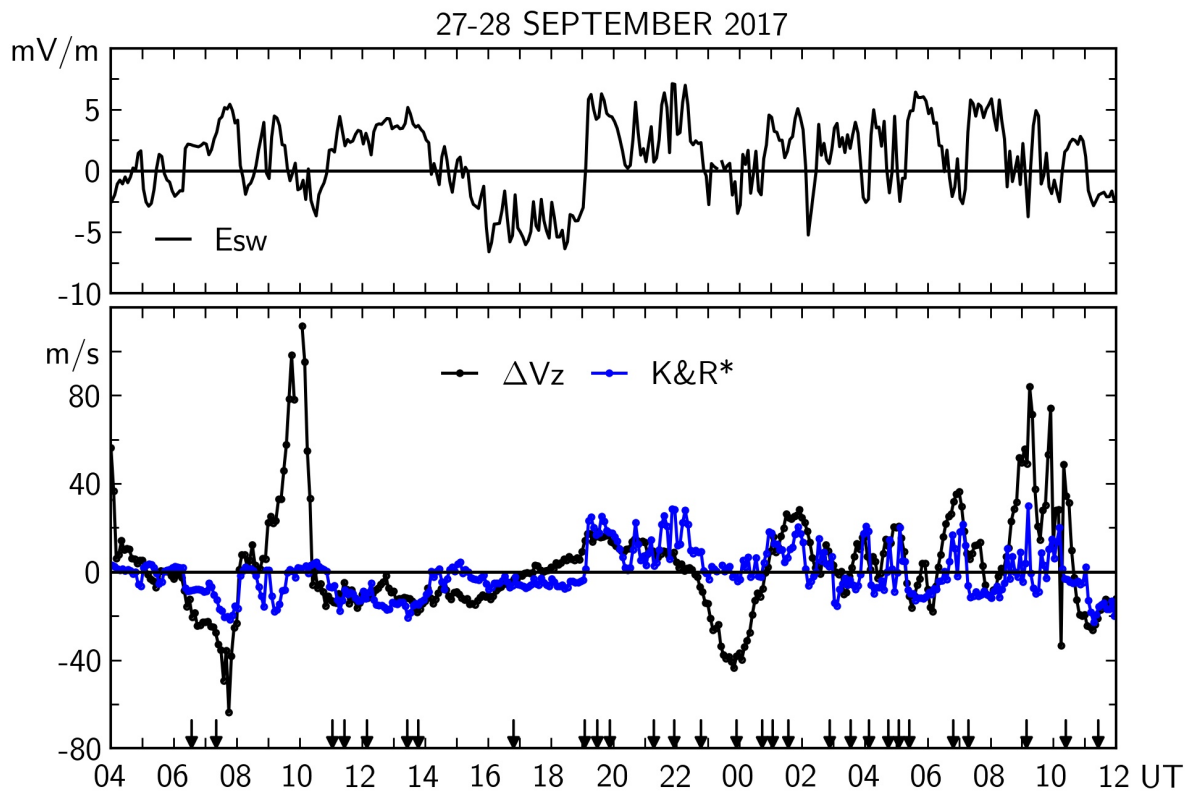
FIGURE 4.29 – (Top panel) Solar wind east-west electric field. (Bottom panel) Vertical disturbance drifts and their predictions from the K-R model using a different proportional factor (K&R*). The small arrows indicate substorm onset times.

be completely ruled out, which was observed in other studies (FEJER; JENSEN; SU, 2008a; HUANG; CHEN, 2008; HUANG; FOSTER; KELLEY, 2005), given that disturbance dynamo generates a downward plasma drift in the evening equatorial region. In more details, auroral electrojet recovery, which occurs when the IMF Bz turns northward or even when it is southward but decreasing, that is, when shielding electric fields dominate (see Section 2.3.3), can produce a strong westward electric field. This can completely suppress the PRE or even cause a significant downward movement of plasma. As a result, this stabilizes the F layer, which would typically be unstable under normal PRE conditions, suppressing the spread F. Since the K-R model do not show a downward drift at ~0000 UT, the direct use of the ratio of the interplanetary electric field to the equatorial zonal electric field is clearly not complete to describe the penetration effect.

Figure 4.30 shows in the top panel the WDC-Kyoto AE and the SME indices for the 27-28 September 2017 geomagnetic storm. The bottom panel presents the Jicamarca perturbation drifts and the corresponding disturbance dynamo vertical drifts predicted by the Fejer and Scherliess (1997a) model. For this moderate storm, the SME index is very similar to the AE index, except for a few periods where the SME is evidently larger than the AE. Due to this, the F-S prediction using the SME is larger than the AE prediction,

for example, in the period between 0700 UT and 1000 UT on the 28th, considering that several hours have passed since the onset of the storm. Hence, Figure 4.30 shows that the residual drifts during this period are indeed mostly accounted for by disturbance dynamo electric fields, even though, as shown in Figure 4.29, these drifts might also have an influence from prompt penetration. In contrast, the residual drifts from 0800 UT to 1000 UT on the 27th are only partially predicted by the F-S model, meaning that not all the expected disturbance dynamo drifts are predicted in this period.
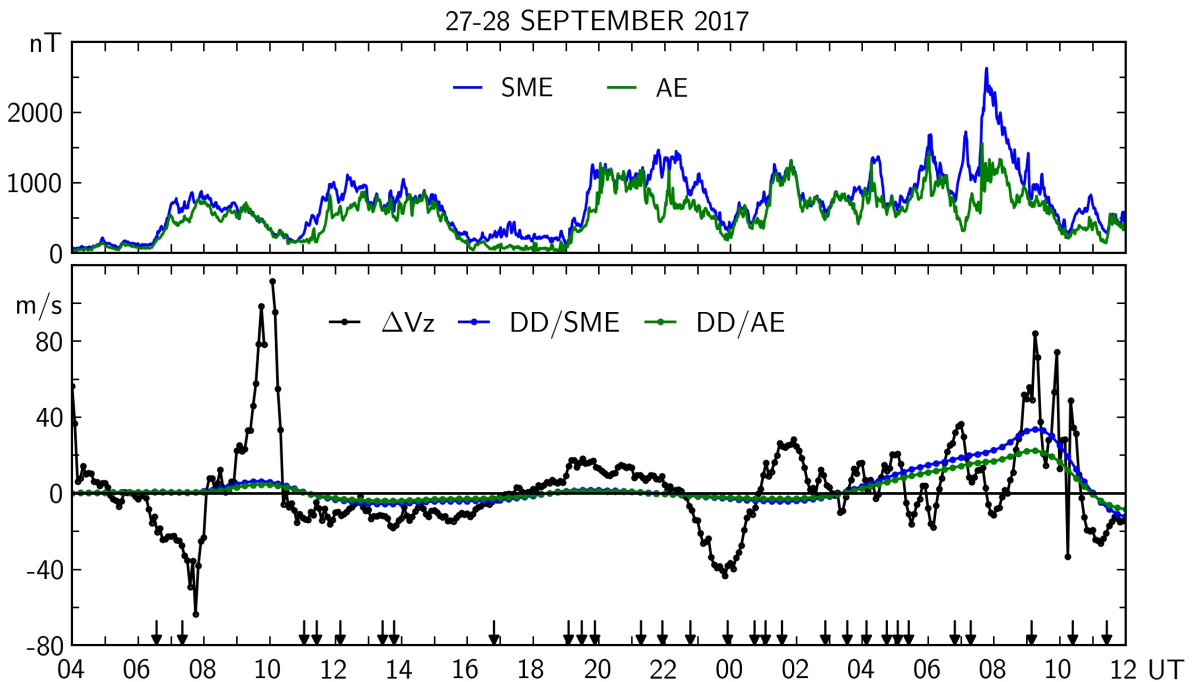
FIGURE 4.30 – (Top panel) Auroral AE and SME electrojet indices. (Bottom panel) Vertical disturbance drifts and corresponding predictions from the Scherliess-Fejer model using AE and SME indices as input parameters. The small arrows indicate substorm onset times.

The observed drift perturbations of the 27-28 September 2017 storm are overall consistent with prompt penetration driven undershielding and overshielding effects, substorms and disturbance dynamo electric fields. The drifts in the postmidnight sector and early morning at Jicamarca can be mostly accounted for by disturbance dynamo electric fields, whereas the premidnight drifts can be largely associated with prompt penetration electric fields. In both periods, substorms induced strong drift perturbations. The drifts during the day and afternoon were not strongly affected by prompt penetration, even though the IMF Bz was fluctuating between northward and southward, so that some disturbance would be expected. As mentioned earlier, the penetration efficiency is higher for later local time periods, as was also shown here. Additionally, an interesting feature during the IMF Bz fluctuation was the PRE suppression, noted by a strong downward drift (∼-45 m/s) at sunset, generated by

overshielding electric fields. Hence, as was the case for the 23-24 April 2023 storm, in addition to prompt penetration electric fields driven by IMF Bz southward turning, the residual drifts were also affected by overshielding electric fields, substorms and disturbance dynamo electric fields.

4.5.3   07-08 September 2017

In this section, we investigate the equatorial ionosphere F-region response over Peru during the 07-08 September 2017 severe storm first and second main phases. The study utilizes data from the Jicamarca ISR, focusing on vertical drift and spread F measurements. Additionally, low and high latitude ionospheric parameters and indices related to solar wind/magnetospheric activity complement the analysis.

Measurement Techniques and Data

We used Jicamarca incoherent scatter radar measurements from 16 LT (21 UT) on September 7, 2017 to 15 LT (20 UT) September 8, 2017. Again, we also use 1-min SuperMAG ground-based magnetic field, WDC, 1-min Kyoto AE index, and 5-min ACE satellite solar wind measurements during this storm.

In the present study, we used 5-min vertical averaged from 200 km to 945 km. We extended the altitudinal range in this case because the drift velocity data at lower altitudes showed a significant presence of spread F occurrences. These velocities contain spread F measurements. Once again, it is important to mention that ambient plasma drifts cannot be reliably obtained in strong spread F regions. For this storm, the standard deviations of our height averaged drifts are ∼5 m/s during the day and ∼15 m/s during the night for the vertical component. We deleted height-averaged drifts with standard deviations larger than 40 m/s. We did not use the zonal drift component because the errors were too large.

Results

The 07-08 September 2017 large geomagnetic storm started at ∼2345 UT on the 6th with the arrival of the first of two interplanetary coronal mass ejections (ICMEs) and ended at ∼1900 UT on the 8th. The storm first main phase lasted from 2130 UT on the 7th to ∼0200 UT on the 8th. The first main phase was significantly strengthened by the arrival of the second ICME at ∼2300 UT. The second main phase started at 1136 UT on 8 September and ended at ∼1900 UT on this same day. Figure 4.31 shows solar wind parameters from ACE and geomagnetic indices from SuperMAG during the 07-08 September 2017 encompassing the storm first and second main phases. In the storm first main phase, the SMR ring current index reached a minimum of -154 nT at 0125 UT and

the SMU/SML indices had large variations. In the second main phase, the SMR had a minimum of -161 nT at 1400 UT with very strong auroral current indices. The Kp index reached values of 8 and 8+ during the first and second storm main phases, respectively.
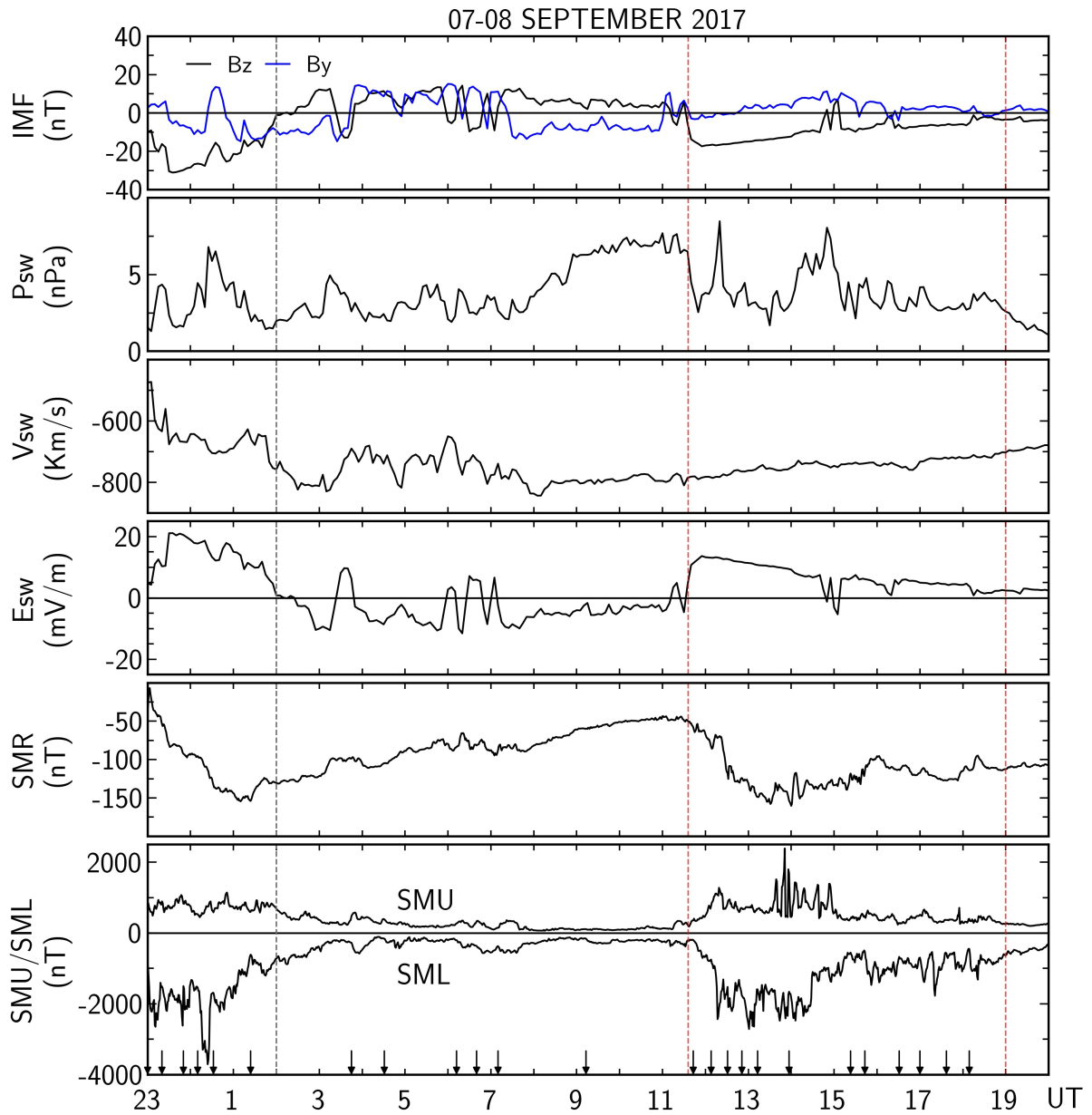
FIGURE 4.31 – (From top to bottom) IMF Bz/By, solar wind dynamic pressure, solar wind speed, solar wind east-west electric field, SuperMAG ring current (SMR), auroral current (SMU/SML) indices, and substorm onset times (small arrows in the bottom panel) during the 07-08 September 2017 geomagnetic storm. The vertical dashed gray line marks the end of the storm main phase, whereas the red lines delimit the storm second main phase.

As shown in Figure 4.31, following the first main phase onset, the initially large southward IMF Bz and large solar wind eastward electric field gradually decreased and reversed signal at the end of the storm first main phase marked by the vertical dashed

gray line in this Figure. In the storm second main phase (vertical dashed red lines in Figure 4.31), the IMF Bz was initially largely southward and then gradually decreased with a few peaks. The IMF By presented several fluctuations with generally small values up to the start of the storm second main phase (first vertical dashed red line), when this parameter became steadily positive as a sign of its recovery. The solar wind speed was very large in the storm first phase, and combined with the strong southward Bz, it shows that the solar wind and magnetosphere are strongly connected (e.g., NEWELL *et al.*, 2008). The dynamic pressure presented brief changes throughout the storm first and second main phases, especially during ∼24-01 UT on the 7th, ∼1220 UT, and ∼14-15 UT on the 8th. Figure 4.31 shows numerous fast recurring (quasi-periods of ∼30 min) substorms from about the start up to the end of the storm first and second main phases. In the recovery phase, after ∼1430 UT, the recurrence times increased to ∼60 min up to ∼19 UT.

To show the parameters in more details, we separated the figures of the 07-08 September 2017 geomagnetic storm, except for Figure 4.38, into the first and second main phases. Figure 4.32 presents in the three top panels the ACE interplanetary electric field and the SuperMAG ring current and auroral geomagnetic indices with substorm onset times, whereas the fourth panel shows the height-averaged Jicamarca vertical plasma drift with their standard deviations superposed on the corresponding quiet-time drift patterns from 2300 UT to 1000 UT, which encompasses the storm first main phase.

Figure 4.32 illustrates a rapid increase in the Jicamarca upward drifts from around 2330 UT to 0000 UT (1830-1900 LT), following the increase in the interplanetary electric field. Between approximately 0000 UT and 0020 UT, the IMF Bz shown in Figure 4.31 showed a negative peak that was associated with large changes in the SMU/SML indices. The IMF By also changed signs sharply. From about 0020 UT to 0200 UT, the solar wind zonal electric field decreased slowly, with faster decreases around 0115 UT and 0145 UT. Equatorial electrodynamic perturbations generally matched expectations of southward Bz-driven undershielding eastward electric fields, albeit sometimes with markedly different magnitudes. For example, around 0100-0200 UT, the Jicamarca data indicated eastward electric field perturbations of about 2 mV/m. The IMF Bz northward turn at 0200 UT initially resulted in a decrease in the vertical drifts at the equator, as the interplanetary electric field approached values close to zero before continuing to decrease. After this, eastward overshielding electric fields were observed at Jicamarca, since the drifts increased again. However, the drifts magnitudes are significantly different from those expected from prompt penetration effects. Figure 4.32 indicates that the Jicamarca drifts had, in general, large values up to ∼0200-0300 UT. Moreover, Fejer *et al.* (2021) mentioned that the 0000-0200 UT large downward drifts are due to substorm effects. We also suggest that in our
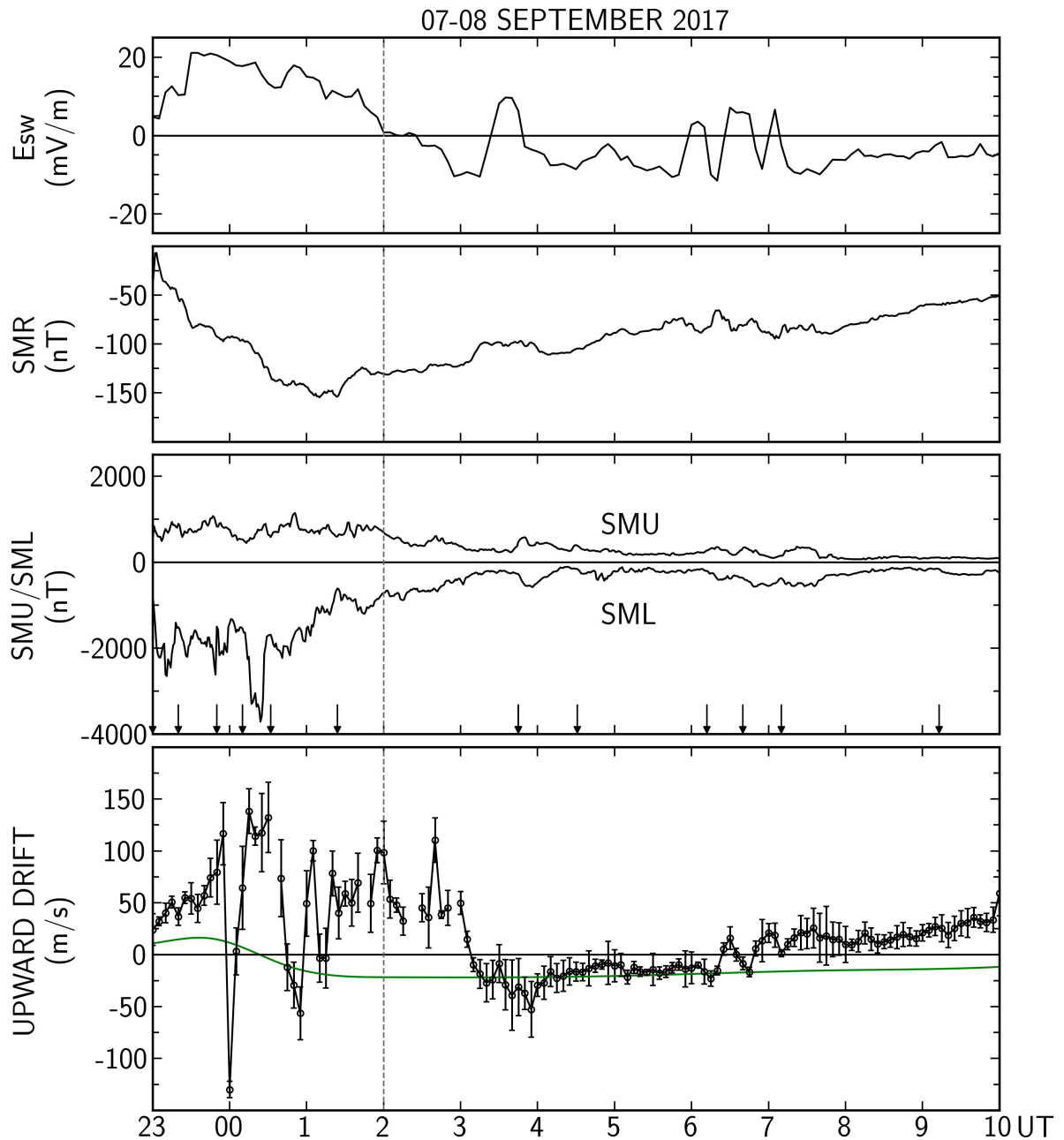
FIGURE 4.32 – (Top three panels) Solar wind motional east-west electric field, SuperMAG ring current (SMR), auroral current (SMU/SML) indices, and substorm onset times (small arrows). (Bottom panel) Height-averaged Jicamarca vertical plasma drifts. The green curve denotes the quiet time vertical drift pattern. The vertical dashed gray line marks the end of the storm main phase.

2024 study (FEJER; LARANJA; CONDOR, 2024).

The transition from undershielding to overshielding conditions at Jicamarca typically occurs around 0200-0300 UT (2100-2200 LT) (FEJER; SCHERLIESS, 1997a; FEJER; JENSEN; SU, 2008a; SAZYKIN, 2000), as is seen in Figure 4.32. After approximately 0600 UT, Figure 4.32 indicates smaller eastward and westward electric field perturbations in the postmidnight and daytime sectors, respectively, consistent with disturbance dynamo

vertical drift and electrojet current effects (FEJER; SCHERLIESS, 1997a).

Rout *et al.* (2019) noted that prior to the shock-driven second ICME at around 2300 UT, the IMF Bz had already turned southward. This event triggered a substantial substorm-like variation in the SML index, reaching approximately -2500 nT. They concluded that before 0000 UT on the 8th, strong substorm-induced eastward electric fields were present, alongside storm-time prompt penetration undershielding electric fields. Subsequently, they showed that substorms can significantly increase prereversal enhancement drift velocities even during periods of modest geomagnetic activity and small interplanetary electric fields. Determining the relative contributions of substorm electric fields to disturbance vertical drifts near dusk during large geomagnetic storms remains challenging due to the higher penetration efficiency of interplanetary electric fields near sunset compared to daytime (FEJER *et al.*, 2021).

Figure 4.33 shows the same parameters of Figure 4.32, but encompassing the storm second main phase, from 1000 UT to 2000 UT. Figure 4.33 reveals that, aside from brief periods immediately after the onset of the storm second main phase and near rapid changes in IMF Bz (for example, around 1500 UT, 1620 UT, and 1815 UT), the equatorial vertical drifts did not follow the interplanetary electric fields as would typically be anticipated (FEJER; NAVARRO, 2022). The large upward drifts from 1000 UT to ∼1040 UT occurred during a period of small northward IMF Bz. Hence, overshielding electric fields could not have caused the entire velocity increase. We speculate that the significant dynamic pressure change around this time may account for it.

In Figure 4.33, the vertical drifts started to fluctuate rapidly (with time scales of about 30 min) around the onset of the first substorm at ∼1140 UT, lasting until ∼1400 UT, with brief perturbations coinciding with rapid changes in IMF Bz (as shown in Figure 4.31). During this period, all SuperMAG-identified substorms were associated with short-lived prompt penetration events, characterized by upward drift perturbations during substorm expansion phases. Furthermore, the short-lived vertical drift perturbations shown during ∼1400-1500 UT could have been due to substorms not identified by SuperMAG. In reality, since the second phase was significantly influenced by substorms, this was the reason we chose to separate the two phases, so that the effect of the substorms could be better appreciated.

Two significant events generated westward electric fields at Jicamarca. They are evident around 1230-1400 UT and 1500-1530 UT in Figure 4.33, with the former coinciding with the onset of a substorm likely triggered by a sudden change in solar wind dynamic pressure (see Figure 4.31). The latter, an overshielding event, was driven by abrupt northward shifts in IMF Bz and dynamic pressure transients, and ended with a substorm onset. After ∼1500 UT (1000 LT), nearly hourly recurring substorm onsets were observed by SuperMAG, accompanied by prompt penetration vertical drift
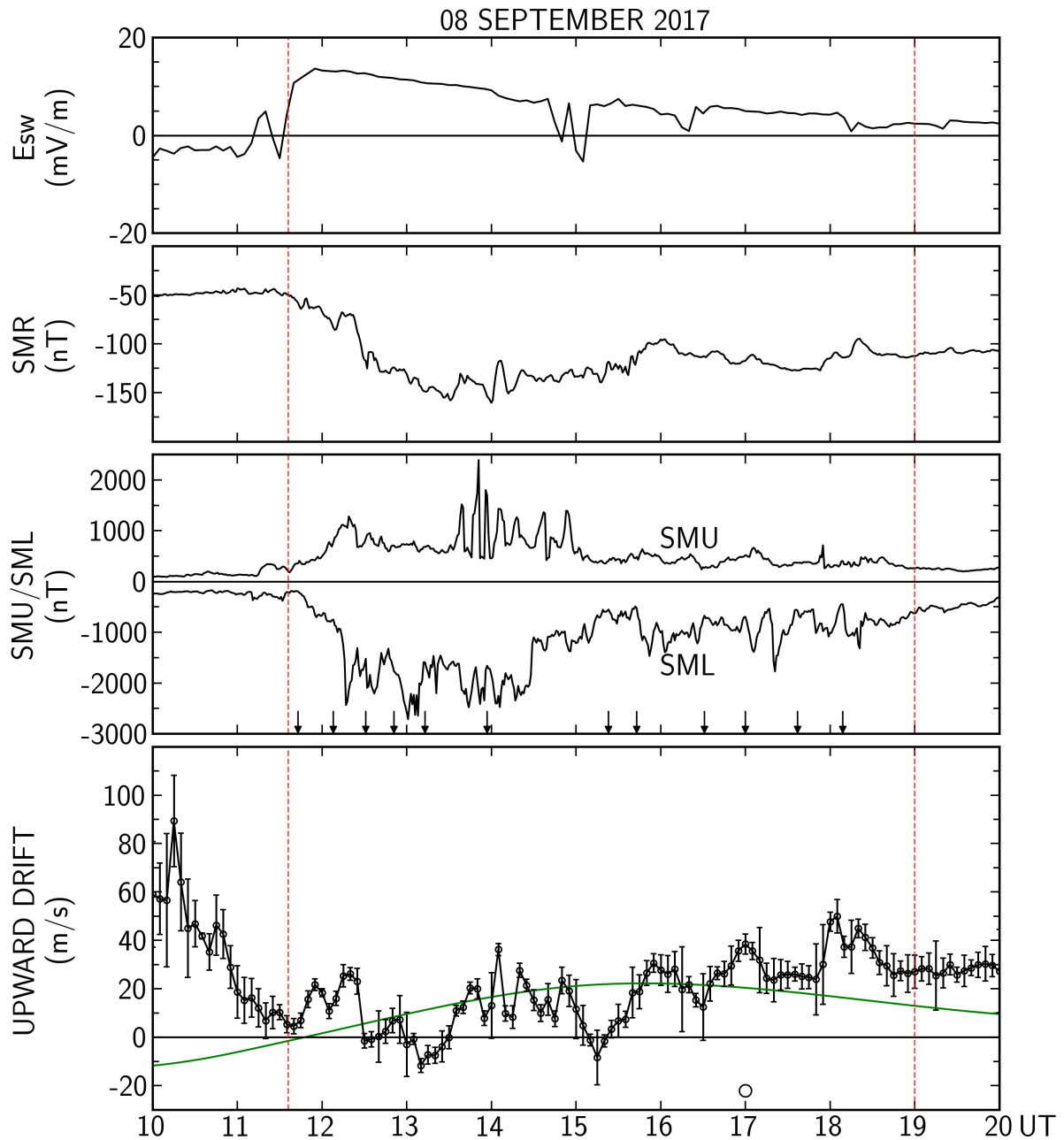
FIGURE 4.33 – Same as Figure 4.32, but for the storm second main phase.

perturbations of 20 m/s. Additionally, the drift measurements indicate approximately 30-min substorm-like drift perturbations similar to those seen during the storm main phase.

Figure 4.34 shows from top to bottom the solar wind electric field, auroral electrojet indices with substorm onset times, Jicamarca vertical drifts, and backscattered power from equatorial spread F plasma irregularities from 1800 LT to 0500 LT (2300 UT to 1000 UT). This Figure indicates that there were no irregularities in the plasma before approximately 1830 LT. However, after ~1840 LT, irregularities in the valley region (HYSELL et al., 1990), appeared. Fejer et al. (2021) discussed that these irregularities were created in
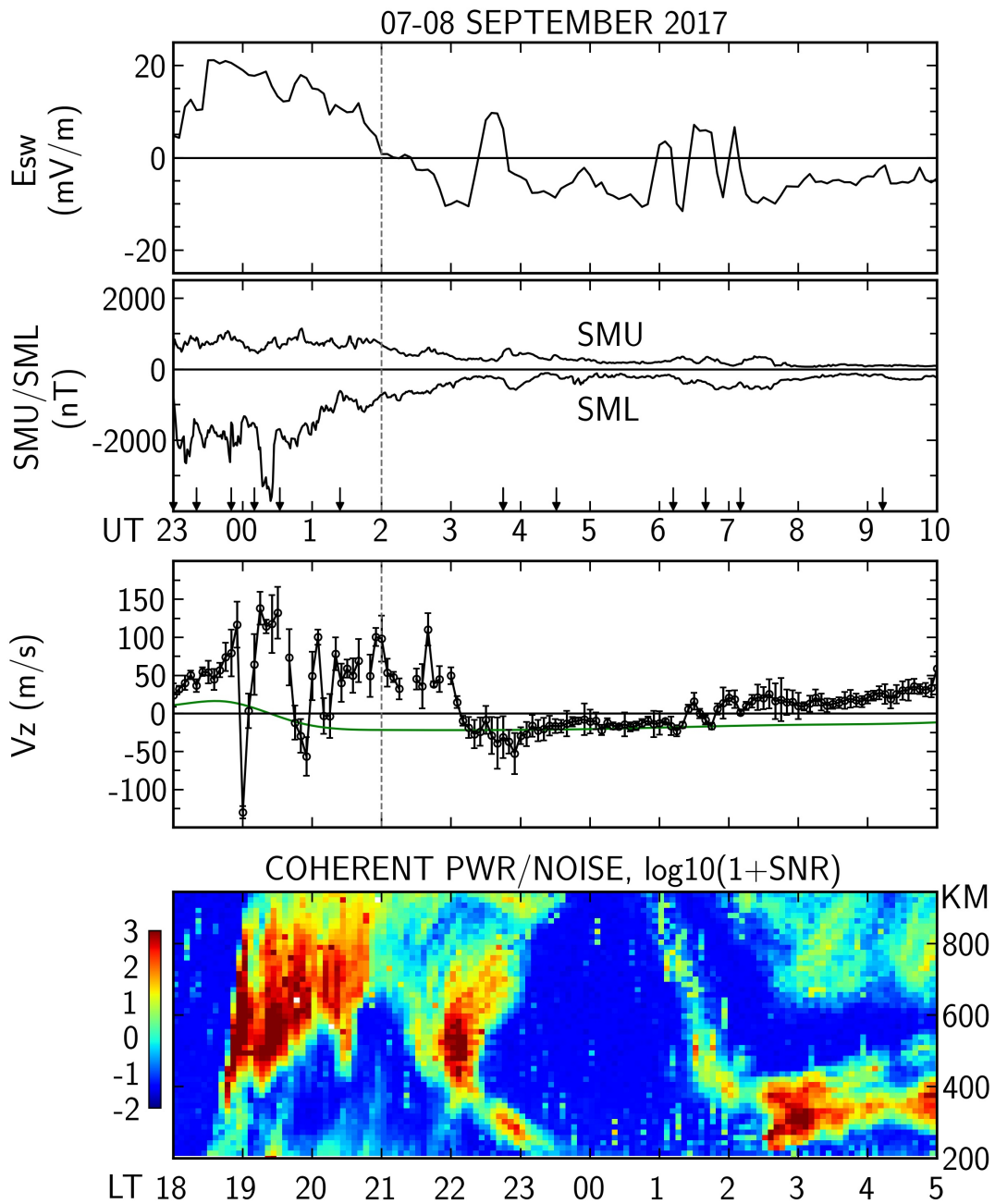
FIGURE 4.34 – (Top two panels) Solar wind east-west electric field, auroral current (SMU/SML) indices, and substorm onset times (small arrows). (Third panel) Height-averaged Jicamarca vertical plasma drifts and their quiet-time values (green curve). (Fourth panel) Coherent backscattered power from 3-m plasma density irregularities. The vertical dashed gray line marks the end of the storm main phase.

the E region due to intense electric fields during the storm-time condition and migrated upwards at the same velocity as the surrounding plasma. As the vertical drifts increased, the altitudinal range of strong spread F echoes also expanded.

Figure 4.34 displays a significant and rapid increase in upward drifts at ∼1830-1900 LT (2330-0000 UT), resulting in the quick rise of spread F irregularities. This was then

followed by a brief but intense decrease in plasma irregularities below approximately 400 km and a notable reduction in the strength of backscattered power from the spread F irregularities at higher altitudes, indicating a large downward drift (westward electric field) disturbance. This is in accordance with the ∼-130 m/s downward drift at 0000 UT (1900 LT). Figure 4.34 also shows considerable upward drifts with occasional, strong, very brief downward drift disturbances between 2000 LT and 2200 LT. Intense spread F echoes and significant vertical drift disturbances were observed until around 2230 LT when the drifts changed direction, leading to a short period with minimal spread F activity. This was succeeded by a phase of generally minor upward drifts and increased spread F activity, lasting until approximately sunrise.

Figure 4.35 shows again the same parameters presented in Figure 4.34, but this time encompassing the storm second main phase. The most noticeable feature in this figure is the strong spread F extending up to 700 km generated by the large upward drift at ∼1020 UT (0520 LT). The irregularities are observed until ∼1100 UT (0600 LT) and then suddenly decease due to the drifts decrease to about 15 m/s. At approximately 0720 LT (1220 UT) there is a small spread F over Jicamarca driven by substorm upward drifts. This irregularity abruptly vanished due to westward electric fields at ∼1230 UT, when it is already daytime in Peru.

Although the equatorial data during the 07-08 September 2017 event exhibited features consistent with standard prompt penetration electric fields, there were also unexplained results. Fejer *et al.* (2021) suggested that substorms possibly linked to large IMF By changes also played a significant role in the substantial equatorial vertical drift fluctuations near the storm's main phase. This will be discussed in more details in the next section.

Discussion

Figure 4.36 shows, in the top panel, the interplanetary electric field for the period illustrated in Figure 4.32. The bottom panel shows daytime and evening vertical drift perturbations obtained from Figure 4.32 by removing the corresponding quiet-time values, the prompt penetration drifts from the F-S model, the K-R model shifted by 17 min to account the propagation time from the front of the magnetopause to the equatorial ionosphere, and the M-M model. We extended the K-R model daytime prescription up to 03 UT (22 LT). Again, in addition to prompt penetration electric fields driven by IMF Bz southward turning, the residual drifts were also clearly affected by overshielding electric fields, dynamic pressure changes, substorms and disturbance dynamo electric fields.

For the 07-08 September 2017 storm first main phase, the Fejer-Scherliess model predicts very different prompt penetration vertical drifts compared to the residual drifts. This model only predicts the correct sign from 2300 UT to ∼0050 UT and 0700 UT to 0900 UT, although with very a different pattern from that of the residuals. Additionally,
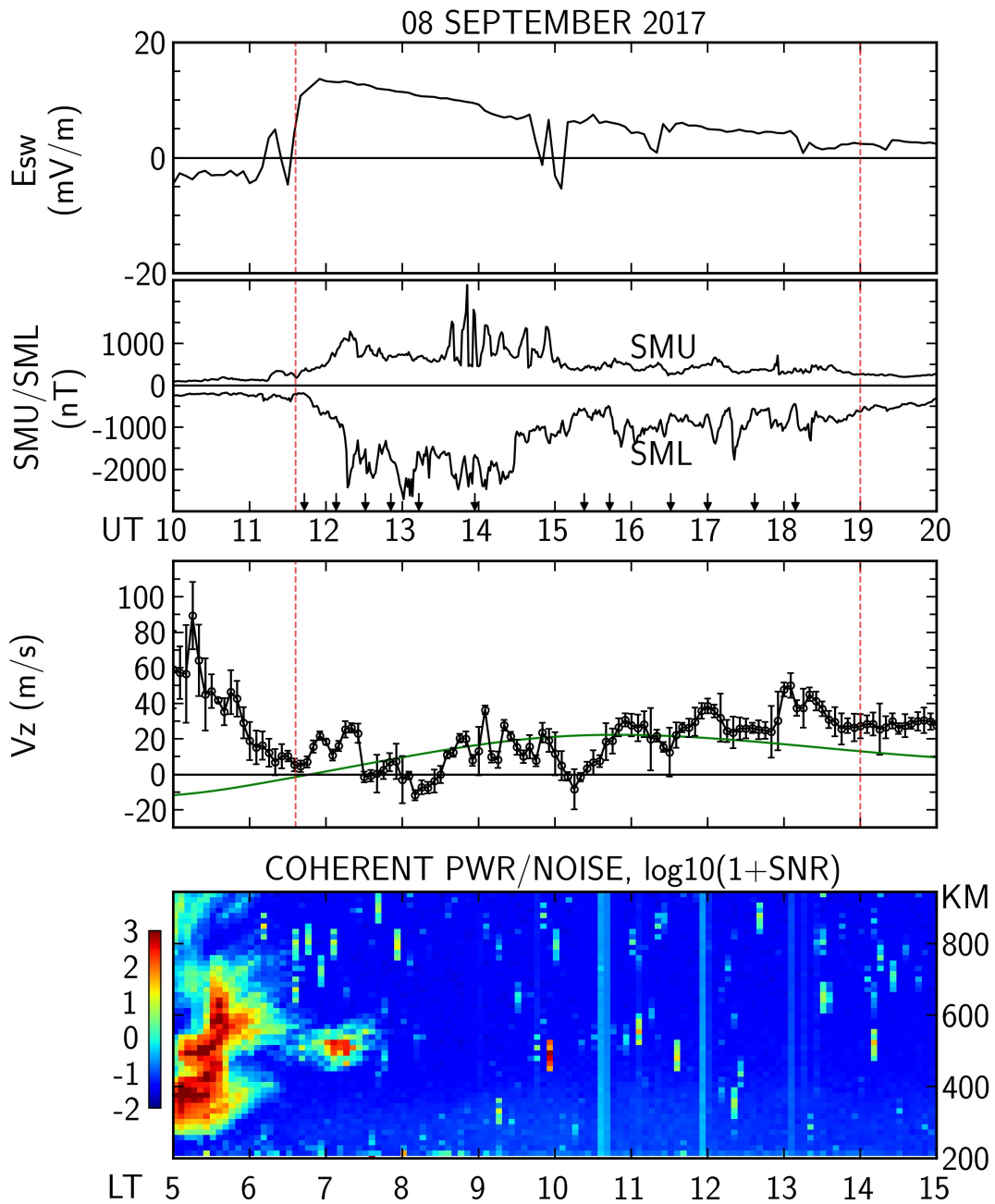
FIGURE 4.35 – Same as Figure 4.34, but for the storm second main phase.

Figure 4.36 indicates that the prediction of the K-R model agrees well with the residual drifts when these are generated by a southward IMF Bz, directly associated with the interplanetary electric field presented in the upper panel of this Figure. For example, from 2300 UT to ∼0120 UT, the K-R prescription is similar to the residual drifts, however, the effects of substorms is clear during this period and is also affecting the residual drifts. From ∼0200 UT to 0300 UT, the IMF Bz northward excursion generated eastward overshielding electric fields, perceived as upward drifts during this period. Hence, these drifts were not predicted by the K-R model. Again, the M-M model significantly underestimated the observed prompt penetration electric fields except from
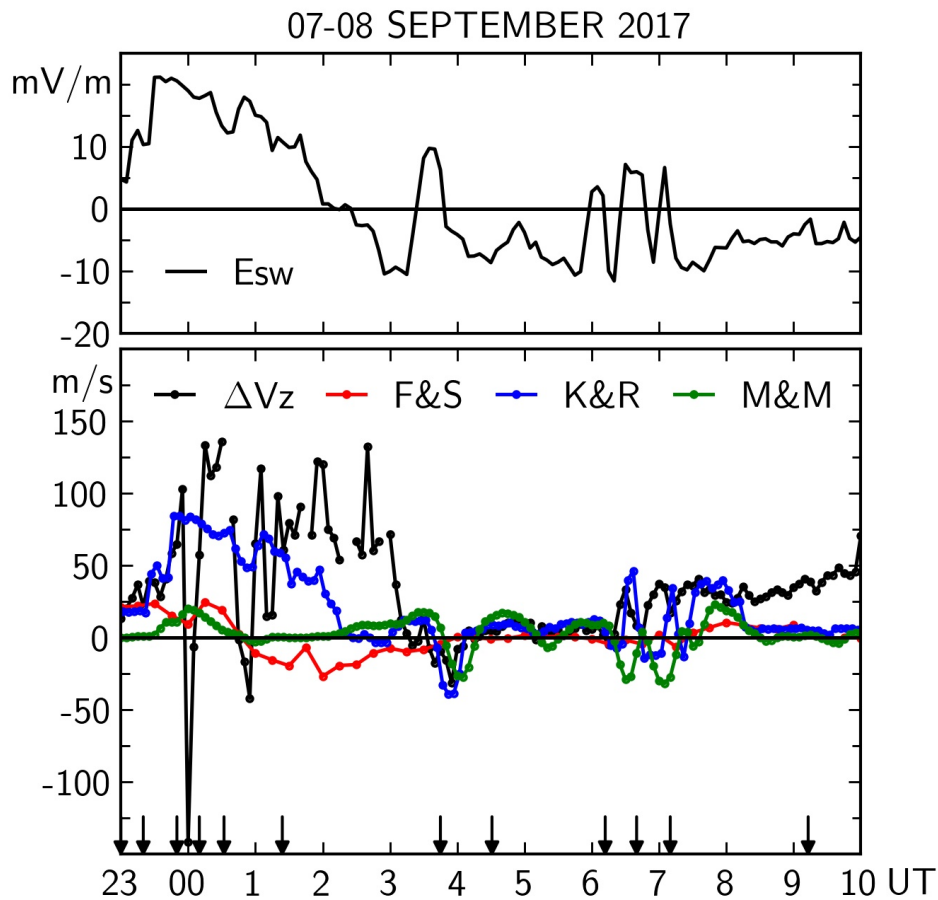
FIGURE 4.36 – (Top panel) Solar wind east-west electric field. (Bottom panel) Vertical disturbance drifts and their predictions from the F-S (F&S), M-M (M&M) and from the K-R (K&R) procedure. The small arrows indicate substorm onset times.

0350 UT to 0600 UT (2250-0100 LT).

Figure 4.37 shows the same parameters as Figure 4.36, but for the period 1000-2000 UT. We reversed the K-R drifts back to upward at 1200 UT because we expect the residual drifts to be upward at this time. The K-R drifts follow, in general, the residual drifts variations from 1500 UT to 2000 UT, but most of the time with different magnitudes and signs. From ∼1200 UT to 1700 UT, the S-F model had, in general, the same sign as the residual drifts, but with very different magnitudes. Hence, according to Figures 4.36 and 4.37, it is confirmed, again, that this model is generally not well suited for accurate modeling the prompt penetration equatorial drifts. As for the M-M prescription, it only agreed reasonably well with the residual drifts for 1500-1700 UT. Solar wind dynamic pressure increases were believed to drive, for the 1000-1100 UT period, a large increase in the early morning upward equatorial drifts. As for the period from 1200 UT to 2000 UT, substorms are suggested to have played a major role in the drifts minor fluctuations, since the interplanetary electric field was decreasing and nearly steady.

Figure 4.38 shows in the top panel the WDC-Kyoto AE and the SME indices for
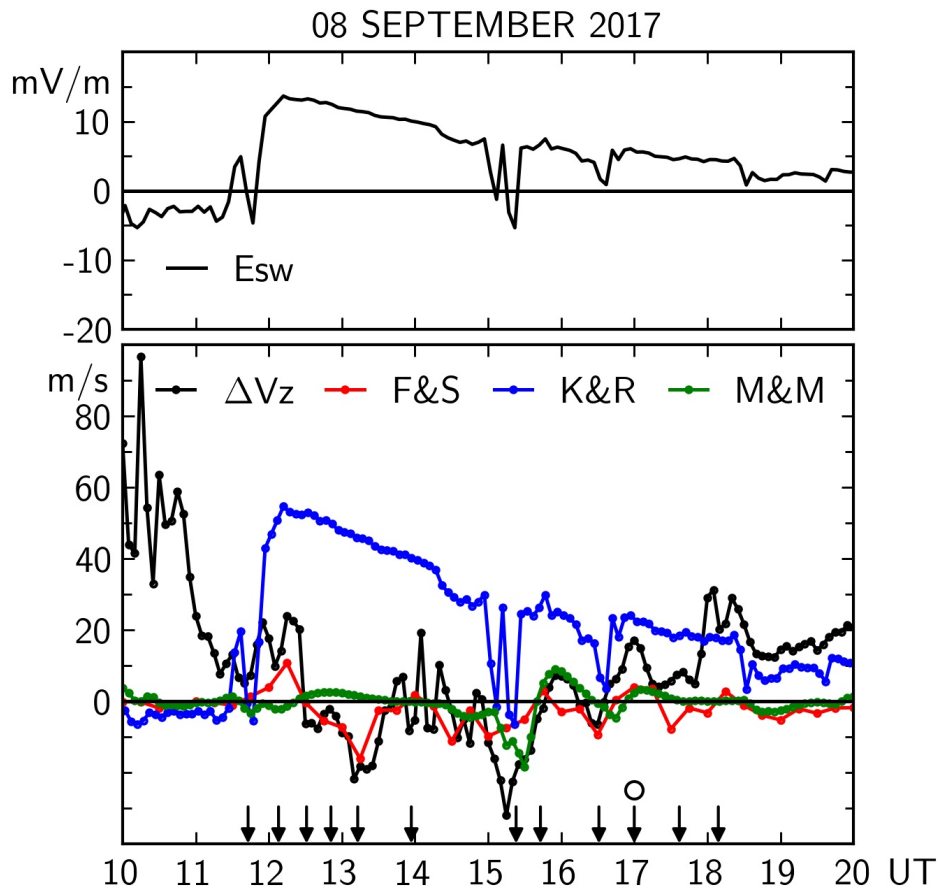
FIGURE 4.37 – Same as Figure 4.36, but from 1000 UT to 2000 UT.

the 07-08 September 2017 geomagnetic storm. The bottom panel presents the same period shown in Figure 4.31, encompassing the storm first and second main phases, of the Jicamarca perturbation drifts, and the corresponding disturbance dynamo vertical drifts predicted by the Fejer and Scherliess (1997a) model. For this large storm, the SME index is considerably larger than the AE index during the first and second main phases. As noted earlier, the SuperMAG SME is derived from ∼300 ground magnetometers, compared to ∼13 observatories used to derive the AE index. Nevertheless, due to the 15-min averages of these indices for the F-S model input, the difference between the blue (SME) and green (AE) curves in the lower panel of Figure 4.38 is small. This Figure shows that the F-S model predicts reasonably well the drifts during 0600-1000 UT (0100-0600 LT).

The observed drift perturbations of the 07-08 September 2017 storm are overall consistent with strong prompt penetration driven undershielding and overshielding effects and substorms. Substorms played an important role on the very large eastward electric fields over Jicamarca before ∼0000 UT on the 8th and up to ∼0300 UT on this same day. Additionally, the radar data reveal a few extra substorm-like drift signatures, with daytime prompt penetration electric fields exhibiting eastward (westward) orientation during substorm expansion (recovery) phases. Following a substorm onset
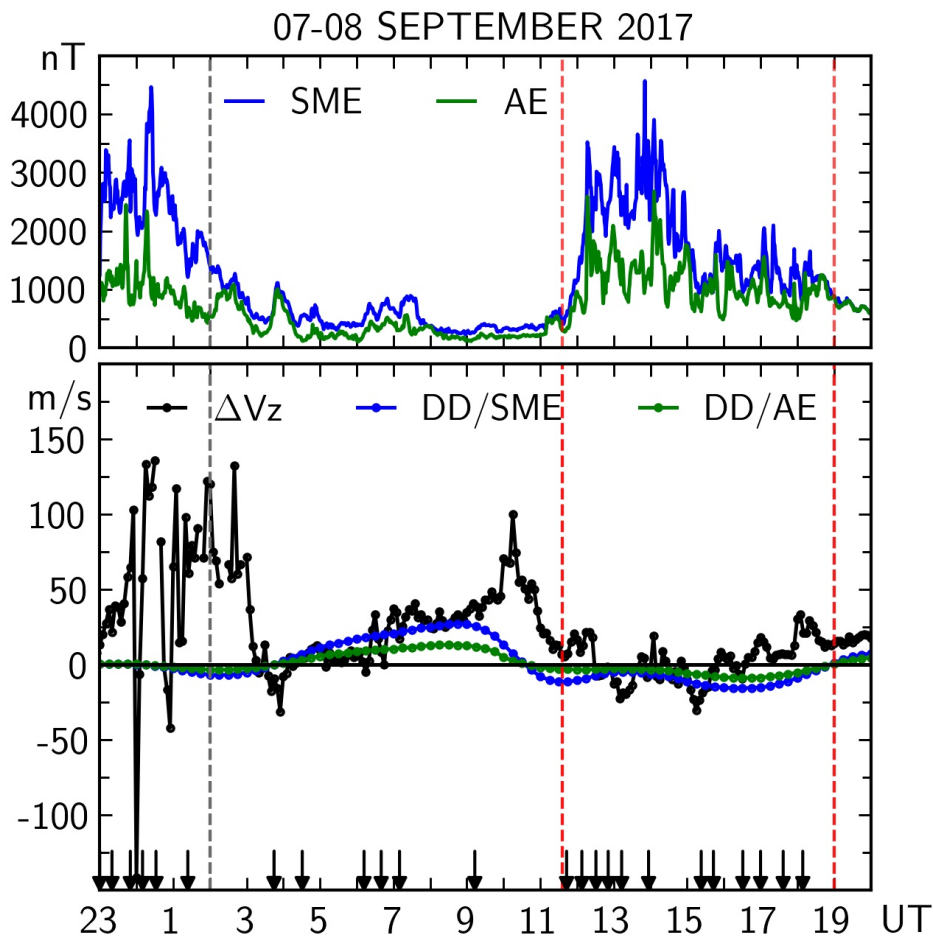
FIGURE 4.38 – (Top panel) Auroral AE and SME electrojet indices. (Bottom panel) Vertical disturbance drifts and corresponding predictions from the Scherliess-Fejer model using AE and SME indices as input parameters. The small arrows indicate substorm onset times.

likely linked to a significant change in solar wind dynamic pressure at 0000 UT on the 8th, a notable overshielding event occurred, possibly due to increased Region 2 field-aligned currents (FEJER; NAVARRO, 2022). Fejer and Navarro (2022) suggested that recurrence rates during this geomagnetic storm were much faster than typically reported in substorm studies.

As noted in the Figures shown in this section, the 07-08 September 2017 large geomagnetic storm is associated with very large early night equatorial vertical drift fluctuations during a period of strong southward IMF Bz (Figures 4.33 and 4.35). Fejer and Navarro (2022) suggested that these prompt penetration drifts were caused by strong substorm activity and rapid dipolarization of magnetotail field lines during IMF By recovery. To understand the overall effect of magnetic reconfiguration or dipolarization, consider a simplified two-step process. First, a rapid magnetic reconfiguration occurs with an induction electric field but no potential electric field.

This weakens the dawn-to-dusk cross-tail current, making the shielding-layer field lines near the inner edge of the plasma sheet more dipolar. As a result, the equatorial mapping point of a field line from a specific ionospheric location shifts earthward, driven by an $\mathbf{E} \times \mathbf{B}$ drift in the induction field, affecting only the magnetospheric end of the field line (FEJER *et al.*, 1990b). In contrast to the 07-08 September 2017 nighttime substorm event, however, the very large vertical drift perturbations in the early night of 23 April 2023 were associated with steadily increasing westward IMF By instead of its recovery. Although the relationship between IMF By and the subsequent late upward equatorial drift reversal remains unclear, it is evident that a strong southward IMF Bz is necessary. We note that the amplitudes of the nighttime prompt penetration vertical drifts associated with the 07-08 September 2017 and 23-24 April 2023 substorms were much larger than those associated with daytime magnetospheric substorms measured under similar geophysical conditions, under such large southward IMF Bz. This suggests that magnetospheric storm-time substorms drive larger equatorial prompt penetration electric field in the premidnight sector than during daytime.

4.5.4   09-10 November 2004

We now proceed to investigate the very intense 09-10 November 2004 geomagnetic storm. The November 2004 storm was actually defined as two major storms, one on 07-08 and the other on 09-10. Since Jicamarca ISR data is only available for the second storm, we will focus on the 09-10 November 2004 electrodynamics. We use again ISR Jicamarca data for the vertical drift and spread F measurements along with interplanetary parameters and geomagnetic indices. The 09-10 November 2004 geomagnetic storm was extensively studied previously (e.g., FEJER *et al.*, 2007; HAUNG; ZHANG, 2021; KELLER; RETTERER, 2008), but has not been compared in detail with several empirical models.

Measurement Techniques and Data

From November 7th to 12th, 2004, solar activity was on the decline, marked by a daily F10.7 index of approximately 130 sfu. During this period, two severe geomagnetic storms occurred. Specifically, we will delve into the second storm, occurring between November 9th and 10th, as this is the timeframe for which Jicamarca ISR vertical drift data is available. The time period studied here is from 1200 UT (0700 LT) on November 09, 2004 to 1800 UT (1300 LT) November 10, 2004. We also used 1-min SuperMAG ground-based magnetic field, WDC, 1-min Kyoto AE index, and 5-min ACE satellite solar wind measurements.

We used 5-min vertical drifts averaged from 200 km to 945 km. For this storm, we excluded heights with large errors. These velocities contain spread F measurements. The

standard deviations of our height-averaged drifts are ∼3 m/s during the day and ∼10 m/s during the night for the vertical component, and ∼40 m/s during the day and ∼40 m/s at night for the zonal. Hence, we did not use the zonal drifts due to their large errors.

Results

Figure 4.39 shows interplanetary parameters and geomagnetic indices during the magnetic storm on November 09-10, 2004. Just for context, the first super storm was initiated by a CME during 07-08 November, with storm sudden commencement (SSC) at 0257 UT and storm main phase (first main phase) onset at ∼2130 UT on 07 November. The SMR index reached -368 nT and Kp reached 9 during this storm first main phase. While the storm was recovering, the next CME during 09-12 November reintensified the storm, with second main phase onset at ∼1200 UT on 09 November, with SMR reaching ∼-280 nT and Kp reaching 9 during the storm second main phase, shown in Figure 4.39.

Figure 4.39 illustrates a surge in solar wind speed that occurred concurrently with an increase in solar wind dynamic pressure around 1800 UT on the 9th. During this period, there were significant fluctuations in solar wind dynamic pressure, accompanied by substantial IMF Bz and IMF By values. The IMF Bz was southward and small up to ∼18 UT, when it increased to approximately -30 nT until ∼21 UT. After this time, the IMF Bz was strongly northward until ∼02 UT. In the period between 0130 UT and 1200 UT on November 10 the IMF Bz was recovering, but it was still southward, inducing continuous prompt penetration electric fields for ∼10 hours, as will be shown later. The IMF By was positive and negative with small magnitudes until 1800 UT, when it became positive with magnitude up to 20 nT between 1800 UT and 2100 UT. It then presented eastward and westward excursions until ∼2300 UT, when it increased to -40 nT and started to recover at ∼0400 UT.

Figure 4.39 shows that the interplanetary electric field had large positive values between 1800 UT and 2100 UT, and then large negative values between 2100 UT and 0100 UT, when it started to recover. The SMR index reached its minimum value of about -280 nT at 2104 UT on the 9th and at 0932 UT on the 10th. Moderately active conditions persisted between these highly disturbed periods. SMU and SML indices were very variable, with numerous fast recurring (∼30 min) substorms during the whole storm-time period. The recovery phase os this major storm lasted at least until the end of the Jicamarca measurements (November 13, 2004).

Figure 4.40 presents in the three top panels the ACE interplanetary electric field and the SuperMAG ring current and auroral geomagnetic indices with substorm onset times, whereas the fourth panel show the height averaged Jicamarca vertical plasma drift with their standard deviations superposed on the corresponding quiet-time drift patterns from 1200 UT on November 09 to 1800 UT on November 10, which encompasses the storm
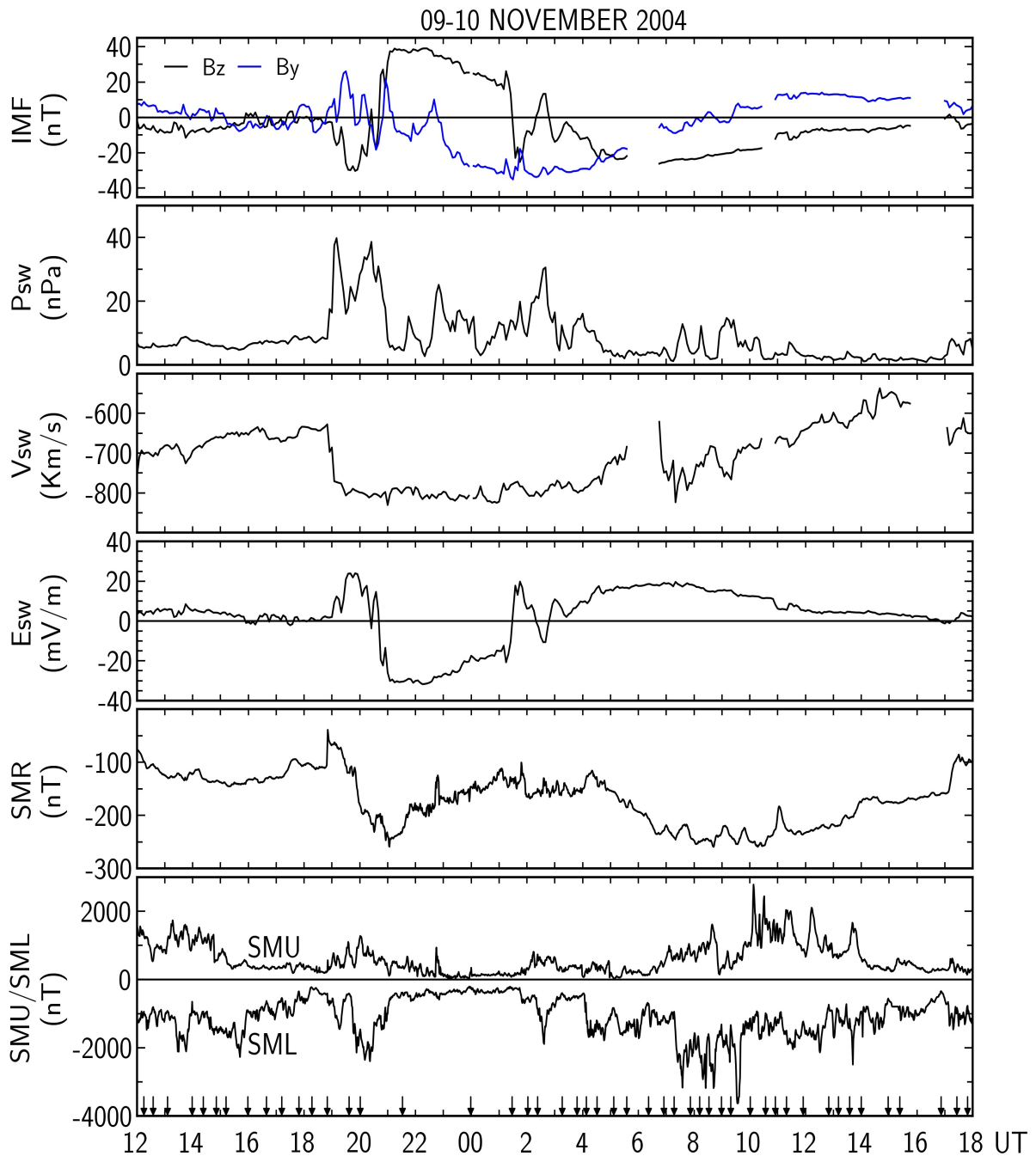
FIGURE 4.39 – (From top to bottom) IMF Bz/By, solar wind dynamic pressure, solar wind speed, solar wind east-west electric field, SuperMAG ring current (SMR), auroral current (SMU/SML) indices, and substorm onset times (small arrows in the bottom panel) during the 09-10 November 2004 geomagnetic storm.

second main phase. Initially, there was a rapid increase in the Jicamarca drifts to about 20 m/s, followed by a more gradual rise to about 40 m/s half an hour later. A substantial surge occurred around 1920 UT, with upward drifts reaching approximately 120 m/s by 2000 UT, indicating an eastward electric field of over 3 mV/m, the largest daytime value ever measured by the radar (FEJER *et al.*, 2007). Rapid changes in the interplanetary electric field around 2020 UT led to more gradual variations in the equatorial ionospheric

electric fields. Moreover, the ratio between prompt penetration electric fields and the solar wind exhibited marked changes during this storm's main phase, as shown in Figure 4.40.
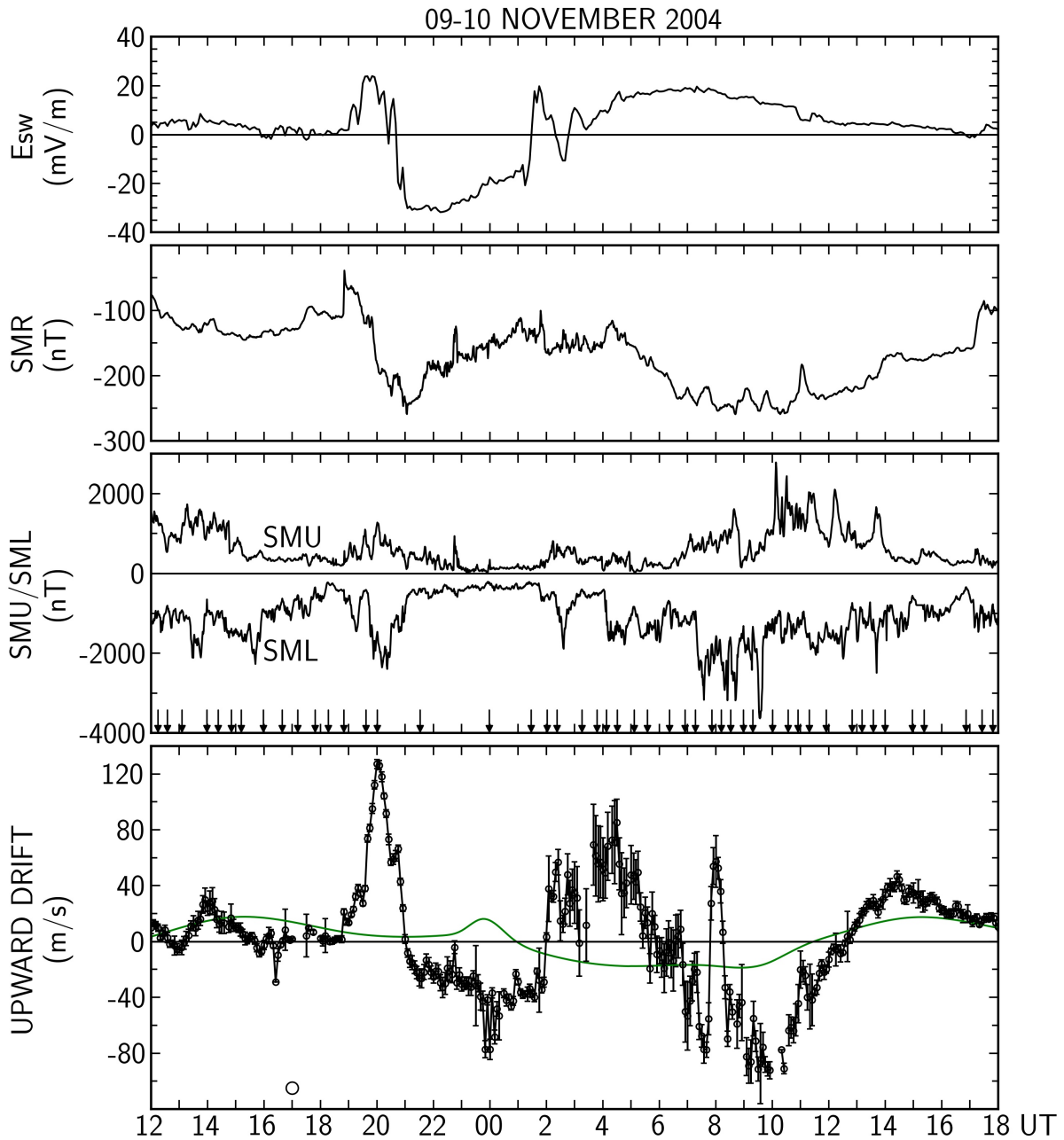
FIGURE 4.40 – (Top three panels) Solar wind motional east-west electric field, SuperMAG ring current (SMR), auroral current (SMU/SML) indices, and substorm onset times (small arrows). (Bottom panel) Height-averaged Jicamarca vertical plasma drifts. The green curve denotes the quiet time vertical drift pattern.

The upward ion drifts observed between 1900 UT and 2100 UT on November 9th and the subsequent downward ion drifts from 2100 UT on November 9th to around 0200 UT on November 10th were evidently linked to the positive interplanetary electric field (southward IMF Bz) and negative interplanetary electric field (northward IMF Bz),

respectively. The reversal of the vertical drifts coincided with reversals in the solar wind electric field/IMF Bz. During the period from 0200 UT to 1200 UT (2100-0700 LT), disturbance dynamo drifts are expected to consistently be upward (HUANG; ZHANG, 2021). Thus, since the observed vertical drifts changed from upward to downward around 0100 LT (0600 UT), it suggests that disturbance dynamo electric fields could only partially be responsible for the significant deviations of the vertical ion drifts from the quiet-time patterns during these intervals.

The equatorial electric fields decreased rapidly at about 2100 UT, following the sudden decrease of the interplanetary electric field and onset of the storm recovery phase. Figure 4.40 shows relatively large downward perturbation drifts from about 2100 UT to 0200 UT. Fejer *et al.* (2007) uses magnetometer data in the Pacific region during this same period to show that the corresponding magnetometer data generally followed the quiet time pattern. They suggest that this indicates that even though the initial decrease of the Jicamarca downward drifts was due to prompt penetration electric fields, the longer lasting downward drifts after about 2200 UT were mostly due to westward disturbance dynamo electric fields, since prompt penetration would have driven much larger decreases in dayside magnetometer measurements. In contrast, Huang and Zhang (2021) suggested that the direction of the downward vertical drifts from about 2100 UT to 0200 UT aligned with the drifts typically associated with shielding electric fields, since they occurred during continuous northward IMF Bz. Another mechanism during northward IMF involves polar electric fields associated with reverse convection, which can penetrate to equatorial latitudes, resulting in downward equatorial vertical drifts on the dayside and evening sector (HUANG, 2019). Both the shielding/overshielding process, the polar reverse convection, and disturbance dynamo electric fields can contribute to the observed downward vertical drifts during the 4.5-hour period of northward IMF. It is interesting to note that the westward interplanetary electric field from 2100 UT to 0200 UT may have suppressed the PRE, as suggested by Abdu *et al.* (2009).

Figure 4.40 illustrates significant electrodynamic disturbances occurring roughly between 0200 UT and 0700 UT. During this period, Jicamarca data primarily indicate upward perturbation drifts (eastward electric fields) generated by prompt penetration electric fields, except for brief and intense perturbations during rapid changes in the solar wind electric field. Additionally, Figure 4.40 displays large upward drift velocities followed by westward current perturbations between 0400 UT and 0700 UT, coinciding with a period of very substantial and nearly constant solar wind electric field. This suggests that the equatorial zonal electric fields were likely to be reversing its sign around this time. Furthermore, significant but short-lived velocity perturbations occurred over Jicamarca from about 0700 UT to 0900 UT (0200-0400 LT), reaching velocities as high as approximately 80 m/s. During this interval, the interplanetary

electric field remained large and constant, but notable fluctuations in the SML index were observed, indicating significant substorm-driven overshielding electric fields. Following 1200 UT on November 10th, the storm entered a recovery phase, albeit with minor fluctuations still discernible, in which the drifts started to be comparable to the quiet-time pattern (green curve).

Discussion

In this section, as was done for the other geomagnetic storms studied here, we evaluate to what extent the disturbance drifts of the November 2004 (obtained by removing the quiet-time component) storm second main phase can be explained by prompt penetration and disturbance dynamo drifts predicted by empirical vertical drift models. Figure 4.41 shows, from 1200 UT on November 09 to 1800 UT on November 10, the interplanetary electric field (upper panel) and vertical drift perturbations and the prompt penetration drifts from the F-S model, the K-R model shifted by 17 min to account the propagation time from the front of the magnetopause to the equatorial ionosphere, and the M-M model (lower panel). In the same manner as for the April 2023 storm, we extended the K-R model daytime prescription up to 0600 UT (0100 LT), to coincide with the measured vertical drifts. Additionally, we reversed the sign of the K-R drifts after 0600 UT (multiplied by -1), assuming that the penetration electric fields reversed around this time.

Figure 4.41 shows that, again, the F-S model predicts very different prompt penetration vertical drifts compared to the residuals. The sign of the drifts from this model are, in general, the same of the residual drifts until 0900 UT (0400 LT). The F-S model predicts, with a much lower amplitude, the upward drift from ∼0700 UT to 0900 UT, indicating that this peak was had an influence of the steady solar wind electric field, inducing prompt penetration drifts at lower latitudes. As mentioned above, this upward peak was also strongly influenced by substorm activity.

The prediction of the K-R model is the most accurate for the November 09-10, 2004 geomagnetic storm compared to the others studied here so far. Figure 4.41 indicates that the prediction of this model agrees very well with the residual drifts. The residual drifts in this case are, except for a few brief periods, directly associated with the interplanetary electric field presented in the upper panel of Figure 4.41. From 1200 UT to 1700 UT (0700-1200 LT) on November 09, the K-R prescription slightly overestimates the residual drifts. However, the residuals during this period have a very similar pattern of that of the K-R prediction, suggesting that a different proportionality factor would work better in this case. We tried the K-R* model during this period, but the improvement was too small. Additionally, as will be discussed below, disturbance dynamo drifts may have had an influence in these morning downward drifts over Jicamarca. Our K-R drifts reversal at ∼0600 UT (0100 LT) match fairly well the

residual drifts up to 1200 UT on November 10. The fluctuations from 0600 UT to 1800 UT, especially the peak at ∼0800 UT, may be associated with substorm onset events. The M-M model underestimated and overestimated the residual drifts in certain time periods. For example, the M-M model predicts the upward peak at ∼2000 UT, but strongly underestimates it, even though the solar wind electric had large fluctuations. From 2100 UT to 2300 UT, the M-M model predicts the correct Jicamarca residual drift sign, but with a much greater amplitude and apparently out of phase. In the other periods, the model is, again, not accurate in its residual drift predictions.
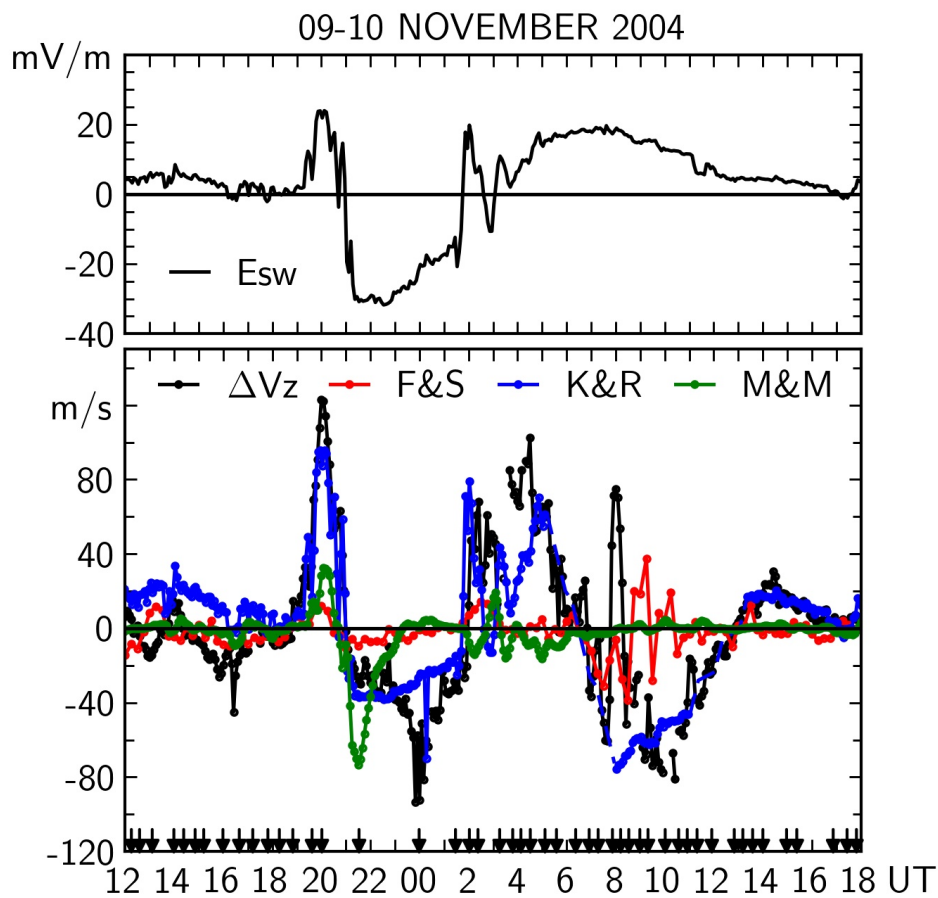
FIGURE 4.41 – (Top panel) Solar wind east-west electric field. (Bottom panel) Vertical disturbance drifts and their predictions from the F-S (F&S), M-M (M&M) and from the K-R (K&R) procedure. The small arrows indicate substorm onset times.

Figure 4.42 shows in the top panel the WDC-Kyoto AE and the SME indices for the 09-10 November 2004 geomagnetic storm. The bottom panel presents the Jicamarca perturbation drifts and the corresponding disturbance dynamo vertical drifts predicted by the F-S model. The SME and AE indices display the same pattern but, as expected, SME is larger than AE at all times. Figure 4.42 shows that the F-S model predicts, with a much lower amplitude, the drifts from 1200 UT on November 09 to 0200 UT on November 10. Hence, small downward disturbance dynamo drifts are expected in the morning over

Jicamarca, from 1200 UT to 1700 UT (0700-1200 LT) on the 9th, as well as in the afternoon, although penetration is also present, as shown in Figure 4.41. Furthermore, the downward disturbance dynamo drifts from 2100 UT to 0200 UT are underestimated by the model, even though penetration is also present. After this period, since the AE and SME indices are still very large, penetration electric fields are expected to dominate over disturbance winds.
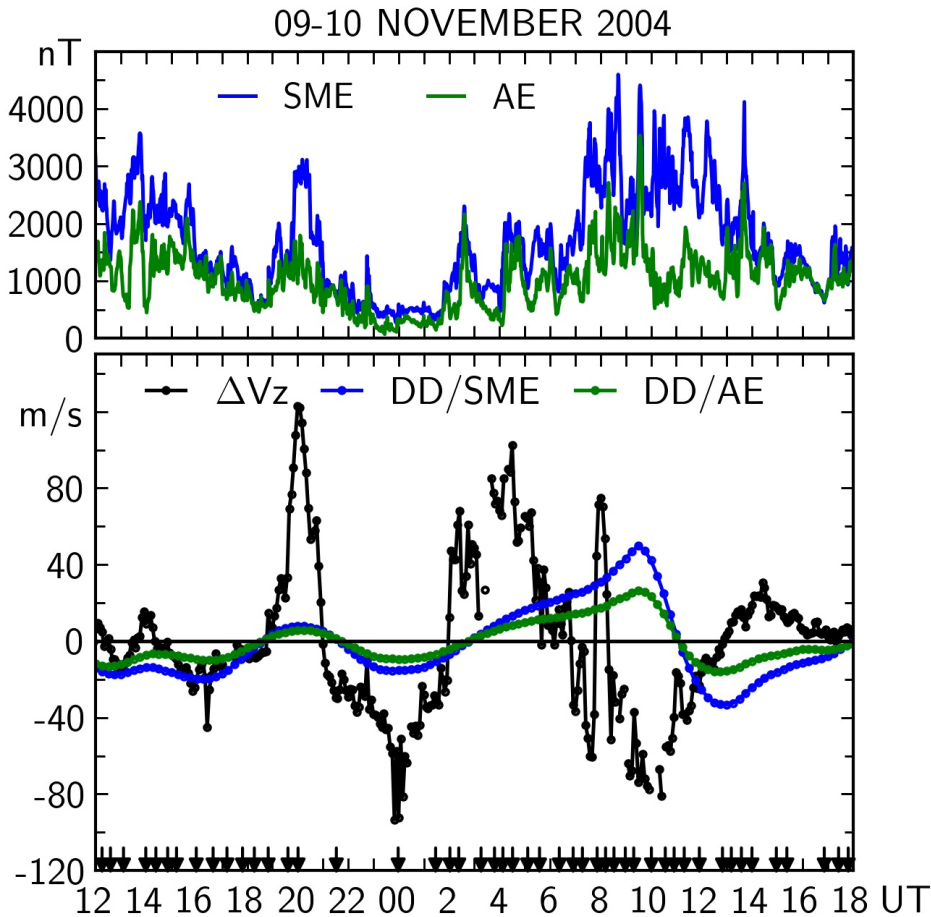
FIGURE 4.42 – (Top panel) Auroral AE and SME electrojet indices. (Bottom panel) Vertical disturbance drifts and corresponding predictions from the Scherliess-Fejer model using AE and SME indices as input parameters. The small arrows indicate substorm onset times.

The most significant prompt penetration vertical plasma drift perturbations, reaching about 120 m/s, were recorded over Jicamarca in the afternoon of November 9, 2004. These occurred following rapid increases in the interplanetary electric field by approximately 30 mV/m. Subsequently, the solar wind decreased rapidly after this intense prompt penetration event, resulting in equatorial westward electric fields persisting for about 4 hours, primarily due to prompt penetration and disturbance dynamo effects. On November 10th, large-magnitude, short-lived prompt penetration electric fields were observed on the nightside over Jicamarca.

The disturbance drifts during the April 2023 geomagnetic storm shown in Section 4.5.1 displayed upward vertical drifts up to ∼0100 LT during strong southward IMF Bz and undershielding conditions. The 09-10 November, 2004, geomagnetic storm shown in this section is very similar to the April 2023 in this manner, showing unusual drifts during the night. On the 10th, under strongly southward IMF Bz, the Jicamarca vertical drifts reversed to downward at ∼0100-0200 LT (0600-0700 UT), as shown in Figures 4.40-4.42. As in our case, the IMF By was also strongly negative during the 23 April 2023 storm late vertical drift reversal. Fejer, Laranja and Condor (2024) suggest that under steady southward IMF Bz and frequent substorm activity, the vertical drift reversal to downward occurs later. Hence, increased IMF Bz and By, along with intense substorm activity may influence the late vertical drift reversal during storm times.

4.5.5   17-18 April 2002

The last storm evaluated in this chapter is the 17-18 April 2002 strong geomagnetic storm. This storm was driven by a CME that triggered double-peaked moderate/strong geomagnetic storms on 17 and 19 April. To study the 17-18 April 2002 storm, we use Jicamarca ISR data for the vertical drift along with interplanetary parameters and geomagnetic indices, as was performed for the previous storms studied here.

Measurement Techniques and Data

We used Jicamarca incoherent scatter radar measurements from 03 LT (08 UT) on April 17, 2002 to 07 LT (12 UT) April 18, 2002, which encompasses the storm main phase. We also use 1-min SuperMAG ground-based magnetic field, WDC, 1-min Kyoto AE index, and 5-min ACE satellite solar wind measurements.

In the present study, we used 5-min vertical drifts averaged from 250 km to 945 km for the vertical component. These velocities include measurements of spread F. We deleted height-averaged drifts with standard deviations larger than 30 m/s. The standard deviations of our height-averaged drifts are ∼1 m/s during the day and ∼2 m/s during the night. For this storm, there is no zonal drift data available at Madrigal (`http://jro-db.igp.gob.pe/madrigal/`).

Results

Figure 4.43 shows solar wind parameters from ACE and geomagnetic indices from SuperMAG during 17-18 April 2002. The main phase of this storm started at 1800 UT with the minimum SMR index value of approximately -120 nT. A secondary minimum is found at 0800 UT on the 18th when the SMR reached -148 nT. Since there is geomagnetic activity before the main phase, we chose to plot the parameters shown in Figure 4.43

earlier. The Kp index reached 7+ during 1500-1800 UT on 17 April, and remained at disturbed levels for the most part until 20 April (not shown in Figure 4.43).
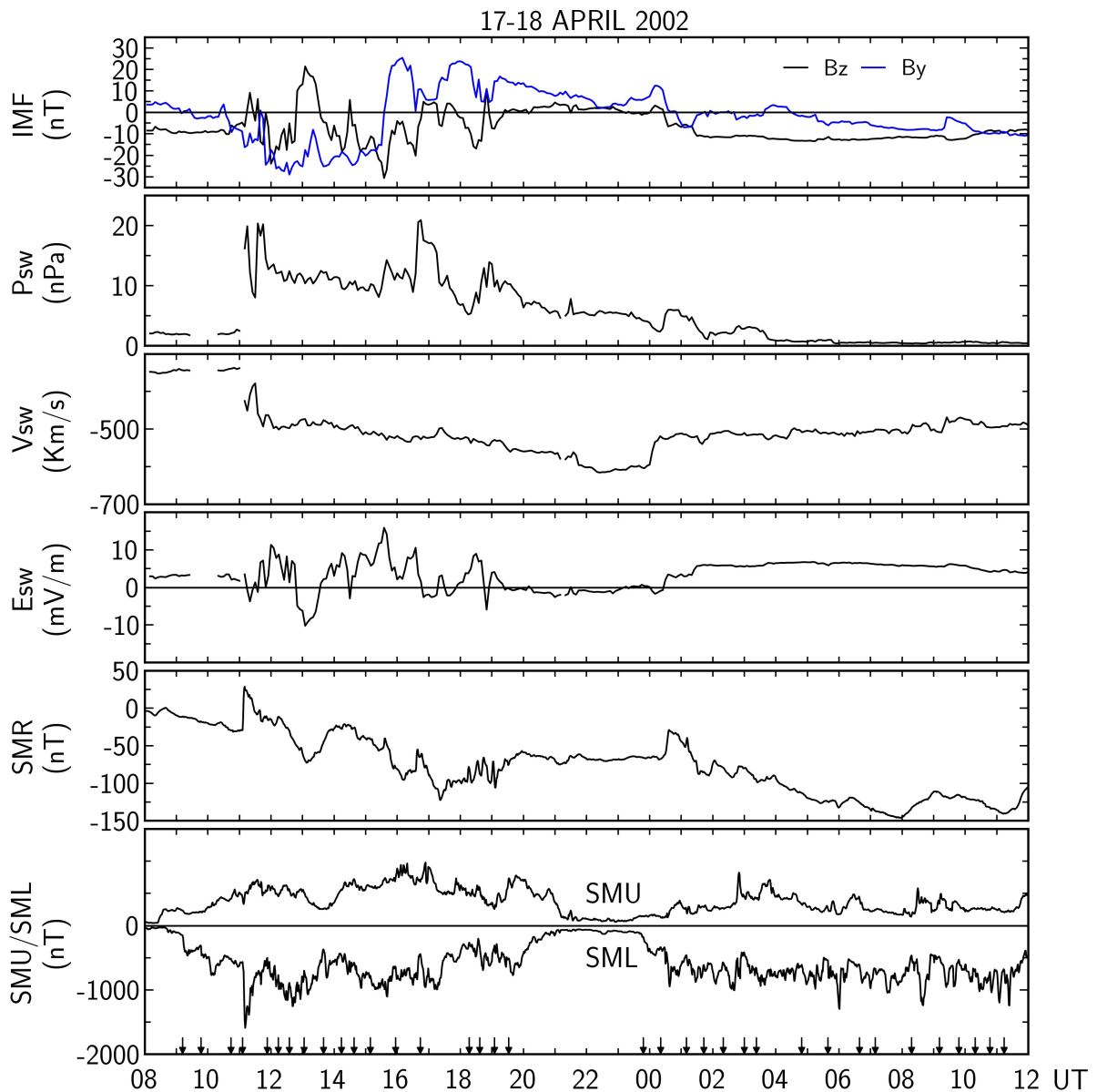
FIGURE 4.43 – (From top to bottom) IMF Bz/By, solar wind dynamic pressure, solar wind speed, solar wind east-west electric field, SuperMAG ring current (SMR), auroral current (SMU/SML) indices, and substorm onset times (small arrows in the bottom panel) during the 17-18 April 2002 geomagnetic storm.

Figure 4.43 shows that on 17 April, the IMF Bz component is already southward and changes direction between southward and northward several times throughout the day. In particular, the IMF Bz remained southward for 3 hours, from 1330 UT to 1630 UT, reaching magnitudes of 30 nT. After that, the IMF strongly decreased to values close to 2 nT until 0000 UT of the 18th, when it became steadily negative up to 1200 UT on the 18th. The IMF By became strongly negative between 1100 UT and 1530 UT on the 17th, when it became strongly positive and then started to recover from 1900 UT on the

18th. The solar wind dynamic pressure had large increases and amplitude fluctuations from 1100 UT to 2100 UT on the 17th, after which it started to decrease slowly. The solar wind speed increased from 1100 UT, which together with the dynamic pressure increase, means a strong solar wind-magnetosphere coupling conditions.

The interplanetary electric field presented several positive and negative fluctuations on the 17th, with magnitudes of up to 10 mV/m, as shown in Figure 4.43. On the 18th, the interplanetary electric field was eastward and steady. The SMU and SML auroral current indices had numerous fluctuations throughout the whole storm-time period, with several fast recurring substorms observed by the SML index.
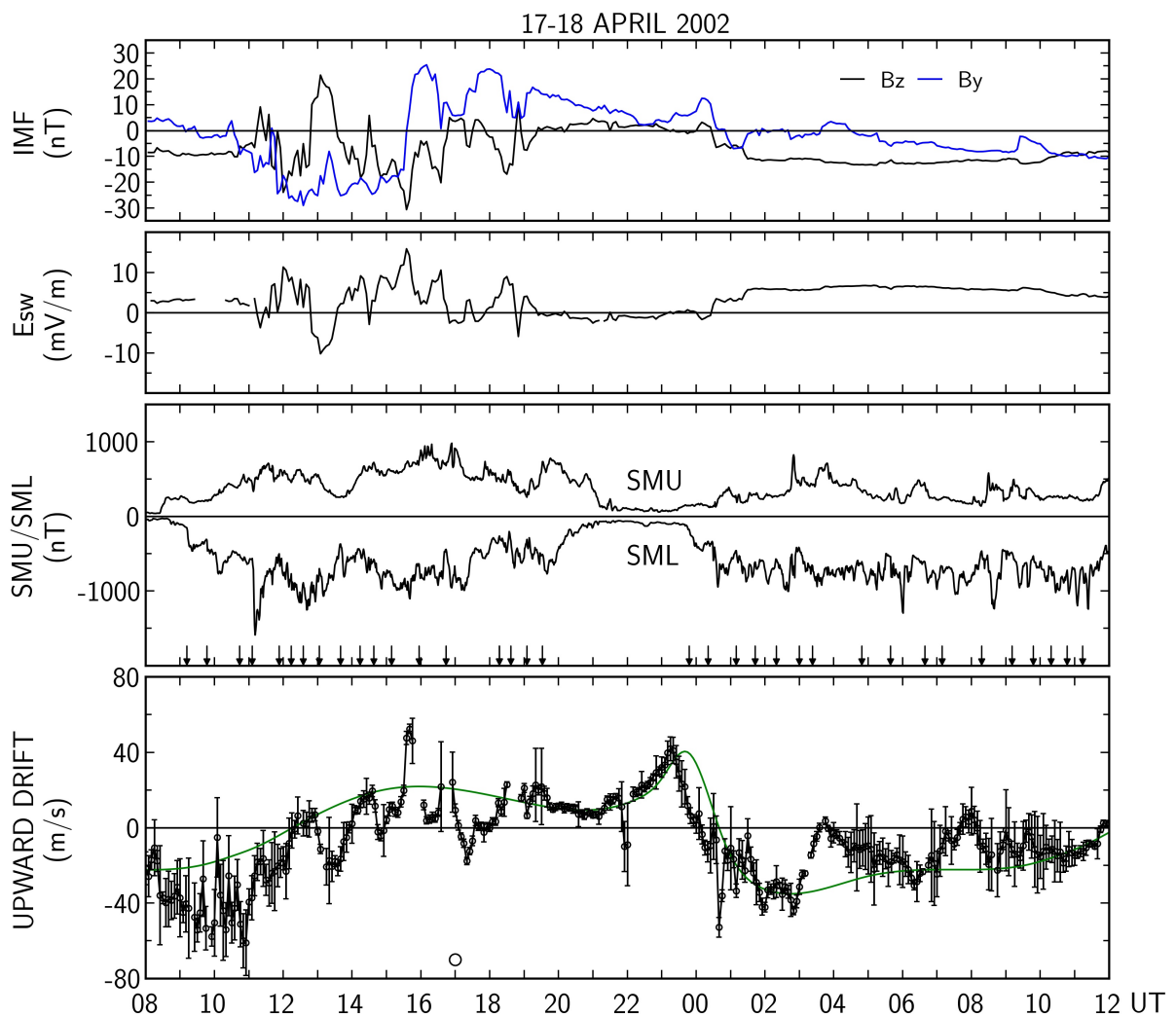
FIGURE 4.44 – (Top three panels) Solar wind motional east-west electric field, SuperMAG ring current (SMR), auroral current (SMU/SML) indices, and substorm onset times (small arrows). (Bottom panel) Height-averaged Jicamarca vertical plasma drifts. The green curve denotes the quiet time vertical drift pattern.

Figure 4.44 presents in the three top panels the ACE IMF By and Bz components, the solar wind electric field, and the SuperMAG ring current and auroral geomagnetic indices with substorm onset times, whereas the fourth panel shows the height-averaged

Jicamarca vertical plasma drifts with their standard deviations superposed on the corresponding quiet-time drift patterns from 0800 UT to 1200 UT on 17-18 April 2002, which encompasses the storm main phase. Figure 4.44 shows strong downward fluctuations in the vertical drifts from ~0800 UT to 1200 UT (0300-0700 LT). These can be associated with westward undershielding electric fields, since the IMF Bz is turned southward during this period. However, the interplanetary electric field is small between 0800 UT and 1200 UT, so that the drifts variations cannot only be accounted for by undershielding. Substorms might also play an important role during this time. The IMF Bz has a rapid northward excursion between 1100 UT and 1200 UT (0600-0700 LT), which possibly generated an increase in the vertical drifts. After that, there is a strong IMF Bz southward turn between ~1200 UT and 1230 UT, which was accompanied by an eastward interplanetary electric field that was associated with eastward equatorial electric fields, generating upward plasma drifts. Hence, from 1200 UT (0700 LT), the prompt penetration electric fields at the equator seem to have reversed polarity.

Figure 4.44 shows that from 1230 UT to ~1400 UT, the vertical drifts become downward due to a strong IMF Bz northward turning, associated with westward penetration (overshielding) electric fields. The Jicamarca drifts follow, in general, the interplanetary electric field variations until ~2000 UT (1500 LT), associated with prompt penetration undershielding electric fields. From 2000 UT to 0000 UT (1500-1900 LT), the vertical drifts are very close to their quiet time values, which is consistent with an absence of a noticeable geomagnetic activity in the three top panels of Figure 4.44. From 0000 UT to 1200 UT (1900-0700 LT) on the 18th, both the IMF components and the interplanetary electric field are steady and recovering, with small magnitude values. Hence, we can associate the drift perturbations with substorm activity, small dynamic pressure changes, and disturbance dynamo electric fields, since we expect disturbance winds to have arrived the equatorial region after midnight. In reality, after 1110 UT, the drifts seem to follow the quiet-time pattern and to enter the recovery phase.

Discussion

We close the April 2002 storm section with the evaluation of the Jicamarca disturbance drifts in comparison with prompt penetration and disturbance dynamo drifts predicted by empirical vertical drift models. Kelley *et al.* (2003) also discuss the penetration of electric fields in the equatorial region during this storm using a proportionality factor and find reasonable agreement, but only for the 1000-2200 UT period on the 17th. Here we investigate the whole storm-time period. Figure 4.45 shows, from 0800 UT on April 17 to 1200 UT on April 18, the interplanetary electric field (upper panel) and vertical drift perturbations and the prompt penetration drifts from the F-S model, the K-R model and the M-M model (lower panel). In the same manner as for the 27-28 September 2017 storm, we used the K-R prescription for the whole period studied here, and since we do

not know the exact drift reversal time to downward, we reversed the K-R drifts from 0300 UT to 1200 UT (2200-0700 LT).

Figure 4.45 demonstrates that the F-S model consistently underestimates the residual drifts throughout the storm-time period. Only a few residual drift variations are followed by the F-S drifts, and these are mostly in the period from 0800 UT to 1200 UT. The M-M model shown in Figure 4.45 again strongly differ from the residual drifts, except for the period from 1400 UT to 1700 UT, in which the M-M follows the Jicamarca residuals sign and variation, but not their amplitude.
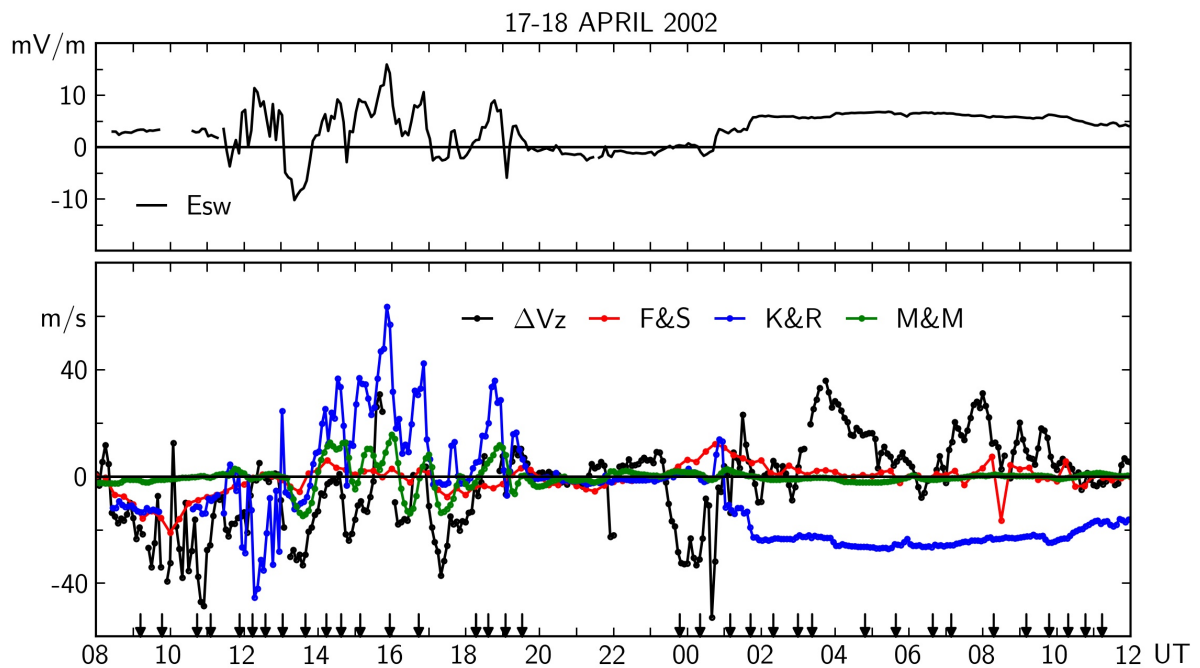
FIGURE 4.45 – (Top panel) Solar wind east-west electric field. (Bottom panel) Vertical disturbance drifts and their predictions from the F-S (F&S), M-M (M&M) and from the K-R (K&R) procedure. The small arrows indicate substorm onset times.

The K-R drifts shown in Figure 4.45 are only similar to the residual drifts when the interplanetary electric field is largely fluctuating, i.e., from 1400 UT to 1700 UT on the 17th, and even in this case the model overestimates the residual drifts. In more details, the K-R drifts from 1400 UT to 1700 UT are larger than the residual but follow the residual overall pattern. Hence, this indicates that perhaps a different solar wind to equatorial electric field ratio would work better during this period. In the same manner as the 27-28 September 2017 storm, we use the modified K-R model, the K-R* model, from 1400 UT to 1700 UT on the 17th. Again, the K-R* model uses a ratio of 0.05 (5%) of the interplanetary electric field for southward IMF and 0.2 (20%) for northward IMF. Figure 4.46 shows the interplanetary electric field in the upper panel and the Jicamarca residual drifts along with the K-R* prescription in the bottom panel. We note that, indeed, there is a small improvement in the model prediction compared to the residual drifts in the

period between 1400 UT and 1700 UT on the 17th. However, disturbance dynamo drifts
may have also contributed to the observed drifts, possibly making our new proportionality
factor more effective due to the dynamo's influence on the residual drifts. After 0000 UT
(1900 LT), when the interplanetary electric field is steady, the K-R prediction is very
different from the residual drifts, where we speculate that substorms and disturbance
dynamo electric fields dominate.
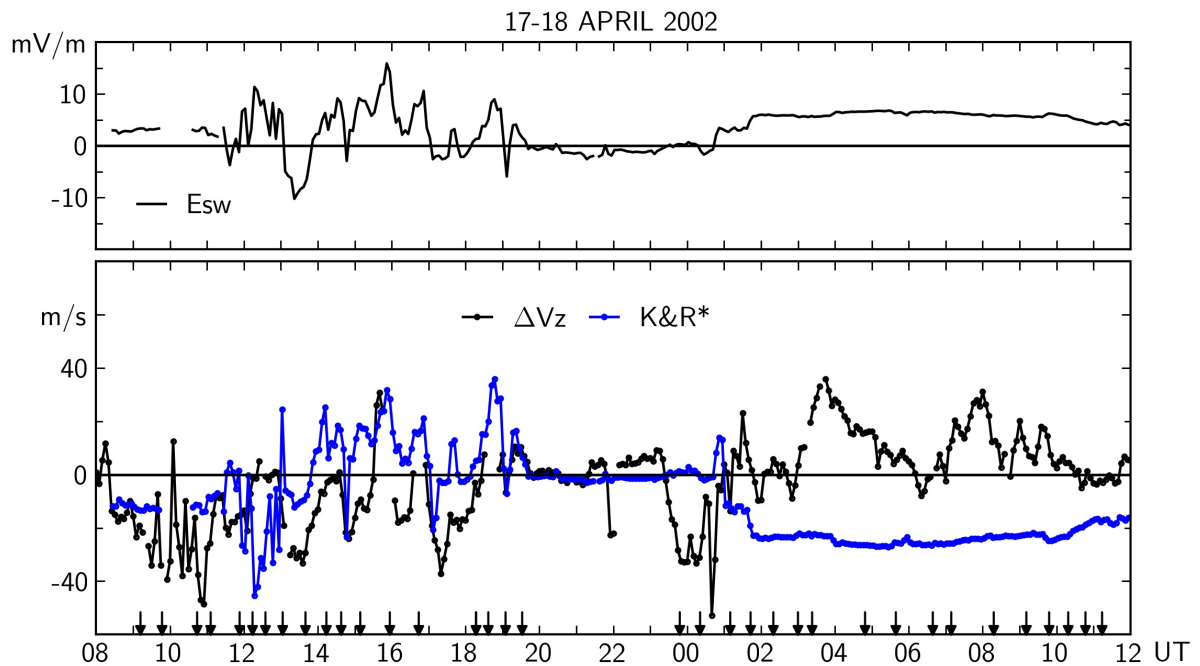
FIGURE 4.46 – (Top panel) Solar wind east-west electric field. (Bottom panel) Vertical
disturbance drifts and their predictions from the K-R* (K&R*) procedure. The small
arrows indicate substorm onset times.

Figure 4.47 shows in the top panel the WDC-Kyoto AE and the SME indices for the 17-
18 April 2002 geomagnetic storm. The bottom panel presents the Jicamarca perturbation
drifts and the corresponding disturbance dynamo vertical drifts predicted by the F-S
model. The SME and AE indices display the same pattern but the SME is larger than
AE at all times. Figure 4.47 confirms that the drifts from 1200 UT to 1800 UT (0700-1300
LT) might also have had an influence from disturbance dynamo electric fields, which was
not clear when evaluating Figures 4.44 and 4.45. Hence, these drifts were affected by both
storm-time processes. The IMF Bz fluctuated between southward and northward several
times, and the pattern of the vertical drifts generally matched these changes. However, the
amplitude of the residuals was similar to that of the disturbance dynamo drifts, making
it difficult to determine which contribution dominated during this period.

From 0000 UT to 1200 UT, Figure 4.47 shows that the disturbance dynamo electric
fields have indeed dominated the Jicamarca residual drifts variations. In particular, it is
clear that the postmidnight and early morning Jicamarca drifts, i.e., from 0600 UT to
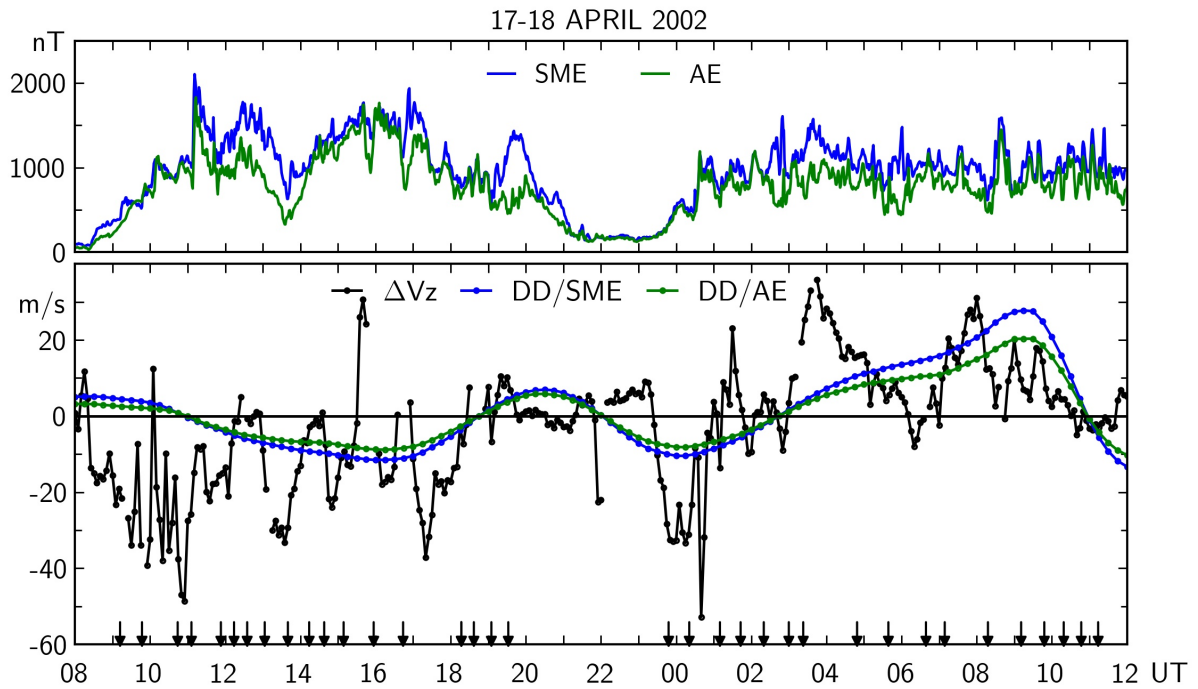
FIGURE 4.47 – (Top panel) Auroral AE and SME electrojet indices. (Bottom panel) Vertical disturbance drifts and corresponding predictions from the Scherliess-Fejer model using AE and SME indices as input parameters. The small arrows indicate substorm onset times.

1200 UT (0100-0700 LT), were mostly generated by disturbance winds. Furthermore, it is also clear now that the large drift increases between 0100 UT and 0400 UT were affected by strong substorm onset events. Hence, our observations of how the ionosphere reacts during the April 2002 storm revealed a complex pattern in the plasma drifts. Longer-lasting variations superimposed with short-lived disturbance are seen during the whole storm-time period.

4.5.6   Conclusions on the Storms' Evaluation

We showed in this section a comparison between five different geomagnetic storms and their effects at the equator. In ascending order of intensity, we illustrated the effects of one moderate storm (27-28 September 2017), one strong storm (17-18 April 2002), two severe storms (23-24 April 2023 and 07-08 September 2017), and one intense storm (09-10 November 2004). The similarities between these different cases lie in the magnetospheric mechanisms generating measurable equatorial electric field impacts. Undershielding and overshielding electric fields driven by IMF Bz sign changes, substorms driven by IMF Bz northward turns and dynamic pressure changes, eastward equatorial electric fields induced by dynamic pressure changes, and disturbance dynamo electric fields were common features in all five storms studied here. The differences lie in

the strength of each of these effects depending on the local time period, IMF Bz intensity, interplanetary electric field penetration efficiency, and substorm and disturbance dynamo electric fields dominance over undershielding driven by IMF Bz southward turning.

In summary, we showed that very large equatorial disturbance vertical and zonal plasma drifts were observed during the 23-24 April severe geomagnetic storm. The daytime disturbance prompt penetration vertical drifts were generally proportional to changes in the interplanetary electric field but were also strongly affected by solar wind dynamic pressure changes, and possibly by substorms and disturbance dynamo electric fields. As is often the case, the relative contributions of these different disturbance processes cannot be fully determined. The nighttime measurements showed unusually large amplitude substorm-driven prompt penetration vertical drifts superposed on large undershielding upward drifts up to about midnight, which are not well reproduced by either current empirical or theoretical models. Our results also suggest that the substorm-driven prompt penetration electric field efficiency is much higher in the premidnight sector than during the day. These short-lived substorms significantly modulate the growth rate of the Rayleigh-Taylor instability and therefore the structuring of equatorial and low latitude spread-F irregularities.

The observed drift perturbations of the 27-28 September 2017 storm are overall consistent with prompt penetration driven undershielding and overshielding effects, substorms and disturbance dynamo electric fields. The drifts in the postmidnight sector and early morning at Jicamarca can be mostly accounted for by disturbance dynamo electric fields, whereas the premidnight drifts can be largely associated with prompt penetration electric fields. In both periods, substorms induced strong drift perturbations. Additionally, during this moderate storm, disturbance winds arrived earlier at the equator and were sometimes stronger than the prompt penetration electric fields, given that the interplanetary electric field was characterized by, in general, small magnitudes. Another important feature occurring during this storm is the possible PRE and consequent spread F suppression due to a westward interplanetary electric field at the PRE time, although disturbance dynamo may also have influenced the PRE suppression.

The 07-08 September 2017 intense storm suggests that substorms likely play a crucial role in shaping the behavior of plasma in the ionosphere during geomagnetic storms, even if the substorms are relatively weak or short-lived, particularly in the evening and if the IMF Bz is relatively steady. This highlights the challenge of accurately assessing the impact of substorms on the ionosphere during storms. Additionally, these vertical drift fluctuations during strong southward IMF Bz might also be attributed to rapid magnetotail field line dipolarization during IMF By recovery, as suggested by previous studies.

The 09-10 November 2004 very intense storm demonstrated that prompt penetration electric fields prevail as the dominant electric field for an extended period (10-13 hours) in the equatorial ionosphere during the storm's main phase. These observations suggest that the arrival of disturbance winds at the equatorial region does not automatically signify a change in dominance from prompt penetration to disturbance dynamo electric fields. Instead, disturbance dynamo electric fields become dominant in the equatorial region when the IMF Bz turns northward or when the magnitude of southward IMF Bz significantly weakens, at least for this large geomagnetic storm, which was not the case for the 27-28 September 2017 moderate storm. Additionally, the Jicamarca radar data during 09-10 November 2004 shows that the vertical drifts are continuously enhanced in the upward direction for when there is a continuous southward IMF (for example, between 1900 UT and 2100 UT on November 09) and that the enhanced upward drifts are approximately proportional to the solar wind electric field. The November 2004 intense geomagnetic storm, compared to the others discussed above, is the one in which the equatorial disturbance drifts best matched the solar wind electric field, as seen for the great correlation between these drifts and the K-R model.

Both the April 2023 and the November 2004 geomagnetic storm displayed upward vertical drifts until around 0100 LT under strong southward IMF Bz and with strongly negative IMF By. Fejer, Laranja and Condor (2024) suggest that steady southward IMF Bz and frequent substorm activity may play a role on the delay of the drift reversal to downward. We believe that a strong IMF Bz and By and frequent substorm activity can contribute in the drift reversal to downward, as indicated by the patterns observed in the storms studied here.

The 17-18 April 2002 showed again that, when the IMF Bz is steady, substorms dominate the major short-term disturbances, and that in this case they can be embedded in the disturbance dynamo drifts, which are longer-lasting. Substorms causing strong short-term disturbances under steady southward IMF Bz are also observed in the 07-08 September storm. However, in the 07-08 September 2017 storm, substorms dominated the drifts behavior. This difference can be due to the local time occurrence of the storm, since in the 07-08 September 2017 storm the IMF Bz was steady during the day and evening, and in the April 2002 the IMF Bz was steady in the premidnight and postmidnight sectors, when we expect disturbance dynamo drifts to be most intense. Hence, when the IMF Bz is steady, the substorm efficiency appears to increase regardless of the local time, at least for the storms studied here. Furthermore, in the April 2002 storm, the appearance and dominance of disturbance winds in the equatorial drifts occurred even if the IMF Bz was steadily southward for ~12 hours. The F-S disturbance dynamo model predicted reasonably well the residual drifts in this case, whereas the K-R* model, compared to S-F and M-M, predicted similar drifts to the

residuals in some periods. Still, for both storms (07-08 September 2017 and April 2002), the effect of prompt penetration should not be neglected and set to zero because it is certainly present, but to what extent these different contributions can be separated is a very difficult task in the current ionospheric modeling.

An important caveat in the storms' analysis that must be taken into account is that the deduction of the drift residuals (Jicamarca disturbance drifts) from height-averaged values does not consider the great day-to-day variability of the quiet-time drift velocities. Therefore, the disturbance drifts might not be accurate, making the comparison with the empirical models sometimes inaccurate.

We have also illustrated the possibility that the interplanetary electric field to the zonal equatorial electric field ratio can change in some periods, at least for the data studied here. In our analysis, we used a different proportionality factor during the night and the morning at Jicamarca, i.e., from 2200 LT to 1200 LT (0300-1700 UT) during two selected storms. We suggested a ratio of 0.05 (5%) of the interplanetary electric field for southward IMF Bz and 0.2 (20%) for northward IMF Bz during these periods. The new ratio worked better in the night of the 28 September 2017 moderate storm and in the morning of the 17 April 2002 moderate/strong storm than the regular ratio of 0.1 (10%) for southward IMF Bz and 0.03 (3%) for northward IMF Bz used in the K-R model. Therefore, since the proportionality factor for a northward IMF Bz is larger than for southward, we speculate the possible dominance of overshielding electric fields over undershielding during these periods, although more data is needed to either confirm or discard this possibility. Additionally, it is important to mention that other effects, such as the disturbance dynamo, may have contributed in the same direction as these proportionality factors. Hence, it is also important to keep in mind that we are using a small number of samples, so that we can only suggest that the ratios are consistent with our limited data. Our goal here was just to show that the model may change in a particular case and that it may change depending on the local time. We wanted to check if our proposed parametrization is consistent with our data, knowing that the disturbance electric fields and drifts are due to various processes difficult to separate and that additional parameters (e.g., IMF By) are likely also important.

Our findings suggest that the usual explanation for how electric fields affect the ionosphere might not be sufficient. We observed that the electric fields in the equatorial ionosphere are highly sensitive to changes caused by magnetospheric substorms. Substorms seem to have a significant impact during active periods, especially when the IMF Bz remains steady for an extended period. Hence, the development of magnetospheric convection models including magnetospheric substorms and extending down to equatorial latitudes is clearly needed for improved predictions of the global ionospheric response to magnetic storms. Furthermore, the main limitation of local time

empirical equatorial electrodynamic models (e.g., K-R and Manoj-Maus) is that they do not fully take into account the near past history of geomagnetic activity which can significantly precondition the ionospheric response.   Nevertheless, the K-R prompt penetration empirical model had the best overall performance compared to the F-S and the M-M models which, for at least some periods of each storm studied here, this model predicted the disturbance equatorial drifts reasonably well, as showed above. This can be explained by the direct correlation between the interplanetary electric field and the equatorial zonal electric field, although a much more complex relation is observed, especially according to different local times, where the efficiency may change, and not by simple proportionality factors.

As for the disturbance dynamo Fejer and Scherliess (1997a) model, accurately predicted the postmidnight upward drifts for all evaluated storms except the one on November 9-10, 2004. This storm was the most intense showed here, and that is the probable explanation of why disturbance dynamo electric fields took longer to dominate in the equatorial region.   The F-S model also reasonably predicted the morning downward drifts in all storms, though it is challenging to separate these from the contributions of penetration drifts. As mentioned in Section 2.3.4, the S-F disturbance dynamo model was originally calibrated using the AE index. However, due to the higher accuracy and similarity of the SME index to AE, we compared the outcomes using both indices. Since the SME index sometimes provides more accurate drift predictions, we conclude that it can be used as input to the Fejer and Scherliess (1997a) disturbance dynamo model, as well as the prompt penetration model.

In the near future, it will certainly be important to use other models that use coupling between the solar wind and the magnetosphere to determine additional prompt penetration parameters (e.g., IMF By), such as the ones using the *merging electric field* (also called reconnection electric field). Proposed by Xiong *et al.* (2015), this parameter is used to check the response of vertical plasma drift to enhanced solar wind input into the ionosphere-thermosphere system, being correlated with prompt penetration electric fields. Hence, the incorporation of additional factors in the magnetosphere-ionosphere system modeling is of crucial importance.

5 Summary and Conclusions

This thesis underscores the importance of an experimental/observational approach to ionospheric study, utilizing both satellite and ground-based instruments to provide a comprehensive and multifaceted understanding of ionospheric conditions. To achieve this, we performed three main studies, which are the ion density climatology using the FPMU probe, the vertical drift velocity climatology using the IVM on board the C/NOFS satellite, and the investigation of equatorial perturbation electric fields during five geomagnetic storms using Jicamarca data and empirical models.

We have presented the climatological analysis of mid- and low-latitude plasma densities derived from 12 years of FPMU measurements aboard the ISS during periods of low and moderate solar activity. Our findings regarding daytime climatology, focusing on the evolution, seasonality, and solar flux dependency of the EIA and the location of its crests, are consistent with previous experimental results. Moreover, our analysis of FPMU data during evening and early night periods highlights the significant influence of the PRE on the longitudinal variation of EIA crest-to-trough ratios and the role of meridional thermospheric winds in hemispheric asymmetries. Around this time, the IRI density estimations consistently underestimate the observed moderate flux in-situ data across all seasons. Additionally, we have observed strong seasonal and longitudinal variations in ion density across the American and Atlantic sectors during the evening and nighttime periods, particularly in the South American region. We have also examined two midlatitude summer nighttime anomalies, the Weddell Sea anomaly in the South Pacific during the December solstice and the North Atlantic density enhancement during the June solstice. Our analysis suggests similarities between these anomalies, with both being more pronounced during periods of higher solar activity and exhibiting all-night lifetimes at the altitude of the ISS, contrary to previous findings, possibly due to altitude-related effects. Furthermore, we have identified a distinctive structure in the southern crest of the EIA during the December solstice and equinox, which, to our knowledge, has not been previously reported. In the South Atlantic region, this density bulge in the EIA was more pronounced during periods of moderate solar flux, possibly resulting from plasma transport from the Weddell Sea anomaly, since this anomaly was identified in the early morning for the first time.

The vertical ion drift data from the C/NOFS satellite reveals significant seasonal and longitudinal variations near the equator. Downward afternoon drifts are consistently observed throughout the seasons and across the entire Brazilian territory, which contradicts the established understanding that negative velocities should not occur during the daytime. This discrepancy underscores the critical difficulty in the precise measurement of ambient ion drift. While caution is appropriate due to the potential for instrumental error, a suggestion of a possible influence of semidiurnal tides on ionospheric drifts is given according to previous studies. Semidiurnal tides enhance prenoon drifts, can potentially reverse afternoon drifts, and contribute to upward drifts after midnight, particularly in the Brazilian region where there is a significant magnetic declination. Furthermore, the equatorial vertical ion drift varies with solar activity. Solar cycle effects are prominent near dusk, with a significant PRE increase under high solar flux. During low solar flux, the PRE is weaker, where this difference is more evident during December solstice. The drifts are near zero at sunset transitioning to downward at night during June solstice. Significant longitudinal variability is observed in late afternoon and evening, especially during the June solstice, with reversal times varying between sectors. Nighttime measurements exhibit larger variations due to irregularities, with upward drifts observed after sunset especially during the equinoxes. These findings highlight the complexity and seasonal variability of equatorial ionospheric dynamics, influenced by solar activity variations, tidal effects, and longitudinal asymmetries.

As for our disturbed time investigation, one important feature of the equatorial ionosphere is its reaction to the penetration electric field. We compared the effects of five geomagnetic storms of varying intensities on the equatorial region: a moderate storm (27-28 September 2017), a strong storm (17-18 April 2002), two severe storms (23-24 April 2023 and 07-08 September 2017), and a very intense storm (09-10 November 2004). Across all storms, we observed common magnetospheric mechanisms affecting equatorial electric fields, such as undershielding and overshielding electric fields, substorms, and disturbance dynamo electric fields. However, the strength of these effects varied with local time, IMF Bz intensity, solar wind electric field penetration efficiency, and the dominance of substorm and disturbance dynamo electric fields. The K-R prompt penetration empirical vertical drift model performed better compared to the F-S and the M-M models, even if the proportionality factor between the solar wind electric field and the equatorial zonal electric electric field is not a constant and not the only parameter in the magnetosphere-ionosphere interplay. Additional parameters, such as IMF By and the effects of substorms, should be incorporated into future models, as these factors likely played a significant role in the delayed drift reversal to downward during the nights of the storms on 23-24 April 2023 and 09-10 November 2004. Additionally, the F-S disturbance dynamo model performed reasonably well for most

storms in the postmidnight sector. The observed drift patterns during different storms highlight the complexity of equatorial ionospheric dynamics and the influence of magnetospheric substorms. Improved models incorporating substorm effects are needed for more accurate predictions of ionospheric responses to magnetic storms, especially considering the limitations of existing empirical models in capturing the full range of geomagnetic activity. Hence, the improvement and use of existing models to add new factors in the magnetosphere-ionosphere system modeling is of crucial importance. Therefore, ionospheric modeling under disturbed geomagnetic conditions remains an emerging area in the ionospheric investigation.

Bibliography

ABDU, M. A. Outstanding problems in the equatorial ionosphere-thermosphere electrodynamics relevant to spread f. **Journal of Atmospheric and Solar-Terrestrial Physics**, Elsevier, v. 63, n. 9, p. 869–884, 2001.

ABDU, M. A.; BATISTA, I. S.; BRUM, C. G. M.; MACDOUGALL, J. W.; SANTOS, A. M.; SOUZA, J. R.; SOBRAL, J. H. A. Solar flux effects on the equatorial evening vertical drift and meridional winds over brazil: A comparison between observational data and the iri model and the hwm representations. **Advances in space research**, Elsevier, v. 46, n. 8, p. 1078–1085, 2010.

ABDU, M. A.; BITTENCOURT, J. A.; BATISTA, I. S. Magnetic declination control of the equatorial f region dynamo electric field development and spread f. **Journal of Geophysical Research: Space Physics**, Wiley Online Library, v. 86, n. A13, p. 11443–11446, 1981.

ABDU, M. A.; KHERANI, E. A.; BATISTA, I. S.; SOBRAL, J. H. A. Equatorial evening prereversal vertical drift and spread f suppression by disturbance penetration electric fields. **Geophysical Research Letters**, Wiley Online Library, v. 36, n. 19, 2009.

ABDU, M. A.; NOGUEIRA, P. A. B.; SANTOS, A. M.; SOUZA, J. R.; BATISTA, I. S.; SOBRAL, J. H. A. Impact of disturbance electric fields in the evening on prereversal vertical drift and spread f developments in the equatorial ionosphere. *In*: COPERNICUS GMBH. **Annales Geophysicae**. **Proceedings** [...]. [*S.l.: s.n.*], 2018. v. 36, n. 2, p. 609–620.

AKASOFU, S.-I.; MENG, C.-I. A study of polar magnetic substorms. **Journal of Geophysical Research**, Wiley Online Library, v. 74, n. 1, p. 293–313, 1969.

ANDRIOLI, V. F.; XU, J.; BATISTA, P. P.; RESENDE, L. C. A.; SILVA, L. A. D.; MARCHEZI, J. P.; LI, H.; WANG, C.; LIU, Z.; GUHARAY, A. New findings relating tidal variability and solar activity in the low latitude mlt region. **Journal of Geophysical Research: Space Physics**, Wiley Online Library, v. 127, n. 3, p. e2021JA030239, 2022.

APPLETON, E. V. Two anomalies in the ionosphere. **Nature**, Nature Publishing Group, v. 157, n. 3995, p. 691–691, 1946.

BAILEY, G. J.; BALAN, N.; SU, Y. Z. The sheffield university plasmasphere ionosphere model-a review. **Journal of Atmospheric and Solar-Terrestrial Physics**, Elsevier, v. 59, n. 13, p. 1541–1552, 1997.

BAILEY, G. J.; SELLEK, R. A mathematical model of the earth's plasmasphere and its application in a study of he+ at l= 3. *In*: **Annales Geophysicae**. **Proceedings** [...]. [*S.l.: s.n.*], 1990. v. 8, p. 171–189.

BAILEY, G. J.; SELLEK, R.; RIPPETH, Y. A modelling study of the equatorial topside ionosphere. *In*: **Annales geophysicae**. **Proceedings** [...]. [*S.l.: s.n.*], 1993. v. 11, n. 4, p. 263–272.

BAILEY, G. J.; SU, Y. Z.; OYAMA, K.-I. Yearly variations in the low-latitude topside ionosphere. *In*: SPRINGER VERLAG GÖTTINGEN, GERMANY. **Annales Geophysicae**. **Proceedings** [...]. [*S.l.: s.n.*], 2000. v. 18, n. 7, p. 789–798.

BALAN, N.; BAILEY, G. J.; ABDU, M. A.; OYAMA, K.-I.; RICHARDS, P. G.; MACDOUGALL, J. W.; BATISTA, I. S. Equatorial plasma fountain and its effects over three locations: Evidence for an additional layer, the f 3 layer. **Journal of Geophysical Research: Space Physics**, Wiley Online Library, v. 102, n. A2, p. 2047–2056, 1997a.

BALAN, N.; LIU, L.; LE, H. A brief review of equatorial ionization anomaly and ionospheric irregularities. **Earth and Planetary Physics**, Wiley Online Library, v. 2, n. 4, p. 257–275, 2018b.

BALAN, N.; OTSUKA, Y.; BAILEY, G. J.; FUKAO, S. Equinoctial asymmetries in the ionosphere and thermosphere observed by the mu radar. **Journal of Geophysical Research: Space Physics**, Wiley Online Library, v. 103, n. A5, p. 9481–9495, 1998.

BALAN, N.; OTSUKA, Y.; FUKAO, S. New aspects in the annual variation of the ionosphere observed by the mu radar. **Geophysical research letters**, Wiley Online Library, v. 24, n. 18, p. 2287–2290, 1997b.

BALAN, N.; RAJESH, P. K.; SRIPATHI, S.; TULASI RAM, S.; LIU, J.-Y.; BAILEY, G. J. Modeling and observations of the north–south ionospheric asymmetry at low latitudes at long deep solar minimum. **Advances in Space Research**, Elsevier, v. 52, n. 3, p. 375–382, 2013.

BALAN, N.; SOUZA, J. R.; BAILEY, G. J. Recent developments in the understanding of equatorial ionization anomaly: A review. **Journal of Atmospheric and Solar-Terrestrial Physics**, Elsevier, v. 171, p. 3–11, 2018a.

BANKOV, L.; HEELIS, R. A.; PARROT, M.; BERTHELIER, J. J.; MARINOV, P.; VASSILEVA, A. Wn4 effect on longitudinal distribution of different ion species in the topside ionosphere at low latitudes by means of demeter, dmsp-f13 and dmsp-f15 data. *In*: COPERNICUS GMBH. **Annales geophysicae**. **Proceedings** [...]. [*S.l.: s.n.*], 2009. v. 27, n. 7, p. 2893–2902.

BARJATYA, A.; SWENSON, C. M.; THOMPSON, D. C.; WRIGHT, K. H. Invited article: Data analysis of the floating potential measurement unit aboard the international space station. **Review of Scientific Instruments**, American Institute of Physics, v. 80, n. 4, p. 041301, 2009.

BATISTA, I. S.; ABDU, M. A. Equatorial f region vertical plasma drifts: Seasonal and longitudinal asymmetries in the american sector. **Journal of Geophysical Research: Space Physics**, Wiley Online Library, v. 91, n. A11, p. 12055–12064, 1986.

BATISTA, I. S.; DIOGO, E. M.; SOUZA, J. R.; ABDU, M. A.; BAILEY, G. J. Equatorial ionization anomaly: The role of thermospheric winds and the effects of the geomagnetic field secular variation. **Aeronomy of the Earth's Atmosphere and Ionosphere**, Springer, p. 317–328, 2011.

BATISTA, I. S.; MEDEIROS, R. T.; ABDU, M. A.; SOUZA, J. R.; BAILEY, G. J.; DE PAULA, E. R. Equatorial ionospheric vertical plasma drift model over the brazilian region. **Journal of Geophysical Research: Space Physics**, Wiley Online Library, v. 101, n. A5, p. 10887–10892, 1996.

BERGIN, A.; CHAPMAN, S. C.; WATKINS, N. W.; MOLONEY, N. R.; GJERLOEV, J. W. Extreme event statistics in dst, sym-h, and smr geomagnetic indices. **Space Weather**, Wiley Online Library, v. 21, n. 3, p. e2022SW003304, 2023.

BILITZA, D.; ALTADILL, D.; REINISCH, B. W.; GALKIN, I.; SHUBIN, V.; TRUHLIK, V. The international reference ionosphere: Model update 2016. *In*: **EGU general assembly conference abstracts**. **Proceedings** [...]. [*S.l.: s.n.*], 2016. p. EPSC2016–9671.

BILITZA, D.; ALTADILL, D.; TRUHLIK, V.; SHUBIN, V.; GALKIN, I.; REINISCH, B. W.; HUANG, X. International reference ionosphere 2016: From ionospheric climate to real-time weather predictions. **Space weather**, Wiley Online Library, v. 15, n. 2, p. 418–429, 2017.

BILITZA, D.; PEZZOPANE, M.; TRUHLIK, V.; ALTADILL, D.; REINISCH, B. W.; PIGNALBERI, A. The international reference ionosphere model: A review and description of an ionospheric benchmark. **Reviews of Geophysics**, Wiley Online Library, v. 60, n. 4, p. e2022RG000792, 2022.

BILITZA, D.; REINISCH, B. W. International reference ionosphere 2007: Improvements and new parameters. **Advances in space research**, Elsevier, v. 42, n. 4, p. 599–609, 2008.

BIRKELAND, K. **On the cause of magnetic storms and the origin of terrestrial magnetism**. [*S.l.*]: H. Aschehoug & Company, 1908.

BITTENCOURT, J. A. **Fundamentals of plasma physics**. [*S.l.*]: Spring, 2004.

BITTENCOURT, J. A.; SAHAI, Y. F-region neutral winds from ionosonde measurements of hmf2 at low latitude magnetic conjugate regions. **Journal of Atmospheric and Terrestrial Physics**, Elsevier, v. 40, n. 6, p. 669–676, 1978.

BLANC, M. Midlatitude convection electric fields and their relation to ring current development. **Geophys. Res. Lett**, v. 5, n. 3, p. 203–206, 1978.

BLANC, M. Magnetospheric convection effects at mid-latitudes: 3. theoretical derivation of the disturbance convection pattern in the plasmasphere. **J. Geophys. Res. Space Phys**, v. 88, n. A1, p. 235–251, 1983.

BLANC, M.; RICHMOND, A. D. The ionospheric disturbance dynamo. **Journal of Geophysical Research: Space Physics**, Wiley Online Library, v. 85, n. A4, p. 1669–1686, 1980.

BONNEVIER, B.; BOSTRÖM, R.; ROSTOKER, G. A three-dimensional model current system for polar magnetic substorms. **Journal of Geophysical Research**, Wiley Online Library, v. 75, n. 1, p. 107–122, 1970.

BOOKER, H. G.; WELLS, H. W. Scattering of radio waves by the f-region of the ionosphere. **Terrestrial Magnetism and Atmospheric Electricity**, Wiley Online Library, v. 43, n. 3, p. 249–256, 1938.

BOSTRÖM, R. A model of the auroral electrojets. **Journal of Geophysical Research**, Wiley Online Library, v. 69, n. 23, p. 4983–4999, 1964.

BOWLES, K. Progress report# 1 lima radar observatory-international cooperative project-national bureau of standards and instituto geofísico del perú. National Bureau of Standards Report, 1961.

BROADWATER, D. J. **A Comparison of Ionospheric Model Performance for International Space Station Orbits**. Thesis (Doutorado) — AIR FORCE INST OF TECH WRIGHT-PATTERSON AFB OH GRADUATE SCHOOL OF, 2013.

BURNS, A. G.; SOLOMON, S. C.; WANG, W.; QIAN, L.; ZHANG, Y.; PAXTON, L. J. Daytime climatology of ionospheric nmf2 and hmf2 from cosmic data. **Journal of Geophysical Research: Space Physics**, Wiley Online Library, v. 117, n. A9, 2012.

BURNS, A. G.; ZENG, Z.; WANG, W.; LEI, J.; SOLOMON, S. C.; RICHMOND, A. D.; KILLEEN, T. L.; KUO, Y.-H. Behavior of the f2 peak ionosphere over the south pacific at dusk during quiet summer conditions from cosmic data. **Journal of Geophysical Research: Space Physics**, Wiley Online Library, v. 113, n. A12, 2008.

CAI, X.; BURNS, A. G.; WANG, W.; COSTER, A. J.; QIAN, L.; LIU, J.; SOLOMON, S. C.; EASTES, R. W.; DANIELL, R. E.; MCCLINTOCK, W. E. Comparison of gold nighttime measurements with total electron content: Preliminary results. **Journal of Geophysical Research: Space Physics**, Wiley Online Library, v. 125, n. 9, p. e2019JA027767, 2020.

CHANDRA, H.; RASTOGI, R. G. Geomagnetic storm effects on ionospheric drifts & the equatorial e s, over the magnetic equator. **Indian J. Radio Space Phys**, v. 3, n. 4, p. 332–336, 1974.

CHANG, F.-Y.; LIU, J.-Y.; CHANG, L. C.; LIN, C.-H.; CHEN, C.-H. Three-dimensional electron density along the wsa and msna latitudes probed by formosat-3/cosmic. **Earth, Planets and Space**, Springer, v. 67, p. 1–8, 2015.

CHANG, F.-Y.; LIU, J.-Y.; FANG, T.-W.; RAJESH, P. K.; LIN, C.-H. Plasma depletion bays in the equatorial ionosphere observed by formosat-3/cosmic during 2007–2014. **Journal of Geophysical Research: Space Physics**, Wiley Online Library, v. 125, n. 9, p. e2019JA027501, 2020.

CHANG, L. C.; LIU, H.; MIYOSHI, Y.; CHEN, C.-H.; CHANG, F.-Y.; LIN, C.-H.; LIU, J.-Y.; SUN, Y.-Y. Structure and origins of the weddell sea anomaly from tidal and planetary wave signatures in formosat-3/cosmic observations and gaia gcm simulations. **Journal of Geophysical Research: Space Physics**, Wiley Online Library, v. 120, n. 2, p. 1325–1340, 2015.

CHEN, C.-H.; SAITO, A.; LIN, C.-H.; LIU, J.-Y. Long-term variations of the nighttime electron density enhancement during the ionospheric midlatitude summer. **Journal of Geophysical Research: Space Physics**, Wiley Online Library, v. 117, n. A7, 2012.

CHOI, J. M.; LIN, C.-H.; RAJESH, P. K.; PARK, J.; KWAK, Y.-S.; CHEN, S.-P.; LIN, J. T.; CHANG, M. T. Comparisons of in situ ionospheric density using ion velocity meters onboard formosat-7/cosmic-2 and icon missions. **Earth, Planets and Space**, Springer, v. 75, n. 1, p. 15, 2023.

CLAUER, C. R.; MCPHERRON, R. L. Mapping the local time-universal time development of magnetospheric substorms using mid-latitude magnetic observations. **Journal of Geophysical Research**, Wiley Online Library, v. 79, n. 19, p. 2811–2820, 1974.

COFFEY, V. N.; SAZYKIN, S.; CHANDLER, M. O.; HAIRSTON, M. R.; MINOW, J. I.; ANDERSON, B. Observations of deep ionospheric f-region density depletions with fpmu instrumentation and their relationship with the global dynamics of the june 22-23, 2015 geomagnetic storm. *In*: **Applied Space Environments Conference (ASEC) 2017**. **Proceedings** [...]. [*S.l.: s.n.*], 2017.

COFFEY, V. N.; WRIGHT, K. H.; MINOW, J. I.; SCHNEIDER, T. A.; VAUGHN, J. A.; CRAVEN, P. D.; CHANDLER, M. O.; KOONTZ, S. L.; PARKER, L. N.; BUI, T. H. Validation of the plasma densities and temperatures from the iss floating potential measurement unit. **IEEE transactions on plasma science**, IEEE, v. 36, n. 5, p. 2301–2308, 2008.

COWLEY, S. W. H. Magnetosphere-ionosphere interactions: A tutorial review. **Magnetospheric Current Systems, Geophys. Monogr. Ser**, v. 118, p. 91–106, 2000.

COXON, J. C.; MILAN, S. E.; CLAUSEN, L. B. N.; ANDERSON, B. J.; KORTH, H. The magnitudes of the regions 1 and 2 birkeland currents observed by ampere and their role in solar wind-magnetosphere-ionosphere coupling. **Journal of Geophysical Research: Space Physics**, Wiley Online Library, v. 119, n. 12, p. 9804–9815, 2014.

CRAIN, D. J.; HEELIS, R. A.; BAILEY, G. J. Effects of electrical coupling on equatorial ionospheric plasma motions: When is the f region a dominant driver in the low-latitude dynamo? **Journal of Geophysical Research: Space Physics**, Wiley Online Library, v. 98, n. A4, p. 6033–6037, 1993.

CUMMINGS, W. D.; DESSLER, A. J. Field-aligned currents in the magnetosphere. **Journal of Geophysical Research**, Wiley Online Library, v. 72, n. 3, p. 1007–1013, 1967.

DAGLIS, I. A.; THORNE, R. M.; BAUMJOHANN, W.; ORSINI, S. The terrestrial ring current: Origin, formation, and decay. **Reviews of Geophysics**, Wiley Online Library, v. 37, n. 4, p. 407–438, 1999.

DAO, E.; KELLEY, M. C.; RODDY, P. A.; RETTERER, J.; BALLENTHIN, J. O.; DE LA BEAUJARDIERE, O.; SU, Y. J. Longitudinal and seasonal dependence of nighttime equatorial plasma density irregularities during solar minimum detected on the c/nofs satellite. **Geophysical Research Letters**, Wiley Online Library, v. 38, n. 10, 2011.

DE LA BEAUJARDIERE, O. C/nofs: A mission to forecast scintillations. **Journal of Atmospheric and Solar-Terrestrial Physics**, Elsevier, v. 66, n. 17, p. 1573–1591, 2004.

DE LA BEAUJARDIERE, O.; RETTERER, J.; PFAFF, R. F.; RODDY, P. A.; ROTH, C.; BURKE, W. J.; SU, Y. J.; KELLEY, M. C.; ILMA, R. R.; WILSON, G. R. C/nofs observations of deep plasma depletions at dawn. **Geophysical Research Letters**, Wiley Online Library, v. 36, n. 18, 2009.

DEBCHOUDHURY, S.; BARJATYA, A.; MINOW, J. I.; COFFEY, V. N.; CHANDLER, M. O. Observations and validation of plasma density, temperature, and abundance from a langmuir probe onboard the international space station. **Journal of Geophysical Research: Space Physics**, Wiley Online Library, v. 126, n. 10, p. e2021JA029393, 2021.

DEBCHOUDHURY, S.; BARJATYA, A.; MINOW, J. I.; COFFEY, V. N.; PARKER, L. N. Climatology of deep o+ dropouts in the night-time f-region in solar minimum measured by a langmuir probe onboard the international space station. **Journal of Geophysical Research: Space Physics**, Wiley Online Library, v. 127, n. 7, p. e2022JA030446, 2022.

DUBAZANE, M. B.; HABARULEMA, J. B. An empirical model of vertical plasma drift over the african sector. **Space Weather**, Wiley Online Library, v. 16, n. 6, p. 619–635, 2018.

DUDENEY, J. R.; PIGGOTT, W. R. Antarctic ionospheric research. **Upper atmosphere research in Antarctica**, Wiley Online Library, v. 29, p. 200–235, 1978.

EASTES, R. W.; KARAN, D. K.; MARTINIS, C.; DANIELL, R. E.; GAN, Q.; BURNS, A. G.; MCCLINTOCK, W. E. Gold observations of longitudinal variations in the nighttime equatorial ionization anomaly (eia) crests' latitudes. **Journal of Geophysical Research: Space Physics**, Wiley Online Library, v. 128, n. 4, p. e2022JA031007, 2023.

ENGLAND, S. L.; MAUS, S.; IMMEL, T. J.; MENDE, S. B. Longitudinal variation of the e-region electric fields caused by atmospheric tides. **Geophysical Research Letters**, Wiley Online Library, v. 33, n. 21, 2006.

ERLANDSON, R. E.; ZANETTI, L. J.; POTEMRA, T. A.; BYTHROW, P. F.; LUNDIN, R. Imf by dependence of region 1 birkeland currents near noon. **Journal of Geophysical Research: Space Physics**, Wiley Online Library, v. 93, n. A9, p. 9804–9814, 1988.

EVANS, J. V. Cause of the mid-latitude evening increase in fo f 2. **Journal of Geophysical Research**, Wiley Online Library, v. 70, n. 5, p. 1175–1185, 1965.

FARLEY, D. T.; BALSEY, B. B.; WOODMAN, R. F.; MCCLURE, J. P. Equatorial spread f: Implications of vhf radar observations. **Journal of Geophysical Research**, Wiley Online Library, v. 75, n. 34, p. 7199–7216, 1970.

FARLEY, D. T.; BONELLI, E.; FEJER, B. G.; LARSEN, M. F. The prereversal enhancement of the zonal electric field in the equatorial ionosphere. **Journal of Geophysical Research: Space Physics**, Wiley Online Library, v. 91, n. A12, p. 13723–13728, 1986.

FARLEY, D. T.; MCCLURE, J. P.; STERLING, D. L.; GREEN, J. L. Temperature and composition of the equatorial ionosphere. **Journal of Geophysical Research**, Wiley Online Library, v. 72, n. 23, p. 5837–5851, 1967.

FEJER, B. G. Low latitude electrodynamic plasma drifts: A review. **Journal of Atmospheric and Terrestrial Physics**, Elsevier, v. 53, n. 8, p. 677–693, 1991.

FEJER, B. G. The electrodynamics of the low-latitude ionosphere: Recent results and future challenges. **J. Atmos. Sol. Terr. Phys**, v. 59, n. 13, p. 1465–1482, 1997.

FEJER, B. G. Low latitude storm time ionospheric electrodynamics. **J. Atmos. Sol. Terr. Phys**, v. 64, n. 12-14, p. 1401–1408, 2002.

FEJER, B. G.; DE PAULA, E. R.; HEELIS, R. A.; HANSON, W. B. Global equatorial ionospheric vertical plasma drifts measured by the ae-e satellite. **Journal of Geophysical Research: Space Physics**, Wiley Online Library, v. 100, n. A4, p. 5769–5776, 1995.

FEJER, B. G.; EMMERT, J. T. Low-latitude ionospheric disturbance electric field effects during the recovery phase of the 19–21 october 1998 magnetic storm. **Journal of Geophysical Research: Space Physics**, Wiley Online Library, v. 108, n. A12, 2003.

FEJER, B. G.; FARLEY, D. T.; BALSLEY, B. B.; WOODMAN, R. F. Radar studies of anomalous velocity reversals in the equatorial ionosphere. **J. Geophys. Res**, v. 81, n. 25, p. 4621–4626, 1976.

FEJER, B. G.; JENSEN, J. W.; KIKUCHI, T.; ABDU, M. A.; CHAU, J. L. Equatorial ionospheric electric fields during the november 2004 magnetic storm. **Journal of Geophysical Research: Space Physics**, Wiley Online Library, v. 112, n. A10, 2007.

FEJER, B. G.; JENSEN, J. W.; SU, S.-Y. Quiet time equatorial f region vertical plasma drift model derived from rocsat-1 observations. **Journal of Geophysical Research: Space Physics**, Wiley Online Library, v. 113, n. A5, 2008.

FEJER, B. G.; JENSEN, J. W.; SU, S.-Y. Seasonal and longitudinal dependence of equatorial disturbance vertical plasma drifts. **Geophysical Research Letters**, Wiley Online Library, v. 35, n. 20, 2008.

FEJER, B. G.; KELLEY, M. C. Ionospheric irregularities. **Reviews of Geophysics**, Wiley Online Library, v. 18, n. 2, p. 401–454, 1980.

FEJER, B. G.; KELLEY, M. C.; SENIOR, C.; DE LA BEAUJARDIERE, O.; HOLT, J. A.; TEPLEY, C. A.; BURNSIDE, R.; ABDU, M. A.; SOBRAL, J. H. A.; WOODMAN, R. F. Low-and mid-latitude ionospheric electric fields during the january 1984 gismos campaign. **Journal of Geophysical Research: Space Physics**, Wiley Online Library, v. 95, n. A3, p. 2367–2377, 1990.

FEJER, B. G.; LARANJA, S. R.; CONDOR, P. Multi-process driven unusually large equatorial perturbation electric fields during the april 2023 geomagnetic storm. **Frontiers in Astronomy and Space Sciences**, Frontiers, v. 11, p. 1351735, 2024.

FEJER, B. G.; MAUTE, A. Equatorial ionospheric electrodynamics. **Ionosphere Dynamics and Applications**, Wiley Online Library, p. 159–183, 2021.

FEJER, B. G.; NAVARRO, L. A. First observations of equatorial ionospheric electric fields driven by storm-time rapidly recurrent magnetospheric substorms. **Journal of Geophysical Research: Space Physics**, Wiley Online Library, v. 127, n. 12, p. e2022JA030940, 2022.

FEJER, B. G.; NAVARRO, L. A.; SAZYKIN, S.; NEWHEART, A. M.; MILLA, M. A.; CONDOR, P. Prompt penetration and substorm effects over jicamarca during the september 2017 geomagnetic storm. **Journal of Geophysical Research: Space Physics**, Wiley Online Library, v. 126, n. 8, p. e2021JA029651, 2021.

FEJER, B. G.; SCHERLIESS, L. Time dependent response of equatorial ionospheric electric fields to magnetospheric disturbances. **Geophysical Research Letters**, Wiley Online Library, v. 22, n. 7, p. 851–854, 1995.

FEJER, B. G.; SCHERLIESS, L. Empirical models of storm time equatorial zonal electric fields. **Journal of Geophysical Research: Space Physics**, Wiley Online Library, v. 102, n. A11, p. 24047–24056, 1997.

FEJER, B. G.; SCHERLIESS, L. Empirical models of storm time equatorial zonal electric fields. **J. Geophys. Res. Space Phys**, v. 102, n. A11, p. 24047–24056, 1997.

FEJER, B. G.; SCHERLIESS, L.; DE PAULA, E. R. Effects of the vertical plasma drift velocity on the generation and evolution of equatorial spread f. **J. Geophys. Res. Space Phys**, v. 104, n. A9, p. 19859–19869, 1999.

FEJER, B. G.; SPIRO, R. W.; WOLF, R. A.; FOSTER, J. C. Latitudinal variation of perturbation electric fields during magnetically disturbed periods-1986 sundial observations and model results. **Ann. Geophys**, v. 8, n. 6, p. 441–454, 1990.

FEJER, B. G.; SPIRO, R. W.; WOLF, R. A.; FOSTER, J. C. Latitudinal variation of perturbation electric fields during magnetically disturbed periods-1986 sundial observations and model results. *In*: **Annales geophysicae. Proceedings** [...]. [*S.l.: s.n.*], 1990. v. 8, p. 441–454.

FESEN, C. G.; ROBLE, R. G.; RIDLEY, E. C. Thermospheric tides at equinox: Simulations with coupled composition and auroral forcings: 2. semidiurnal component. **Journal of Geophysical Research: Space Physics**, Wiley Online Library, v. 96, n. A3, p. 3663–3677, 1991.

FRITTS, D. C.; VADAS, S. L. Gravity wave penetration into the thermosphere: sensitivity to solar cycle variations and mean winds. *In*: COPERNICUS GMBH. **Annales Geophysicae. Proceedings** [...]. [*S.l.: s.n.*], 2008. v. 26, n. 12, p. 3841–3861.

FULLER-ROWELL, T. J.; AKMAEV, R. A.; WU, F.; ANGHEL, A.; MARUYAMA, N.; ANDERSON, D. N.; CODRESCU, M. V.; IREDELL, M.; MOORTHI, S.; JUANG, H. M. Impact of terrestrial weather on the upper atmosphere. **Geophysical Research Letters**, Wiley Online Library, v. 35, n. 9, 2008.

FULLER-ROWELL, T. J.; MILLWARD, G. H.; RICHMOND, A. D.; CODRESCU, M. V. Storm-time changes in the upper atmosphere at low latitudes. **Journal of atmospheric and solar-terrestrial physics**, Elsevier, v. 64, n. 12-14, p. 1383–1391, 2002.

GANUSHKINA, N. Y.; LIEMOHN, M. W.; DUBYAGIN, S. Current systems in the earth's magnetosphere. **Reviews of Geophysics**, Wiley Online Library, v. 56, n. 2, p. 309–332, 2018.

GJERLOEV, J. W. The supermag data processing technique. **Journal of Geophysical Research: Space Physics**, Wiley Online Library, v. 117, n. A9, 2012.

GONZALES, C. A.; KELLEY, M. C.; FEJER, B. G.; VICKREY, J. F.; WOODMAN, R. F. Equatorial electric fields during magnetically disturbed conditions 2. implications of simultaneous auroral and equatorial measurements. **Journal of Geophysical Research: Space Physics**, Wiley Online Library, v. 84, n. A10, p. 5803–5812, 1979.

GONZALEZ, W. D.; JOSELYN, J. A.; KAMIDE, Y.; KROEHL, H. W.; ROSTOKER, G.; TSURUTANI, B. T.; VASYLIUNAS, V. M. What is a geomagnetic storm? **Journal of Geophysical Research: Space Physics**, Wiley Online Library, v. 99, n. A4, p. 5771–5792, 1994.

HAERENDEL, G.; ECCLES, J. V.; CAKIR, S. Theory for modeling the equatorial evening ionosphere and the origin of the shear in the horizontal plasma flow. **Journal of Geophysical Research: Space Physics**, Wiley Online Library, v. 97, n. A2, p. 1209–1223, 1992.

HAGAN, M. E.; FORBES, J. M. Migrating and nonmigrating semidiurnal tides in the upper atmosphere excited by tropospheric latent heat release. **Journal of Geophysical Research: Space Physics**, Wiley Online Library, v. 108, n. A2, 2003.

HANSON, W. B.; SANATANI, S. Relationship between fe+ ions and equatorial spread f. **Journal of Geophysical Research**, Wiley Online Library, v. 76, n. 31, p. 7761–7768, 1971.

HARTMAN, W. A.; SCHMIDL, W. D.; MIKATARIAN, R.; GALKIN, I. Correlation of irtam and fpmu data confirming the application of irtam to support iss program safety. **Advances in Space Research**, Elsevier, v. 63, n. 6, p. 1838–1844, 2019.

HEELIS, R. A. Low-and middle-latitude ionospheric dynamics associated with magnetic storms. **Washington DC American Geophysical Union Geophysical Monograph Series**, v. 181, p. 51–61, 2008.

HINES, C. O. Internal atmospheric gravity waves at ionospheric heights. **Canadian Journal of Physics**, NRC Research Press Ottawa, Canada, v. 38, n. 11, p. 1441–1481, 1960.

HUANG, C. M.; CHEN, M. Q. Formation of maximum electric potential at the geomagnetic equator by the disturbance dynamo. **Journal of Geophysical Research: Space Physics**, Wiley Online Library, v. 113, n. A3, 2008.

HUANG, C.-S. Eastward electric field enhancement and geomagnetic positive bay in the dayside low-latitude ionosphere caused by magnetospheric substorms during sawtooth events. **Geophysical Research Letters**, Wiley Online Library, v. 36, n. 18, 2009.

HUANG, C.-S. Storm-to-storm main phase repeatability of the local time variation of disturbed low-latitude vertical ion drifts. **Geophys. Res. Lett**, v. 42, n. 14, p. 5694–5701, 2015.

HUANG, C.-S. The characteristics and generation mechanism of small-amplitude and large-amplitude esf irregularities observed by the c/nofs satellite. **Journal of Geophysical Research: Space Physics**, Wiley Online Library, v. 122, n. 8, p. 8959–8973, 2017.

HUANG, C.-S. Long-lasting penetration electric fields during geomagnetic storms: Observations and mechanisms. **Journal of Geophysical Research: Space Physics**, Wiley Online Library, v. 124, n. 11, p. 9640–9664, 2019.

HUANG, C.-S. Systematical analyses of global ionospheric disturbance current systems caused by multiple processes: Penetration electric fields, solar wind pressure impulses, magnetospheric substorms, and ulf waves. **Journal of Geophysical Research: Space Physics**, Wiley Online Library, v. 125, n. 9, p. e2020JA027942, 2020.

HUANG, C.-S.; DE LA BEAUJARDIERE, O.; RODDY, P. A.; HUNTON, D. E.; BALLENTHIN, J. O.; HAIRSTON, M. R.; PFAFF, R. F. Large-scale quasiperiodic plasma bubbles: C/nofs observations and causal mechanism. **Journal of Geophysical Research: Space Physics**, Wiley Online Library, v. 118, n. 6, p. 3602–3612, 2013.

HUANG, C.-S.; DE LA BEAUJARDIERE, O.; RODDY, P. A.; HUNTON, D. E.; LIU, J.-Y.; CHEN, S.-P. Occurrence probability and amplitude of equatorial ionospheric irregularities associated with plasma bubbles during low and moderate solar activities (2008–2012). **Journal of Geophysical Research: Space Physics**, Wiley Online Library, v. 119, n. 2, p. 1186–1199, 2014.

HUANG, C.-S.; FOSTER, J. C.; KELLEY, M. C. Long-duration penetration of the interplanetary electric field to the low-latitude ionosphere during the main phase of magnetic storms. **Journal of Geophysical Research: Space Physics**, Wiley Online Library, v. 110, n. A11, 2005.

HUANG, C.-S.; HAIRSTON, M. R. The postsunset vertical plasma drift and its effects on the generation of equatorial plasma bubbles observed by the c/nofs satellite. **Journal of Geophysical Research: Space Physics**, Wiley Online Library, v. 120, n. 3, p. 2263–2275, 2015.

HUANG, C.-S.; KELLEY, M. C.; HYSELL, D. L. Nonlinear rayleigh-taylor instabilities, atmospheric gravity waves and equatorial spread f. **Journal of Geophysical Research: Space Physics**, Wiley Online Library, v. 98, n. A9, p. 15631–15642, 1993.

HUANG, C.-S.; RICH, F. J.; DE LA BEAUJARDIERE, O.; HEELIS, R. A. Longitudinal and seasonal variations of the equatorial ionospheric ion density and eastward drift velocity in the dusk sector. **Journal of Geophysical Research: Space Physics**, Wiley Online Library, v. 115, n. A2, 2010.

HUANG, C.-S.; SAZYKIN, S.; CHAU, J. L.; MARUYAMA, N.; KELLEY, M. C. Penetration electric fields: Efficiency and characteristic time scale. **Journal of Atmospheric and Solar-Terrestrial Physics**, Elsevier, v. 69, n. 10-11, p. 1135–1146, 2007.

HUANG, C.-S.; SAZYKIN, S.; SPIRO, R. W.; GOLDSTEIN, J.; CROWLEY, G.; RUOHONIEMI, J. M. **Storm-time penetration electric fields and their effects**. [*S.l.*]: Wiley Online Library, 2006.

HUANG, C.-S.; YUMOTO, K.; ABE, S.; SOFKO, G. Low-latitude ionospheric electric and magnetic field disturbances in response to solar wind pressure enhancements. **Journal of Geophysical Research: Space Physics**, Wiley Online Library, v. 113, n. A8, 2008.

HUANG, C.-S.; ZHANG, Y. Equatorial plasma drifts during the magnetic storm on november 7–11, 2004: Identifications of the roles of penetration and disturbance dynamo electric fields with multi-instrumental measurements. **Journal of Geophysical Research: Space Physics**, Wiley Online Library, v. 126, n. 9, p. e2021JA029386, 2021.

HYSELL, D. L.; KELLEY, M. C.; SWARTZ, W. E.; WOODMAN, R. F. Seeding and layering of equatorial spread f by gravity waves. **Journal of Geophysical Research: Space Physics**, Wiley Online Library, v. 95, n. A10, p. 17253–17260, 1990.

IIJIMA, T.; POTEMRA, T. A. The amplitude distribution of field-aligned currents at northern high latitudes observed by triad. **Journal of Geophysical Research**, Wiley Online Library, v. 81, n. 13, p. 2165–2174, 1976.

IMMEL, T. J.; SAGAWA, E.; ENGLAND, S. L.; HENDERSON, S. B.; HAGAN, M. E.; MENDE, S. B.; FREY, H. U.; SWENSON, C. M.; PAXTON, L. J. Control of equatorial ionospheric morphology by atmospheric tides. **Geophysical Research Letters**, Wiley Online Library, v. 33, n. 15, 2006.

IYEMORI, T.; TAKEDA, M.; NOSE, M.; ODAGI, Y.; TOH, H. Mid-latitude geomagnetic indices "asy" and "sym" for 2009 (provisional). **Data Analysis Center for Geomagnetism and Space Magnetism, Graduate School of Science, Kyoto University, Japan**, 2010.

JIN, H.; MIYOSHI, Y.; FUJIWARA, H.; SHINAGAWA, H. Electrodynamics of the formation of ionospheric wave number 4 longitudinal structure. **Journal of Geophysical Research: Space Physics**, Wiley Online Library, v. 113, n. A9, 2008.

JOHANSSON, G. **Beamforming and timing design issues for a large aperture array radar applied to atmospheric research**. Thesis (Doutorado) — Luleå tekniska universitet, 2009.

KARAN, D. K.; MARTINIS, C.; EASTES, R. W.; DANIELL, R. E.; MCCLINTOCK, W. E.; HUANG, C.-S. Gold observations of equatorial plasma bubbles reaching mid-latitudes during the 23 april 2023 geomagnetic storm. **Authorea Preprints**, Authorea, 2023.

KEILING, A.; RAMOS, C.; VU, N.; ANGELOPOULOS, V.; NOSÉ, M. Statistical properties and proposed source mechanism of recurrent substorm activity with one-hour periodicity. **Journal of Geophysical Research: Space Physics**, Wiley Online Library, v. 127, n. 3, p. e2021JA030064, 2022.

KELLEY, M. C. **The Earth's ionosphere: Plasma physics and electrodynamics**. [S.l.]: Academic press, 2009.

KELLEY, M. C.; FEJER, B. G.; GONZALES, C. A. An explanation for anomalous equatorial ionospheric electric fields associated with a northward turning of the interplanetary magnetic field. **Geophysical Research Letters**, Wiley Online Library, v. 6, n. 4, p. 301–304, 1979.

KELLEY, M. C.; ILMA, R. R.; CROWLEY, G. On the origin of pre-reversal enhancement of the zonal equatorial electric field. *In*: COPERNICUS GMBH. **Annales geophysicae**. **Proceedings** [...]. [*S.l.: s.n.*], 2009. v. 27, n. 5, p. 2053–2056.

KELLEY, M. C.; MAKELA, J. J.; CHAU, J. L.; NICOLLS, M. J. Penetration of the solar wind electric field into the magnetosphere/ionosphere system. **Geophysical Research Letters**, Wiley Online Library, v. 30, n. 4, 2003.

KELLEY, M. C.; RETTERER, J. First successful prediction of a convective equatorial ionospheric storm using solar wind parameters. **Space Weather**, Wiley Online Library, v. 6, n. 8, 2008.

KHADKA, S. M.; VALLADARES, C. E.; SHEEHAN, R.; GERRARD, A. J. Effects of electric field and neutral wind on the asymmetry of equatorial ionization anomaly. **Radio Science**, AGU, v. 53, n. 5, p. 683–697, 2018.

KIKUCHI, T.; ARAKI, T.; MAEDA, H.; MAEKAWA, K. Transmission of polar electric fields to the equator. **Nature**, v. 273, n. 5664, p. 650–651, 1978.

KIKUCHI, T.; TSUNOMURA, S.; HASHIMOTO, K.; NOZAKI, K. Field-aligned current effects on midlatitude geomagnetic sudden commencements. **Journal of Geophysical Research: Space Physics**, Wiley Online Library, v. 106, n. A8, p. 15555–15565, 2001.

KIL, H.; CHOI, H.-S.; HEELIS, R. A.; PAXTON, L. J.; COLEY, W. R.; MILLER, E. S. Onset conditions of bubbles and blobs: A case study on 2 march 2009. **Geophysical Research Letters**, Wiley Online Library, v. 38, n. 6, 2011.

KIL, H.; KWAK, Y.-S.; LEE, W. K.; MILLER, E. S.; OH, S. J.; CHOI, H.-S. The causal relationship between plasma bubbles and blobs in the low-latitude f region during a solar minimum. **Journal of Geophysical Research: Space Physics**, Wiley Online Library, v. 120, n. 5, p. 3961–3969, 2015.

KIL, H.; OH, S. J.; PAXTON, L. J.; FANG, T.-W. High-resolution vertical e× b drift model derived from rocsat-1 data. **Journal of Geophysical Research: Space Physics**, Wiley Online Library, v. 114, n. A10, 2009.

KINTNER, P. M.; COSTER, A. J.; FULLER-ROWELL, T. J.; MANNUCCI, A. J.; MENDILLO, M.; HEELIS, R. A. Midlatitude ionospheric dynamics and disturbances: Introduction. **Washington DC American Geophysical Union Geophysical Monograph Series**, v. 181, p. 1–7, 2008.

KINTNER, P. M.; COSTER, A. J.; FULLER-ROWELL, T. J.; MANNUCCI, A. J.; MENDILLO, M.; HEELIS, R. A. **Midlatitude ionospheric dynamics and disturbances**. [*S.l.*]: John Wiley & Sons, 2013.

KIRCHHOFF, V. Principios basicos em espalhamento incoerente e sua contribuicao para o estudo da fisica da atmosfera superior. 1978.

KUDEKI, E.; BHATTACHARYYA, S.; WOODMAN, R. F. A new approach in incoherent scatter f region exb drift measurements at jicamarca. **J. Geophys. Res. Space Phys**, v. 104, n. A12, p. 28145–28162, 1999.

KUMAR, A.; CHAKRABARTY, D.; PANDEY, K.; FEJER, B. G.; SUNDA, S.; SEEMALA, G. K.; SRIPATHI, S.; YADAV, A. K. Evidence for the significant differences in response times of equatorial ionization anomaly crest corresponding to plasma fountains during daytime and post-sunset hours. **Journal of Geophysical Research: Space Physics**, Wiley Online Library, v. 126, n. 3, p. e2020JA028628, 2021.

KUYENG, K.; SCIPION, D.; CONDOR, P.; MANAY, E.; MILLA, M. A. Preliminary results of new operation mode julia medium power at jro'. *In*: **2023 CEDAR Workshop**. San Diego, CA, USA: [*s.n.*], 2023. 25-30 June, viewed 30 November, 2023,. Available at: http://hdl. handle. net/20. 500. 12816/5441.

LARANJA, S. R.; FEJER, B. G.; RIDENTI, M. A.; AMORIM, J.; SWENSON, C. M. Ion density climatology based on fpmu measurements on board the international space station. **Journal of Geophysical Research: Space Physics**, Wiley Online Library, v. 128, n. 12, p. e2023JA031980, 2023.

LI, G.; NING, B.; LIU, L.; ZHAO, B.; YUE, X.; SU, S.-Y.; VENKATRAMAN, S. Correlative study of plasma bubbles, evening equatorial ionization anomaly, and equatorial prereversal e× b drifts at solar maximum. **Radio Science**, AGU, v. 43, n. 04, p. 1–11, 2008.

LIN, C.-H.; LIU, C.-H.; LIU, J.-Y.; CHEN, C.-H.; BURNS, A. G.; WANG, W. Midlatitude summer nighttime anomaly of the ionospheric electron density observed by formosat-3/cosmic. **Journal of Geophysical Research: Space Physics**, Wiley Online Library, v. 115, n. A3, 2010.

LIN, C.-H.; LIU, J.-Y.; CHENG, C. Z.; CHEN, C.-H.; LIU, C.-H.; WANG, W.; BURNS, A. G.; LEI, J. Three-dimensional ionospheric electron density structure of the weddell sea anomaly. **Journal of Geophysical Research: Space Physics**, Wiley Online Library, v. 114, n. A2, 2009.

LIN, C.-H.; WANG, W.; HAGAN, M. E.; HSIAO, C. C.; IMMEL, T. J.; HSU, M. L.; LIU, J.-Y.; PAXTON, L. J.; FANG, T.-W.; LIU, C.-H. Plausible effect of atmospheric tides on the equatorial ionosphere observed by the formosat-3/cosmic: Three-dimensional electron density structures. **Geophysical Research Letters**, Wiley Online Library, v. 34, n. 11, 2007.

LIU, H.; LÜHR, H.; WATANABE, S.; KÖHLER, W.; HENIZE, V.; VISSER, P. Zonal winds in the equatorial upper thermosphere: Decomposing the solar flux, geomagnetic activity, and seasonal dependencies. **Journal of Geophysical Research: Space Physics**, Wiley Online Library, v. 111, n. A7, 2006.

LIU, H.; THAMPI, S. V.; YAMAMOTO, M. Phase reversal of the diurnal cycle in the midlatitude ionosphere. **Journal of Geophysical Research: Space Physics**, Wiley Online Library, v. 115, n. A1, 2010.

LIU, J.; WANG, W.; BURNS, A. G.; SOLOMON, S. C.; ZHANG, S.; ZHANG, Y.; HUANG, C.-S. Relative importance of horizontal and vertical transports to the formation of ionospheric storm-enhanced density and polar tongue of ionization. **Journal of Geophysical Research: Space Physics**, Wiley Online Library, v. 121, n. 8, p. 8121–8133, 2016.

LIU, J.-Y.; KAN, K.-W.; CHAO, C.-K.; CHANG, F.-Y. Nighttime wavenumber-four and plasma depletion bays observed by formosat-5/aip, icon/ivm, and cosmic-2/ro data. **Advances in Space Research**, Elsevier, 2023.

LIU, J.-Y.; LIN, C.-H.; LIN, C.-Y.; LEE, I. T.; SUN, Y.-Y.; CHEN, S.-P.; CHANG, F.-Y.; RAJESH, P. K.; HSU, C. T.; MATSUO, T. Retrospect and prospect of ionospheric weather observed by formosat-3/cosmic and formosat-7/cosmic-2. **Terrestrial, Atmospheric and Oceanic Sciences**, Springer, v. 33, n. 1, p. 20, 2022.

LUAN, X.; SOLOMON, S. C. Meridional winds derived from cosmic radio occultation measurements. **Journal of Geophysical Research: Space Physics**, Wiley Online Library, v. 113, n. A8, 2008.

LUAN, X.; WANG, P.; DOU, X.; LIU, Y. C. M. Interhemispheric asymmetry of the equatorial ionization anomaly in solstices observed by cosmic during 2007–2012. **Journal of Geophysical Research: Space Physics**, Wiley Online Library, v. 120, n. 4, p. 3059–3073, 2015.

LÜHR, H.; KERVALISHVILI, G. Field-aligned currents in the magnetosphere–ionosphere. **Magnetospheres in the Solar System**, Wiley Online Library, p. 193–205, 2021.

MA, R.; XU, J.; LIAO, H. The features and a possible mechanism of semiannual variation in the peak electron density of the low latitude f2 layer. **Journal of atmospheric and solar-terrestrial physics**, Elsevier, v. 65, n. 1, p. 47–57, 2003.

MACPHERSON, B.; GONZALEZ, S. A.; BAILEY, G. J.; MOFFETT, R. J.; SULZER, M. P. The effects of meridional neutral winds on the o+-h+ transition altitude over arecibo. **Journal of Geophysical Research: Space Physics**, Wiley Online Library, v. 103, n. A12, p. 29183–29198, 1998.

MANOJ, C.; MAUS, S. A real-time forecast service for the ionospheric equatorial zonal electric field. **Space Weather**, Wiley Online Library, v. 10, n. 9, 2012.

MANOJ, C.; MAUS, S.; LÜHR, H.; ALKEN, P. Penetration characteristics of the interplanetary electric field to the daytime equatorial ionosphere. **Journal of Geophysical Research: Space Physics**, Wiley Online Library, v. 113, n. A12, 2008.

MARUYAMA, N.; RICHMOND, A. D.; FULLER-ROWELL, T. J.; CODRESCU, M. V.; SAZYKIN, S.; TOFFOLETTO, F. R. Interaction between direct penetration and disturbance dynamo electric fields in the storm-time equatorial ionosphere. **Geophys. Res. Lett**, v. 32, n. 17, 2005.

MATSUSHITA, S. Ionospheric variations associated with geomagnetic disturbances. **J. Geomagn. Geoelectr**, v. 5, n. 4, p. 109–135, 1953.

MATSUSHITA, S.; BALSLEY, B. B. Comments on nishida's reply. **Planet. Space Sci**, v. 21, n. 7, p. 1260–1262, 1973.

MCPHERRON, R. L. Earth's magnetotail. **Magnetotails in the solar system**, Wiley Online Library, p. 61–84, 2015.

MCPHERRON, R. L.; CHU, X. The midlatitude positive bay index and the statistics of substorm occurrence. **Journal of Geophysical Research: Space Physics**, Wiley Online Library, v. 123, n. 4, p. 2831–2850, 2018.

MCPHERRON, R. L.; RUSSELL, C. T.; AUBRY, M. P. Satellite studies of magnetospheric substorms on august 15, 1968: 9. phenomenological model for substorms. **Journal of Geophysical Research**, Wiley Online Library, v. 78, n. 16, p. 3131–3149, 1973.

MILLWARD, G. H.; MÜLLER-WODARG, I. C. F.; AYLWARD, A. D.; FULLER-ROWELL, T. J.; RICHMOND, A. D.; MOFFETT, R. J. An investigation into the influence of tidal forcing on f region equatorial vertical ion drift using a global ionosphere-thermosphere model with coupled electrodynamics. **Journal of Geophysical Research: Space Physics**, Wiley Online Library, v. 106, n. A11, p. 24733–24744, 2001.

MOTOBA, T.; KIKUCHI, T.; OKUZAWA, T.; YUMOTO, K. Dynamical response of the magnetosphere-ionosphere system to a solar wind dynamic pressure oscillation. **Journal of Geophysical Research: Space Physics**, Wiley Online Library, v. 108, n. A5, 2003.

NAPPO, C. J. **An introduction to atmospheric gravity waves**. [*S.l.*]: Academic press, 2013.

NAVARRO, L. A.; FEJER, B. G.; SCHERLIESS, L. Equatorial disturbance dynamo vertical plasma drifts over jicamarca: Bimonthly and solar cycle dependence. **J. Geophys. Res. Space Phys**, v. 124, n. 6, p. 4833–4841, 2019.

NEWELL, P. T.; SOTIRELIS, T.; LIOU, K.; RICH, F. J. Pairs of solar wind-magnetosphere coupling functions: Combining a merging term with a viscous term works best. **J. Geophys. Res. Space Phys**, v. 113, n. A4, 2008.

NEWHEART, A. M.; SAZYKIN, S.; COFFEY, V. N.; CHANDLER, M. O.; COSTER, A. J.; FEJER, B. G.; MINOW, J. I.; SWENSON, C. M. Observations of night-time equatorial ionosphere structure with the fpmu on board the international space station. **Journal of Geophysical Research: Space Physics**, Wiley Online Library, v. 127, n. 11, p. e2022JA030373, 2022.

NICOLLS, M. J.; KELLEY, M. C.; CHAU, J. L.; VELIZ, O.; ANDERSON, D.; ANGHEL, A. The spectral properties of low latitude daytime electric fields inferred from magnetometer observations. **Journal of atmospheric and solar-terrestrial physics**, Elsevier, v. 69, n. 10-11, p. 1160–1173, 2007.

NIEHOF, J. T.; MORLEY, S. K.; WELLING, D. T.; LARSEN, B. A. The spacepy space science package at 12 years. **Frontiers in Astronomy and Space Sciences**, Frontiers, v. 9, 2022.

NISHIDA, A. Coherence of geomagnetic dp 2 fluctuations with interplanetary magnetic variations. **Journal of Geophysical Research**, Wiley Online Library, v. 73, n. 17, p. 5549–5559, 1968.

NISHIDA, A. Geomagnetic dp 2 fluctuations and associated magnetospheric phenomena. **Journal of Geophysical Research**, Wiley Online Library, v. 73, n. 5, p. 1795–1803, 1968.

NOPPER, R. W.; CAROVILLANO, R. L. Polar-equatorial coupling during magnetically active periods. **Geophysical Research Letters**, Wiley Online Library, v. 5, n. 8, p. 699–702, 1978.

OLABODE, A. O.; ARIYIBI, E. A. Geomagnetic storm main phase effect on the equatorial ionosphere over ile–ife as measured from gps observations. **Scientific African**, Elsevier, v. 9, p. e00472, 2020.

ONOHARA, A. N.; BATISTA, I. S.; BATISTA, P. P. Wavenumber-4 structures observed in the low-latitude ionosphere during low and high solar activity periods using formosat/cosmic observations. *In*: COPERNICUS GMBH. **Annales Geophysicae**. **Proceedings** [...]. [*S.l.: s.n.*], 2018. v. 36, n. 2, p. 459–471.

OSSAKOW, S. L. Spread-f theories-a review. **Journal of Atmospheric and Terrestrial Physics**, Elsevier, v. 43, n. 5-6, p. 437–452, 1981.

OYAMA, K.-I.; BALAN, N.; WATANABE, S.; TAKAHASHI, T.; ISODA, F.; BAILEY, G. J.; OYA, H. Morning overshoot of te enhanced by downward plasma drift in the equatorial topside ionosphere. **Journal of geomagnetism and geoelectricity**, Society of Geomagnetism and Earth, Planetary and Space Sciences, v. 48, n. 7, p. 959–966, 1996.

PATRA, A. K.; CHAITANYA, P. P.; OTSUKA, Y.; YOKOYAMA, T.; YAMAMOTO, M.; STONEBACK, R. A.; HEELIS, R. A. Vertical exb drifts from radar and c/nofs observations in the indian and indonesian sectors: Consistency of observations and model. **Journal of Geophysical Research: Space Physics**, Wiley Online Library, v. 119, n. 5, p. 3777–3788, 2014.

PENNDORF, R. The average ionospheric conditions over the antarctic. **Geomagnetism and Aeronomy: studies in the ionosphere, geomagnetism and atmospheric radio noise**, Wiley Online Library, v. 4, p. 1–45, 1965.

PFAFF, R. F.; URIBE, P.; FOURRE, R.; KUJAWSKI, J.; MAYNARD, N.; ACUNA, M.; ROWLAND, D.; FREUDENREICH, H.; BROMUND, K.; MARTIN, S. The vector electric field investigation (vefi) on the c/nofs satellite. **Space Science Reviews**, Springer, v. 217, p. 1–88, 2021.

PRAKASH, S. Production of electric field perturbations by gravity wave winds in the e region suitable for initiating equatorial spread f. **Journal of Geophysical Research: Space Physics**, Wiley Online Library, v. 104, n. A5, p. 10051–10069, 1999.

QIAN, L.; BURNS, A. G.; SOLOMON, S. C.; WANG, W. Annual/semiannual variation of the ionosphere. **Geophysical Research Letters**, Wiley Online Library, v. 40, n. 10, p. 1928–1933, 2013.

RASTOGI, R. G. The effect of geomagnetic activity on the f2 region over central africa. **J. Geophys. Res**, v. 67, n. 4, p. 1367–1374, 1962.

RASTOGI, R. G.; PATEL, V. L. Effect of interplanetary magnetic field on ionosphere over the magnetic equator. **Proc. Indian Acad. Sci**, v. 82, n. 4, p. 121–141, 1975.

REEVES, G. D.; HENDERSON, M. C.; SKOUG, R. M.; THOMSEN, M. F.; BOROVSKY, J. E.; FUNSTEN, H. O.; BRANDT, P. C.; MITCHELL, D. J.; JAHN,

J. M.; POLLOCK, C. J. Image, polar, and geosynchronous observations of substorm and ring current ion injection. **GEOPHYSICAL MONOGRAPH-AMERICAN GEOPHYSICAL UNION**, AGU AMERICAN GEOPHYSICAL UNION, v. 142, p. 91–102, 2003.

REN, Z.; WAN, W.; LIU, L.; XIONG, J. Intra-annual variation of wave number 4 structure of vertical e× b drifts in the equatorial ionosphere seen from rocsat-1. **Journal of Geophysical Research: Space Physics**, Wiley Online Library, v. 114, n. A5, 2009.

RICHARDS, P. G.; MEIER, R. R.; CHEN, S.-P.; DROB, D. P.; DANDENAULT, P. Investigation of the causes of the longitudinal variation of the electron density in the weddell sea anomaly. **Journal of Geophysical Research: Space Physics**, Wiley Online Library, v. 122, n. 6, p. 6562–6583, 2017.

RICHARDS, P. G.; MEIER, R. R.; CHEN, S.-P.; DANDENAULT, P. Investigation of the causes of the longitudinal and solar cycle variation of the electron density in the bering sea and weddell sea anomalies. **Journal of Geophysical Research: Space Physics**, Wiley Online Library, v. 123, n. 9, p. 7825–7842, 2018.

RICHMOND, A. D.; LATHUILLERE, C.; VENNERSTRØM, S. Winds in the high-latitude lower thermosphere: Dependence on the interplanetary magnetic field. **Journal of Geophysical Research: Space Physics**, Wiley Online Library, v. 108, n. A2, 2003.

RILEY, P. **Electrodynamics of the low-latitude ionosphere**. [*S.l.*]: Rice University, 1994.

RISHBETH, H.; GARRIOTT, O. K. Introduction to ionospheric physics. **Introduction to ionospheric physics**, 1969.

RODRIGUES, F. S.; CROWLEY, G.; AZEEM, S. M. I.; HEELIS, R. A. C/nofs observations of the equatorial ionospheric electric field response to the 2009 major sudden stratospheric warming event. **Journal of Geophysical Research: Space Physics**, Wiley Online Library, v. 116, n. A9, 2011.

RÖTTGER, J. Wave-like structures of large-scale equatorial spread-f irregularities. **Journal of Atmospheric and Terrestrial Physics**, Elsevier, v. 35, n. 6, p. 1195–1206, 1973.

ROUT, D.; PANDEY, K.; CHAKRABARTY, D.; SEKAR, R.; LU, X. Significant electric field perturbations in low latitude ionosphere due to the passage of two consecutive icmes during 6–8 september 2017. **Journal of Geophysical Research: Space Physics**, Wiley Online Library, v. 124, n. 11, p. 9494–9510, 2019.

SAGAWA, E.; IMMEL, T. J.; FREY, H. U.; MENDE, S. B. Longitudinal structure of the equatorial anomaly in the nighttime ionosphere observed by image/fuv. **Journal of Geophysical Research: Space Physics**, Wiley Online Library, v. 110, n. A11, 2005.

ŠAULI, P.; ABRY, P.; ALTADILL, D.; BOŠKA, J. Detection of the wave-like structures in the f-region electron density: Two station measurements. **Studia Geophysica et Geodaetica**, Springer, v. 50, n. 1, p. 131–146, 2006.

SAVITZKY, A.; GOLAY, M. J. Smoothing and differentiation of data by simplified least squares procedures. **Analytical chemistry**, ACS Publications, v. 36, n. 8, p. 1627–1639, 1964.

SAZYKIN, S. **Theoretical studies of penetration of magnetospheric electric fields to the ionosphere. Available from Dissertations & Theses at Utah State University; ProQuest Dissertations & Theses Global**. 2000. Retrieved from. Available at: https://login. dist. lib. usu. edu/login?url=https://www. proquest. com/dissertations-theses/theoretical-studies-penetration-magnetospheric/docview/304634273/se-2.

SCHERLIESS, L.; FEJER, B. G. Storm time dependence of equatorial disturbance dynamo zonal electric fields. **Journal of Geophysical Research: Space Physics**, Wiley Online Library, v. 102, n. A11, p. 24037–24046, 1997.

SCHERLIESS, L.; FEJER, B. G. Radar and satellite global equatorial f region vertical drift model. **Journal of Geophysical Research: Space Physics**, Wiley Online Library, v. 104, n. A4, p. 6829–6842, 1999.

SCHERLIESS, L.; THOMPSON, D. C.; SCHUNK, R. W. Longitudinal variability of low-latitude total electron content: Tidal influences. **Journal of Geophysical Research: Space Physics**, Wiley Online Library, v. 113, n. A1, 2008.

SCHUNK, R. W.; NAGY, A. F. **Ionospheres: physics, plasma physics, and chemistry**. [*S.l.*]: Cambridge university press, 2009.

SEABOLD, S.; PERKTOLD, J. statsmodels: Econometric and statistical modeling with python. *In*: **9th Python in Science Conference**. **Proceedings** [...]. [*S.l.: s.n.*], 2010.

SENIOR, C.; BLANC, M. Convection in the inner magnetosphere-model predictions and data. **Ann. Geophys**, v. 5, p. 405–420, 1987.

SETTY, C.; GUPTA, A. B.; NAGPAL, O. P. Ionospheric response to internal gravity waves observed at delhi. **Journal of Atmospheric and Terrestrial Physics**, Elsevier, v. 35, n. 7, p. 1351–1361, 1973.

SHARP, D. H. Overview of rayleigh-taylor instability. Los Alamos National Lab. , NM (USA), 1983.

SINGH, S.; JOHNSON, F. S.; POWER, R. A. Gravity wave seeding of equatorial plasma bubbles. **Journal of Geophysical Research: Space Physics**, Wiley Online Library, v. 102, n. A4, p. 7399–7410, 1997.

SISCOE, G. L.; LOTKO, W.; SONNERUP, B. U. O. A high-latitude, low-latitude boundary layer model of the convection current system. **Journal of Geophysical Research: Space Physics**, Wiley Online Library, v. 96, n. A3, p. 3487–3495, 1991.

SPANN, J.; SWENSON, C. M.; DURAO, O.; LOURES, L.; HEELIS, R. A.; BISHOP, R.; LE, G.; ABDU, M. A.; KRAUSE, L.; FRY, C. The scintillation prediction observations research task (sport): an international science mission using a cubesat. 2017.

SPIRO, R. W.; WOLF, R. A.; FEJER, B. G. Penetrating of high-latitude-electric-field effects to low latitudes during sundial 1984. *In*: **Annales Geophysicae**. **Proceedings** [...]. [*S.l.: s.n.*], 1988. v. 6, p. 39–49.

SPIRO, R. W.; WOLF, R. A.; FEJER, B. G. Penetration of high-latitude-electric-field effects to low latitudes during sundial 1984. **Ann. Geophys**, v. 6, p. 39–50, 1988.

STOLLE, C.; LÜHR, H.; FEJER, B. G. Relation between the occurrence rate of esf and the equatorial vertical plasma drift velocity at sunset derived from global observations. *In*: COPERNICUS PUBLICATIONS GÖTTINGEN, GERMANY. **Annales Geophysicae**. **Proceedings** [...]. [*S.l.: s.n.*], 2008. v. 26, n. 12, p. 3979–3988.

STONEBACK, R. A.; HEELIS, R. A.; BURRELL, A. G.; COLEY, W. R.; FEJER, B. G.; PACHECO, E. Observations of quiet time vertical ion drift in the equatorial ionosphere during the solar minimum period of 2009. **Journal of Geophysical Research: Space Physics**, Wiley Online Library, v. 116, n. A12, 2011.

TAPPING, K. F. The 10. 7 cm solar radio flux (f10. 7). **Space weather**, Wiley Online Library, v. 11, n. 7, p. 394–406, 2013.

TAYLOR, M. J.; PAUTET, P. D.; MEDEIROS, A. F.; BURITI, R. A.; FECHINE, B. J.; FRITTS, D. C.; VADAS, S. L.; TAKAHASHI, H.; SABBAS, F. T. Characteristics of mesospheric gravity waves near the magnetic equator, brazil, during the spreadfex campaign. *In*: COPERNICUS GMBH. **Annales Geophysicae**. **Proceedings** [...]. [*S.l.: s.n.*], 2009. v. 27, n. 2, p. 461–472.

THAMPI, S. V.; BALAN, N.; LIN, C.-H.; LIU, H.; YAMAMOTO, M. Mid-latitude summer nighttime anomaly (msna)–observations and model simulations. *In*: COPERNICUS PUBLICATIONS GÖTTINGEN, GERMANY. **Annales Geophysicae**. **Proceedings** [...]. [*S.l.: s.n.*], 2011. v. 29, n. 1, p. 157–165.

TSUNOMURA, S. Numerical analysis of global ionospheric current system including the effect of equatorial enhancement. **Ann. Geophys**, v. 17, p. 692–706, 1999.

TSUNOMURA, S.; ARAKI, T. Numerical simulations of equatorial enhancement of geomagnetic sudden commencement. **Planet. Space Sci**, v. 32, n. 5, p. 599–604, 1984.

TULASI RAM, S.; AJITH, K. K.; YOKOYAMA, T.; YAMAMOTO, M.; NIRANJAN, K. Vertical rise velocity of equatorial plasma bubbles estimated from equatorial atmosphere radar (ear) observations and hirb model simulations. **Journal of Geophysical Research: Space Physics**, Wiley Online Library, v. 122, n. 6, p. 6584–6594, 2017.

TULASI RAM, S.; SU, S.-Y.; LIU, C.-H. Formosat-3/cosmic observations of seasonal and longitudinal variations of equatorial ionization anomaly and its interhemispheric asymmetry during the solar minimum period. **Journal of Geophysical Research: Space Physics**, Wiley Online Library, v. 114, n. A6, 2009.

VASYLIUNAS, V. M. The interrelationship of magnetospheric processes. *In*: SPRINGER. **Earth's Magnetospheric Processes: Proceedings of a Symposium Organized by the Summer Advanced Study Institute and Ninth ESRO Summer School, Held in Cortina, Italy, August 30-September 10, 1971**. **Proceedings** [...]. [*S.l.: s.n.*], 1972. p. 29–38.

VICKREY, J. F.; SWARTZ, W. E.; FARLEY, D. T. Postsunset observations of ionospheric-protonospheric coupling at arecibo. **Journal of Geophysical Research: Space Physics**, Wiley Online Library, v. 84, n. A4, p. 1310–1314, 1979.

WAN, W.; LIU, L.; PI, X.; ZHANG, M.-L.; NING, B.; XIONG, J.; DING, F. Wavenumber-4 patterns of the total electron content over the low latitude ionosphere. **Geophysical Research Letters**, Wiley Online Library, v. 35, n. 12, 2008.

WANG, W.; BURNS, A. G.; KILLEEN, T. L. A numerical study of the response of ionospheric electron temperature to geomagnetic activity. **Journal of Geophysical Research: Space Physics**, Wiley Online Library, v. 111, n. A11, 2006.

WANLISS, J. A.; SHOWALTER, K. M. High-resolution global storm index: Dst versus sym-h. **Journal of Geophysical Research: Space Physics**, Wiley Online Library, v. 111, n. A2, 2006.

WEI, Y.; ZHAO, B.; GUOZHU, L.; WAN, W. Electric field penetration into earth's ionosphere: a brief review. **Sci. Bull**, v. 60, n. 8, p. 748–761, 2015.

WHALEN, J. A. Linear dependence of the postsunset equatorial anomaly electron density on solar flux and its relation to the maximum prereversal e× b drift velocity through its dependence on solar flux. **Journal of Geophysical Research: Space Physics**, Wiley Online Library, v. 109, n. A7, 2004.

WHARTON, L. E.; SPENCER, N. W.; BRINTON, H. C. Correlations between neutral meridional winds and ion densities observed on ae-e. **Journal of Geophysical Research: Space Physics**, Wiley Online Library, v. 85, n. A9, p. 4653–4657, 1980.

WOLF, R. A. Effects of ionospheric conductivity on convective flow of plasma in the magnetosphere. **J. Geophys. Res**, v. 75, n. 25, p. 4677–4698, 1970.

WOLF, R. A.; HAREL, M.; SPIRO, R. W.; VOIGT, G. H.; REIFF, P. H.; CHEN, C. K. Computer simulation of inner magnetospheric dynamics for the magnetic storm of july 29, 1977. **J. Geophys. Res. Space Phys**, v. 87, n. A8, p. 5949–5962, 1982.

WOODMAN, R. F. Vertical drift velocities and east-west electric fields at the magnetic equator. **Journal of Geophysical Research**, Wiley Online Library, v. 75, n. 31, p. 6249–6259, 1970.

WOODMAN, R. F.; FARLEY, D. T.; BALSLEY, B. B.; MILLA, M. A. The early history of the jicamarca radio observatory and the incoherent scatter technique. **History of Geo-and Space Sciences**, Copernicus GmbH, v. 10, n. 2, p. 245–266, 2019.

WOODMAN, R. F.; HAGFORS, T. Methods for the measurement of vertical ionospheric motions near the magnetic equator by incoherent scattering. **Journal of Geophysical Research**, Wiley Online Library, v. 74, n. 5, p. 1205–1212, 1969.

XIONG, C.; LÜHR, H. The midlatitude summer night anomaly as observed by champ and grace: Interpreted as tidal features. **Journal of Geophysical Research: Space Physics**, Wiley Online Library, v. 119, n. 6, p. 4905–4915, 2014.

XIONG, C.; LÜHR, H.; FEJER, B. G. Global features of the disturbance winds during storm time deduced from champ observations. **Journal of Geophysical Research: Space Physics**, Wiley Online Library, v. 120, n. 6, p. 5137–5150, 2015.

XIONG, C.; LÜHR, H.; FEJER, B. G. The response of equatorial electrojet, vertical plasma drift, and thermospheric zonal wind to enhanced solar wind input. **Journal of Geophysical Research: Space Physics**, Wiley Online Library, v. 121, n. 6, p. 5653–5663, 2016.

XIONG, C.; LÜHR, H.; MA, S. Y. The magnitude and inter-hemispheric asymmetry of equatorial ionization anomaly-based on champ and grace observations. **Journal of Atmospheric and Solar-Terrestrial Physics**, Elsevier, v. 105, p. 160–169, 2013.

XIONG, C.; STOLLE, C.; MICHAELIS, I.; LÜHR, H.; ZHOU, Y.; WANG, H.; KERVALISHVILI, G.; RAUBERG, J. Correlation analysis of field-aligned currents from the magnetic measurements of grace follow-on mission. **Earth, Planets and Space**, Springer, v. 73, p. 1–13, 2021.

YANG, T.-Y.; PARK, J.; KWAK, Y.-S.; OYAMA, K.-I.; MINOW, J. I.; LEE, J. Morning overshoot of electron temperature as observed by the swarm constellation and the international space station. **Journal of Geophysical Research: Space Physics**, Wiley Online Library, v. 125, n. 2, p. e2019JA027299, 2020.

YIN, Y.; GONZÁLEZ-CASADO, G.; ROVIRA-GARCIA, A.; JUAN, J. M.; SANZ, J.; SHAO, Y. Summer nighttime anomalies of ionospheric electron content at midlatitudes: Comparing years of low and high solar activities using observations and tidal/planetary wave features. **Remote Sensing**, MDPI, v. 14, n. 5, p. 1237, 2022.

YIZENGAW, E.; MOLDWIN, M. B.; ZESTA, E.; BIOUELE, C. M.; DAMTIE, B.; MEBRAHTU, A.; RABIU, B.; VALLADARES, C. F.; STONEBACK, R. A. The longitudinal variability of equatorial electrojet and vertical drift velocity in the african and american sectors. *In*: COPERNICUS GMBH. **Annales Geophysicae. Proceedings** [...]. [*S.l.: s.n.*], 2014. v. 32, n. 3, p. 231–238.

ZENG, Z.; BURNS, A. G.; WANG, W.; LEI, J.; SOLOMON, S. C.; SYNDERGAARD, S.; QIAN, L.; KUO, Y.-H. Ionospheric annual asymmetry observed by the cosmic radio occultation measurements and simulated by the tiegcm. **Journal of Geophysical Research: Space Physics**, Wiley Online Library, v. 113, n. A7, 2008.

ZHANG, Y.; PAXTON, L. J. Space physics and aeronomy, ionosphere dynamics and applications. John Wiley & Sons, 2021.

ZOLESI, B.; CANDER, L. R. **Ionospheric prediction and forecasting**. [*S.l.*]: Springer, 2014.

FOLHA DE REGISTRO DO DOCUMENTO

^{1.} CLASSIFICAÇÃO/TIPO	^{2.} DATA	^{3.} DOCUMENTO Nº	^{4.} Nº DE PÁGINAS
TD	14 de agosto de 2024	DCTA/ITA/TD-038/2024	192

^{5.} TÍTULO E SUBTÍTULO:

A Long-term Quiet- and Storm-time Investigation of the Ionosphere using Satellite and Radar Data

^{6.} AUTORA(ES):

Sophia Rodrigues Laranja

^{7.} INSTITUIÇÃO(ÕES)/ÓRGÃO(S) INTERNO(S)/DIVISÃO(ÕES):

Instituto Tecnológico de Aeronáutica – ITA

^{8.} PALAVRAS-CHAVE SUGERIDAS PELA AUTORA:

Equatorial Ionosphere; Mid-latitude Ionosphere; Ionospheric Climatology; Ionospheric Disturbances; Ionosphere/Magnetosphere Interactions; Electric Fields; Ionospheric Structures.

^{9.} PALAVRAS-CHAVE RESULTANTES DE INDEXAÇÃO:

Ionosfera; Climatologia; Campos elétricos; Anomalias magnéticas; Magnetosfera; Medidas de densidade; Plasmas (Física); Física.

^{10.} APRESENTAÇÃO: (**X**) **Nacional** ( ) **Internacional**

ITA, São José dos Campos. Curso de Doutorado. Programa de Pós-Graduação em Física. Área de Dinâmica Não Linear e Sistemas Complexos. Orientador: Prof. Dr. Marco Antonio Ridenti. Coorientadores: Prof. Dr. Jayr de Amorim Filho e Prof. Dr. Bela G. Fejer. Defesa em 12/08/2024. Publicada em 2024.

^{11.} RESUMO:

The Earth's ionosphere exhibits the highest level of complexity in middle and low latitudes. To understand the physics of these regions, it is common to resort to experimental techniques and theoretical models. Therefore, this thesis investigates the fundamental processes at middle and low latitudes under both quiet and active geomagnetic conditions, utilizing experimental data and theoretical foundations for this purpose. Through the integration of satellite and ground-based data, three primary studies were conducted: the examination of ion density climatology using the FPMU (Floating Potential Measurement Unit) Langmuir probe on board the International Space Station, analysis of vertical drift velocity climatology utilizing the IVM (Ion Velocity Meter) on board the C/NOFS satellite, and investigation of equatorial perturbation electric fields during geomagnetic storms utilizing Jicamarca ISR (Incoherent Scatter Radar) data and empirical vertical drift models. Our findings from the ion density analysis revealed significant variations across seasons and longitudes, with notable anomalies observed during the solstices, including a newly found bulge in the equatorial ionization anomaly southern crest over the South Atlantic. Quiet-time vertical ion drift data near the equator showed significant seasonal and longitudinal variations due to factors like tropospheric nonmigrating tides, F region winds, and the geographic-geomagnetic equator displacement. Additionally, downward afternoon drifts were observed in all seasons, contradicting the existing knowledge of this region. During geomagnetic storms, common features included changes in equatorial electric fields driven by IMF Bz variations, substorms, and disturbance dynamo electric fields, with their strength varying based on factors like local time and solar wind intensity. Notably, during intense storms, the dominance of prompt penetration electric fields was prolonged, delaying the transition from upward to downward drifts. This thesis underscores the complex dynamics of the equatorial ionosphere, promoting the need for improved models to accurately predict the ionospheric responses to diverse geomagnetic conditions.

^{12.} GRAU DE SIGILO:

(**X**) **OSTENSIVO**   ( ) **RESERVADO**   ( ) **SECRETO**